Polariton quantum fluids in one-dimensional synthetic lattices : localization, propagation and interactions

Valentin Goblot

Polariton quantum fluids in one-dimensional synthetic lattices: localization, propagation and interactions

Thèse de doctorat de l'Université Paris-Saclay
préparée à l'Université Paris-Sud

École doctorale n°572
Ondes et Matière (EDOM)
Spécialité de doctorat: Optique et photonique

Thèse présentée et soutenue à Palaiseau, le 31/01/2019, par

Valentin GOBLOT

Composition du Jury :

M. Antoine BROWAEYS
Directeur de recherche, Institut d'Optique Graduate School   Président
Mme Anna MINGUZZI
Directrice de recherche, Université Grenoble-Alpes, CNRS   Rapporteur
M. Daniele SANVITTO
CNR Researcher, CNR Nanotec, Lecce (Italy)   Rapporteur
M. Quentin GLORIEUX
Maître de conférences, Sorbonne Université   Examinateur
Mme Päivi TÖRMÄ
Professor, Aalto University (Finland)   Examinateur
Mme Jacqueline BLOCH
Directrice de recherche, Université Paris-Saclay, CNRS   Directrice de thèse
M. Alberto AMO GARCIA
Chargé de recherche, Université de Lille, CNRS   Invité

Résumé

Les microcavités à semiconducteurs apparaissent aujourd'hui comme une plateforme particulièrement propice à l'étude des fluides quantiques en interactions. Dans ces cavités, la lumière et les excitations électroniques sont confinées dans de petits volumes et leur couplage est rendu si fort que les propriétés optiques sont gouvernées par des quasi-particules hybrides lumière-matière appelées polaritons de cavité. Ces quasi-particules se propagent comme des photons, mais interagissent avec leur environnement via leur partie matière. Elles peuvent occuper massivement un même état quantique et se comporter comme une onde macroscopique cohérente et non-linéaire. On parle alors de fluide quantique de lumière.

Dans cette thèse, nous étudions la dynamique de fluides quantiques de polaritons dans différentes microstructures unidimensionnelles. La technologie de gravure de microcavités planaires, développée au C2N, permet de réaliser une ingénierie complète du potentiel dans lequel nous générons ces fluides de polaritons et d'implémenter des géométries complexes.

Dans une première partie, nous avons étudié les propriétés de localisation des états propres de réseaux synthétiques quasi-périodiques. De tels réseaux, qualifiés de quasi-cristallins, sont connus pour présenter des propriétés de localisation d'une grande variété, notamment en raison de leur absence de périodicité. Par exemple, deux modèles célèbres de quasi-cristaux avec des propriétés très différentes sont le modèle de Fibonacci et le modèle de Aubry-André-Harper. Nous étudions le diagramme de phase de localisation des modes propres lors d'une déformation originale d'un quasi-cristal, une déformation continue entre ces deux modèles. L'exploration théorique de diagramme de phase a dévoilé une nouvelle transition de type délocalisation-localisation, transition que nous avons pu observer expérimentalement.

Une deuxième partie de la thèse est consacrée à l'étude de la dynamique non-linéaire de deux fluides contra-propageant dans un canal unidimensionnel. La compétition entre énergie cinétique et énergie d'interactions conduit alors à l'apparition de solitons sombres, dont le nombre discret et la position peuvent être contrôlés optiquement. La nature discrète de ces solitons, excitations non-linéaires d'un superfluide, est révélée par leur apparition et disparition brutale lors d'un scan de la puissance d'excitation, ainsi que lors d'un scan d'une différence de phase imprimée sur les deux fluides. Nous avons de plus mis en évidence une bistabilité

contrôlée par cette différence de phase.

La dernière partie du travail concerne l'étude des non-linéarités pour un fluide de polaritons occupant une bande plate. Une telle bande peut être obtenue par ingénierie d'un réseau de Lieb de micropiliers. Dans la bande plate, l'énergie cinétique du fluide est nulle, si bien que sa propagation est gelée. Nous observons alors la formation de domaines non-linéaires de taille quantifiée. Nous montrons que ces domaines appartiennent à une catégorie de solitons de gap spécifique, appelée ondes de Bloch tronquées. Nous mettons également en évidence une multistabilité entre domaines de différentes tailles lors du scan de la puissance d'excitation.

Ce travail ouvre des perspectives prometteuses, tout particulièrement pour l'exploration de phases topologiques de bosons en interactions. De plus, augmenter les interactions polariton-polariton permettrait de générer des états corrélés à plusieurs photons, et à plus long terme d'envisager l'utilisation de notre plate-forme comme un simulateur quantique.

Remerciements

Mes trois années de thèse (plus quelques mois), commencées au Laboratoire de Photonique et Nanostructure (LPN), qui devait par la suite devenir le Centre de Nanosciences et de Nanotechnologies (C2N), ont été riches sur le plan scientifique, mais également sur le plan humain. Je tiens ici à remercier l'ensemble des personnes qui ont contribué à mon travail, et sans qui je n'aurais pas pu mener cette thèse à bien.

Pour commencer, je remercie les membres de mon jury, pour avoir accepté de lire mon manuscrit et évaluer mon travail, pour leurs questions pertinentes et la discussion stimulante lors de la soutenance.

Je veux bien sûr remercier chaleureusement Jacqueline Bloch, qui a été ma directrice de thèse et m'a encadré pendant ces trois années. Par sa rigueur scientifique et sa confiance, elle a su toujours me pousser à rechercher une compréhension profonde des phénomènes observés, et fait comprendre qu'en sciences il vaut mieux privilégier la qualité à la quantité. Et le tout toujours dans la bienveillance et la bonne humeur.

Un grand merci également à Alberto Amo, qui a co-encadré mon travail avant son départ vers Lille. Son dynamisme et sa façon de toujours voir le côté positif des choses resteront pour moi un exemple à suivre. La complémentarité de ce duo avec Jacqueline m'a grandement aidé à surmonter les obstacles rencontrés.

Je remercie également Sylvain Ravets, qui a récemment rejoint le groupe en tant que permanent. J'ai eu grâce à lui le plaisir de découvrir la suite des aventures des gaz 2D d'électrons en cavité.

Une grande partie de ce travail de thèse repose sur des échantillons d'une qualité exceptionnelle, fabriqués dans les salles blanches du C2N. Je remercie ainsi Aristide Lemaître, qui réalise la croissance des échantillons, et Luc Le Gratiet, Abdou Harouri, et Isabelle Sagnes qui se chargent de la partie gravure (et fournissent de belles images SEM). Grâce à eux, j'ai pu m'initier un peu aux différentes techniques de salle blanche, qui étaient pour moi bien mystérieuses.

Il me faut aussi remercier les théoriciens avec qui j'ai pu collaborer au cours de mes différents projets: Iacopo Carusotto de l'université de Trento pour ses conseils sur les simulations et ses remarques avisées dans le cadre de l'étude des solitons sombres ; Oded Zilberberg de l'ETH Zürich, qui nous a proposé d'utiliser les polaritons pour explorer le diagramme de phase de localisation du modèle de Aubry-André-Haper-Fibonacci de quasi-cristaux, et ses étudiants Antonio Štrkalj et Jose Lado

Contents

Introduction

Quantum fluids are systems whose properties are governed by the laws of quantum mechanics, at a macroscopic scale. This definition can apply to many different systems, such as liquid helium or superconducting materials, but perhaps the most famous example are Bose-Einstein condensates (BEC) of cold atoms, in which a macroscopic number of atoms occupy a single quantum state and exhibit extended spatial coherence [1]. Predicted by Einstein in 1925 and first experimentally realized in 1995 [2], atomic BEC have allowed thorough exploration of the physics of quantum fluids, and their fascinating properties. A particularly rich situation occurs when inter-particle interactions are present. In this case, spectacular effects can be observed, such as superfluidity [3] and superconductivity [4].

Polaritons in semiconductor microcavities have recently emerged as a powerful platform for the study of quantum fluids [5]. In a semiconductor microcavity, the photonic mode of a semiconductor-based optical Fabry-Pérot cavity is coupled to the exciton transition of a quantum well embedded in the cavity. If the coupling strength between the two overcomes the loss, the regime of strong coupling is reached, in which a photon in the cavity can be emitted and re-absorbed several times in the quantum well before escaping the cavity. This process of coherent energy transfer between the photonic and excitonic modes is known as Rabi oscillations. In this situation, photons and excitons are no longer eigenstates of the system. The new eigenstates are quasiparticles called polaritons.

The first experimental observation of polaritons in semiconductor microcavities was reported in 1992, in a pioneering work of C. Weisbuch and Y. Arakawa [6]. Due to their hybrid light-matter nature, polaritons present a number of properties that have attracted a lot of interest following this first discovery. From their photonic part, they inherit a very light effective mass (induced by the vertical confinement of light in the optical cavity), whereas the excitonic part provides strong interactions. Additionally, polaritons behave as bosonic quasiparticles. Soon after their discovery, it was thus predicted that they could undergo bosonic condensation and macroscopically occupy a single quantum state [7], at temperatures much higher than in atomic condensates due to the low effective mass. First observations of bosonic stimulation effects were reported in the early 2000s [8, 9], and definitive experimental evidence for Bose-Einstein condensation of polariton was provided in 2006 by the groups of B. Deveaud and Le Si Dang [10]. This opened the way to the use of polaritons

as a platform for the study of interacting quantum fluids of light. Since polaritons are an intrinsically dissipative system, they allow for the exploration of the physics of quantum fluids out of thermal equilibrium. In the past decade, taking advantage of the strong nonlinearity brought by polariton-polariton interactions, a wide range of hydrodynamic effects have been observed, perhaps the most spectacular of them is superfluidity [11], but also the controlled nucleation of vortices [12–14], and solitons [15–17].

An additional degree of freedom of microcavity polaritons is the ability to engineer the eigenmodes and band structure. For example, at C2N, a technology for etching microstructure out of planar microcavities was developed. We can thus fabricate synthetic lattices, in which polaritons are strongly confined. In this way, careful design of the structure geometry allows emulating a wide range of 1D and 2D Hamiltonians. Several other techniques have been implemented by other groups to enable band structure engineering [18], offering the possibility to use polaritons as a very versatile photonic simulator [19]. In the recent years, studies of polaritons in 0D traps [20, 21], synthetic molecules of coupled pillars [22, 23], 1D potentials [24–26] and 2D lattices [27–29] have been reported.

In this thesis, we investigate the linear and nonlinear dynamics of polaritons fluids in various 1D microstructures. Etching 1D microstructures presents several advantages. First, it enables precise engineering of the band structure. Second, constraining the polariton flow in a 1D channel facilitates its manipulation. These two combined features open the way to the exploration of a large variety of fundamental physical problems. In the present work, we use 1D microstructures for polaritons to address a set of experimentally open questions, such as the localization of waves in quasiperiodic potentials, the response of a nonlinear polariton fluid to constraints on its kinetic energy at its boundaries, or the nonlinear dynamics of a quantum fluid in a system where its kinetic energy is completely quenched.

The present manuscript is organized as follows.

In the **first chapter**, we introduce the physics of microcavity polaritons. We describe their two basic components, photons confined in a cavity and excitons in a semiconductor quantum well, and discuss the conditions for strong coupling between the two. Polaritons are the quasi-particles resulting from this strong coupling. We detail the polariton-polariton interaction mechanism, and discuss the non-resonant and resonant excitation schemes for the injection of a polariton fluid. We also provide information on the experimental methods (sample structure, optical setup and optical characterization of planar samples).

The **second chapter** is dedicated to the confinement of polaritons in lower dimensional microstructures. We present the etching technique used at C2N to fabricate structures with designed geometry out of a planar sample. We show how this etching allows to emulate a wide range of Hamiltonians. In particular, Hamiltonian engineering can be based on two approaches: designing a 1D potential for polaritons, in a nearly-free particle approach, or forming arrays of coupled pillars, for a tight-binding approach.

In the **third chapter**, we use 1D microstructures for polaritons to study the linear localization properties of light in quasicrystals. We first consider two models of quasicrystals: the Fibonacci model, and the Aubry-Andryé-Harper model. These two models have been extensively studied, and are known to show very different localization properties. We investigate the localization properties in a family of quasicrystals obtained by continuously deforming one model into the other, following a theoretical proposal from Oded Zilberberg. In collaboration with his group, we establish a theoretical localization phase diagram in the continuous deformation, where the localization properties are so far unexplored. There, we identify a novel and unexpected delocalization phase transition. We then implement the model with 1D quasiperiodic microstructures for polaritons. Experiments in both non-resonant photoluminescence and resonant spectroscopy are used to reconstruct the experimental localization phase diagram, and in particular we evidence the presence of this exotic delocalization phase transition.

In the **fourth chapter**, we address the counter-propagation of two nonlinear polaritons fluids, injected in a 1D channel. At high excitation power, the interaction energy in the fluid competes with the kinetic energy, and the interplay between the two is responsible for a self-organization of the fluid into a train of dark solitons. When scanning the excitation power, the abrupt disappearance of solitons reflects the discrete nature of these nonlinear excitations. We also impose a phase twist across the wire, to accommodate additional kinetic energy into the fluid. We find that the phase twist controls the position of the soliton train, but also the parity of their number. We evidence a novel type of bistable behavior, appearing when scanning the phase twist up and down, at constant power.

In the **fifth chapter**, we study the nonlinear dynamics of a polariton fluid in a flat band. A flat band corresponds to infinite effective mass, and thus the kinetic energy is quenched in such a band. The influence of interactions in a flat band is still an open question experimentally. We engineer a 1D Lieb lattice of coupled micropillars, which hosts a flat band due to geometric frustration. Polaritons are directly injected into the flat band, using resonant excitation. In the nonlinear regime, due to the absence of kinetic energy, propagation of the fluid is frozen and we observe the formation of nonlinear domains of quantized size. The size of the domain increases with pumping power, and we report multistability of the domains. We show that the domains classify as Truncated Bloch Waves (TBW), a specific family of gap solitons. We thus report the formation of TBW in a driven dissipative context. We also discuss the influence of disorder on the behavior of the nonlinear fluid.

Finally, our results are summarized in the conclusion, and we discuss general perspectives of our work.

Contents

14

Introduction to microcavity polaritons

The first chapter of this thesis is dedicated to the presentation of microcavity polaritons. Polaritons are bosonic quasiparticles, arising from the strong coupling between photons confined in a cavity and excitons trapped in a quantum well. These two elementary components are described in sections 1.1 and 1.2. In section 1.3, we discuss the condition for the strong coupling regime, and show that when this regime is reached, polaritons emerge as new eigenstates of the system. These half-light half-matter quasiparticles interact via their excitonic component. The polariton-polariton interaction mechanism is detailed in section 1.4, and we discuss collective properties of polaritons fluids that arise from the combination of these interactions, their bosonic nature and finite lifetime. In particular, we consider two different excitation schemes: non-resonant and resonant excitation. Section 1.5 concludes this chapter with experimental details concerning the sample structure, optical setup and methods used to characterize our samples.

1.1 Confinement of light in optical cavities

In this section, we introduce the first component necessary to the formation of polaritons: optical microcavities in which photons are strongly confined along the z direction. Most of the properties of our microcavities can be understood from the simple Fabry-Pérot cavity with perfect mirrors. We first present the properties of such cavities. We then describe Distributed Bragg Reflectors and conclude with semiconductor microcavities.
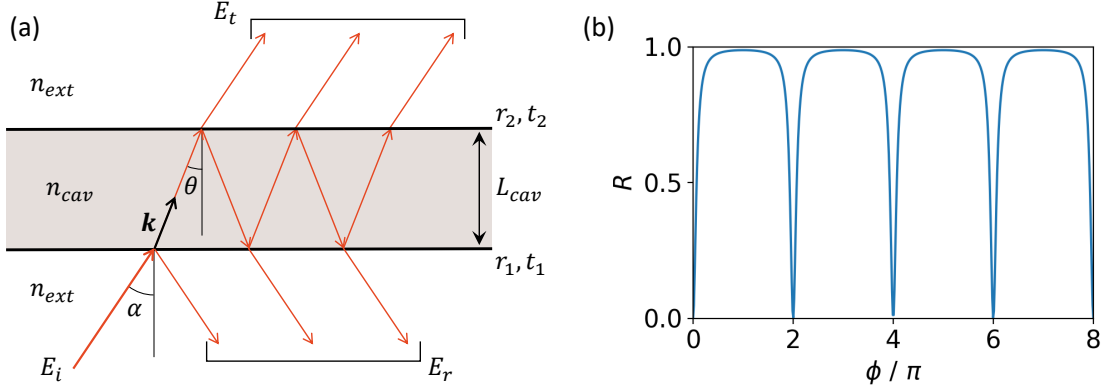
Figure 1.1: (a) Schematic representation of a Fabry-Pérot cavity. (b) Reflection coefficient R as a function of ϕ, calculated for $r_1^2 = r_2^2 = 0.8$.

1.1.1 Fabry-Pérot cavity

A Fabry-Pérot cavity, schematically illustrated in Fig. 1.1(a), consists in two mirrors, separated by a layer of length L_{cav} and optical index n_{cav}. The mirrors have reflectivity coefficients r_1, r_2 and transmission t_1, t_2.

The transmission and reflection properties of this cavity are the result of interferences due to multiple reflections of the incident field inside the cavity. Let us consider a plane wave, with complex amplitude E_i and wavelength λ in vacuum, incident on mirror 1 with an angle of incidence α. Snell-Descartes law gives the angle θ of propagation inside the cavity: $n_{ext} \sin \alpha = n_{cav} \sin \theta$ (in the following we consider $n_{ext} = 1$). The phase difference for the wave induced by a round-trip in the cavity is $\phi = 4\pi n_{cav} L_{cav} \cos(\theta)/\lambda$. Thus, the transmitted field writes:

$$E_t = E_i t_1 t_2 e^{i\phi/2} \sum_{j=0}^{\infty} (r_1 r_2 e^{i\phi})^j = E_i t_1 t_2 e^{i\phi/2} \frac{1}{1 - r_1 r_2 e^{i\phi}} \tag{1.1}$$

We deduce the transmission and reflection coefficients of the Fabry-Pérot cavity for the intensity:

$$T = \left| \frac{E_t}{E_i} \right|^2 = \frac{(t_1 t_2)^2}{1 + (r_1 r_2)^2 - 2 r_1 r_2 \cos \phi} \quad , \quad R = 1 - T \tag{1.2}$$

Note that we have neglected any source of loss (absorption in the mirror or layers, diffusion, etc.).

The reflection coefficient R is plotted as a function of ϕ in Fig. 1.1(b). Sharp reflectivity dips are observed for $\phi = 2\pi p$, with p integer, corresponding to destructive interference between the multiple reflections inside the cavity. In other words, a Fabry-Pérot cavity only transmits discrete modes, labeled with integer p. These resonances occur for wavelengths given by the relation

$$n_{cav} L_{cav} \cos(\theta) = \frac{p\lambda}{2} \tag{1.3}$$

In normal incidence, the free spectral range ΔE (energy difference between two modes) and full width at half maximum (FWHM) of a given mode γ_c are:

$$\Delta E = \frac{\pi \hbar c}{L_{cav} n_{cav}} \tag{1.4}$$

$$\gamma_C = \frac{\hbar c}{L_{cav} n_{cav}} \frac{1 - r_1 r_2}{\sqrt{r_1 r_2}} \tag{1.5}$$

Based on these quantities, we can define two figures of merit that characterize the cavity: the finesse $\mathcal{F}$ and the quality factor $\mathcal{Q}$, with

$$\mathcal{F} = \frac{\Delta E}{\gamma_C} = \pi \frac{\sqrt{r_1 r_2}}{1 - r_1 r_2} \tag{1.6}$$

$$\mathcal{Q} = \frac{E}{\gamma_C} = p\mathcal{F} = p\pi \frac{\sqrt{r_1 r_2}}{1 - r_1 r_2} \tag{1.7}$$

The finesse corresponds to the number of times a photon bounces off the mirrors before escaping the cavity. The photon stays in the cavity for a characteristic time $\tau = \hbar/\gamma_c = \hbar \mathcal{Q}/E$. Note that $\mathcal{F}$ is simply related to the characteristic of the mirrors, whereas $\mathcal{Q}$ depends on the considered mode p.

Finally, let us consider a plane wave with finite angle of incidence $\alpha \neq 0$. We note $\boldsymbol{k} = \boldsymbol{k}_z + \boldsymbol{k}_\parallel$ the wave vector of the incident field inside the cavity (see Fig. 1.1(a)). The norm of $\boldsymbol{k}$ is given by $k = \sqrt{k_z^2 + k_\parallel^2} = 2\pi n_{cav}/\lambda$. Given that $k_z = k \cos\theta$, the quantization condition from Eq. (1.3) transforms into:

$$k_z = \frac{p\pi}{L_{cav}} \tag{1.8}$$

The dispersion relation for the optical modes in the cavity is then given by:

$$E_C(\boldsymbol{k}) = \frac{\hbar c}{n_{cav}} \sqrt{\left(\frac{p\pi}{L_{cav}}\right)^2 + k_\parallel^2} \tag{1.9}$$

For small values of $k_\parallel \ll k$, this relation can be approximated as a parabola. This allows to define an effective mass m_{ph} for photons in the cavity:

$$E_C(k_\parallel) = \frac{p\hbar c\pi}{L_{cav} n_{cav}} + \frac{\hbar^2 k_\parallel^2}{2m_{ph}} \tag{1.10}$$

with

$$m_{ph} = \frac{p\hbar\pi n_{cav}}{cL_{cav}} \tag{1.11}$$

Due to the vertical confinement, photons in the cavity acquire a parabolic dispersion, i.e. a finite effective mass for their in-plane motion.
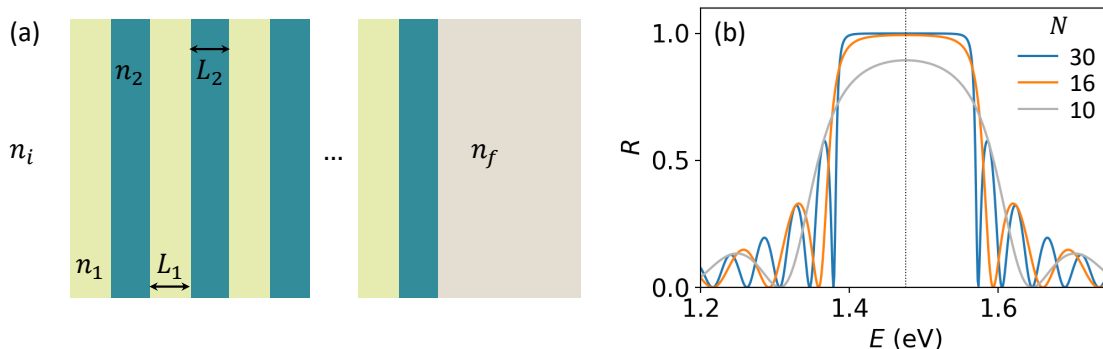
Figure 1.2: (a) Schematic representation of a Distributed Bragg Reflector. (b) Reflectivity spectrum of a AlAs/GaAs DBR, calculated with the transfer matrix method, at normal incidence and for different number of pairs N. The DBR is designed with $\lambda_{Bragg} = 840$ nm, indicated by the vertical dashed line.

1.1.2 Distributed Bragg Reflectors

In order to get a cavity with very high quality factor, i.e. long lifetime of the photons inside the cavity, it is necessary to use mirrors with very high reflectivity. This can be achieved with Distributed Bragg Reflectors (DBR), also known as Bragg mirrors.

A DBR consists in a periodic stack of dielectric layers with two different refractive index n_1, n_2, as depicted in Fig. 1.2(a). The layer thickness is chosen such that $L_1 n_1 = L_2 n_2$ (equal optical thickness). We consider a stack with N pairs of layers, in contact with a material of index n_i (n_f) on the incident (transmission) side.

The optical transmission and reflection properties of such a structure, arising from interference between multiple reflections at each interface, can be determined with the transfer matrix method [30]. We find that a DBR acts as a mirror with high reflectivity, on a broad energy range, called stop band.

In normal incidence, the reflectivity is maximal for the wavelength λ_{Bragg} such that $n_{1,2} L_{1,2} = \lambda_{Bragg}/4$. For $N \gg 1$, and considering $n_1 < n_2$, the reflectivity at λ_{Bragg} is approximately given by [30]:

$$R(\lambda_{Bragg}) \approx 1 - 4 \frac{n_i}{n_f} \left(\frac{n_1}{n_2} \right)^{2N} \tag{1.12}$$

The stop band is centered on λ_{Bragg}, and its FWHM in energy, noted δE, is proportional to the refractive index contrast:

$$\delta E = \frac{2\hbar c}{\lambda_{Bragg}} \frac{n_2 - n_1}{n_2 + n_1} \tag{1.13}$$

For example, in Fig. 1.2(b) we have computed the reflectivity at normal incidence of a GaAs/AlAs DBR, for different number of pairs N (we have used $n_{GaAs} = 3.54$, $n_{AlAs} = 2.96$). Increasing the number of pairs increases the reflectivity of the stop

band, allowing to get arbitrarily high reflectivity $R = 1 - \varepsilon$ for high N. Thus, DBR are an excellent choice, in view of fabricating cavities with high quality factor.

Different to the case of a metallic mirror, the electric field penetrates inside the structure. For a DBR with low index material first on the incident side (i.e $n_1 < n_2$, see Fig. 1.2(a)), the penetration length inside the mirror, at λ_{Bragg}, is given by:

$$L_{Bragg} = \frac{\lambda_{Bragg}}{2n_i} \frac{n_1 n_2}{n_2 - n_1} \tag{1.14}$$

The above definition of a penetration depth allows to take into account the energy-dependent phase for the reflected field $\phi(E)$:

$$\phi(E) \approx \frac{n_i L_{Bragg}}{\hbar c}(E - E_{Bragg}) \tag{1.15}$$

where $E_{Bragg} = hc/\lambda_{Bragg}$ is the energy corresponding to λ_{Bragg}. The DBR can thus be modeled as a mirror with zero thickness, and complex reflection coefficient r, with phase $\phi(E)$.

1.1.3 Bragg mirror microcavity

Finally, we consider the case of a microcavity formed by two DBR, separated by a layer of length L_{cav} and index n_{cav} (Fig. 1.3(a)). The exact optical transmission and reflection properties can be obtained by the transfer matrix method. An example of reflectivity spectrum in normal incidence is presented in Fig. 1.3(b). In the energy range corresponding to the DBR stop band, the structure behaves as a Fabry-Pérot interferometer, with highly reflective mirrors.

A very narrow reflectivity dip is observed at the center of the stop band. It corresponds to a cavity mode, with wavelength λ such that $n_{cav} L_{cav} = p\lambda/2$. Usually, the cavity and DBR are designed such that $\lambda = \lambda_{Bragg}$ (but this is not a necessary condition). From Eq. (1.5) and Eq. (1.13), we notice that the width of the stop band δE is narrower than the free spectral range ΔE of the cavity, explaining why a single mode is observed. Due to the almost unitary mirror reflectivity, very high quality factors $\mathcal{Q}$ can be achieved in GaAs-based semiconductor microcavities, typically above 200000.

The amplitude of the electric field inside the cavity can also be calculated with the transfer matrix method. The electric field distribution for a $\lambda/2$ cavity ($n_{cav} L_{cav} = \lambda/2$, i.e. $p = 1$) is shown in Fig. 1.3(c). The mode is confined within the cavity, with a strong enhancement of the field with respect to its value outside the cavity. Additionally, the field decays exponentially in each Bragg mirror, with a decay given by the penetration length L_{Bragg}.

1.2 Quantum well excitons

Semiconductor materials are characterized by the presence of an energy gap separating their conduction and valence bands. The ground state of the system corresponds
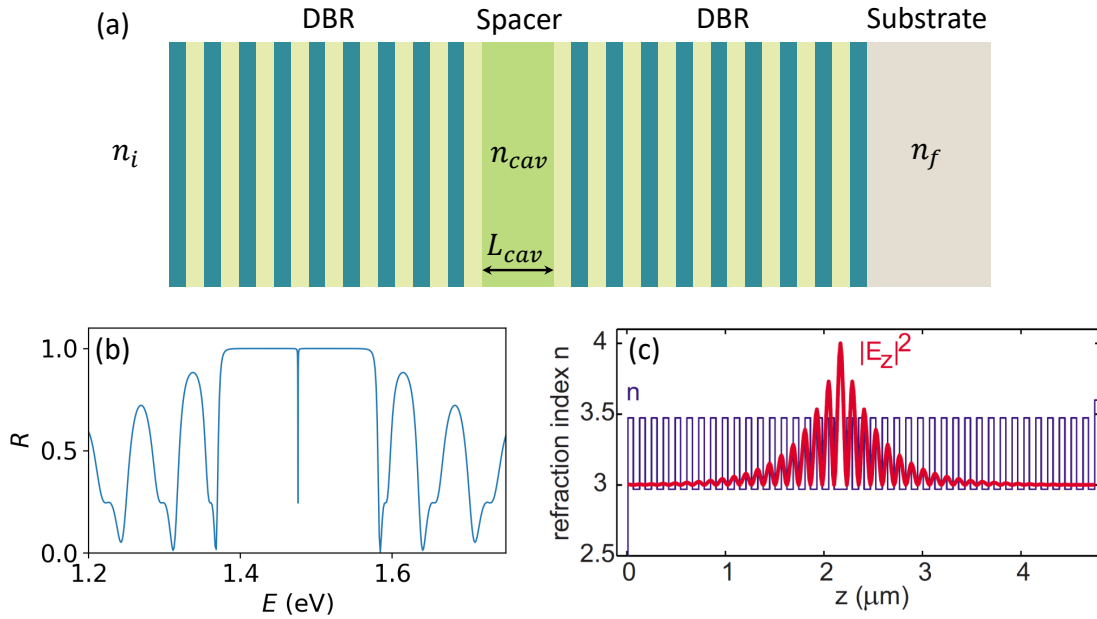
Figure 1.3: (a) Schematic representation of a microcavity. (b) Reflectivity spectrum, calculated at normal incidence, of a $\lambda/2$ microcavity with GaAs/AlAs mirrors (18 pairs) and AlAs spacer. The cavity mode is at $\lambda = 840$ nm (c) Electric field amplitude of the confined cavity mode (red line) and refractive index in the different layers (blue). Image taken from [31].

to a completely full valence band, and completely empty conduction band. However, in semiconductors the gap width is relatively small, such that an electron from the valence band can be easily excited to the conduction band, e.g. by applying a voltage or by optical excitation. In this case, the valence band lacks a single negative charge. This empty state in the valence band can be described as a quasi-particle of positive charge $+e$, referred to as hole. The elementary excitation of a semiconductor thus corresponds to the creation of an electron-hole pair. Taking into account attractive Coulomb interaction between the electron and hole, a bound state is formed, known as exciton [32]. In this section, we describe excitonic states both in bulk semiconductors and in the case of a quantum well, and discuss their coupling to the electromagnetic field.

1.2.1 Excitons in bulk semiconductors

In the bulk of a semiconductor with direct gap, each electronic band can be approximated by a parabola close to $k = 0$. In the conduction band, electrons can then de described as free particles with positive effective mass m_e, directly related to the curvature of the parabola. For the valence band, the negative band curvature corresponds to a positive hole effective mass m_h. Thus, the dispersion relations for
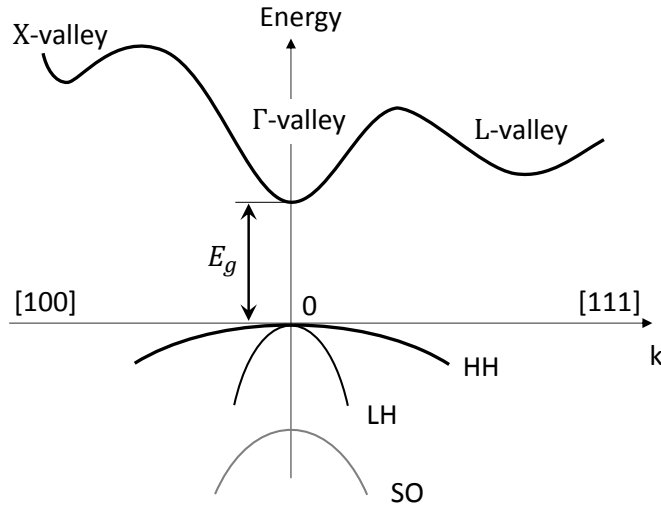
Figure 1.4: Schematic band structure of bulk GaAs. The bandgap is direct, with a minimum at Γ-point. The valence band is split into light- and heavy-hole bands (LH and HH, respectively). The split-off band (SO) is at lower energy and can be neglected. Note that at 4K, $E_g = 1.52$ meV. Figure reproduced from [33].

the conduction and valence bands can be written:

$$E_c(\boldsymbol{k}) = E_g + \frac{\hbar^2 k^2}{2m_e}$$
$$E_v(\boldsymbol{k}) = -\frac{\hbar^2 k^2}{2m_h}$$

$$(1.16)$$

where E_g is the energy gap width (and k is the norm of wave vector $\boldsymbol{k}$).

For example, the band structure of GaAs is represented in Fig. 1.4. Note that due to effects of the electron spin, the valence band is split into several subbands. Indeed, as for most semiconductors, GaAs has a unique conduction band, which corresponds to electronic states with total angular momentum $J = 1/2$. But for the valence band, the total angular momentum can take the values $J = 1/2$ and $J = 3/2$, giving rise to different bands. The band with $J = 1/2$ (split-off hole band) has lower energy than $J = 3/2$ and can be neglected. Additionally, the band with $J = 3/2$, is split into two subbands, corresponding to angular momentum projection $J_z = \pm 3/2$ and $J_z = \pm 1/2$. These subbands are degenerate at $k = 0$, but have a different effective mass: holes in the band $J_z = \pm 3/2$ ($J_z = \pm 1/2$) are called heavy holes (light holes), with mass m_{hh} (m_{lh}) such that $m_{hh} > m_{lh}$. In the following, we only consider the valence band with highest energy, i.e. the heavy hole band.

To describe the eigenstates of a single electron-hole pair, Coulomb interaction needs to be taken into account. The Hamiltonian of the system becomes:

$$H = E_g + \frac{p_e^2}{2m_e} + \frac{p_h^2}{2m_h} - \frac{e^2}{\kappa |r_e - r_h|}$$

$$(1.17)$$

where $\boldsymbol{p}_e$ and $\boldsymbol{r}_e$ (resp. $\boldsymbol{p}_h$ and $\boldsymbol{r}_h$) are the momentum and position vectors for the electron (hole). κ is the static dielectric constant of the bulk semiconductor.

It is convenient to work in the center of mass frame, introducing the center of mass position $\boldsymbol{R}$ and relative position $\boldsymbol{r}$, defined as:

$$\boldsymbol{R} = \frac{m_e}{M}\boldsymbol{r}_e + \frac{m_h}{M}\boldsymbol{r}_h, \quad \boldsymbol{r} = \boldsymbol{r}_e - \boldsymbol{r}_h \tag{1.18}$$

with $M = m_e + m_h$. The corresponding momenta are noted $\boldsymbol{P}$ and $\boldsymbol{p}$. We also define the reduced mass $\mu = m_e m_h / M$.

In the center of mass frame, H rewrites as the sum of two terms:

$$H = H_{cen} + H_{rel} \tag{1.19}$$

with:

$$H_{cen} = E_g + \frac{P^2}{2M} \tag{1.20}$$

$$H_{rel} = \frac{p^2}{2\mu} - \frac{e^2}{\kappa r} \tag{1.21}$$

These two terms commute with each other (as one depends only on $\boldsymbol{R}$, and the other on $\boldsymbol{r}$). Thus, the eigenstates of H take the form

$$\Psi_{\boldsymbol{K},n}(\boldsymbol{R},\boldsymbol{r}) = \frac{1}{\sqrt{V}} e^{i\boldsymbol{K}.\boldsymbol{R}} \phi_n(\boldsymbol{r}) \tag{1.22}$$

This form is the product of a plane wave with wave vector $\boldsymbol{K}$, eigenstate of H_{cen}, and an envelope function $\phi_n(\boldsymbol{r})$, eigenstate of H_{rel}. As the latter corresponds to an hydrogenoid Hamiltonian, the envelope functions $\phi_n(\boldsymbol{r}) = \phi_{nlm}(\boldsymbol{r})$ are the orbitals of an hydrogenoid atom ($1s$, $2s$, $2p$, etc.).

The $n = 1s$ state, with lowest energy, is given by $\phi_{1s}(\boldsymbol{r}) = e^{-r/a_B}/\sqrt{\pi a_B^3}$, where a_B is the exciton Bohr radius, that characterizes the spatial extension of the exciton:

$$a_B = \frac{\hbar^2 \kappa^2}{2\mu e^2} \tag{1.23}$$

In the end, we obtain the eigenenergies of the system:

$$E(\boldsymbol{K},n) = E_g + \frac{\hbar^2 K^2}{2M} - \frac{E_b}{n} \tag{1.24}$$

with $E_b = \hbar^2/2\mu a_B^2$ the binding energy of the $1s$ exciton.

Note that the above derivation also applies for the light hole, simply plugging the proper value of its effective mass. Thus, two different types of excitons exist, namely heavy-hole and light-hole excitons. They are described by the same formalism, but with different effective mass, and hence different Bohr radius and binding energy. The heavy-hole exciton is strongest bound. In GaAs, its Bohr radius is $a_B \approx 10$ nm and binding energy $E_b \approx 4$ meV. In particular because of this relatively low binding energy, excitons in GaAs can only be observed at cryogenic temperatures.
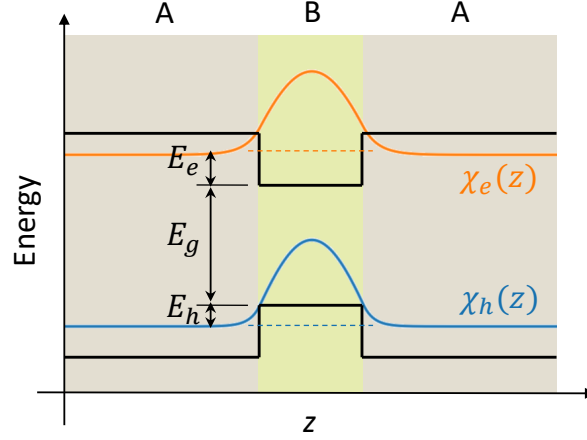
Figure 1.5:   Confined electron and hole states $\chi_e(z), \chi_h(z)$ in a semiconductor QW. Black lines: edges of the conduction and valence bands in materials A, B. The energies of the confined states are indicated by dashed lines.

1.2.2   Excitons in quantum wells

We now consider the case of a semiconductor quantum well, a heterostructure in which excitons are confined along one spatial direction z, while they are free to move in the (x, y) plane. A quantum well can be fabricated by growing a sequence of three 2D layers of semiconductors, where a material B, with a typical thickness comparable to the bulk exciton Bohr radius, is sandwiched between two layers of a material A characterized by a higher energy gap. The difference of energy gaps creates an effective potential well for the electrons and holes. This is illustrated in Fig. 1.5, in which the extrema of the valence and conduction bands in materials A and B are plotted along the growth direction z.

The addition of a confinement potential $V_{e,h}(z)$ along the z direction for electron and holes to the electron-hole pair Hamiltonian H (Eq. (1.17)) modifies the exciton wave function (as in the previous section, we only consider heavy holes). We can assume that these functions are separable in z and in-plane coordinates (x, y). Noting $\boldsymbol{\rho}_{e,r}$ the in-plane vector position, the coordinates in the in-plane center of mass frame are $\boldsymbol{R}_\parallel = (m_e \boldsymbol{\rho}_e + m_h \boldsymbol{\rho}_h)/M$ and $\boldsymbol{\rho} = \boldsymbol{\rho}_e - \boldsymbol{\rho}_h$. The excitonic wave functions are then of the form:

$$\Psi_{\boldsymbol{K}_\parallel, n}(\boldsymbol{R}_\parallel, \boldsymbol{\rho}, z_e, z_h) = \frac{1}{\sqrt{S}} e^{i\boldsymbol{K}_\parallel \cdot \boldsymbol{R}_\parallel} \chi_e(z_e) \chi_h(z_h) \phi_n(\boldsymbol{\rho}) \tag{1.25}$$

where $\boldsymbol{K}_\parallel$ is a wave-vector in the (x, y) plane. $\phi_n(\boldsymbol{\rho})$ are the solutions of a 2D hydrogenoid Hamiltonian (2D equivalent of Eq. (1.21)).

In the above expression, $\chi_e(z)$ and $\chi_h(z)$ are the ground-state solutions of the 1D Schrödinger equation for electrons and holes in the rectangular potential $V_{e,h}(z)$, represented in Fig. 1.5. The corresponding energies are noted $E_{e,h}$. Note that for

the values of potential well width and depth typical of GaAs quantum wells, a single confined state exists within, for both the electron and hole.

Finally, the exciton eigenenergies are given by:

$$E_n(\boldsymbol{K}_\parallel) = E_g + E_e + E_h + \frac{\hbar^2 K_\parallel^2}{2M} - \frac{E_b}{\left(n - \frac{1}{2}\right)^2} \tag{1.26}$$

If we consider the $1s$ exciton ($n = 1$), it has parabolic dispersion, with energy at $K = 0$ given by $E_X = E_g + E_e + E_h - 4E_b$.

We point out that the binding energy is modified with respect to the bulk case. This is because the Bohr radius a_B^* for a 2D hydrgenoid atom differs from the 3D case. More precisely, in a purely 2D case, we have $a_B^* = a_B/2$. Thus, the exciton binding energy in a quantum well is $E_b^* = 4E_b$. In real QW structures, the exciton is not exactly two-dimensional, and its binding energy is between E_b and $4E_b$. The confinement in the quantum well increases the overlap between the electron and hole wave functions with respect to the bulk, resulting in an enhancement of the exciton binding energy.

In this thesis, we will consider $In_x Ga_{1-x}As$ QW with low indium content, for reasons that are explained later. The binding energy of the exciton in a 8 nm QW with x = 0.05 indium fraction is $E_b^* = 7$ meV, corresponding to a Bohr radius $a_B^* = 10$ nm. Additionally, a QW with low indium content is only a shallow trap (due to the small difference of bandgap with GaAs). In particular, because the confinement energy of a particle in a well is inversely proportional to its mass, light holes are only weakly confined in shallow QWs. The only relevant excitons in our samples are thus heavy-hole excitons.

Finally, since their two constituents (electrons and holes), are fermions, it follows that excitons behave as bosonic quasiparticles. They have integer pseudo-spin. This is however only valid in the limit of low exciton densities. At high density, Coulomb attraction between electrons and holes is screened by the presence of a high number of particles, and excitons dissociate into a plasma of unbound electrons and holes [34–36]. This transition, happens for densities $n \sim a_B^{*-2}$, i.e on the order of 10^{11} cm^{-2} in GaAs [37]. All experimental situations discussed in this thesis are below this limit.

1.2.3 Exciton-photon coupling

Let us now describe the interaction between an exciton and light. The electron and hole in an exciton form a dipole, that interacts with the electromagnetic field. In the dipolar approximation, and in Coulomb gauge, the exciton-photon interaction Hamiltonian is:

$$H_{int} \approx -\frac{e}{m}\boldsymbol{p}.\boldsymbol{A} \tag{1.27}$$

where $\boldsymbol{p}$ is the momentum vector of an electron, with charge $-e$ and mass m, and $\boldsymbol{A}$ is the magnetic vector potential associated with the electromagnetic field.

An exciton can thus be created by photon absorption, or on the other way around a photon can be emitted by electron-hole recombination of the exciton. The probability of absorption or emission of a photon is directly proportional to the matrix element $\langle \boldsymbol{K}|\boldsymbol{p}.\boldsymbol{A}|0\rangle$, where $|0\rangle$ is the ground state and $|\boldsymbol{K}\rangle$ the excitonic state, with wave vector $\boldsymbol{K}$. This matrix element is non-zero only in specific cases, corresponding to a few selection rules that need to be satisfied for the optical transition to be allowed.

The first selection rule concerns conservation of angular momentum. Heavy-hole excitons can have angular momentum $J = \pm 1$ or $J = \pm 2$, since electrons in the conduction band have $J = \pm 1/2$ and heavy holes $J = 3/2$. As the a photon has angular momentum projection ± 1, conservation of angular momentum imposes $J = \pm 1$ for excitons to be coupled to the electromagnetic field. Excitons with $J = \pm 2$ do not radiate, they are called dark excitons.

Second, the in-plane wave vector is conserved. An exciton with wave vector $\boldsymbol{K}$ couples only to photons with same wave vector $\boldsymbol{k}_\parallel$ in the quantum well plane. As translational symmetry is broken in the z direction, no conservation rules apply to the wave vector component k_z of the photon, in contrast with excitons in bulk materials.

Finally, energy needs to be conserved. Together with conservation of in-plane wave vector, this imposes an upper bound on the exciton wave vector $\boldsymbol{K}$. The energy of a photon propagating with wave vector $\boldsymbol{k}$ in the well material, of index n, has energy $\hbar c k / n$ (so-called light cone). Recall that for the photon, $k^2 = k_\parallel^2 + k_z^2$ Thus, we define k_{rad} such that $\hbar c k_{rad}/n = E_X + \hbar^2 k_{rad}^2/2M$. In this way, k_{rad} corresponds to the intersection of the parabolic exciton dispersion with the light cone edge. For $K < k_{rad}$, the exciton energy is inside the light cone: there exist a value of $k_z > 0$ for the photon such that both energy and in-plane momentum conservation is fulfilled. This is no longer the case if the exciton energy is out of the light cone: excitons with $K > k_{rad}$ do not radiate.

In the case where the optical transition is allowed, the probability of the transition is characterized by the oscillator strength f, defined as:

$$f = \frac{2}{m\hbar\omega} \left|\langle \boldsymbol{K}|\boldsymbol{p}.\boldsymbol{A}|0\rangle\right|^2 \tag{1.28}$$

where $\hbar\omega$ is the energy of the transition.

1.3 Microcavity polaritons

We have presented the two building blocks of a microcavity structure for polaritons. Now, we address the strong coupling of excitons and photons in a cavity, achieved by inserting the QW at the center of the optical cavity. In the strong coupling regime, new eigenstates emerge, corresponding to half-light half-matter quasiparticles: cavity polaritons.

1.3.1 Strong light-matter coupling

In the previous section, we have detailed the coupling mechanism for excitons to the electromagnetic field. In particular, excitons can recombine by emitting a photon, with a probability related to the oscillator strength f.

Let us now consider the case where the quantum well is embedded inside a microcavity, with the cavity mode resonant with the excitonic transition. Upon exciton recombination, the photon is emitted in the mode of the cavity. Due to the high reflectivity of the cavity mirrors, the photon makes several round-trips inside the cavity and stays for a time $\tau_C = \hbar/\gamma_C$ before escaping. Thus, it has a finite probability of being re-absorbed in the QW, and create an exciton again. In this way, multiple emission and re-absorption events can occur before the photon finally escapes the cavity. This coherent transfer of a single excitation between the QW and the cavity mode is called Rabi oscillations. In particular, the oscillations correspond to a renormalization of the exciton and photon energies. This is the strong coupling regime, where the eigenstates of the system are no longer bare excitons and photons, but a superposition of both, which can be described as a quasi-particle known as polariton.

The conditions for the strong coupling regime can be expressed more formally, using a semi-classical description of the excitonic transition and cavity mode as two coupled Lorentz oscillators [38, 39]. The coupling strength between the two is

$$g_0 = \sqrt{\frac{2c\gamma_0}{n_{cav}L_{eff}}} \propto \sqrt{\frac{f}{L_{eff}}} \tag{1.29}$$

where γ_0 is the exciton radiative decay rate in the absence of the cavity, and $L_{eff} = L_{cav} + 2L_{Bragg}$ is the effective cavity length, that takes into account penetration of the electric field in the dielectric mirrors.

The coupling is essentially governed by two terms. First, the oscillator strength f, which depends on the local electric field amplitude at the position of the QW. Thus, the QW is placed at an anti-node of the intra-cavity field, where the electric field amplitude is maximal, to maximize the coupling. Second, g depends on the volume over which the electromagnetic fielc is confined, given by L_{eff}. The microcavity enables to reach very small mode volume, hence big g. The coupling can also be enhanced by inserting multiple quantum wells in the cavity (for N wells, the coupling scales as $\sqrt{N}$). In GaAs based cavity, couplings of few meV can thus typically be achieved.

The exciton-photon coupling lifts the degeneracy of the exciton and photon energy when their dispersions cross. The resulting energy splitting is called Rabi splitting Ω_R, or normal mode splitting. We have:

$$\Omega_R = 2\sqrt{g_0^2 - \frac{(\gamma_C^2 + \gamma_X^2)}{4}} \tag{1.30}$$

where γ_X is the non-radiative exciton decay rate. Note first that for $g_0 < (\gamma_C^2 + \gamma_X^2)/4$, Ω_R is purely imaginary. The coupling does not affect the real part of the eigenenergies, but modifies the decay rates of each mode (imaginary part of the eigenenergy). This is a regime of weak coupling. In the opposite case, when $g_0 > (\gamma_C^2 + \gamma_X^2)/4$, the dissipation is low enough for the coherent transfer of population between the oscillators, realizing the strong coupling regime. In practice, an empirical condition for the experimental observation of the strong coupling regime is to have the energy splitting bigger than the exciton and photon linewidth, i.e. $\Omega_R \gg \gamma_0, \gamma_C$. We can then make the approximation $\Omega_R \approx 2g_0$.

The first theoretical discussion of the strong coupling regime in solid state system was made by Hopfield in 1958 [40]. It was also largely explored in the field of atoms in a cavity, with the theoretical work of Jaynes and Cummings [41]. The first evidence of strong coupling in semiconductor microcavities with embedded QW was reported by the group of Weisbuch and Arakawa in 1992 [6], marking the experimental discovery of cavity polaritons.

1.3.2 Quantum description of polaritons

We now present a quantum mechanical description of polaritons, using the formalism of second quantization. The annihilation and creation operators for a photon with in-plane wave vector $\boldsymbol{k}$ are noted $a_{\boldsymbol{k}}^\dagger, a_{\boldsymbol{k}}$, and $b_{\boldsymbol{k}}^\dagger, b_{\boldsymbol{k}}$ for the exciton. They obey bosonic commutation relations. For simplicity, we will omit the z component of the photon wave vector.

The total Hamiltonian for exciton and cavity coupled with Rabi splitting Ω_R is $H = \sum_{\boldsymbol{k}} H_{\boldsymbol{k}}$, with:

$$H_{\boldsymbol{k}} = E_C(k)a_{\boldsymbol{k}}^\dagger a_{\boldsymbol{k}} + E_X(k)b_{\boldsymbol{k}}^\dagger b_{\boldsymbol{k}} + \frac{\Omega_R}{2}\left(a_{\boldsymbol{k}}^\dagger b_{\boldsymbol{k}} + b_{\boldsymbol{k}}^\dagger a_{\boldsymbol{k}}\right) \tag{1.31}$$

where $E_X(k), E_C(k)$ are the parabolic exciton and photon dispersions.

The Hamiltonian (1.31) can be diagonalized in the following way:

$$H_{\boldsymbol{k}} = E_{LP}(k)p_{\boldsymbol{k}}^\dagger p_{\boldsymbol{k}} + E_{UP}(k)q_{\boldsymbol{k}}^\dagger q_{\boldsymbol{k}} \tag{1.32}$$

where we have introduced the operators $p_{\boldsymbol{k}}^\dagger, q_{\boldsymbol{k}}^\dagger$, obtained form the photon and exciton operators by application of the unitary transformation

$$\begin{pmatrix} p_{\boldsymbol{k}}^\dagger \\ q_{\boldsymbol{k}}^\dagger \end{pmatrix} = \begin{pmatrix} c_k & x_k \\ -x_k & c_k \end{pmatrix} \begin{pmatrix} a_{\boldsymbol{k}}^\dagger \\ b_{\boldsymbol{k}}^\dagger \end{pmatrix} \tag{1.33}$$

The coefficients c_k, x_k are called Hopfield coefficients [40]. They are real positive,
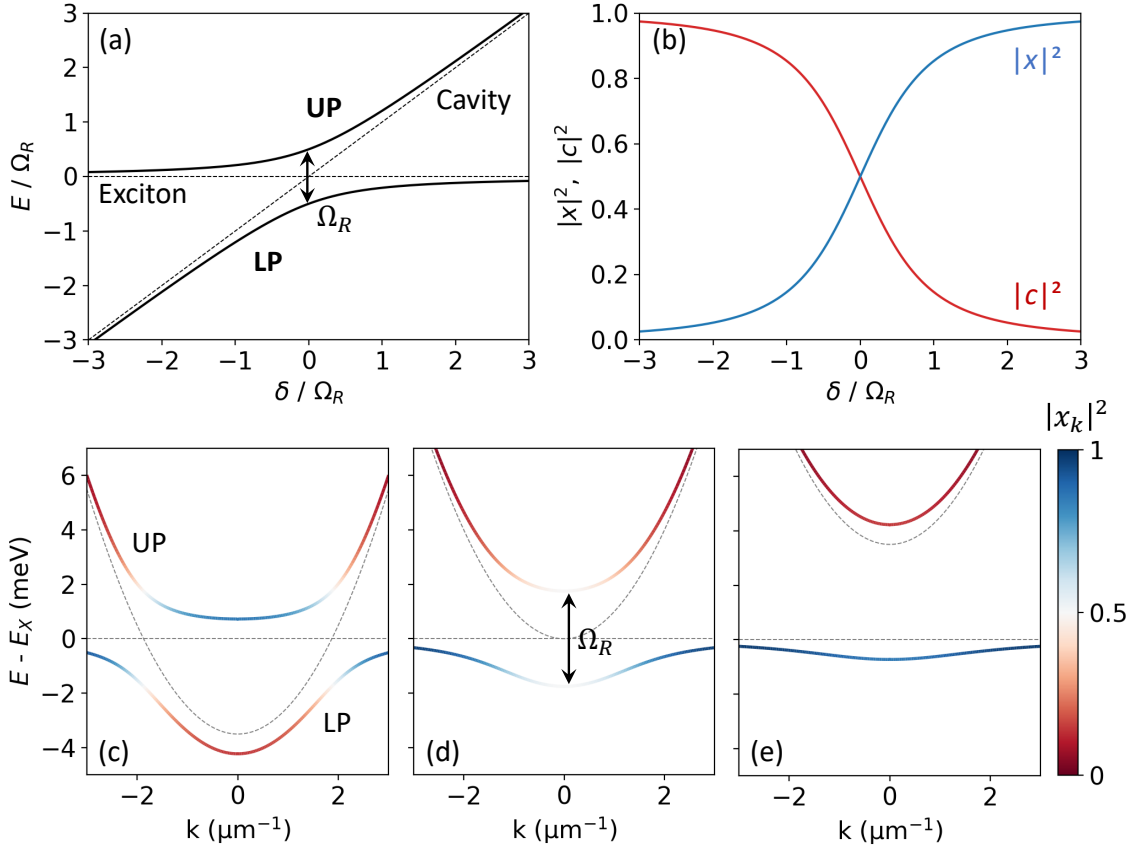
Figure 1.6: (a) Lower and upper polariton branches as a function of δ. Dashed lines correspond to bare exciton and cavity energies. (b) Corresponding excitonic and photonic fraction $|x|^2, |c|^2$ for the lower polariton. (c-e) Polariton dispersion, calculated with (c) $\delta(0) = -\Omega_R$, (d) $\delta(0) = 0$ and (e) $\delta(0) = +\Omega_R$. The color indicates the excitonic fraction of each branch. Dashed lines are the bare exciton and cavity dispersions.

depend only on the norm of $\boldsymbol{k}$, and are given by:

$$|x_k|^2 = \frac{1}{2}\left(1 + \frac{\delta(k)}{\sqrt{\delta(k)^2 + \Omega_R^2}}\right) \tag{1.34}$$

$$|c_k|^2 = \frac{1}{2}\left(1 - \frac{\delta(k)}{\sqrt{\delta(k)^2 + \Omega_R^2}}\right) \tag{1.35}$$

where $\delta(k) = E_C(k) - E_X(k)$ is the detuning between the cavity and exciton. Note that $|x_k|^2 + |c_k|^2 = 1$.

The operators $p_{\boldsymbol{k}}^\dagger, q_{\boldsymbol{k}}^\dagger$ are creation operators for new quasiparticles, eigenstates of the exciton-cavity coupling Hamiltonian, and referred to as lower and upper po-

lariton, respectively. Thus, a polariton is a coherent superposition of an exciton and a photon. The Hopfield coefficients $|x|^2, |c|^2$ give respectively the weight of the excitonic/photonic component for the lower polariton (the opposite for the upper polariton). For example, at $\delta = 0$, we have $|x|^2 = |c|^2 = 1/2$ for both the upper and lower polaritons, corresponding to maximally mixed half-light half-matter polaritons.

The eigenenergies of $H_{\boldsymbol{k}}$, corresponding to lower and upper polariton branches, are given by:

$$E_{LP,UP}(k) = \frac{1}{2}\left(E_C(k) + E_X(k) \mp \sqrt{\delta(k)^2 + \Omega_R^2}\right) \tag{1.36}$$

Note that $E_{LP}(k) < E_{UP}(k)$ (hence the denomination of "lower" and "upper" for the two branches).

The lower and upper polariton energy are plotted in Fig. 1.6(a) as a function of δ. An avoided crossing is observed close to $\delta = 0$, characteristic of the strong coupling. The minimal energy splitting between the lower and upper branches is Ω_R (occurring for $\delta = 0$). In Fig. 1.6(b), we show the excitonic and photonic fractions $|x|^2, |c|^2$ versus δ, for the lower polariton. Starting from $\delta < 0$, the lower polariton is almost completely photonic ($|c|^2 \approx 1$): the lower polariton coincides with the photonic mode. The excitonic fraction continuously increases as δ is increased, and for positive δ the lower polariton is exciton-like ($|x|^2 \approx 1$), meaning that it coincides with the exciton. The behavior is the opposite for the upper polariton.

Figure 1.6(c-e) represent the polariton dispersion for different values of $\delta(k = 0)$. In each case, the color of the line indicates the excitonic fraction $|x_k|^2$. The anti-crossing is observed at k such that $\delta(k) \approx 0$. The lower and upper polariton exchange their excitonic or photonic nature at the vicinity of the anti-crossing (Fig. 1.6(c)). Note also that the anticrossing is responsible for the apparition of an inflexion point in the lower polariton dispersion, where the band curvature becomes negative. Moreover, close to the bottom of their relative dispersion, in $k = 0$, both the lower and upper polariton can be approximated by a parabola, $E_{LP,UP}$. Taylor expansion of the polariton dispersion (1.36) around $k = 0$ allows determining the effective polariton mass $m_{LP,UP}$. For the lower polariton, we find:

$$\frac{1}{m_{LP}} = \frac{|x_0|^2}{M} + \frac{|c_0|^2}{m_{ph}} \tag{1.37}$$

where M, m_{ph} are the exciton and photon effective mass. Note that $M \gg m_{ph}$, so in general we can approximate $m_{LP} = m_{ph}/|c_0|^2$ (for cavity-exciton detuning $\delta(0) \lesssim 0$), typically on the order of $10^{-5} m_e$, where m_e is the electron mass. For the same reason, in all practical cases we can assume a flat exciton dispersion ($E_X(k) = E_X$).

So far, we have neglected the finite exciton and photon linewidth, in particular assuming $\Omega_R = 2g_0$. Finite lifetime due to dissipation can be accounted for in a simple way, by considering complex energies $E_j(k) - i\gamma_j$, with $j = X, C$, for

the exciton and cavity mode in the Hamiltonian (1.31). Also replacing $\Omega_R/2$ with g_0, diagonalization of H allows to retrieve Eq. (1.30) for the Rabi splitting value. More interesting, we find complex eigenenergies. The real part gives the polariton dispersion and is identical to Eq. (1.36). The imaginary part corresponds to the lower and upper polariton linewidth, $\gamma_{LP}(k), \gamma_{UP}(k)$. We find:

$$\gamma_{LP}(k) = |x_k|^2 \gamma_X + |c_k|^2 \gamma_C \tag{1.38}$$

$$\gamma_{UP}(k) = |c_k|^2 \gamma_X + |x_k|^2 \gamma_C \tag{1.39}$$

In general, the non-radiative exciton lifetime, $\tau_X = \hbar/\gamma_X$, exceeds hundreds of ps, while the cavity lifetime, $\tau_C = \hbar/\gamma_C$, is around 10 ps. Similar to the effective mass, we can thus consider $\gamma_{LP} \approx |c_k|^2 \gamma_C$.

1.3.3   Polariton pseudo-spin

Polaritons also possess a pseudo-spin degree of freedom, inherited from their components: excitons and photons. In particular, we have mentioned that only exciton with total angular momentum $J = 1$ couple to the electromagnetic field. The angular momentum projection for the exciton takes two possible values: $J_z = +1$, when the hole and electron have ($J_{z,h} = +3/2, J_{z,e} = -1/2$), and $J_z = -1$ for ($J_{z,h} = -3/2, J_{z,e} = +1/2$). If we note $|\uparrow\rangle, |\downarrow\rangle$ these two states, then in normal incidence, $|\uparrow\rangle$ is excited by photons with right circular polarization (σ^+), while $|\uparrow\rangle$ is excited by left circular polarization (σ^-).

Therefore, polaritons have total angular momentum $J = 1$, and only two values of the angular momentum projection are possible: $J_z = \pm 1$. More precisely, there is a one-to-one mapping between the polariton J_z and photons that escape the cavity: polaritons with $J_z = \pm 1$ emit (or are excited by) circularly polarized $\sigma^\pm$ photons. In consequence, polaritons behave as particles with pseudo-spin 1/2, and their pseudo-spin can be represented on the Bloch sphere. The polariton pseudo-spin can be reconstructed by measuring the polarization of photons emitted by the cavity.

The spin degree of freedom of polaritons is a valuable asset in the emulation of a wide range of Hamiltonians. For example, the formation of spin textures due to a form of spin-orbit coupling for polaritons has been reported [42]. In principle, we need to consider spin-dependent polariton operators $p_{\sigma,\boldsymbol{k}}$, where $\sigma = \pm 1$ describes the polariton spin in a chosen basis (e.g. circular left-right, or linear horizontal-vertical). However, in this thesis, we will only deal with experimental situations where the two spin components can be considered completely independent (i.e. there exists a pseudo-spin basis in which the system Hamiltonian is diagonal), and we omit the spin degree of freedom.

1.4   Nonlinear polariton fluids

In the previous section, we have introduced a single-particle Hamiltonian for polaritons in microcavities. However, a key asset of polaritons is that their excitonic

component brings strong nonlinearities, in the form of polariton-polariton interactions. In this section, we detail this interaction mechanism. We then discuss how this feature, in combination with the bosonic character of polaritons and their driven dissipative nature, makes of polaritons an ideal platform for the study of nonlinear Bose fluids, out of thermal equilibrium.

1.4.1 Polariton-polariton interaction

To understand polariton-polariton interactions, we first need to focus on exciton-exciton interactions. Indeed, Coulomb interactions between electrons and holes can be recast as a two-body contact interaction for excitons, given by the Hamiltonian [5]:

$$H_{XX} = \int d^2\boldsymbol{r} \frac{V_{XX}}{2} \hat{\Psi}_X^\dagger(\boldsymbol{r}) \hat{\Psi}_X^\dagger(\boldsymbol{r}) \hat{\Psi}_X(\boldsymbol{r}) \hat{\Psi}_X(\boldsymbol{r}) \tag{1.40}$$

where we have introduced the field operator for the exciton $\hat{\Psi}_X(\boldsymbol{r})$, defined as :

$$\hat{\Psi}_X(\boldsymbol{r}) = \frac{1}{\sqrt{V}} \sum_{\boldsymbol{k}} b_{\boldsymbol{k}} e^{i\boldsymbol{k}.\boldsymbol{r}} \tag{1.41}$$

The term V_{XX} is the effective interaction potential between two excitons. An approximation for the value of this coefficient was derived in Refs. [43, 44], and is:

$$V_{XX} \approx 6e^2 a_B^*/\epsilon \tag{1.42}$$

where a_B^* is the 2D exciton Bohr radius and ϵ the dielectric constant of the QW material. Note that the interaction constant V_{XX} is also often noted g_{exc} in the literature, which is the notation we use in the following.

The polariton-polariton interaction Hamiltonian is deduced by writing H_{XX} in the basis of lower and upper polariton operators. Considering only the lower polariton branch, and neglecting completely the upper polariton, we find an effective polariton-polariton contact interaction, with interaction constant:

$$g = |x|^4 g_{exc} \tag{1.43}$$

Note that $g > 0$, corresponding to repulsive interactions.

The precise determination of g_{exc} is challenging experimentally, especially at the single-particle level. In most cases, its value is thus inferred from the collective nonlinearity of a macroscopic polariton population. For this reason, values of g_{exc} varying over more than two orders of magnitude can be found in the literature, but estimations from different groups with different methods have converged towards the value $g \approx 30\mu\text{eV}.\mu\text{m}^2$ [45–48], in agreement with theoretical predictions [43].

Finally, in the above we have considered a single value for the exciton spin. Thus the interaction constant that we derived concerns only interactions between excitons of the same spin. Interactions between excitons with opposite spin also exist, but they are, in general, much weaker than same-spin interactions [49]. Here, we will neglect them.

1.4.2 Mean-field description

We have seen that polaritons have repulsive interactions due to their excitonic component, but in state-of-the-art GaAs based microcavities, the typical interaction energy g/A for two polaritons confined within an area A is below the polariton linewidth. This implies that effects of interactions at the single-particle level are very weak, preventing for example the observation of the theoretically proposed polariton blockade [50], even though intense efforts are currently under progress to reach this regime [47, 48].

However, nonlinear effects can still be observed, when the polariton population is high enough for the total interaction energy to be above the polariton linewidth. Thus, in the nonlinear experiments discussed in this thesis, we will always deal with relatively high polariton density (typically $10^2 - 10^3 \mu m^{-2}$). In this case, quantum fluctuations can be neglected, and a mean-field approach is sufficient to describe the system evolution. The main effect of interactions will be a local blueshift of magnitude gn of the polariton dispersion, where n is the local polariton density.

Here, we present the description of polaritons in the mean-field approximation. We focus on the lower polariton branch, neglecting the upper polariton. For simplicity, we omit indices LP in the notations.

We recall that the lower polariton field operator is given by:

$$\hat{\Psi}(\boldsymbol{r}) = \frac{1}{\sqrt{V}} \sum_{\boldsymbol{k}} \hat{p}_{\boldsymbol{k}} e^{i\boldsymbol{k}.\boldsymbol{r}} \tag{1.44}$$

with $\hat{p}_{\boldsymbol{k}}$ the annihilation operator for lower polariton with in-plane wave vector $\boldsymbol{k}$. The mean-field approximation consists in replacing $\hat{\Psi}(\boldsymbol{r}, t)$ with a classical field $\Psi(\boldsymbol{r}, t)$, where $\Psi(\boldsymbol{r}, t) = \langle \hat{\Psi}(\boldsymbol{r}, t) \rangle$. The coherent evolution of the wave function $\Psi(\boldsymbol{r}, t)$ is then given by the following nonlinear Schrödinger equation [5]:

$$i\hbar \frac{\partial \Psi(\boldsymbol{r}, t)}{\partial t} = \left(-\frac{\hbar^2}{2m} \nabla^2 + g|\Psi(\boldsymbol{r}, t)|^2 \right) \Psi(\boldsymbol{r}, t) \tag{1.45}$$

The above equation is also known as Gross-Pitaevskii equation [1], and is used to describe dilute Bose gases at low temperatures, as well as $\chi^{(3)}$ nonlinear optical media.

The Gross-Pitaevskii equation describes the evolution of a conservative system, but polaritons are an inherently dissipative system. To take losses into account, a non-hermitian term needs to be added to Eq.(1.45), resulting in the dissipative Gross-Pitaevskii equation:

$$i\hbar \frac{\partial \Psi(\boldsymbol{r}, t)}{\partial t} = \left(-\frac{\hbar^2}{2m} \nabla^2 + g|\Psi(\boldsymbol{r}, t)|^2 - i\frac{\hbar\gamma}{2} \right) \Psi(\boldsymbol{r}, t) \tag{1.46}$$

This additional term corresponds to particle loss with a rate γ.

As polaritons continuously escape the cavity, the system also needs to be pumped. Several pumping terms can be included in Eq. (1.46), corresponding to
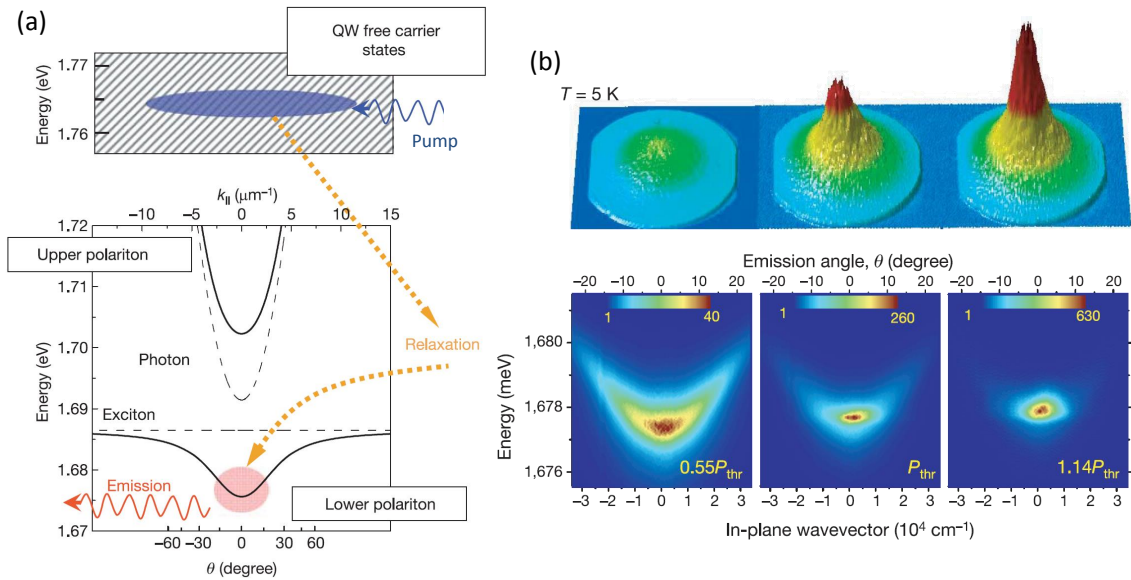
Figure 1.7: (a) Schematic representation of carrier relaxation under non-resonant excitation. (b) Evidence for polariton condensation in a CdTe based microcavity. Momentum-space resolved polariton emission for increasing pumping power, (bottom row) for the lowest polariton energy and (top row) corresponding full energy spectrum, along one direction. Both panels taken from [10]

different experimental configurations. Two types of pumping schemes can be distinguished: non-resonant excitation, and resonant excitation. They are described in the following sections.

1.4.3 Polariton condensation under non-resonant excitation

We first consider non-resonant excitation. In this scheme, illustrated in Fig. 1.7(a), the energy of the excitation laser is set far higher in energy than the lower polariton branch, typically ~ 100 meV, e.g. in first reflectivity dip on the high-energy side of the stop band of the cavity, and well above the semiconductor bandgap. Thus, the non-resonant laser creates free electron-hole pairs in the QW. These free carriers then relax towards lower energy states by acoustic and optical phonon emission, down to the exciton energy. Since high-momentum excitons do not radiate, they are long-lived (compared to other timescales of the system, in particular radiative), and consequently the relaxation of electrons and holes leads to the formation of an exciton reservoir. From this reservoir, further relaxation down to the lower polariton states occurs, assisted by acoustic phonon emission. As a result, all lower polariton states are populated.

Due to the bosonic nature of polaritons, stimulated relaxation can occur if the polariton occupation of a given state exceeds 1. This can be achieved by increasing the power of the non-resonant pump, and results in a macroscopically occupied

polariton state, a situation referred to as polariton laser. More specifically, if the relaxation rates are sufficiently large with respect to the radiative decay rate (photons escaping the cavity), bosonic stimulation occurs for the lowest energy state, at $k = 0$. In this case, we speak of a Bose-Einstein condensate of polaritons. Such a condensate, however, is strongly out of thermodynamic equilibrium, as it is the result of a dynamic balance between particles continuously escaping the cavity and excitons relaxing towards the condensate.

Bose-Einstein condensation of polaritons was first observed by the group of B. Deveaud and Le Si Dang in CdTe microcavities [10] (Fig. 1.7(b)). This work has sparked the interest in polaritons as a suitable system to study the physics of dilute Bose gases. Polariton condensation has since been reported by many other groups (see for example Ref. [31] for a review) and it has even been achieved at room temperature [51], using organic cavities with strong exciton binding energy.

The non-resonant pumping can be accounted for in Eq. (1.46) by adding gain as a non-Hermitian term, proportional to the density of excitons in the reservoir $n_R(\boldsymbol{r}, t)$. In this case, the dynamics of the exciton reservoir also needs to be taken into account. We get the following set of coupled equation [52]:

$$i\hbar\frac{\partial\Psi(\boldsymbol{r},t)}{\partial t} = \left(-\frac{\hbar^2}{2m}\nabla^2 + g|\Psi(\boldsymbol{r},t)|^2 + 2g_R n_R(\boldsymbol{r},t) - i\frac{\hbar}{2}(Rn_R(\boldsymbol{r},t) - \gamma)\right)\Psi(\boldsymbol{r},t)$$
(1.47)

$$\frac{\partial n_R(\boldsymbol{r},t)}{\partial t} = P(\boldsymbol{r}) - (\gamma_R + R|\Psi(\boldsymbol{r},t)|^2)n_R(\boldsymbol{r},t)$$
(1.48)

where $P(\boldsymbol{r})$ is the pumping rate, R the relaxation rate of the reservoir into the condensate, and γ_R the exciton loss rate. We have also added a term $2g_R n_R(\boldsymbol{r}, t)$ in Eq. (1.47), corresponding to interactions between polaritons and excitons in the reservoir. The exciton-polariton coupling constant is $g_R = |x|^2 g_{exc}$ (with $|x|^2$ the excitonic fraction at $k = 0$). Note that $g_R = |x|^2 g_{exc} > g$. Additionally, the exciton density in the reservoir is higher than the condensate polariton density. Thus, an important feature of non-resonantly pumped polariton condensates is that the interactions are in general dominated by interactions with the exciton reservoir, and polariton-polariton interactions are negligible. As we discuss in the next chapter, this issue can be circumvented by engineering a potential for polaritons, which allows to separate spatially the condensate from the exciton reservoir.

Finally, note that if the pump power is increased too much, strong coupling is bleached due to the screening of excitons in the QW, and in this case a conventional photon lasing regime is observed.

1.4.4 Resonant injection of polariton fluids

Another possible scheme of excitation is to use a laser in resonance (or quasi-resonant) with the lower polariton branch. In this case, polaritons are injected directly into the lower band, and their energy is fixed by the resonant pump. It is

also possible to control the velocity of the injected polaritons, by tuning the angle of incidence of the pump beam. An important advantage of this scheme is that the population of incoherent excitons in the reservoir is negligible in a first approximation, and we can reach regimes where the dynamics is governed by polariton-polariton interactions. For this reason, it is the scheme that we will use to inject and investigate the behavior of nonlinear polariton fluids in various one-dimensional potentials, in chapters 4 and 5.

The resonant pump is added in Eq. (1.46) as a coherent drive term $F(\boldsymbol{r}, t)$, proportional to the intra-cavity field of the pump laser, resulting in the driven-dissipative Gross-Pitaevskii equation [5]:

$$i\hbar \frac{\partial \Psi(\boldsymbol{r}, t)}{\partial t} = \left(-\frac{\hbar^2}{2m} \nabla^2 + g|\Psi(\boldsymbol{r}, t)|^2 - i\frac{\hbar\gamma}{2} \right) \Psi(\boldsymbol{r}, t) + iF(\boldsymbol{r}, t) \qquad (1.49)$$

This excitation scheme has been used to explore a great range of nonlinear phenomena. For example, optical parametric oscillations (OPO) [8, 53–55], bistability [56] and multistability [46, 57, 58], or squeezing [59] have been reported, similar to optical media with $\chi^{(3)}$ Kerr nonlinearity. But the possibility to inject a fluid with controlled velocity also enables to study quantum hydrodynamics effects. Perhaps one of the most spectacular of these effects is superfluidity, which has been reported in a resonantly injected polariton fluid [11]. Formation of bright solitons [17], integer and half-integer vortices [12, 13, 60], or dark solitons [15, 16, 61] have also been observed. A review of resonantly excited polariton fluids can be found in Ref. [5], and we also give a more detailed introduction to quantum hydrodynamics in chapter 4.

1.5 Experimental methods

In this section, we provide information on various aspects of the experimental methods used throughout this thesis: we detail the structure of our microcavity samples, present the optical experimental setup and finally discuss the optical characterization of planar samples.

1.5.1 Sample structure

The nominal structure of the different samples used in this thesis is presented in Fig. 1.8. It consists in a single 8nm $In_{0.05}Ga_{0.95}As$ QW, placed at the center of a λ cavity. The cavity mirrors have respectively 36 (40) pairs of $Al_{0.1}Ga_{0.9}As/Al_{0.95}Ga_{0.05}As$ layers on the top (bottom) side. Such a structure is optimized for experiments with resonantly injected nonlinear polariton fluids. This structure was designed according to the following criteria.

First, the use of a single QW is motivated by the objective of maximizing polariton-polariton interactions. In a structure with N QW, excitons in different

	Nominal structure		Repetition
	Material	Thickness (nm)	
Top mirror	$Al_{0.1}Ga_{0.9}As$	60.40	x36
	$Al_{0.95}Ga_{0.05}As$	70.30	
$\lambda/2$ cavity	GaAs	114.70	x1
	$In_{0.05}Ga_{0.95}As$	8.00	x1
	GaAs	114.70	x1
Bottom mirror	$Al_{0.95}Ga_{0.05}As$	70.30	x40
	$Al_{0.1}Ga_{0.9}As$	60.40	
Substrate	GaAs	-	-

Figure 1.8: Nominal structure of the microcavity samples.

QW do not interact with each other, and consequently the polariton-polariton interaction strength needs to be renormalized, as $g = |x|^4 g_{exc}/N$. We have already mentioned that increasing N increases the Rabi splitting, but at the very high expense of decreasing the interactions: we thus choose $N = 1$.

Second, we want to use resonant excitation to inject nonlinear polariton fluids in the cavity. In the case of resonant excitation, it is very convenient to work in transmission geometry, where the pump laser is focused on the top side and emission from the sample is collected through the back side. That way, the cavity acts as a filter for the resonant laser: the collected light only corresponds to polariton emission from the cavity. This implies that the GaAs substrate needs to be transparent for the wavelength of the bare exciton and cavity modes. The cavity mode energy is easily tuned by adjusting the spacer and mirrors thickness. For the QW, we use $In_xGa_{1-x}As$, which has a smaller bandgap than GaAs due to the addition of indium. In this way, the exciton energy is below the GaAs bandgap. We design a shallow QW, with x = 0.05 and thickness 8nm, embedded in a GaAs spacer. This ensures narrow linewidth for the exciton, typically around 0.5 meV.

Finally, we use a λ cavity, that has maximal field amplitude at its center. The QW is located at the position of this maximum. The mirrors and cavity spacer are designed for a nominal resonance wavelength $\lambda_0 = 840$ nm. Additionally, a wedge in the spacer and upper mirror thickness is introduced during the sample growth procedure, resulting in in-plane position-dependent energy of the cavity in the final 2D microcavity sample. The number of pairs gives a nominal quality factor approx. 75000 for the cavity mode, limited by residual absorption in the different layers.

The samples are grown by molecular beam epitaxy, in the clean room facilities of C2N. In particular, the samples used in this thesis result from the precious work of Aristide Lemaître, Elisabeth Gallopin and Carmen Gomez.

1.5.2 Experimental setup

A scheme of the setup used for micro-photoluminescence experiments, in transmission geometry, is shown in Fig. 1.9(a).

All the experiments discussed in this thesis are performed under continuous-wave (cw) excitation. To this end, we use a cw monomode Ti:Sapphire, tunable in the range 690-900 nm, and with linewidth below 10 MHz.

The samples are maintained at cryogenic temperatures. Two slightly different cryostat configurations were used in this thesis. In the experiments reported in chapter 3 and 4, the sample was pasted to the cold finger of a continuous-flow cryostat, where the flux of liquid helium was adjusted to reach a temperature of 10K. In chapter 5, the continuous flow cryostat was replaced with a closed-cycle cryostat. Here, the cold finger to which the sample is pasted is cooled down to 4K. In both cases, thermal conduction is assured by the use of a vacuum grease, and the cryostat chamber is under high vacuum with $10^{-5} - 10^{-6}$ mbar pressure.

The main difference between these two configurations concerns how light is focused on or collected from the sample. In the case of the continuous-flow cryostat, we use two microscope objectives with long working distance and high numerical aperture (NA = 0.55 to 0.65), as depicted in the inset of Fig. 1.9(a). The objectives have effective focal length 4 mm. On the other hand, the closed-cycle cryostat has a big inner chamber of diameter 30 cm. Thus, the objectives are replaced with single aspherical lenses, of same focal length and numerical aperture, placed inside the cryostat (Fig. 1.9(a)). This configuration presents the big advantage of reducing the level of vibrations and improves the image quality, with respect to objectives outside of the cryostat.

Finally, we have worked in transmission geometry, and collection and excitation side can be considered independently. On the excitation side, a half-wave ($\lambda/2$) plate associated with a polarizing beam-splitter (PBS) is used to control the pumping power, and a subsequent $\lambda/2$ plate controls the direction of linear polarization of the incident beam. A regular 50:50 beam-splitter (BS) allows to measure the pumping power.

On the collection side, the emission from the sample is collected by the objective (or lens), and focused on the entrance slit of a spectrometer. Note that the spectrometer can also be used as a normal imaging system, by measuring the 0th order of diffraction. A $\lambda/2$ plate and PBS are used for linear polarization selection of the emission. Neutral density (ND) filters can be used to reduce the light intensity on the CCD, and avoid saturation.

Two configurations allow to image either the near-field (real space) or far-field (momentum space) emission from the sample. These two configurations are illustrated in Fig. 1.9(b,c). For real-space imaging, Fig. 1.9(b), light emitted from a single position on the sample is focused on a single pixel on the CCD. An additional telescope and slit may be added on the optical path. A real image is formed in the focal plane of the telescope, where the slit is placed. This allows for spatial filtering
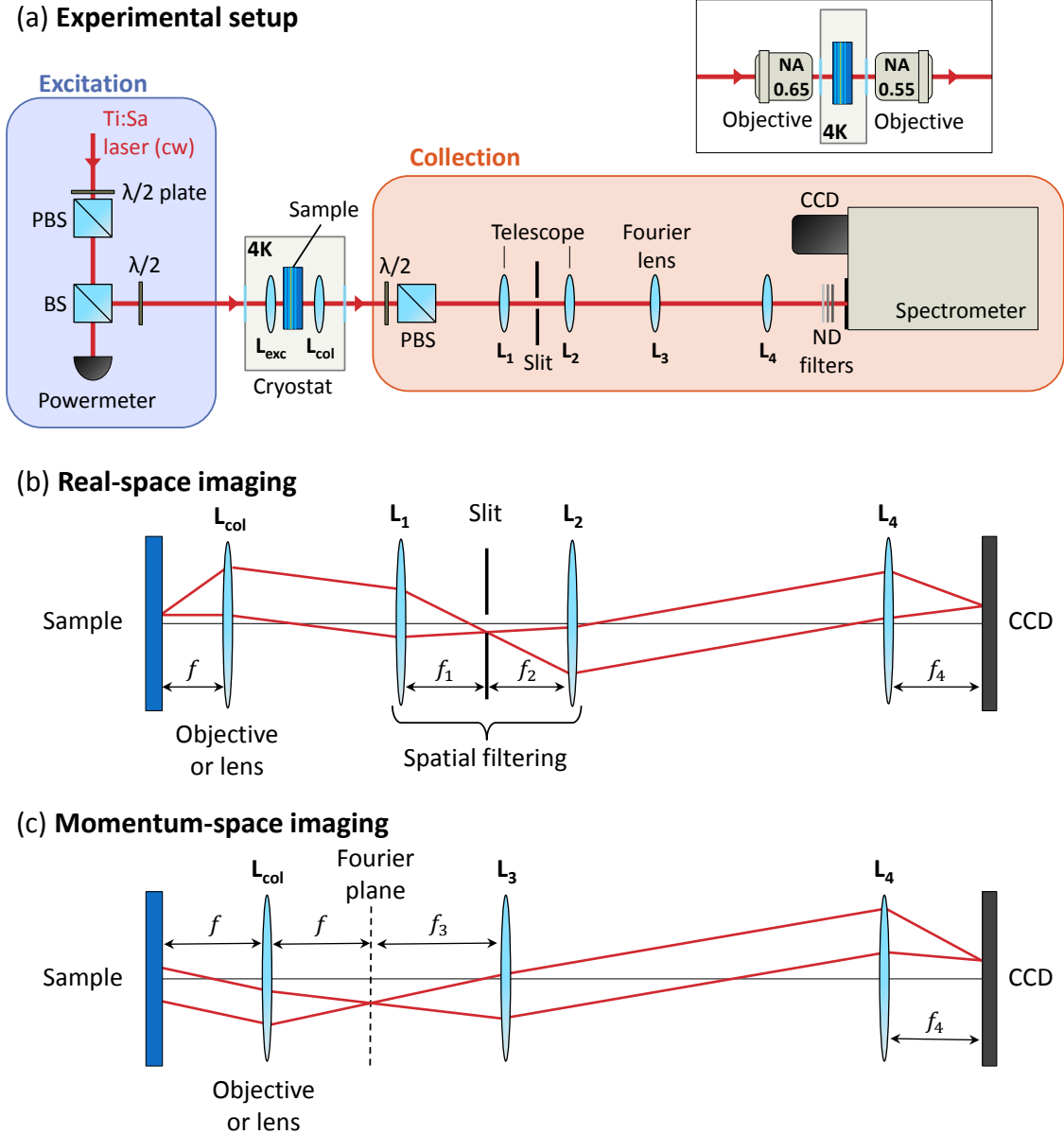
Figure 1.9: (a) Schematic representation of the experimental setup, in transmission configuration. The sample is placed inside the chamber of a closed-cycle cryostat. Inset: with a continuous-flow cryostat, excitation and collection are achieved with long-working distance objectives outside the cryostat. (b),(c) Collection setup for (b) real- and (c) momentum-space imaging. The optical path of two different rays is shown, illustrating the principle of each measurement scheme. Note that when using a microscope objective, the distance between the sample and L_{col} is the objective working distance d, different from its effective focal length f.

Int. (a.u.): 0 ___ 1
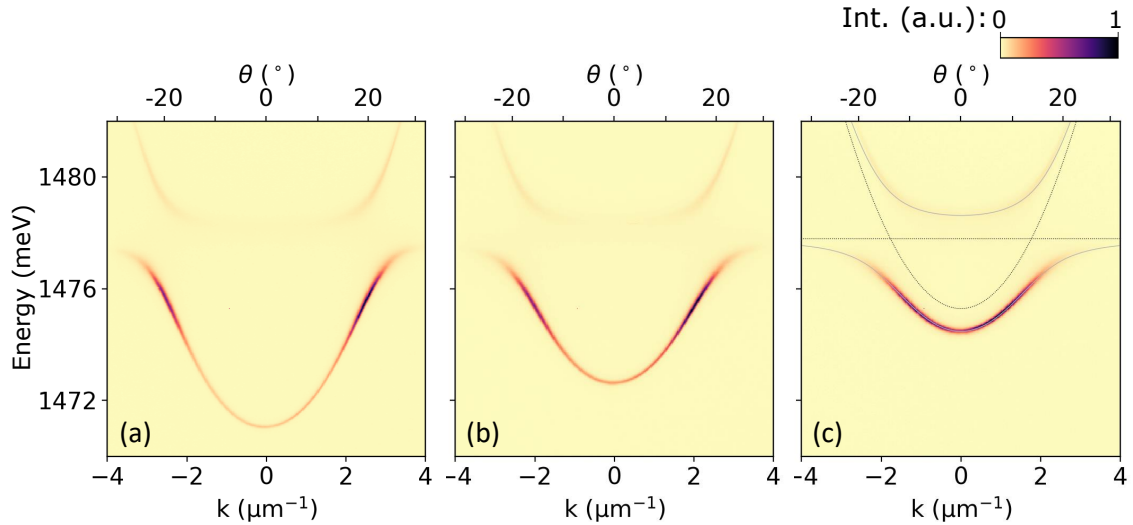
Figure 1.10: Momentum-space photoluminescence spectra, measured at three different positions on a planar microcavity sample, corresponding to three values of the cavity-exciton detuning δ. Angles of emission θ are also indicated. In panel (c), solid lines are the theoretical lower and upper polariton dispersions. Dashed lines denote the bare cavity and exciton energies.

of the image.

For momentum-space imaging, a lens is placed to image the Fourier plane of the objective (Fourier lens L_3). That way, rays emitted from the sample with same angle of emission arrive on the same position on the CCD. It is also possible to measure selectively momentum-space emission after spatial filtering. In this case, it is necessary that L_1 is placed at a distance $f + f_1$ from L_{col} (i.e. L_1 images the Fourier plane of L_{col}.

Note that the setup represented in Fig. 1.9(a) depicts the minimal experimental setup, but in practice the optical setup is highly modular. In the following chapters, it will be adapted for the purposes of the different experiments: addition of a cylindrical lens on the excitation side to create an extended excitation spot, splitting of the incident beam to create multiple spots, addition of an interferometer on the collection side, and so on.

1.5.3   Characterization of planar samples

To conclude this chapter, we discuss the characterization of planar microcavity samples. This characterization is performed under non-resonant excitation. The advantage of the non-resonant excitation scheme is that it enables to populate all the energy states of the system. Under weak pumping power, we can thus have access to all linear eigenstates at once, using the spectrometer to resolve spectrally the photoluminescence (PL) from the cavity (the weak pumping power ensures that we do

not create a significant exciton reservoir, which would blueshift modes locally). For a non-resonant excitation, we set the laser energy to 780 nm (i.e. around 1.6 eV). Additionally, the in-plane polariton wave vector is conserved when a photon escapes the cavity. Thus, angle-resolved measurements of the PL emission provide direct information on the polariton dispersion inside the cavity. For a polariton (photon) with energy E, the relation between the angle of emission outside the cavity θ and in-plane wave vector k is given by $E = \hbar ck/\sin\theta$

Figure 1.10 shows the PL spectrum, resolved in energy and momentum-space, measured on three different positions of a single sample under non-resonant excitation. In each case, the lower and upper polariton branches are identified, with a clear avoided crossing between the two. From each dispersion, we can extract the different parameters of the system: bare exciton energy, E_X, bare cavity energy at $k = 0$, $E_C(0)$, Rabi splitting Ω_R and photon effective mass m_{ph}. The theoretical polariton dispersions for Fig. 1.10(c) are plotted in solid gray lines (dashed lines for bare exciton and cavity energy). The parameters used for these fits are $E_X = 1478.62$ meV, $E_C(0) = 1474.47$ meV, $\Omega_R = 3.3$ meV and $m_{ph} = 4.8 \times 10^{-5}\ m_e$, with m_e the free electron mass.

The three spectra from Fig. 1.10 are well fitted with the same Rabi splitting and photon mass. However, due to the wedge in the cavity introduced during growth, the cavity energy varies with position on the sample. Note that the exciton energy is also slightly dependent on position (there is a small wedge for the QW as well), but much less than the cavity. In conclusion, the wedge allows to tune the cavity-exciton detuning $\delta = E_C(0) - E_X$, which is in particular very useful to probe different excitonic fractions for the lower polariton branch at $k = 0$. The typical detuning gradient in our samples is ~ 6 μeV.μm^{-1}.

Polaritons in low-dimensional microstructures

In this chapter, we present how the potential landscape for polaritons can be designed at will in confined microstructures. Creating a controlled potential is a key asset of microcavity polaritons, as it offers the possibility to engineer the band structure and emulate elaborate Hamiltonians. In this way, polaritons emerge as a versatile platform for photonic simulation. For example, they allow to simulate the physics of electrons in solid state material, and deepen our understanding of their physical properties. New effects, such as exotic transport properties, can even be observed, by engineering artificial Hamiltonians.

We begin with a review of the different experimental techniques that have been developed to implement and control potential landscapes for polaritons. In our group, we developed a technology allowing to etch microstructures out of planar cavities. The etching confines polaritons in structures with lowered dimensionality. We show how this can be used to tailor band structures for polaritons, considering two approaches. We first consider a nearly-free particle approach: we demonstrate how one-dimensional structures can be mapped to a 1D effective potential, determined by the lateral width of the structure. Then, we present a tight-binding approach, relying on arrays of coupled pillars, which offers a very flexible method to emulate a great variety of tight-binding Hamiltonians.

2.1 Potential engineering for polaritons

Several techniques have been implemented to engineer potential landscapes for polaritons. Here we briefly present these techniques. A more comprehensive review can be found in Ref. [18]. On a general level, the different methods can be separated in two categories: either the potential is induced by acting on the excitonic component of polaritons, or on their photonic component.
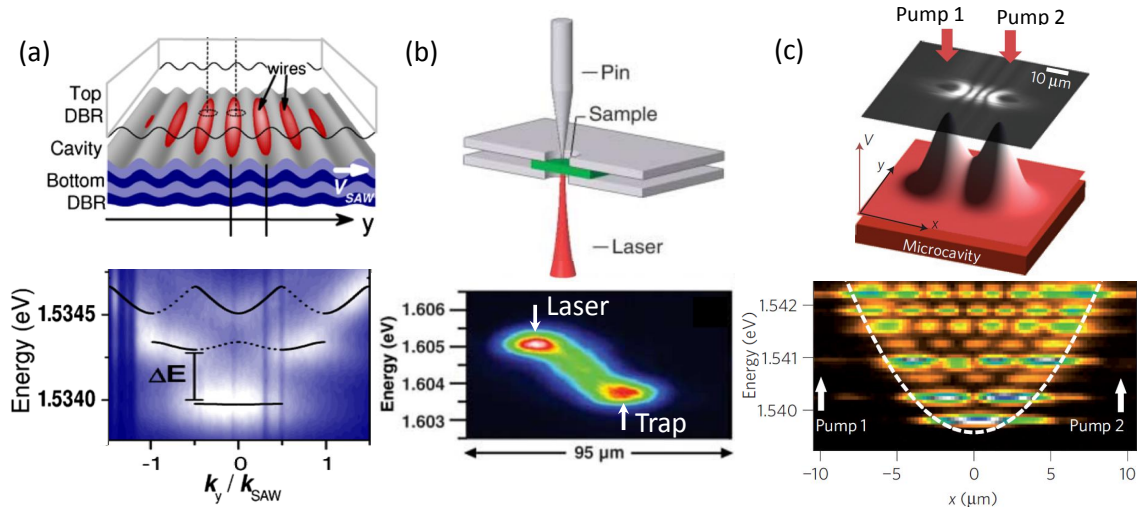
Figure 2.1: Techniques to create an excitonic potential for polaritons: (a) Surface Acoustic Waves, (b) pressure-induced trap and (c) optically-induced exciton reservoir. Images taken respectively from [27], [20] and [62].

2.1.1 Potential induced by the excitonic component

Figure 2.1 summarizes the techniques that act on the excitonic component for the creation of a potential for polaritons.

The first technique, illustrated in Fig. 2.1(a) relies on Surface Acoustic Waves (SAW), and was developed by the group of P. Santos. The exciton energy is sensitive to strains of the material (e.g. GaAs), thus application of a SAW creates a periodic modulation of the exciton energy due to the periodic deformation. The periodic modulation is responsible for a folding of the polariton dispersion along the SAW propagation direction. Note that strictly speaking, the SAW also affects the photonic component by introducing a change in the thickness and refractive index of the cavity layer, but the amplitude of the energy shift is weaker than for the excitonic component. Using this technique, polariton condensation has been reported in 1D and 2D dynamical acoustic lattices [27, 63].

A second technique, that also involves sensitivity of the exciton energy to strain fields, is to apply mechanical pressure on the back of the sample with a tip, as illustrated in Fig. 2.1(b). This technique was developed by the group of D. Snoke. The pressure induces a lowering of the exciton energy at the position of the tip. For example, this technique has been used to trigger polariton condensation in a local trap, spatially separated from the exciton reservoir [20]. As shown in Fig. 2.1(b), lower panel, when the non-resonant pump is located away from the tip position, a polariton flow is observed towards the minimum of the pressure-induced trap (together with an energy relaxation towards the bottom of the trap). The main drawback of this technique is that is does not allow for complex potential geometries.

Finally, a potential arising from the excitonic component can be induced op-

tically, as illustrated in Fig. 2(c). A non-resonant pump beam creates a spatially localized exciton reservoir. At the position of the pump, exciton-exciton interactions cause a local blueshift of the exciton energy, acting as a repulsive potential for polaritons. One of the first group to use this strategy was the group of A. Bramati, to create defects and control optically the flow of a polariton fluid [13, 64]. The technique has been also employed in many other groups [25, 65–67], for example with two pump beams to create a local trap [62], as shown in Fig. 2.1(c) where the different confined modes are visible in the real-space energy spectrum (lower panel), or with periodic arrangements of pump beams to generate 2D lattices [68, 69]. This technique offers the advantage of being all-optical, providing a very good control over the potential geometry. On the other hand, a drawback is that it relies on non-resonant excitation, and thus results in polariton injection correlated with the potential geometry. This can have important effects on the dynamics of the system.

2.1.2   Potential induced by the photonic component

Figure 2.2 summarizes the techniques that act on the photonic component for the creation of a potential for polaritons.

The first technique, presented in Fig. 2.2(a), consist in depositing a patterned thin metallic layer on top of the sample. This layer induces a local change in the dielectric constant of the top mirror of the cavity, resulting in a small shift in the energy of the optical resonance (typically below 1 meV). This technique was developed by the group of Y. Yamamoto. Quite simple to implement, it has been used to realize 1D and 2D periodic potentials [24, 28, 73, 74]. For example, the spontaneous build-up of coherence in an array of 1D polariton condensates has been observed [24], as shown in Fig. 2.2(a), lower panel, where the two peaks ($\theta = \pm 8°$) in momentum space indicate a phase difference of π between neighboring real-space lobes. However, as the additional layer deposited on top only affects the evanescent field in the top mirror, the resulting confinement energy is limited. Additionally, and for the same reason, this technique cannot be used for cavity with high quality factors (in which the evanescent field at the top interface vanishes).

Another strategy to shift the cavity energy is to modify locally the cavity thickness. This can be done during the fabrication process, by etching selectively the spacer above the QW before growing the top DBR. This results in mesas, as illustrated in Fig. 2.2(b), in which the cavity energy is lowered, creating a photonic confinement in the mesa. The etching-before-overgrowth technique, developed in the group of B. Deveaud, has initially been used to realize 0D confining structures [21, 75, 76]. The real-space spectrum of such 0D trap is shown in Fig. 2.2(b), lower panel, together with the two lowest energy modes [21]. More recently, this technique has also been used in the group of S. Höfling to fabricate 2D lattices [77].

Alternatively, confinement of the photonic mode can be achieved by deep etching of the cavity, through the top mirror, QW and bottom mirror, down to the substrate, as illustrated in Fig. 2.2(c). The high refraction index contrast between
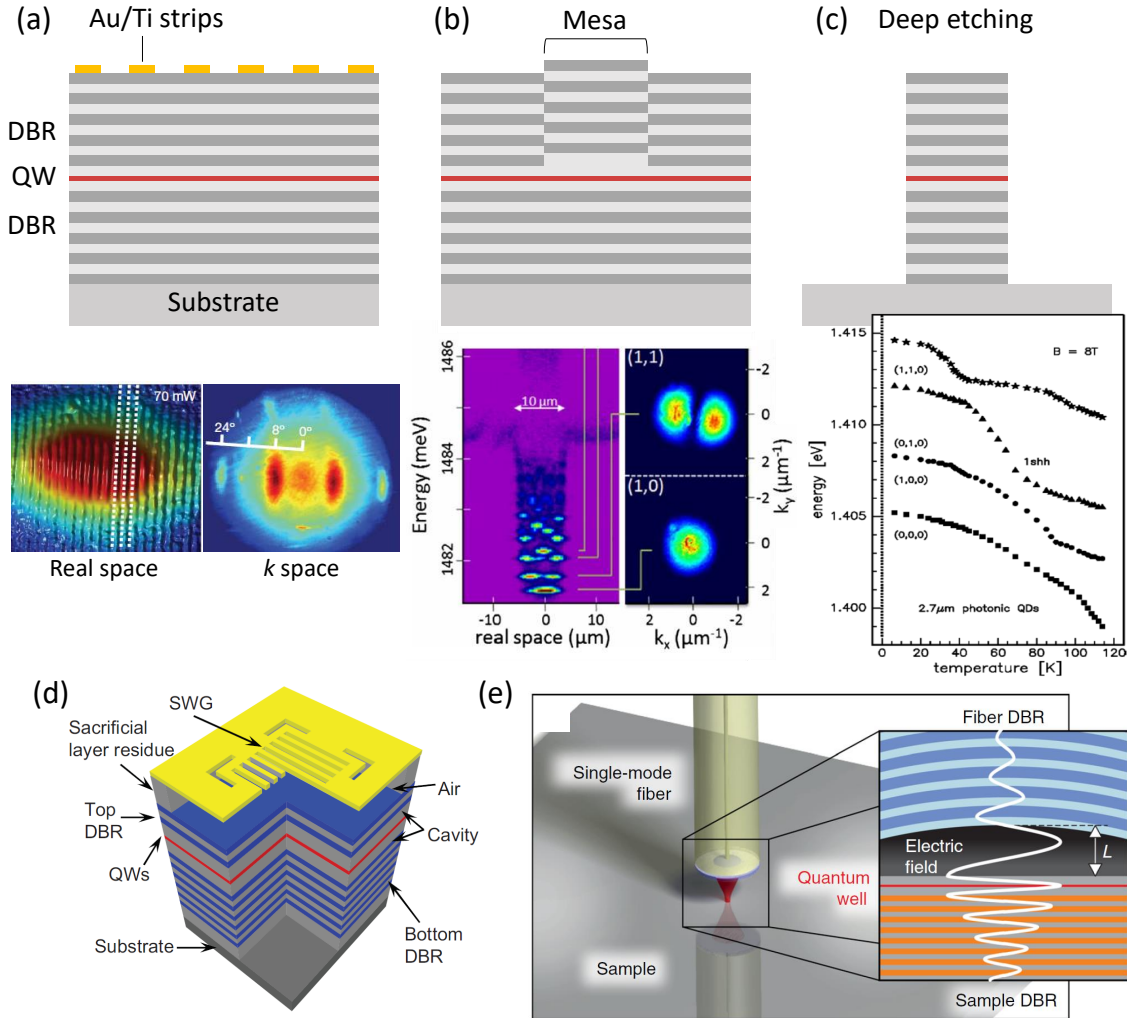
Figure 2.2: Techniques to create an photonic potential for polaritons. (a) Metallic deposition. (Bottom) Real- and momentum-space images of a polariton condensate under a 1D periodic array of metallic strips. Taken from [24]. (b) Etching before top mirror growth. (Bottom) Real-space energy spectrum of a circular 5 μm radius mesa, and *k*-space image of the two lowest energy modes. Taken from [21]. (c) Deep etching. (Bottom) Avoided crossing between confined photonic modes in a pillar and exciton, as a function of temperature. Taken from [70]. (d) Hybrid cavities with photonic crystal as top mirror and (e) open cavity with coated optical fiber. Images taken respectively from [71] and [72].

the semiconductor ($n \approx 3.5$ for GaAs) and air ($n \approx 1$) ensures confinement of the photonic mode inside the structure. This technique was developed in parallel by the groups of J. Bloch [78] and M. Bayer [70], who both first demonstrated strong coupling between exciton and confined photonic modes in etched pillars, as shown in Fig. 2.2(c), lower panel. A big advantage of the etching technique is that structures with almost arbitrary geometry can be fabricated, in which the photonic mode is strongly confined. This enables precise band structure engineering for polaritons. A great variety of structures have been realized in our group, emulating various potentials, but also in other groups [79–82]. Examples of structures realized in our group are discussed ahead in this chapter. The main challenge of the etching technique is to preserve the high quality of the optical properties of the 2D microcavity. The main source of degradation arises from non-radiative exciton recombination at the side walls of the etched QW. To reduce this issue, some groups have reported etching of the top DBR only, to leave the QW intact [83–86].

Finally, new techniques have recently emerged relying on hybrid cavities, where the top and bottom mirror are of different nature. For example, the top DBR has been replaced with a planar photonic crystal [71, 87], as depicted in Fig. 2.2(d). The photonic mode is strongly confined under the photonic crystal, resulting in very small mode volume. Another hybrid system are open cavities, where a concave dielectric DBR deposited at the end of an optical fiber tip serves as top mirror [72]. The concaveness of the fiber tip also causes strong confinement of the photonic mode. The cavity energy can be tuned by adjusting the distance from the fiber to the sample. A pair of coupled photonic traps has also been realized by milling two dips in the fiber tip, opening the way to the realization of more complex potential geometries [88].

2.1.3   Etching technique at C2N

Our samples are obtained by post-growth deep etching of GaAs based microcavities. First, after the microcavity and embedded QW are grown by molecular beam
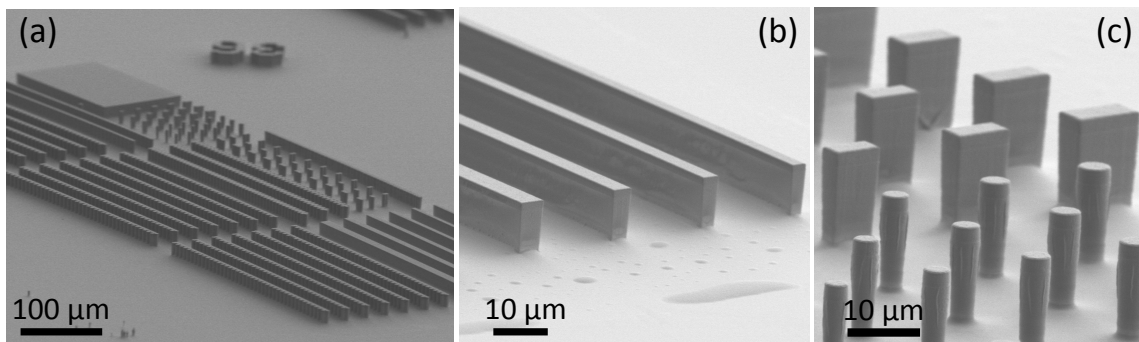
Figure 2.3:   (a) SEM image of a sample after etching with different structures such as (b) 1D wires and (c) circular and rectangular pillars.

epitaxy, a photoresist layer is spin coated on top of the planar cavity. Then, electron-beam lithography is used to draw a mask on the photoresist layer. The mask design can have arbitrary geometry. Finally, Inductive Coupled Plasma etching is used to etch away all the layers of the cavity down to the substrate. Only regions were the photoresist was not shined by the e-beam are etched, imprinting the desired geometry into the sample. Images of a sample after etching, obtained thanks to a Scanning Electron Microscope (SEM), are shown in Fig. 2.3.

We would like to underline here the work done by Luc le Gratiet, Abdelmounaim Harouri and Isabelle Sagnes, who performed the etching processes, and without whom all of our studies would be impossible.

In the rest of this chapter, we show how engineering the structure geometry allows for the emulation of different potentials and Hamiltonians. First, we demonstrate how an effective 1D potential can be derived from 1D structures with modulated lateral width. Then, we discuss the mapping of tight-binding Hamiltonians to arrays of coupled pillars.

2.2 One-dimensional microstructures: mapping to a 1D potential

2.2.1 Derivation of the effective potential

In the following, we discuss how the geometry of a 1D microstructure can be mapped to an effective 1D potential for polaritons. This is particularly useful, as it allows to engineer arbitrary 1D potentials, by careful design of the structure width.

The setting of the problem is the following. The high refraction index contrast between the cavity and air creates confined modes within the structure, with evanescent fields outside. For structures of lateral size d bigger than the penetration depth outside the structure (typically $d > 1.5$ upmum), we can neglect the evanescent fields, and make the approximation that the electromagnetic field amplitude is zero at the edges of the structure. Thus, etching a structure out of a planar cavity is equivalent to setting zero boundary conditions for the polariton wave function $\psi(x,t)$, with specific geometry (i.e. at the structure edges). The linear eigenmodes and eigenenergies of a given structure are solutions, satisfying the zero boundary conditions, of the 2D Schrödinger equation:

$$E\Psi(x,y) = -\frac{\hbar^2}{2m}\nabla^2\Psi(x,y) \tag{2.1}$$

where m is the polariton effective mass and (x,y) are defined only within the structure. We recall that the Schrödinger equation corresponds to the single-particle polariton Hamiltonian (i.e. without polariton-polariton interactions), introduced in the previous chapter. We have set E_0, the lower polariton energy at $k = 0$ (in the planar cavity), as the origin of energies. Note that zero boundary conditions
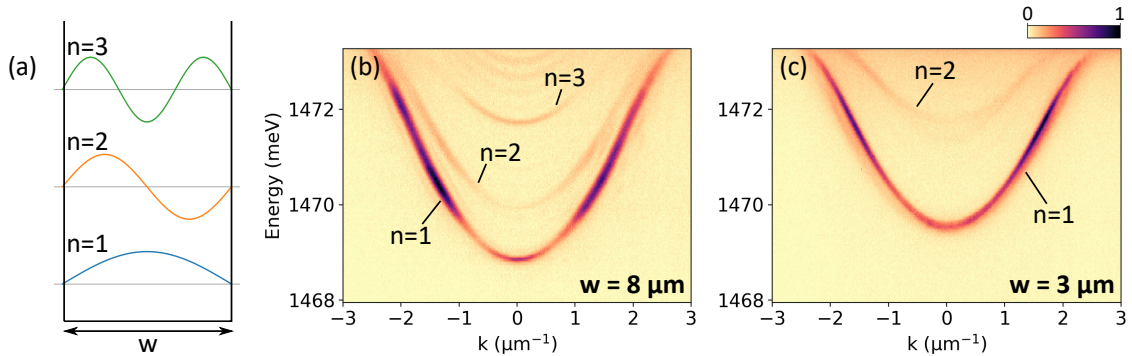
Figure 2.4: (a) Schematic representation of the first three confined modes in an infinite potential well of width w. (b),(c) Measured k-space spectrum, for linearly polarized emission along the long wire direction (TE), and for a wire of width (b) $w = 8$ μm and (c) $w = 3$ μm. 1D subbands and their respective labels are indicated in each panel.

are equivalent to solving Eq. (2.1) on $\mathbb{R}^2$, with the addition of an infinite potential outside the structure. Evanescent fields can be taken into account by considering finite potential, with an amplitude determined by the penetration depth.

Our goal is to reduce the 2D problem to a 1D Schrödinger equation, with an effective 1D potential $V(x)$:

$$E\psi(x) = \left(-\frac{\hbar^2}{2m}\nabla^2 + V(x)\right)\psi(x) \tag{2.2}$$

We recall that in the planar cavity, the solution to Eq. (2.1) are plane waves, leading to the parabolic relation dispersion:

$$E(k) = \frac{\hbar^2}{2m}(k_x^2 + k_y^2) \tag{2.3}$$

with k the in-plane wave vector.

In order to understand how the etching of 1D microstructures can be mapped to an effective 1D potential, let us first consider the case of a simple wire, of width w in the lateral direction (y direction, with $-w/2 \leq y \leq w/2$), similar to those shown in Fig. 2.3(b). For simplicity, we consider an infinite wire in the x direction. In this case, the wave function is separable, $\Psi(x,y) = \psi(x)\phi(y)$. In the x direction, the solutions are still plane waves. In the y direction, as illustrated in Fig. 2.4(a), the lateral confinement imposes cosinusoidal $\phi(y) = cos(k_y y)$, with quantized wave vector k_y:

$$k_{y,n} = \frac{n\pi}{w} \tag{2.4}$$

where n is an integer. The first three lateral eigenmodes are schematically represented in Fig. 2.4(a).

47

The ansatz $\Psi(x,y) = \psi(x)\phi(y)$ can be inserted in the 2D Schrödinger equation. It results in inserting the quantization condition in the 2D dispersion relation. We get a set of 1D subbands, with a parabolic dispersion along x:

$$E_n(k_x) = \frac{\hbar^2}{2m}k_x^2 + \frac{\hbar^2\pi^2}{2mw^2}n^2 \tag{2.5}$$

In particular, the quantization condition corresponds to a confinement energy V_n:

$$V_n = \frac{\hbar^2\pi^2}{2mw^2}n^2 \tag{2.6}$$

Note also that in real space, the lateral profile of the eigenstates from each subband corresponds to the lateral eigenmodes $\phi(y)$, as shown in Fig. 2.4(a) (meaning that a mode from subband n has n bright lobes and $n-1$ nodes).

Figure 2.4(b,c) presents the momentum-space spectrum of wires of width $w = 8$ µm and $w = 3$ µm, measured under non-resonant excitation. The presence of 1D subbands is clearly identified. Additionally, reducing the wire width results in an increase of the splitting between the different bands, and of the confinement energy of the lowest subband ($n = 1$), as predicted by Eq. (2.5).

The next step is to consider a modulated wire, with position-dependent width $w(x)$. The wave functions $\Psi(x,y)$ solutions to Eq. (2.1) are no longer separable. The principle of the mapping is to find a proper basis for the space of solutions, such that we can get rid of the y degree of freedom. In analogy with the simple wire discussed above, we make the approximation that $\Psi(x,y)$ take the form of quasi-transverse modes, almost separable in x and y:

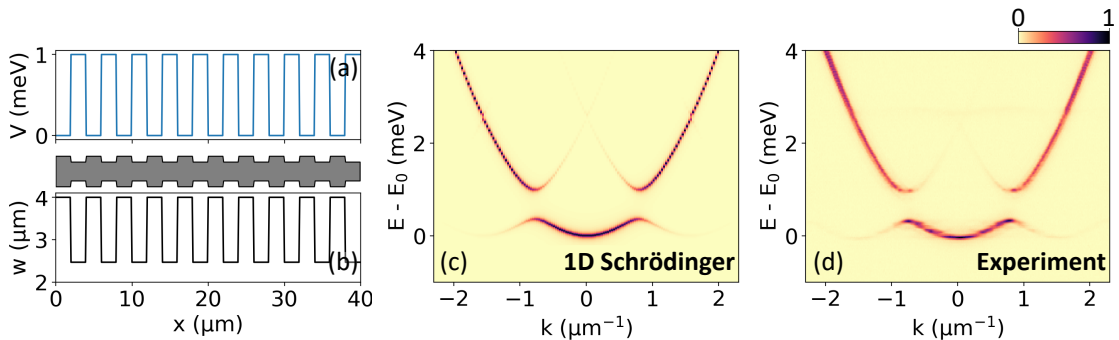$$\Psi(x,y) = \psi(x)\cos(k_{y,n}(x)y) \tag{2.7}$$

Figure 2.5: (a) Periodic 1D potential with steps of length $a = 2$ µm and height 1 meV. (b) Width of the modulated wire, calculated to implement the potential in (a). Top: sketch of the corresponding wire. (c) Calculated local density of states in momentum space for the 1D potential in (a). (d) Measured k-space spectrum for the wire in (b).

with $k_y(x) = n\pi/w(x)$, and $-w(x)/2 \leq y \leq w(x)/2$. With this form, we assume that at each position x along the chain, the lateral profile is an eigenmode of the lateral 1D infinite potential well of width $w(x)$ (remind that this is strictly exact for the wire with constant width). We remind that these eigenmodes are illustrated in Fig. 2.4(a).

Next, we plug the ansatz (2.7) into the 2D Schrödinger equation (2.1). We get:

$$E\Psi(x,y) = -\frac{\hbar^2}{2m}\left[\cos\left(\frac{n\pi}{w(x)}y\right)\frac{\partial^2}{\partial x^2}\psi(x) + \psi(x)\frac{\partial^2}{\partial x^2}\cos\left(\frac{n\pi}{w(x)}y\right)\right.$$
$$\left. + \psi(x)\frac{\partial^2}{\partial y^2}\cos\left(\frac{n\pi}{w(x)}y\right)\right] \quad (2.8)$$

We make the additional approximation that the spatial derivatives of $w(x)$ can be neglected in Eq. (2.8). This assumption of adiabatic width variations simplifies a lot the derivation, as it implies that the second term on the right-hand side in (2.8) is zero. It allows to reduce the 2D Schrödinger equation to an effective 1D equation along the x direction:

$$E\psi(x) = \left(-\frac{\hbar^2}{2m}\nabla^2 + V_n(x)\right)\psi(x) \quad (2.9)$$

where the 1D potential $V_n(x)$ is given by:

$$V_n(x) = \frac{\hbar^2\pi^2}{2mw(x)^2}n^2 \quad (2.10)$$

Eventually, the 1D effective potential is locally equal to the confinement potential in a wire of same width, as given by Eq. (2.6). Note that each subband, labeled with index n, has a different effective potential $V_n(x)$, and consequently they need to be treated separately in Eq. (2.9). In the following we focus on the lowest subband $n = 1$, without loss of generality.

To illustrate the validity of our approach, we consider the example of the periodic 1D potential plotted in Fig. 2.5(a). It consists in steps of length $a = 2$ μm, that alternate between only two possible values, 0 or 1 meV. We etched a structure in order to implement this effective potential. After a preliminary determination of the polariton effective mass in the planar cavity, we chose two widths such that the difference in confinement energy between the two equals 1 meV, according to Eq. (2.10) (for the lowest subband $n = 1$). The resulting width profile is presented in Fig. 2.5(b). The measured momentum-space energy spectrum of this structure is shown in Fig. 2.5(d). A gap opens due to the periodicity of the structure. We can also calculate the momentum-space spectrum associated with the potential from Fig. 2.5(a). To this end, we solve the 1D Schrödinger equation, with the potential from Fig. 2.5(a), Fourier transform the eigenstates and extract the local density of states (LDOS) in momentum space. The result is presented in Fig. 2.5(c). Additionally, in Fig. 2.5(c) the LDOS was convoluted with a Lorentzian, to take into

account the experimental finite linewidth. The excellent agreement between the experiment and numerical simulations confirm the validity of the 1D effective potential mapping.

It is important to point out that a rigorous derivation of the 1D effective potential, taking into account spatial derivatives of $w(x)$, can be found in the Supplemental Material of Ref. [26]. Note, in particular, that in this case x and y are truly not independent, and it is necessary to project the 2D Schrödinger equation on the normalized transverse modes $\sqrt{2/w(x)}\cos(k_y(x)y)$ to derive an effective 1D Schrödinger equation for $\psi(x)$. It leads to an additional term in the effective potential:

$$V(x) = \frac{\hbar^2}{2mw(x)^2}\left[\pi^2 + \frac{\pi^2+3}{12}\left(w'(x)\right)^2\right] \tag{2.11}$$

where $w'(x) = \mathrm{d}w/\mathrm{d}x$ denotes the spatial derivative of $w(x)$. In most of the practical cases however, the approximation of adiabatic width variations is valid and the term proportional to $w'(x)^2$ can be neglected, for example in the case studied in Fig. 2.5. Note also that so far we have ignored couplings between transverse modes of different order. This can be taken into account by writing solutions $\Psi(x,y)$ as a sum of quasi-transverse modes with different n, and introduces additional terms with higher-order derivatives of $w(x)$ in the effective potential.

Finally, note that the etching also introduces an energy splitting between photons linearly polarized, parallel to the wire (TE) and orthogonal to the wire (TM), that is not taken into account in the formalism of the Schrödinger equation (this is because we used a scalar field ψ to describe the lower polariton, effectively considering a single polarization). In a 1D structure, the two polarizations can indeed be considered independent. This will be discussed in more details in the following chapters.

2.2.2 Applications

Figure 2.6 presents examples of 1D structures that have been realized in our group. Optical manipulation and coherent propagation of polariton condensates over long distances (typically above 100 µm) have been demonstrated in microwires [25], as shown in Fig. 2.6(a). Polariton condensation was also studied in periodically modulated wires, such as described previously, see also Fig. 2.6(b). For a small excitation spot, it was shown that for strong non-resonant pumping power, polariton-polariton interactions lead to the formation of gap solitons, i.e. localized states at an energy in the gap that opens due to the periodic modulation [89].

Exploiting the long propagation distances, proof of concepts for polaritonic circuits have been realized. For example, a resonant tunneling diode for polaritons was reported [90]. As shown in Fig. 2.6(c), it consists in a double barrier structure. An effective potential well is created at the position of the central island, with discrete modes within. The energy of the discrete modes in the island can be tuned optically, addressing it with a non-resonant pump that creates an exciton reservoir. In this way, the transmission of a propagating monochromatic polariton fluid through the
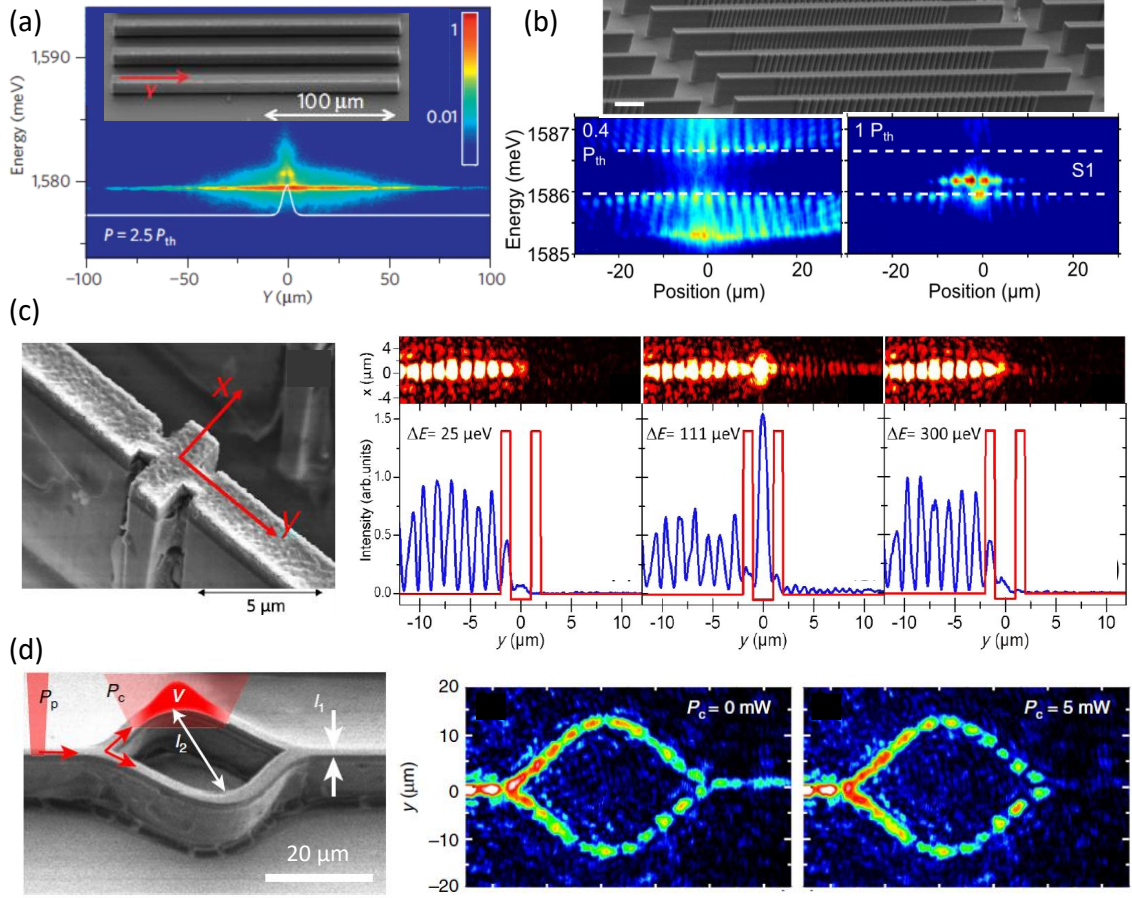
Figure 2.6: Examples of 1D structures for polaritons. (a) Propagation of a polariton condensate in a 1D wire. Taken from [25]. (b) Formation of gap solitons in periodic wires. Taken from [89]. (c) Controlled transmission through a polariton diode. Taken from [90] (d) Controlled transmission through a Mach-Zender interferometer for polaritons. Taken from [91]

island can be controlled: resonant tunneling through the barriers is possible only when a discrete mode is in resonance with the polariton energy. No transmission is observed when the reservoir-induced blueshift is above or below this resonance condition.

A structure combining a similar isolated island and periodically modulated wires was recently used to implement a polariton router [92]. The island is connected on its sides to two modulated wires with different periodicity, i.e different gap energy. Polaritons are injected in the island. Tuning the island energy in the gap of one of the wires allows to route polaritons in the desired direction. A Mach-Zender polariton interferometer has also been realized [91], Fig. 2.6(d). A non-resonant pump addressing one of the two arms of the interferometer allows to control the phase difference for polariton traveling in the two arms. This offers an all-optical
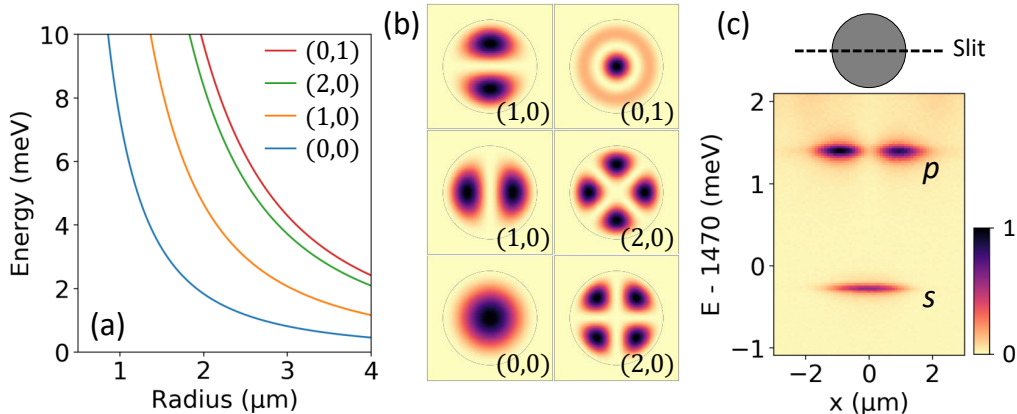
Figure 2.7: (a) Energy E_{nl} of the modes with lowest values of (l, n), versus pillar radius, calculated with a polariton mass $m = 3 \times 10^{-5} \ m_e$. (b) Corresponding calculated eigenmodes. The value of (l, n) are indicated in each panel. The gray line is the pillar edge. (c) Measured real-space spectrum of a 3.9 μm-diameter pillar. The inset on top illustrates the position of the spectrometer slit with respect to the pillar image.

control of the transmission at the output, which can even be completely suppressed if the phase difference is π.

A local modification of the wire width was also used to engineer a defect in the flow of a nonlinear polariton fluid. The formation of an analogue black hole horizon at the defect position was reported [93]. This result will be discussed in details in chapter 4. Finally, wires with a quasiperiodic modulation implementing the Fibonacci sequence have been realized [26, 94], revealing in particular a fractal energy spectrum.

2.3 Arrays of coupled pillars: tight-binding approach

2.3.1 Single circular pillar

In this section, we present how tight-binding Hamiltonians for polaritons can be engineered, using arrays of coupled micropillars.

In this approach, the elementary building block is a single, isolated circular pillar (see Fig. 2.3(c)). We consider a circular pillar, of radius r, and as previously, we assume zero boundary conditions (or equivalently infinite potential outside the structure). In this case, the 2D Schrödinger equation (2.1) can be solved analytically. The eigenenergies are given by the zeros of spherical Bessel functions as follows:

$$E_{nl} = z_{l,n}^2 \frac{\hbar^2}{2mr^2} \qquad (2.12)$$
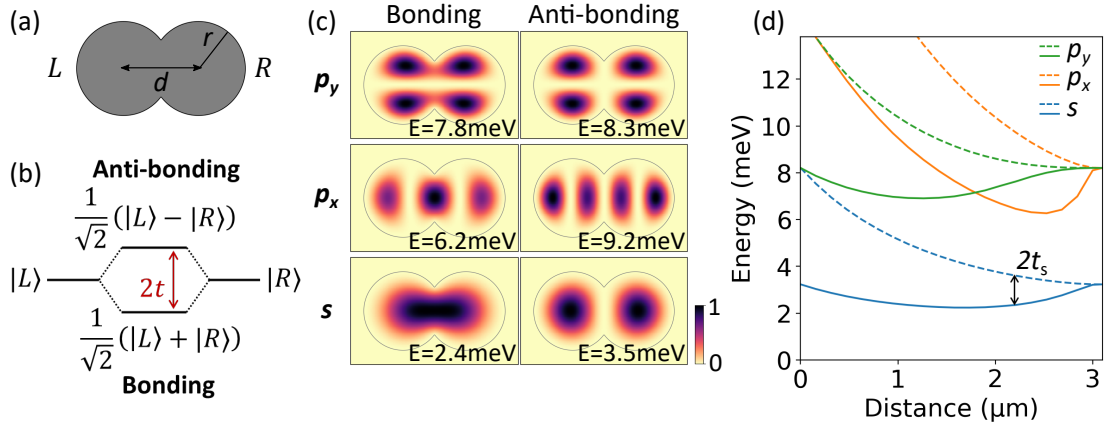
Figure 2.8: (a) Sketch of two coupled pillars. (b) In the tight-binding picture, two modes, noted $|L, R\rangle$, coupled with coupling strength t, give rise to bounding and anti-bounding eigenstates. (c) Lowest energy modes of the structure in panel (a), calculated by solving the 2D Schrödinger equation. The energy associated with a given mode is indicated in each panel. The gray line indicates the structure edges. (d) Energy of the bonding (solid lines) and anti-bonding (dashed) s, p_x and p_y modes, as a function of pillar distance, calculated from the 2D Schrödinger equation for $r = 1.5$ µm.

where $z_{l,n}$ is the nth zero of the lth spherical Bessel function (and m the polariton effective mass). The energy as a function of r are plotted in Fig. 2.7(a) for the first values of (l, n). The analytical expression for the eigenmodes is given by spherical Bessel functions. The six eigenmodes with lowest energy, corresponding to Fig. 2.7(a), are plotted in Fig. 2.7(b). As spherical Bessel functions are the equivalent of spherical harmonics in 2D, the shape of the different eigenmodes correspond to atomic orbitals: the lowest energy mode, with $(l, n) = (0, 0)$ has a single bright lobe and thus corresponds to an s-mode; the next energy mode is twice degenerate, with $(l, n) = (\pm 1, 0)$–it is a p-mode; and so on.

Fig. 2.7(c) presents the measured real-space spectrum for a pillar with $r = 1.95$ µm. The slit of the spectrometer images a central cut of the pillar, as illustrated in the inset. The two lowest energy discrete eigenmodes are visible. In particular, the second mode has two bright lobes and a node at the center, characteristic of a p-state. The lowest mode, with a single lobe, is labeled as an s-state.

We can thus conclude that micropillars behave like artificial atoms. Noteworthy, their eigenenergies can be tuned by adjusting the pillar radius.

2.3.2 Coupled pillars

The key elements to the mapping of a tight-binding Hamiltonian for polaritons, is that the eigenstates in a chain of coupled pillars can be written as linear combinations of the Bessel functions in each individual pillars.

To illustrate this, let us discuss the case of two circular pillars, with same r, separated by a distance $d < 2r$, such that the two pillars overlap, as depicted in Fig. 2.8(a). The solution to the corresponding 2D Schrödinger problem is no longer analytical, but we can compute the eigenmodes numerically. For example, the six lowest energy eigenmodes computed for two overlapping pillars with $r = 1.5$ μm and $d = 2.4$ μm are shown in Fig. 2.8(c). Let us focus on the two modes with lowest energy (bottom row). Looking back at the s-mode in a single pillar (Fig. 2.7(b)), the two modes from Fig. 2.8(b), bottom row, can be described as the linear superposition of the s-mode in the left pillar (noted $|L\rangle$) and s-mode in the right pillar ($|R\rangle$), respectively with the same phase (left panel) or opposite phase (right panel)–note the zero intensity in between the pillars in this latter case. In other words, the two lowest energy eigenmodes can be labeled bonding and anti-bonding s-modes, i.e. $(|L\rangle \pm |R\rangle)/\sqrt{2}$. This corresponds to the tight-binding picture illustrated in Fig. 2.8(b). Thus, writing the wave function $|\psi\rangle$ in the basis of s-modes $\{|L\rangle, |R\rangle\}$, the 2D Schrödinger equation can be mapped to a set of 0D equations describing two coupled modes:

$$E\psi_L = E_0\psi_L - t\psi_R$$
$$E\psi_R = E_0\psi_R - t\psi_L$$

(2.13)

where $\psi_j = \langle\psi|j\rangle$, with $j \in \{L, R\}$, is the wave function amplitude on the left (right) pillar, E_0 is the s-mode energy in the single pillar, and t denotes the coupling amplitude. This coupling between $|L\rangle, |R\rangle$ arises from the overlap between the two pillars, as it describes a probability for a polariton to tunnel from one pillar to the other. More precisely, t is given by $|\langle L|H_0|R\rangle|^2$, where H_0 is the single-particle polariton Hamiltonian that includes the external potential outside the structure (corresponding to Eq. (2.1)). In this sense, increasing the overlap between the two pillars allows to increase t. This is confirmed by the dependence on distance d of the energy splitting between bonding and anti-bonding s-modes, shown in Fig. 2.8(c), blue lines. This plot was obtained by solving the 2D Schrödinger equation, for two pillars of radius $r = 1.5$ μm. The value of t for the tight-binding model (2.13) is given by half the energy splitting between the bonding and anti-bonding modes. Note that as $d \to 0$, the energy of the bonding s-mode tends to the s-mode in a single pillar, whereas the anti-bonding s-mode becomes a p-mode of the single pillar.

Considering the four other eigenmodes plotted in Fig. 2.8(b), we can easily see that the same argument applies: they can be identified as bonding and anti-bonding combinations of p_x, p_y modes. Additionally, the coupling strength for these modes can also be controlled with the pillar distance, as shown in Fig. 2.8(c), green and orange lines.

This line of thought can be naturally extended to arrays of coupled pillars. The eigenmodes of the system can be written using the Bessel functions in individual pillars as a basis for the Hilbert space. Noting $|n\rangle$ the eigenvector from this basis (i.e. Bessel functions in each pillar), the 2D Schrödinger problem is reduced to a
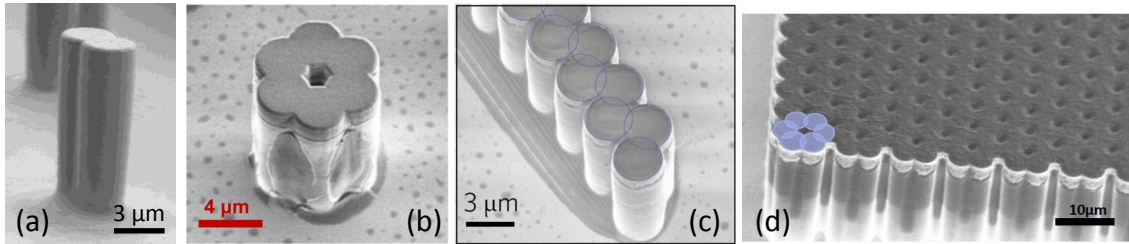
Figure 2.9: Examples of coupled pillars structures: (a) dimer molecule, (b) benzene molecule, (c) 1D SSH lattice and (d) 2D honeycomb lattice.

very general tight-binding Hamiltonian:

$$H = \sum_n E_n |n\rangle\langle n| - \sum_{n,m} t_{n,m} \left(|m\rangle\langle n| + \text{h.c.} \right) \tag{2.14}$$

The lattice geometry completely determines the Hamiltonian. The on-site energies E_n and couplings t_{mn} can be tuned by adjusting the pillars size and relative distance. The number of neighbors per site is directly related to the geometrical arrangement of pillars, and we can implement Hamiltonians for s-orbitals, p-orbitals, d-orbitals, etc., or even a mixing of these modes. Note, though, that since the coupling arises from the overlap between neighboring pillars, we can only implement tight-binding Hamiltonians with nearest-neighbor coupling. For the same reason, only ferromagnetic couplings ($t_{mn} > 0$) can be achieved. However, this approach is highly versatile and offers relatively easy design of Hamiltonians. In the next section we present examples of 0D molecules, 1D and 2D lattices of coupled pillars previously realized in our group.

Finally, let us mention briefly an important limit to the validity of this approach: Bessel functions in individual pillars do not form an orthogonal set of eigenvectors. In fact, we even identified the finite overlap between modes in adjacent pillars as the origin for the couplings. Thus, contrary to the tight-binding picture, the Hamiltonian (2.14) is not written in an orthogonal basis. In the case of two coupled pillars, non-orthogonality is responsible for an asymmetry between the bonding and anti-bonding modes energies with respect to the single pillar. This is visible in Fig. 2.8(c), e.g. for the s-modes: reducing d away from 3 µm, the bonding energy decreases faster than the anti-bonding increases (this is even clearer for strongly coupled p_x modes). Non-orthogonality is stronger for bigger pillars overlap, thus we cannot take d arbitrarily small. Typically, we restrict the parameters to $d \gtrsim 3r/2$. For 1D and 2D lattices, non-orthogonality distorts the bands in the energy spectrum with respect to the ideal tight-binding Hamiltonian case. This will be discussed in more details in chapter 5.

2.3.3 Applications

The method described above was used in our group to implement various tight-binding models of 0D molecules, 1D and 2D lattices. Examples of such structures are shown in Fig. 2.9.

Starting from the simplest case of two coupled pillars (Fig. 2.9(a)), polariton condensation was demonstrated in both bonding and antibonding states, dependent on the position of the non-resonant pumping spot [22]. Strongly nonlinear regimes have been reached, where polariton-polariton interactions play an important role, with the observation of nonlinear Josephson oscillations and self-trapping [95]. More recently, it was also shown that the phase acquired by polaritons hopping between cavities can be controlled through polariton-polariton interactions [46].

More complex molecules with six pillars arranged in a hexagonal geometry have also been realized, constituting a polaritonic analogue of a benzene molecule (Fig. 2.9(b)). Such structures have been used to engineer an analogous of spin-orbit coupling for polaritons, arising from polarization-dependent couplings between neighboring pillars. It was shown that the engineered spin-orbit coupling drives the condensation of polaritons into states with complex polarization textures [23]. This has recently been used to trigger lasing in states carrying finite orbital angular momentum, with a chirality fully controlled by the pump laser polarization [96].

One-dimensional lattices of coupled pillars have also been realized, such as SSH chains (Fig. 2.9(c)) or 1D Lieb lattices. The study of the 1D Lieb lattice is the topic of chapter 5. The SSH lattice has two sites per unit cell, with alternating strong and weak couplings, and is one of the simplest example of lattice with nontrivial topological properties. We have demonstrated lasing in a topologically protected edge state, located in the gap between the p-bands, and robust to local deformations of the lattice [97].

Finally, 2D honeycomb lattices for polaritons have been engineered, to emulate the physics of graphene (Fig. 2.9(d)). In such lattices, the presence of Dirac cones and flat bands in the dispersion was demonstrated [29]. Edge states, both s- and p-bands have also been investigated [98, 99]. Recently, stretched and compressed versions of the honeycomb lattice were implemented, by adjusting the inter-pillar distance along one spatial direction, allowing for the observation of exotic tilted Dirac cones [100].

1D and 2D lattices have also been used to study the spatial and temporal coherence properties of polariton condensates with a negative effective mass, by triggering condensation at the top of s-bands (where the band curvature is negative) [101]. It was shown that negative mass condensates exhibit much longer coherence (specifically spatial coherence) as their positive mass counterparts. A modulational instability is present in positive mass condensates. Condensation in states with negative effective mass allows to tame this instability.

Localization properties of Aubry-André-Harper-Fibonacci quasicrystals

This chapter is dedicated to the study of the localization properties of waves in a specific family of quasicrystals, emulated with 1D polariton microstructures. Quasiperiodic systems, with specific long-range correlations, can exhibit very different localization properties. For example, two famous models of quasicrystals with completely different localization properties are the Fibonacci model and the Aubry-André-Harper (AAH) model. A continuous deformation between these two models was introduced by Kraus and Zilberberg [102], and the question of how localization properties evolve in this continuous deformation is so far an open question, both theoretically and experimentally. Owing to the possibility of controlling precisely the potential for polaritons in 1D structures, and easy access to the polariton wave function by photoluminescence experiments, polaritons are a very suitable platform for the experimental investigation of such problems. Here, we investigate localization properties in the continuous deformation introduced by Kraus and Zilberberg. This work was performed in collaboration with the theory group of Oded Zilberberg, in ETH Zurich.

Section 3.1 presents a short introduction to the physics of quasicrystals. In section 3.2, we focus on two specific models of one-dimensional quasicrystals, namely the Aubry-André-Harper model and the Fibonacci model. The properties of these two models are discussed, with a special focus on the localization properties. We also briefly review their experimental implementation in various systems, including cavity polaritons. Finally, we introduce a continuous deformation from one model to the other, which preserves their topological properties. In section 3.3, we establish a theoretical localization phase diagram in the continuous deformation between the AAH and Fibonacci quasicrystals. The localization properties are studied in

two different cases: in the limit of a tight-binding Hamiltonian, and in the limit of a free particle subject to a quasiperiodic potential, more suited to experiments with polaritons. In both cases, an original delocalization-localization phase transition is discovered when deforming the quasicrystal. In section 3.4, we implement our model with polaritons in one-dimensional modulated wires, with the aim of evidencing this effect. We explore experimentally the localization phase diagram, by means of non-resonant and resonant excitation measurements, and evidence the delocalization-localization transition predicted by our numerical findings. Conclusions and perspectives are discussed in section 3.5.

3.1 Introduction to quasicrystals

In condensed matter systems, quasicrystals (QC) are an intermediate between completely periodic perfect crystals and completely random or disordered media. They are structures that lack translational symmetry, but still exhibit long-range order. In reciprocal space, this order is characterized by sharp Bragg diffraction peaks, as for perfect crystals, but may present noncrystallographic rotational symmetry. This was first observed by Shechtman *et al.* in 1984 [103] (later rewarded with the Nobel prize for Chemistry in 2011), who reported X-ray diffraction pattern of AlMn alloys presenting ten-fold rotational symmetry. Such a symmetry is forbidden by the rules of crystallography in periodic lattices. Shortly after, Levine and Steinhardt interpreted these observations as the diffraction pattern of aperiodic Penrose tilings [104], as illustrated in Fig.3.1. This marked the discovery of QC, which came as a complete surprise, and triggered considerable interest in their exotic properties.

The complexity of QC arise from their combined lack of periodicity, which ex-
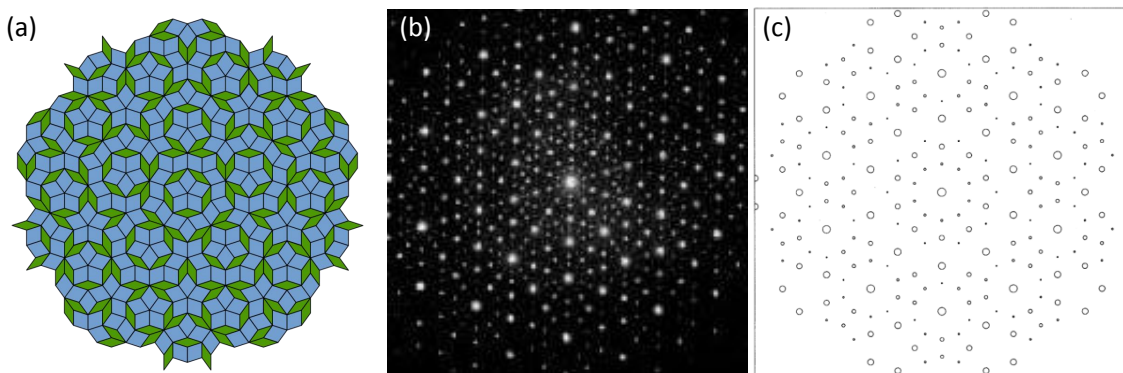

Figure 3.1: (a) Example of aperiodic Penrose tiling. (b) First measurement of the diffraction pattern of a QC, by Shechtman *et al.* [103]. Note the ten-fold rotational symmetry. (c) Position of the Bragg peaks for a QC with geometric configuration from (a), calculated by Levine and Steinhardt [104], and which accounts for the measurements shown (b).

cludes the possibility of describing them with analytic tools such as Bloch's theorem, and existence of long-range order. This has important consequences, especially on the localization properties of the eigenstates. Indeed, in a periodic system, Bloch's theorem implies that all eigenstates are completely delocalized over the whole system. On the hand, in the limit of a perfectly random disordered system, in 1D and 2D all states are exponentially localized due to Anderson localization (in 3D, Anderson localization only occurs above a threshold disorder amplitude). QC are at the boundary between these two limits. In QC, it is actually possible to find extended or localized states, but also so-called "critical" states, which are neither completely extended nor localized. Additionally, the associated energy spectrum usually presents highly fragmented energy bands, with fractal nature. These aspects will be presented in detail the next section.

Shortly after their initial discovery, QC have been engineered in artificial systems, facilitating in particular the experimental investigation of their localization and transport properties. Emulation of QC has been realized with photonic platforms, such as multilayer structures [105, 106], coupled waveguides [107, 108], microwave resonators [109] and cavity polaritons [26, 94]. In this chapter, we will consider only 1D QC, but a review of transport properties in photonic QC in one, two and even three dimensions can be found in Ref. [110]. For example, a surprising regime of transport enhanced by the presence of disorder has been reported in a photonic 2D QC [111]. QC have also been implemented in different systems, such as cold atoms [112–114], or for phonons [115].

In the recent years, specific interest in QC has also arisen from their non-trivial topological properties [102, 116, 117]. In particular, topological edge states have been investigated experimentally, mainly in photonic systems [94, 108, 118, 119], and exploited to implement topological pumping [108], and 4D quantum Hall effect [120–122]. The realization of topological insulators with 2D QC has also been proposed [123–125].

Over the years, many models of QC have been introduced and studied, in particular quasiperiodic sequences like the Thue-Morse, Rudin-Shapiro or frequency doubling sequences [115, 126]. In this chapter, we focus on 1D QC, and more specifically on two most famous models: the Aubry-André-Harper and Fibonacci QC. These two models were proven topologically equivalent, and it is possible to deform continuously one model into the other, but both show very different localization properties. Following a theoretical proposal from Oded Zilberberg, we aim to unify the localization properties of these two model, by exploring the localization phase diagram of the continuous deformation between the two.

3.2 Fibonacci and Aubry-André-Haper QC models

3.2.1 The Aubry-André-Harper model

The Aubry-André-Harper (AAH) model [127, 128] describes a 1D lattice to which a sinusoidal modulation of the on-site energy is applied, with a period incommensurate with the lattice spacing. In the tight-binding formalism, such a situation can be described by the following Hamiltonian:

$$H\psi_n = -t(\psi_{n-1} + \psi_{n+1}) + \lambda \cos(2\pi b n)\psi_n \qquad (3.1)$$

where ψ_n is the wave function amplitude at site n, t the hopping strength, λ the modulation amplitude (or contrast) and b the periodicity of the modulation. If b is an irrational number, the sequence of on-site potential $V_n = \cos(2\pi b n)$ is quasiperiodic, as depicted in Fig. 3.2(a). Note that the sinusoidal modulation can also be applied to the hopping terms (so-called off-diagonal AAH model) ; here we focus on the diagonal model (modulation of the on-site energies).

Aubry and André introduced this model in 1980 [128], and demonstrated that a metal-insulator transition occurs at $\lambda = 2t$ (transition from completely extended to exponentially localized states). Indeed, the AAH Hamiltonian has a self-dual nature: in reciprocal space, Eq. (3.1) becomes

$$H\psi_k = \frac{\lambda}{2}(\psi_{k-1} + \psi_{k+1}) - 2t \cos(2\pi b k)\psi_k \qquad (3.2)$$

where we have introduced the Fourier transformed states $\psi_k = 1/\sqrt{N} \sum_n e^{ikn}\psi_n$, for a lattice with N sites. Eq. (3.2) is of the same form as Eq. (3.1), with interchanged roles for of λ and $2t$: this is precisely the definition of self-duality. It follows that $\lambda = 2t$ is a fixed point of the dual transformation used in Eq. (3.2), corresponding to a localization transition at this point [128, 129]. Noteworthy, the localization transition occurs for *all* states at once. As illustrated in Fig. 3.2(b), eigenstates are extended (delocalized) for $\lambda < 2t$, and localized for $\lambda > 2t$ (only the ground state is plotted in Fig. 3.2(b)).

This localization transition has been reported experimentally in artificial systems such as cold atoms [113], or photons [107]. For cold atoms, the AAH model is implemented using an optical lattice perturbed with a second, weaker, incommensurate lattice [113]. Increasing the amplitude of the second lattice, a transition is observed from ballistic expansion of the condensate to an absence of diffusion, as shown in Fig. 3.3. For photons, in Ref. [107] Lahini *et al.* fabricated 1D arrays of coupled waveguides, as illustrated in Fig. 3.2(c). The on-site energy is tuned by adjusting the refraction index in each waveguide, realizing the quasiperiodic sequence of Fig. 3.2(a). Several samples corresponding to different λ were fabricated. Light was injected in a single site at the input of the lattices, and intensity distribution
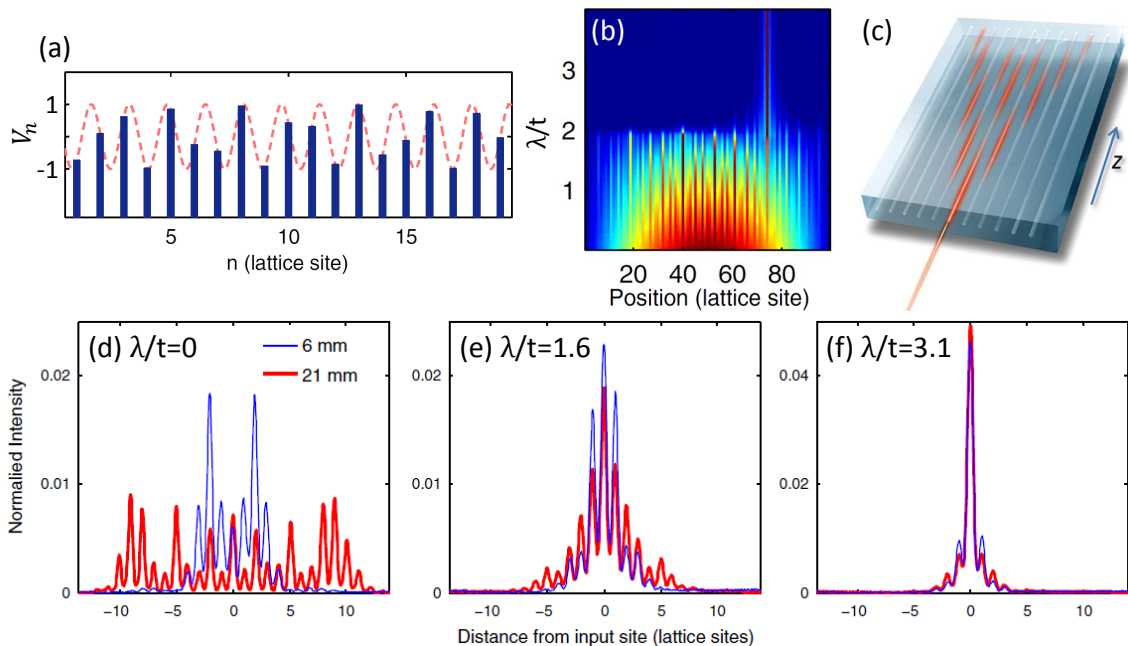
Figure 3.2: (a) A quasiperiodic AAH lattice is obtained by modulating the on-site energies of a periodic lattice (bars) at a frequency incommensurate with the lattice spacing (dashed line). (b) Calculated amplitude profile of the ground state of the incommensurate lattice versus strength of the modulation depth λ. A sharp localization transition is observed at $\lambda = 2t$. (c) Artist view of a lattice of coupled waveguides, excited at a single input site. (d-f) Measurements of a localization transition in lattices as the one depicted in (c), implementing the AAH model. Each panel shows the expansion of a single site initial wave packet after 6 mm of propagation (blue) and 21 mm (red), for various values of λ, (d,e) below and (f) above the localization threshold. Images from [107], except for (c), taken from [108].

at the output was measured, after propagation along the waveguides. As shown in Fig. 3.2(d-f), for $\lambda/t = 0$, the wave packets expand during the propagation, corresponding to the metallic phase (extended states). This is still the case at $\lambda/t = 1.6$, but with a smaller expansion rate. However, for $\lambda/t = 3.1$, the wave packet remains tightly localized to the input site, corresponding to the insulator phase.

It should be noted that the localization transition in the AAH model is different from Anderson localization: in an infinite 1D system (as well as in 2D) with perfectly random disorder, Anderson localization occurs for vanishing disorder amplitude, and all states are exponentially localized [130] (but for finite systems, in case of small disorder the localization length can exceed the system size, so that the states appear as extended states). In the AAH model however, extended states exist for finite disorder due to the specific correlations of this "disorder" (i.e. the modulation of the on-site energy).

If self-duality of the Hamiltonian from Eq. (3.1) is broken, different states un-

Figure 3.3: Observation of the AAH localization transition with cold atoms. (a) Quasiperiodic potential realized in the experiment, with J the hopping between neighboring sites a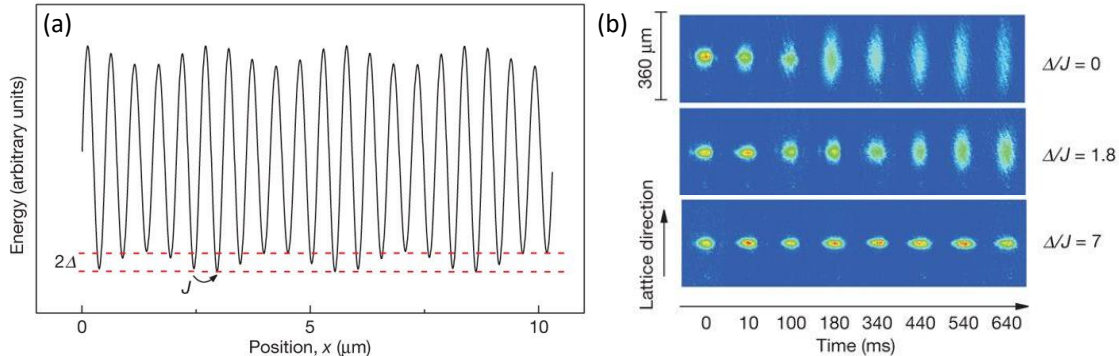nd Δ the contrast of the on-site energy modulation. (b) Images, at different times after initialization, of the Bose–Einstein condensate diffusing along the quasiperiodic lattice, for different values of Δ/J. For $\Delta/J = 7$, the size of the condensate does not increase, indicating localization. Images from [113].

dergo the localization transition at different λ, leading to the appearance of a mobility edge in the energy spectrum. For energies below (respectively above) the mobility edge, all states are localized (extended). Such a mobility edge was predicted [131] and recently observed in an atomic cloud loaded in shallow quasiperiodic optical lattices [132] (in a shallow lattice, the tight-binding approximation is no longer valid, which breaks self-duality).

Aside from its localization properties, the AAH model has also been studied for its topological properties. Following the initial work of Harper [127], it was demonstrated that the energy spectrum of the AAH Hamiltonian is broken into a fractal set of band and gaps, famously known as the Hofstadter butterfly [133], similar to the spectrum of electrons in a periodic 2D lattice in the presence of a magnetic field (2D Hall system). The pioneering work of Thouless *et al.* [134] showed that, in the latter case (2D lattice with a magnetic field), each gap in the spectrum is associated with a quantized and nontrivial Chern number (an integer topological invariant proportional to the Hall conductance). More recently, Kraus *et al.* showed that the 1D AAH model can be exactly mapped to the 2D Hall system [108]. As a consequence, 1D QC can be assigned Chern numbers. The key idea is that an additional degree of freedom can be added to the AAH Hamiltonian as follows:

$$H(\phi)\psi_n = -t(\psi_{n-1} + \psi_{n+1}) + \lambda \cos(2\pi b n + \phi)\psi_n \tag{3.3}$$

The additional degree of freedom, encoded in the phason ϕ, can be considered as an additional dimension, such that the system becomes effectively 2D. However, a change of ϕ corresponds to a translation of the QC (it shifts the origin of the modulation–note that this is only true if b is irrational and the QC of infinite size), and does not affect bulk properties such as the bulk energy spectrum and the Berry
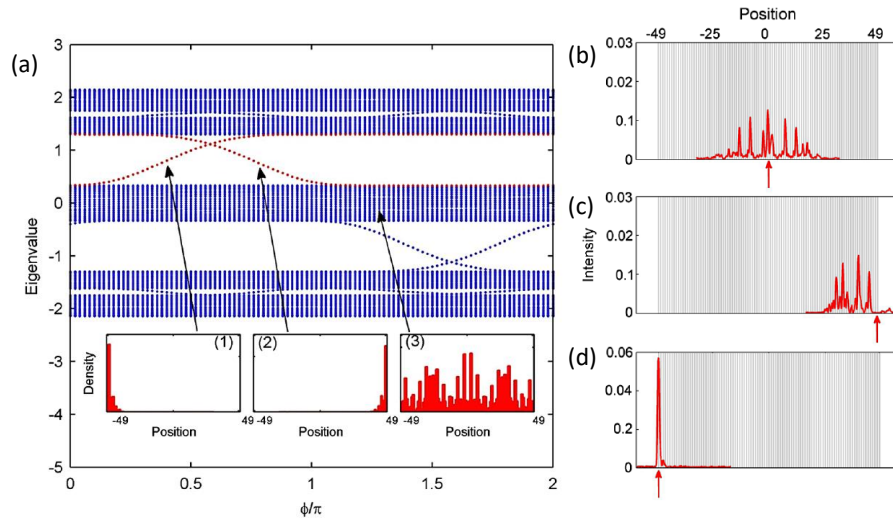
Figure 3.4: (a) Calculated spectrum of Eq. (3.3) as a function of ϕ. The bulk of the spectrum remains fixed, whereas few modes, localized at the boundaries, sweep across the gaps. The insets depict the spatial intensity profile of typical eigenstates: (1) a left edge state, (2) a right edge state, and (3) an extended bulk state within the band. (b-d) Experimental observation of an edge state on the left boundary, for $\phi = \pi/2$. Light is injected into a single waveguide (red arrows), and the intensity profile is measured at the output. (c),(d) An excitation at the central or rightmost site of the lattice results in a significant spread. (e) For an excitation at the leftmost site, light remains tightly localized at the boundary, marking the existence of an edge state. Images from [108].

curvature. Thus, the Chern number can be calculated from the 1D Hamiltonian with any value of ϕ. As illustrated in Fig. 3.4(a), this leads to the presence of edge sates in the different gaps. Kraus *et al.* fabricated arrays of coupled waveguides similar to those discussed earlier (Fig. 3.2), and evidenced the presence of localized edge states for well-chosen values of ϕ (see Fig. 3.4). They further used the topological nature of the edge states to engineer topological pumping across the lattice.

3.2.2 The Fibonacci model

The Fibonacci sequence is probably the theoretically and experimentally most studied QC model since its introduction in the context of QC by the works of Kohmoto *et al.* [135] and Ostlund *et al.* [136]. It consists in a sequence of letters A and B arranged according to the following recursive rule: $S_j = S_{j-1}S_{j-2}$, for $j \geq 2$, with

$S_0 = A$ and $S_1 = AB$. For example, the 6 first Fibonacci words S_j, $j \leq 5$, are:

$$S_0 = A$$
$$S_1 = AB$$
$$S_2 = ABA$$
$$S_3 = ABAAB$$
$$S_4 = ABAABABA$$
$$S_5 = ABAABABAABAAB$$

The Fibonacci sequence corresponds to the infinite chain S_∞. Since the recursive construction methods is a concatenation rule, it is easy to see that the number of letters in the jth Fibonacci word S_j follows the famous Fibonacci series: $1, 2, 3, 5, 8, 13, ...$ (hence its name). Additionally, the ratio of the number of letters A to the number of B in S_j tends towards the golden ratio $\tau = (1 + \sqrt{5})/2$ as $j \to \infty$.

A tight-binding Hamiltonian can be written for a Fibonacci QC, by assigning a different on-site potential $\pm\lambda$ to letters A and B. We get:

$$H\psi_n = -t(\psi_{n-1} + \psi_{n+1}) + \lambda\chi_n\psi_n \qquad (3.4)$$

where χ_n is the characteristic function of S_∞, which takes two possible values: $+1$ if the nth letter of S_∞ is A, -1 for B. Note that Eq. (3.4) corresponds to the diagonal Fibonacci model. Similar to the AAH model, the Fibonacci sequence can also be encoded on the couplings (so-called off-diagonal Fibonacci model).

The early works on the Fibonacci model demonstrated that the eigenstates have exotic localization properties: they are neither completely extended nor localized, but "critical" [137–139]. As illustrated in Fig. 3.5, the critical states are states showing a self-similar structure, with multiple scaling indices (the structure of the wave function remains unchanged when zooming in or our, with a proper scaling coefficient, that can take several values). This fractal nature arises from the recursive construction method of the Fibonacci sequence itself. Additionally, the wave function amplitude shows non-monotonous evolution. The main peaks are separated by a number of sites corresponding to a Fibonacci number, and their amplitude is expected to decay algebraically [137]. Note that for this reason, critical states are sometimes mistakenly classified as states with a power-law decay in the literature. It is in general *not* possible to fit a power-law decay to critical states, as pointed out in Ref. [139].

The energy spectrum also has a rich structure; it is a Cantor set with zero Lebesgue measure [140]. This means that, if one picks an energy, it is in a gap with probability 1: the spectrum is nowhere dense, or in other words the total bandwidth is zero (but there are no isolated points). This is called a singular continuous spectral distribution. Finally, the spectrum also has a self-similar structure, with various scaling indices (it is multifractal, like the eigenstates) [138].

The first experimental implementation of a Fibonacci QC was realized for electrons by Merlin *et al.* as early as in 1985 [142]. It consisted in a GaAs/AlAs superlattice with layers of different lengths, arranged into a Fibonacci sequence. This
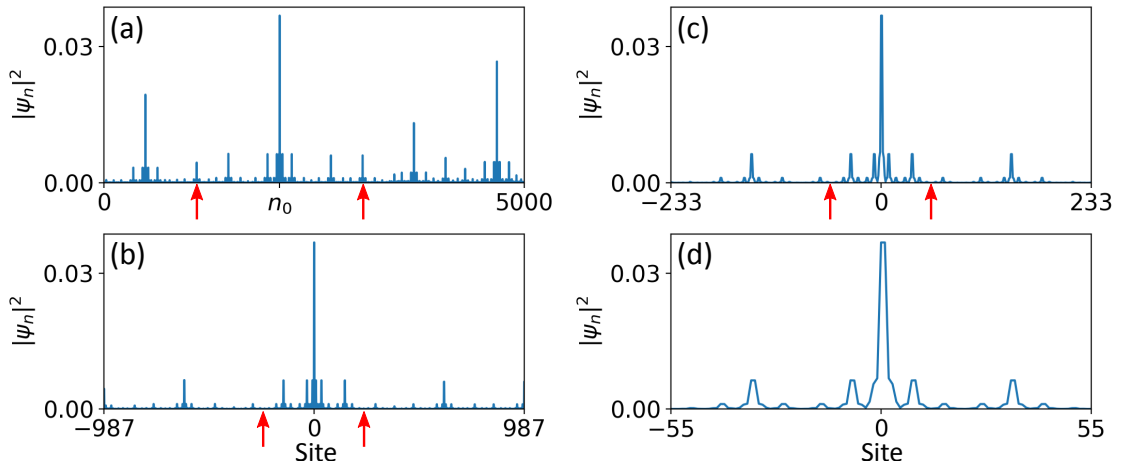
Figure 3.5: Example of a critical wave function, calculated for a Fibonacci QC of 5000 sites. To evidence the self-similarity of the wave function, a zoom on the portion around the maximum (at site n_0) and delimited by the two arrows in (a) is shown (b). (c) and (d) are rescaled with the same procedure. Note that $55, 233$ and 987 all belong to the Fibonacci series.

design was extended to the field of optics by Kohmoto *et al.* [143], who investigated theoretically the optical transmission spectrum of Fibonacci multilayers, predicting multifractal nature for the spectrum. In two parallel pioneering work in 1994, Gellermann *et al.* [105] and Hattori *et al.* [106] fabricated stacks of dielectric layers of SiO_2 and TiO_2, with different thickness and refractive index, arranged into different Fibonacci words, as represented in Fig. 3.6(a). Fig. 3.6(b) shows the experimentally measured transmission spectra, reproduced from Ref. [105], of the structures corresponding to the Fibonacci words S_5 to S_7, compared with theoretical calculations. The self-similarity of the transmission spectrum becomes more apparent as the number of layers is increased. In particular, these experiments showed that the different Fibonacci words have similar transmission spectra when the frequency axis is multiplied by an appropriate scaling factor. Several similar works followed, based on different layer compositions, or with higher order words [110, 144, 145]. However, the main limitation of the multilayer approach is that the transmission spectra gives quite indirect informations on the eigenstates of the system.

In a previous work from our group, Tanese *et al.* implemented the Fibonacci model for polaritons [26]. This work was realized during the PhD thesis of Dimitri Tanese, inspired by a theoretical proposal from Eric Akkermanns and in collaboration with him. The implementation of the Fibonacci model was achieved by etching 1D modulated wires out of a planar cavity. The letters A and B from the Fibonacci words were encoded as blocks of same length a, but of different width $w_{A,B}$ (by extension, we refer to these blocks as letters), resulting in a structure such as the one in Fig. 3.7(a). As discussed in chapter 2, the lateral confinement with letters of 2 different width creates a 1D effective potential as shown in Fig. 3.7, corresponding to
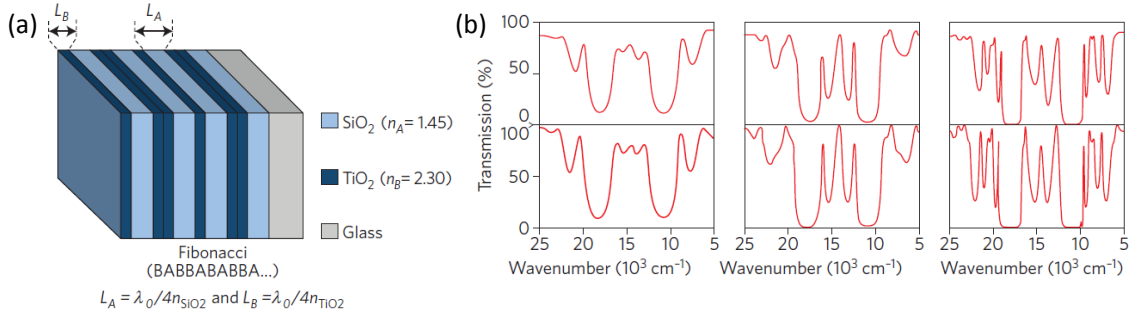
Figure 3.6: (a) Schematic representation of a multilayer Fibonacci structure, composed of two dielectric layers (SiO_2 and TiO_2) of thicknesses L_A and L_B. Image from [110] (note that A and B are exchanged with respect to the Fibonacci sequence described in the main text). (b) Measured (top) and calculated (bottom) optical transmission spectra of such Fibonacci coating stacks, corresponding to the Fibonacci words $S_{5,6,7}$ (from left to right). Results extracted from [105].
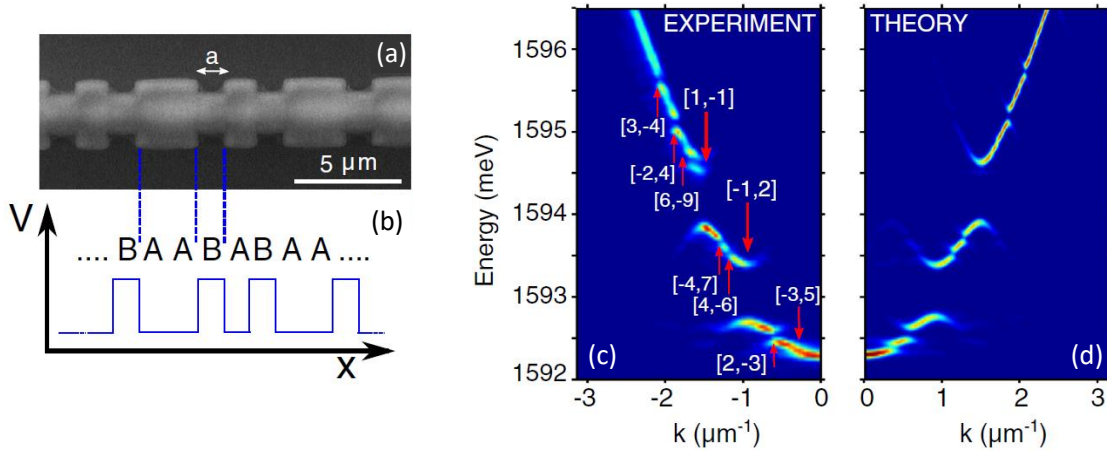
Figure 3.7: (a) SEM image, viewed from top, of a 1D wire for polaritons, fabricated at C2N, and modulated according to the Fibonacci sequence, with wide (narrow) letters A (B), of same length a. (b) Schematic depiction of the corresponding effective 1D potential for polaritons. (c) Measured and (d) calculated momentum-space resolved photoluminescence spectrum of the Fibonacci wire. Red arrows indicate the position of the gaps, labeled with two integers $[p, q]$, as given by the Gap Labeling theorem [141]. Images from [26].
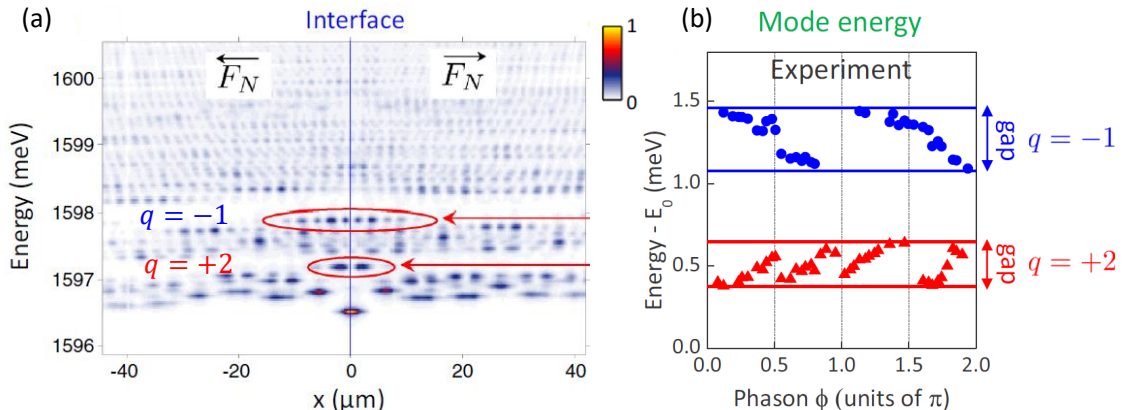
Figure 3.8: (a) Real-space resolved photoluminescence spectrum of a mirror Fibonacci structure (i.e. a Fibonacci word $\overrightarrow{F_N}(\phi)$, concatenated with its mirror $\overleftarrow{F_N}(\phi)$), for a given value of the phason ($\phi = 0.62\pi$). Red arrows indicate edge states, visible in the two lowest main energy gaps, characterized by $q = +2$ and $q = -1$, at the interface between the two Fibonacci words. (b) Measured energy of the edge states of gaps $q = +2$ and $q = -1$ as a function of the phason ϕ. Images from [94].

the Fibonacci sequence. The photoluminescence was measured under non-resonant excitation, both in real- and momentum-space. The fractal nature of the spectrum was clearly evidenced in the momentum-space spectrum, as presented in Fig. 3.7(c), in agreement with theoretical simulations based on a 1D Schrödinger equation, see Fig. 3.7(d). Importantly, the Gap Labeling theorem [141] states that each gap in the spectrum can be identified with a unique pair of integers $[p, q]$. The wave-vector $k_{p,q}$ at which the gap opens is determined by these integers as:

$$k_{p,q} = \frac{\pi}{a}\left(p + \frac{q}{\tau}\right) \tag{3.5}$$

We remind that τ is the golden ratio. This is illustrated in the experiments of Tanese *et al.*, as shown in Fig. 3.7(c) where the integers $[p, q]$ associated with each gaps are indicated. It should be noted that for an infinite system, the set of gaps at $k_{p,q}$ generated by pairs $[p, q]$ is infinite and dense in the interval $[0, \pi/a]$, explaining why the spectrum is singular continuous. The number of gaps visible in the experiments depends on the system size, as well as on the polariton linewidth. The latter is the limiting factor.

The Fibonacci model also has nontrivial topological properties. In fact, the integer q from the pair $[p, q]$ identifying a gap is the Chern number of this gap [141]. This was shown experimentally in another work from our group [94], where Baboux *et al.* investigated the presence of edge states at the interface between a Fibonacci word (respectively noted $\overrightarrow{F_N}$ and $\overleftarrow{F_N} = [\chi_N \chi_{N-1}...\chi_1]$, with N the number of sites). These structures were implemented as modulated 1D wires, as described above. The existence of edge states was evidenced by measuring the real-

space resolved photoluminescence emission under non-resonant excitation, as shown in Fig. 3.8(a). The link between the gap labels $[p, q]$ and their Chern number was shown by scanning a phason degree of freedom ϕ. Indeed, similar to the AAH model, the origin of the topological properties of the Fibonacci model can be understood by the addition of a phason, i.e an additional effective dimension. This was first done in Ref. [102], where Kraus and Zilberberg showed that the characteristic function of the Fibonacci sequence can be written:

$$\chi_n = \text{sgn}\left[\cos(2\pi n\tau^{-1}) - \cos(\pi\tau^{-1})\right] \tag{3.6}$$

with $\text{sgn}(x)$ the sign function ($\text{sgn}(x) = +1$ if $x > 0$, -1 if $x < 0$). A phason ϕ can be included in the above expression, replacing $\cos(2\pi n\tau)$ with $\cos(2\pi n\tau + \phi)$. As in the AAH model, a change of ϕ corresponds to a translation of the QC, for a lattice of infinite size. In the case of a finite chain with N sites, sweeping ϕ from 0 to 2π induces a series of N local changes in the structure, corresponding to the exchange of two letters ($AB \leftrightarrow BA$) at specific locations. Baboux *et al.* fabricated multiple copies of 1D Fibonacci modulated wires with $N = 55$ sites, corresponding to each of the $N = 55$ structures in a sweep of ϕ from 0 to 2π. The energy of the edge states in the two main gaps was measured as a function of ϕ, revealing that the edge states crosses the gap a number of times given by $2q$ (as seen in Fig. 3.8(b)), as expected for a gap with Chern number q (note also that the sign of q determines the direction of the traverses).

Simultaneously to Baboux's work, a similar strategy was used to measure the topological invariants from the diffraction pattern of a Fibonacci sequence implemented with digital mirror devices [119]. The topological properties of the Fibonacci model were also evidenced through topological pumping across a lattice of coupled waveguides [146].

3.2.3 Continuous deformation between the two models

We have seen that the AAH QC and Fibonacci QC share similar topological properties. In fact, Kraus and Zilberberg [102] have shown that the AAH model and Fibonacci model are topologically equivalent, if the modulation frequency of the AAH model is $b = 1/\tau$. To demonstrate this, they introduced a smooth deformation, controlled by a parameter β, transforming the AAH potential into the Fibonacci potential:

$$V_n(\beta) = \frac{\tanh(\beta\left[\cos(2\pi nb) - \cos(\pi b)\right])}{\tanh\beta} \tag{3.7}$$

Note that in the original work of Ref. [102], the phason degree of freedom ϕ, which was included in the term $\cos(2\pi bn)$. Since the phason has no influence on the localization properties (as is corresponds to a translation along the lattice), we ignore this degree of freedom in the rest of the chapter.
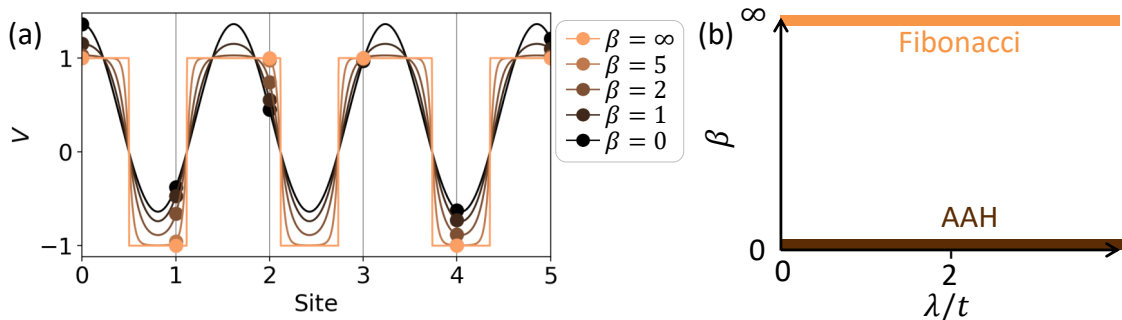
Figure 3.9: (a) Continuous deformation between the Harper and Fibonacci modulations. $V_n(\beta)$ (dots) and its generating function $g(x, \beta)$ (solid lines) are plotted for $b = 1/\tau$ and different values of β. (b) Illustration of the (λ, β) space of the AAHF model: $\beta \to 0$ coresponds to the AAH model, while the Fibonacci model is approached as $\beta \to \infty$, independent of the modulation amplitude λ.

Figure 3.9(a) represents $V_n(\beta)$ for different values of β. We have also plotted the function $g(x, \beta)$ generating the discrete series of V_n, such that $V_n(\beta) = g(n, \beta)$. It is easy to verify that in the limit of small β, this modulation becomes the Harper modulation, with a constant shift: $V_n(\beta \to 0) = \cos(2\pi bn) - \cos(\pi b)$. On the other hand, for $\beta \to \infty$, the modulation approaches the Fibonacci modulation, as illustrated in Fig. 3.9(a): V_n can only take the values ± 1, depending on the sign of $\cos(2\pi nb) - \cos(\pi b)$, which for $b = 1/\tau$ corresponds exactly to the characteristic function of the Fibonacci sequence (Eq. (3.6)).

From the smooth deformation, we defined a generalized Aubry-André-Harper-Fibonacci (AAHF) model, corresponding to the Hamiltonian:

$$H(\beta)\psi_n = -t(\psi_{n-1} + \psi_{n+1}) + \lambda V_n(\beta)\psi_n \tag{3.8}$$

Kraus and Zilberberg have shown that for a fixed b, no gap in the energy spectrum closes when scanning β. In particular, this implies that the Chern number associated with each gap remains constant in the deformation from the AAH to Fibonacci model: both have the same topological properties. Note that strictly speaking, the Fibonacci model corresponds to $b = 1/\tau$, but the topological equivalence between AAHF Hamiltonians with different β holds for any irrational b. It was also demonstrated that the off-diagonal model, with the modulation applied to the couplings, has the same topological properties as the diagonal model from Eq. (3.8) with same b. However, two AAHF QC with different b have gaps with different Chern numbers and are thus topologically distinct.

The existence of topological phase transitions in the AAHF model was explored experimentally by Verbin *et al.* [118], using arrays of coupled waveguides. They observed the presence of edge states at the interface between AAH models with different modulation frequency, confirming the distinct topological properties. On the other hand, no edge state was observed at the interface between a AAH and Fibonacci lattices, confirming their topological equivalence.
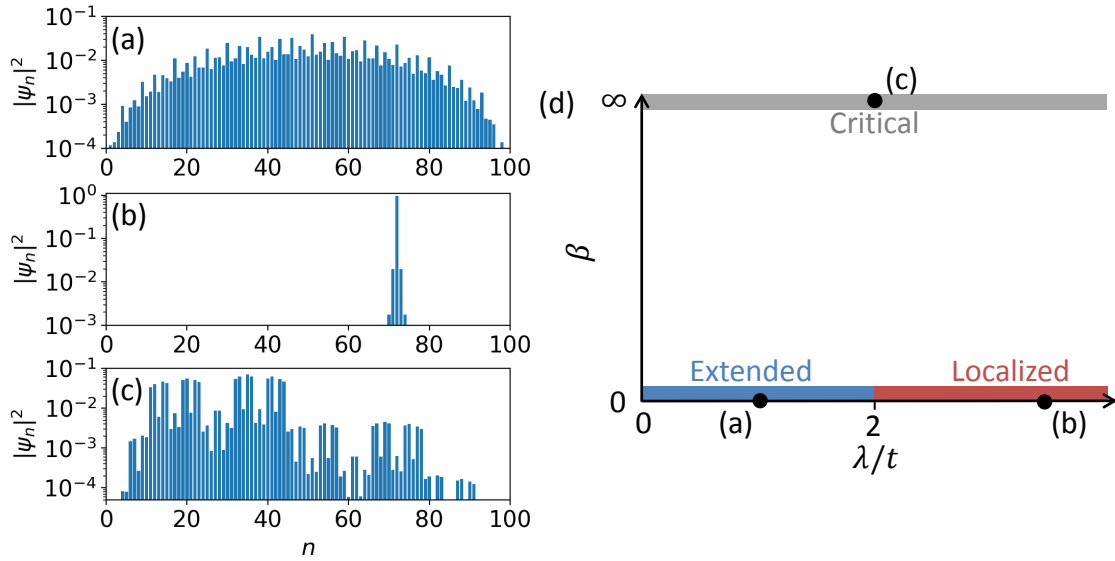
Figure 3.10: (a-c) Examples of (a) extended; (b) localized and (c) critical eigenstates, calculated with (a) $\beta = 0, \lambda/t = 1$; (b) $\beta = 0, \lambda/t = 4$ and (c) $\beta = \infty, \lambda/t = 2$. The occupation per site $|\psi_n|^2$ is in logarithmic scale. (d) Schematic of a diagram for the AAHF model. The localization properties have been explored only in the limits of the AAH ($\beta \to 0$) and Fibonacci ($\beta \to \inf$) models, indicated by thick lines.

The phase space of AAHF models with equivalent topology (i.e. for fixed b) is spanned by the two parameters β and λ/t. This space can be represented as in Fig. 3.9(b), where the limits $\beta \to 0$ and $\beta \to \infty$ corresponds to the AAH model and Fibonacci model, respectively. We have seen that the localization properties of these two models are very different: while a localization transition occurs in the AAH model at $\lambda/t = 2$, all states are critical for any value of λ/t in the Fibonacci model. As a reminder, examples of an extended, localized and critical state are plotted in Fig. 3.10(a-c). These localization properties are summarized in the preliminary phase diagram from Fig. 3.10(d): only two limits of the diagram are determined, and for any other value of (β, λ), the localization properties are so far unexplored, both theoretically and experimentally. Owing to the very different nature of the states in the different limiting cases, we can expect a rich localization phase diagram. For example, one of the open questions is the extent of the extended and localized phases of the AAH limit when increasing β. The exploration of the localization phase diagram of the AAHF model is the objective of the present chapter. This idea originally emanated from Oded Zilberberg, who proposed us to use polaritons for experimental implementation of the AAHF model. The work presented in this chapter is realized in collaboration with his group.

3.3 Theoretical localization phase diagram of the AAHF model

3.3.1 Tight-binding model

First, we investigate the localization phase diagram theoretically, based on the tight-binding Hamiltonian from Eq. (3.8). To this end, we set $b = \tau$ (this choice is motivated below). The tight-binding calculations presented in this section were performed by Antonio Štrkalj and José Lado, in the group of Oded Zilberberg in Zürich.

The localization of the bulk states can be systematically characterized by extracting the localization length from the tails of the wave functions. We define an inverse localization localization length Λ as follows:

$$\Lambda = \lim_{n \to \infty} -\frac{\log(\psi_{n_0}^* \psi_{n_0+n})}{n} \tag{3.9}$$

where ψ_n is the wave function amplitude at site n and n_0 denotes the site where this amplitude is maximal. Computing Λ enables to distinguish between extended and localized states: for a localized state, the wave function decays exponentially, as $\psi_n \propto e^{-\Lambda|n-n_0|}$, with a finite Λ. On the other hand, for an extended state (e.g. a Bloch state), the wave function amplitude does not decay, corresponding to $\Lambda \to 0$.

For a systematic characterization of the localization, we diagonalize the AAHF Hamiltonian for all values of (λ, β). For each set of (λ, β), we compute the inverse localization length for each eigenstate, and finally average Λ over all states. The resulting map of average inverse localization length gives a phase diagram, presented in Fig. 3.11(a). Dark regions corresponds to extended states, while white regions denote localized states. We can first point out that we recover the localization transition at $\lambda/t = 2$, $\beta = 0$, from the AAH model. Moreover, intriguing features are observed: starting from $\beta = 0$ in the localized phase, several delocalization tongues are identified towards high values of β, the main one around $\beta = 2$. This corresponds to a delocalization-localization transition when scanning β at fixed λ.

The phase diagram from Fig. 3.11(a) corresponds to an averaged Λ, and thus we loose some information on the nature of the different states in the spectrum. To gain further insight on the delocalization tongue, we have plotted in Fig. 3.11(b) the inverse localization for each eigenstate in the energy spectrum, in a scan of β for a fixed $\lambda/t = 2.5$. Note that extended states (respectively localized), are represented by blue (orange) dots. We see that, for $\beta \approx 1$, extended states are found only in the lowest energy band. All other states remain localized.

From Fig 3.11(b) we can get an insight on the origin of the delocalization tongue: it occurs at values of β where the width of the lowest band shrinks, due to the specific deformation of the AAHF modulation. As the energy spacing between the different localized modes reduces, the eigenstates get more and more extended, and full delocalization is reached below some threshold spacing value. Increasing
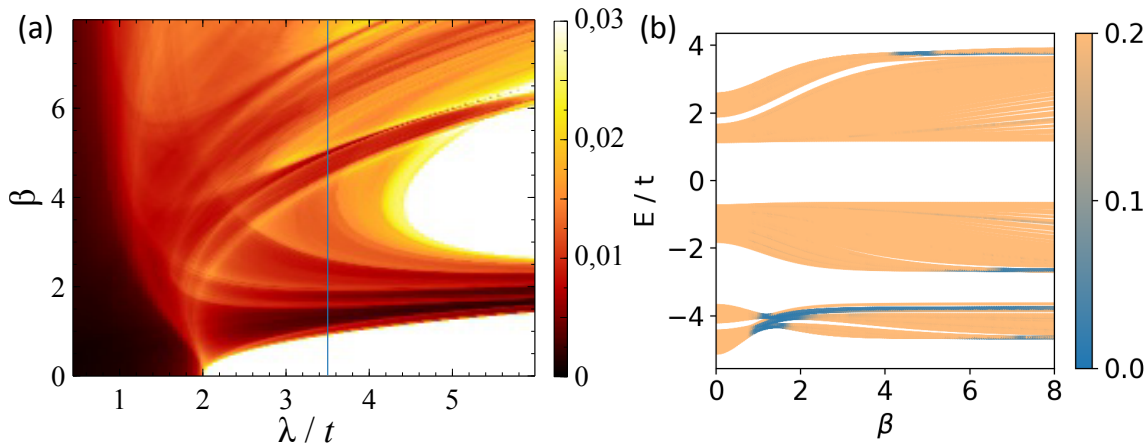
Figure 3.11: (a) Map of the mean of the inverse localization length Λ, versus λ/t and β. (b) Localization of all eigenstates in the energy spectrum in a scan of β at fixed $\lambda/t = 2.5$, as indicated by the blue line in panel (a). Shaded gray regions are the energy gaps.

β further, the energy spacing increases and modes re-localize. This is of course a qualitative argument. Quantitative investigations are still carried out by our collaborators in Zürich to capture analytically this transition.

The localization-delocalization transition that we identified is very peculiar: it corresponds to the opening of a conduction channel in a single band only. In the following, we will focus more specifically on this transition, and in particular one of our goals will be to evidence its existence experimentally.

Finally, let us comment on the choice $b = \tau$. In the previous section, we have considered $b = 1/\tau$, mainly because for $\beta \to \infty$ the AAHF modulation coincides with the definition of the Fibonacci sequence. However, since τ is the golden ratio, we have the relation $\tau = 1 + 1/\tau$. From Eq. (3.7), it follows that the AAHF modulation with $b = \tau$ leads to the same Hamiltonian as for $b = 1/\tau$, with the change of sign $\lambda \to -\lambda$ (plus a translation, or addition of a phason $\phi = \pi$). In other words, for a given λ, the AAHF models with $b = \tau$ and $b = 1/\tau$ have inverted energy spectrum. In particular, this implies that the delocalization-localization transition described above occurs in the upper band for $b = 1/\tau$. As we shall see in the next paragraph, for the implementation of the AAHF model with polaritons it is more convenient to consider the case where this transitions occurs in the lowest band. Note also that this corresponds to the Fibonacci potential implemented for polaritons previously [26, 94], with on-site energy of sites A lower than sites B.

3.3.2 Nearly-free particle model

We want to explore experimentally the phase diagram with polaritons. However, implementing the tight-binding AAHF model with chains of coupled pillars is difficult, because it requires a very fine control of the on-site energies. This is very
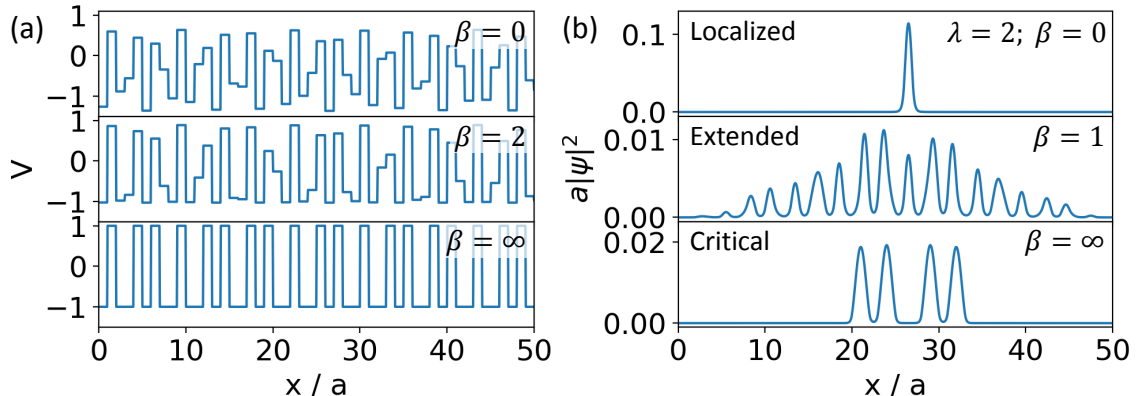
Figure 3.12: (a) One-dimensional potential $V(x)$ on 50 letters, for $\beta = 0$, $\beta = 2$ and $\beta = \infty$ (b) Lowest energy eigenstate, computed for fixed $\lambda = 2$ meV and $\beta = 0$, $\beta = 1$, $\beta = \infty$.

challenging to achieve, especially if we want constant couplings. Thus, we opt for a different approach, inspired from the implementation of the Fibonacci sequence with polaritons from Refs. [26, 94]. The idea is to engineer a 1D quasiperiodic potential corresponding to the modulation from the AAHF model, and study the localization properties for the polariton wave function in such a potential, considering the polariton as a free particle of mass m. In other words, this corresponds to a nearly-free particle approach to the AAHF model.

First, we investigate theoretically the localization phase diagram corresponding to this approach, in particular to see how it compares with the diagram obtained with the tight-binding formalism.

The discrete modulation $V_n(\beta)$ given by Eq. (3.7) is converted into a step-like 1D potential $V(x, \beta)$, defined as:

$$V(x, \beta) = V_{\lfloor x/a \rfloor}(\beta) \tag{3.10}$$

where $\lfloor x \rfloor$ is the floor function, and a is the length of each step (in the following, we refer to steps as letters). Examples of the 1D potential for different values of β are presented in Fig. 3.13(a).

Next, we solve for the eigenstates $\psi(x)$ and eigenenergies E of the linear 1D Schrödinger equation describing the behavior of a particle of mass m in a 1D potential:

$$\left(-\frac{\hbar^2}{2m} \nabla^2 + \lambda V(x, \beta) \right) \psi(x) = E\psi(x) \tag{3.11}$$

We use a mass $m = 3 \times 10^{-5}\, m_e$ (typical polariton mass in our samples), and letter length $a = 2$ μm. Examples of eigenstates are shown in Fig. 3.12(b), calculated for $\lambda = 2$ meV and three values of β: $\beta = 0$, $\beta = 1$ and $\beta = 2$, for which the state is respectively localized, extended and critical.

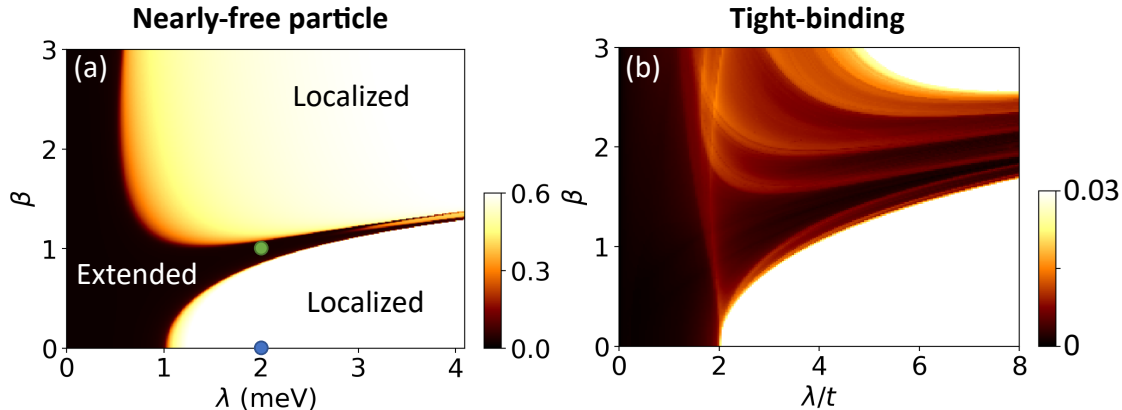**Figure 3.13:** (a) Map of the IPR for the lowest energy eigenstate state of the 1D Schrödinger equation (3.11), in the nearly-free particle approach. The blue (green) dot corresponds to the eigenstate with $\beta = 0$ ($\beta = 1$) in Fig. 3.12(b). (b) Localization diagram from the tight-binding model, averaging Λ over the lowest energy band only.

It should be noted that it is possible to rescale the x axis in the Schrödinger equation (Eq. (3.11)), to the dimensionless $\tilde{x} = x/a$. It follows that the modulation amplitude and eigenenergies can also be rescaled to dimensionless $\tilde{\lambda} = \alpha\lambda$ and $\tilde{E} = \alpha E$, with the rescaling factor $\alpha = 2ma^2/\hbar^2$. We get a dimensionless Schrödinger equation:

$$\left(\nabla^2 + \tilde{\lambda}V(\tilde{x}, \beta)\right)\psi(\tilde{x}) = \tilde{E}\psi(\tilde{x}) \tag{3.12}$$

One consequence is that a change in the value of a results in the same phase diagram, but with a rescaling of the λ axis proportional to a^{-2} (and same rescaling for the energy spectrum). Thus, the choice of a is not critical at this point.

To distinguish systematically between extended and localized states, we introduce a figure of merit different from the inverse localization length Λ used previously: we compute the Inverse Participation Ratio (IPR) of each state. The need for a different figure of merit arises from the fact that extracting the inverse localization length requires chains with a high number of sites N. In 1D numerical simulations, this is computationally heavy. The advantage of the IPR is that it is well defined for chains with moderate number of sites. In our 1D simulations, we use $N = 100$. The IPR of a state ψ is defined as:

$$\text{IPR} = a \int |\psi(x)|^4 \mathrm{d}x \tag{3.13}$$

Note that the above definition is an extension to a continuous 1D system of the IPR defined for a discrete wave function ψ_n as $\text{IPR} = \sum_n |\psi_n|^4$. The participation ratio (PR = IPR^{-1}) indicates the number of sites (or letters in the continuous 1D case) over which an eigenstate has non-vanishing amplitude. Thus, the IPR provides similar information to the inverse localization length. It remains finite for a localized

state (it takes maximal value 1 for a wave function perfectly localized on a single site), and vanishes for extended states.

Figure 3.13(a), presents the IPR for the lowest energy eigenstate only, calculated for all values of (λ, β). As a comparison, in Fig. 3.13(b) we show the phase diagram obtained from the tight-binding model, but where the inverse localization length Λ is averaged only over the lowest energy band. The diagram for the nearly-free model is very close to the diagram from the tight-binding model. In particular, a clear localization transition in observed at $\beta = 0$ (limit of the AAH model), for $\lambda = 1$ meV. More interesting, a similar delocalization tongue is present at high λ, around $\beta \approx 1$. Since a single eigenstate is considered in Fig. 3.13(b), we observe a single delocalization tongue. This is also the case in Fig. 3.13(b) for the tight-binding diagram of the lowest band. Note however a small quantitative difference between the two models, in the value at which the delocalization and subsequent localization transitions are expected when scanning β.

A more significant difference of the nearly-free model with the tight-binding model appears when we consider the full energy spectrum at a given value of (λ, β). For example, in Fig. 3.14 we have plotted the spectrum, resolved both in (a) real and (b) momentum space (simply obtained by Fourier transform of the eigenstates $\psi(x)$), calculated for $\lambda = 2$ meV and $\beta = 0$. On the phase diagram, this is in the localized phase, as indicated by the blue dot in Fig. 3.13(a). The lowest energy state is plotted in Fig. 3.12(b), top panel. In Fig. 3.14 the other states from the lowest band are clearly localized, as evidenced in particular by the broadness of the peaks at $k = 0$ in momentum space (i.e. blurred lowest band). However, the eigenstates in higher energy bands are delocalized (very narrow peaks, thin bands, in k space). This is because in a nearly-free particle model, the kinetic energy is not bound (contrary to the tight-binding model where the kinetic energy is fixed by the hopping t, and is identical for all states). Thus, in the nearly-free particle model the 1D potential
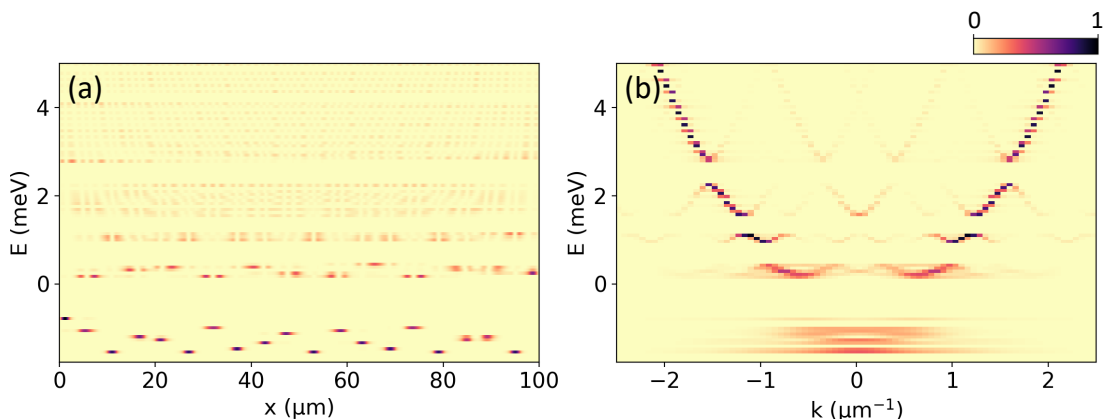

Figure 3.14: (a) Real- and (b) momentum-space resolved energy spectrum, calculated for a chain of 50 letters with $a = 2$ μm and $\lambda = 1.5$ meV, $\beta = 0$, corresponding to the blue dot in the phase diagram from Fig. 3.13(b).

affects mostly the bottom of the parabolic dispersion ($E(k) = \hbar^2 k^2/2m$) of the free particle, where the kinetic energy is low. For higher kinetic energy, the potential is averaged and has barely any effect. As discussed previously, this corresponds to the appearance of a mobility edge in the spectrum [131, 132]. The states in higher bands can also localize, but at higher values of λ with respect to the lowest band.

In conclusion, our numerical simulations indicate that the nearly-free approach results in localization properties very close to the tight-binding model, but for the lowest energy bands only. Thus we choose to implement the nearly-free particle for the experimental investigation of the localization phase diagram with polaritons, since the engineering of this model is simpler as compared to the tight-binding model. In the experiments, we will mainly be interested in the lowest energy bands.

3.4 Experimental investigation of the localization properties

3.4.1 Implementation of the AAHF model with polaritons

In this section, we investigate experimentally the localization phase diagram of the AAHF model with polaritons. The nearly-free AAHF model discussed above is implemented by etching 1D modulated wires (also referred to as chains in the following) out of planar microcavities.

We have introduced in chapter 2 how the geometry of such microstructures can be mapped to a 1D potential profile. Here, let us recall that the lateral confinement in a modulated wire, described by a position-dependent width $w(x)$, creates the following 1D potential for the transverse mode of order n (or nth 1D subband):

$$V(x) = \frac{\hbar^2 \pi^2}{2m} \frac{n^2}{w(x)^2} \tag{3.14}$$

with m the lower polariton mass. We use this relation to design wires implementing the nearly-free AAHF model: the targeted 1D potential corresponding to a given (λ, β) is converted to structure width using Eq. (3.14). Let us discuss in detail this engineering procedure.

First some limitations exist regarding the geometry of the modulated wires feasible in practice. In particular, the width of a letter cannot exceed or be inferior to a maximal and minimal width. If a letter is too narrow, typically below 1.5 µm, strong non-radiative exciton recombinations occur at the outer sides, which broadens the polariton linewidth. On the other hand, if the width is above 4 to 5 µm, the energy spacing between the lowest order $n = 1$ mode and second transverse mode $n = 2$ is too small, such that the 1D approximation is no longer valid. Thus, when designing the modulated wires we set a maximal letter width $w_{max} = 4$ µm (we note V_0 the corresponding lateral confinement potential). The minimal value of the target potential is assigned the letter width w_{max}. Taking this minimal value as a
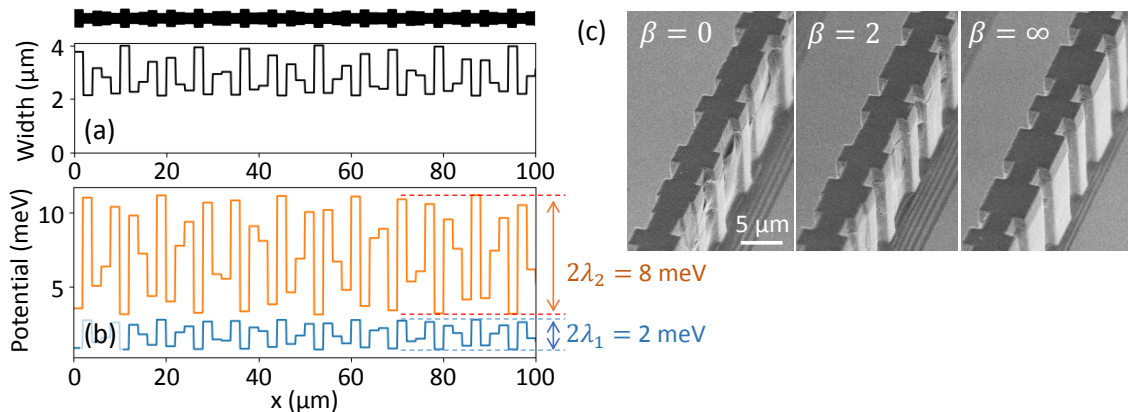
Figure 3.15: (a) Width of the modulated wire, designed to implement the AAHF modulation with $\beta = 0$ and $\lambda = 1$ meV. The corresponding 1D wire is depicted on top. (b) Resulting 1D potential profile along the wire, arising from the lateral confinement, for $n = 1$ modes (blue line) and $n = 2$ modes. The contrast λ_2 for $n = 2$ modes is 4 times stronger than the contrast λ_1 for $n = 1$ modes. (c) SEM images of modulated wires etched out of a planar cavity, implementing the AAHF model for 3 values of β.

reference for the potential ($V = 0$), the wire width is determined from Eq. (3.14) by applying a global offset V_0 to the target potential.

As an illustration, Fig. 3.15(a) presents the width of a wire implementing the step-like AAHF modulation with $\beta = 0$ and $\lambda = 1$ meV for the lowest 1D subband ($n = 1$). The targeted potential profile along the wire is plotted in Fig. 3.15(b), blue line.

Taking into account the lower bound on the letter width, we can achieve modulation amplitude typically up to $\lambda \approx 1.5$ meV for the $n = 1$ transverse modes. In the theoretical localization phase diagram from Fig. 3.13, this would be barely above the localization transition for $\beta = 0$, so access to higher λ is necessary for thorough exploration of the phase diagram. However, a very advantageous feature of the modulated wires is the presence of higher order transverse modes ($n > 1$). The lateral confinement for these modes is significantly stronger than for $n = 1$ modes, since it is proportional to n^2. In other words, a structure designed with a target (λ, β) for $n = 1$ modes also implements the AAHF modulation for $n \geq 2$ modes, with same β but with increased modulation amplitude $\lambda_n = n^2 \lambda$. Thus, $n = 2$ modes undergo a potential with 4 times stronger contrast as $n = 1$ modes ($\lambda_2 = 4\lambda_1$). This is illustrated in Fig. 3.15(b), where we have plotted the calculated 1D potential profile for the $n = 1$ modes (blue line) and $n = 2$ modes (orange), created by the structure width from Fig. 3.15(a). The enhanced contrast for $n = 2$ modes is particularly interesting, as it enables the exploration of high values of λ in the phase diagram, i.e. in the region where we have identified an unexpected delocalization-localization phase transition.
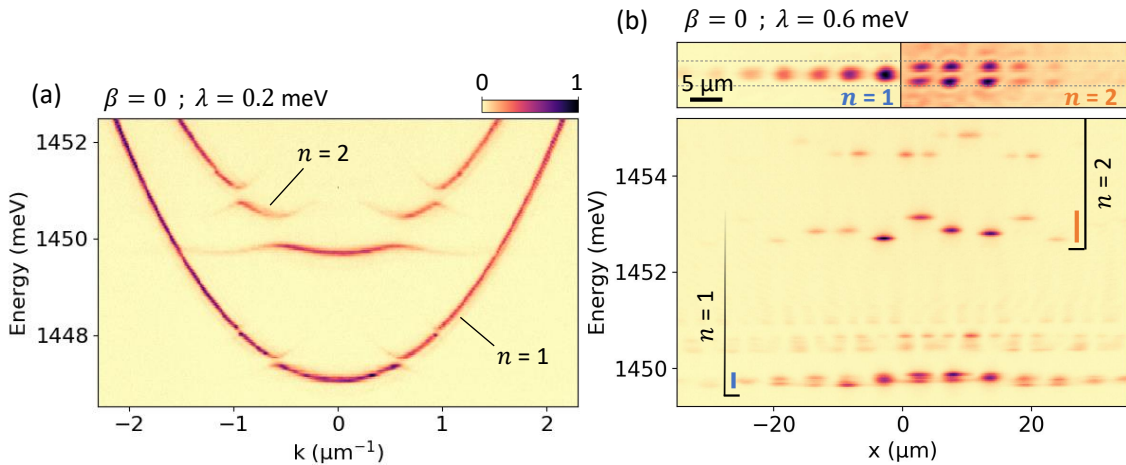
Figure 3.16: (a) Momentum-space resolved photoluminescence spectrum measured for a chain with $\beta = 0$ and $\lambda = 0.2$ mev. Two sets of subbands are clearly identified, corresponding to $n = 1, 2$ modes. (b) Bottom: Real-space resolved spectrum measured for a chain with $\beta = 0$ and $\lambda = 0.6$ mev. Top: corresponding real-space image of the photoluminescence, integrated over the lowest band, for $n = 1$ and $n = 2$ modes. The blue (resp. orange) bar in the lower plot indicates the energy range over which the emission pattern is integrated, for the $n = 1$ ($n = 2$) mode. Dashed gray lines are guides for the eyes, indicating the maximal wire with.

The choice of letter length a is also the result of a trade-off, due to the scaling of λ and eigenenergies with a^{-2}, as described in the previous section. As the letter size decreases, the amplitude of every energy bands increases, which is interesting because the spectral resolution in the experiment is limited by the polariton linewidth, but at the same time the localization transition at $\beta = 0$ occurs at higher λ (additionally it is harder to address a single letter experimentally with the excitation laser spot). On the other hand, in the limit of long letters, the energy bands are very narrow, and due to the finite polariton lifetime, the propagation distance amounts to a small number of letters (which hinders the distinction between localized and extended states). With these considerations, and based on the calculations presented previously, we set $a = 2$ µm. With this value, the localization transition at $\beta = 0$ is expected at $\lambda \approx 1$ (see Fig. 3.13).

Several wires were fabricated, corresponding to a large set of λ and β, in order to explore the localization phase diagram. Examples of structures with $\beta = 0$, $\beta = 2$ and $\beta = \infty$ are shown in Fig. 3.15(c). These structures are characterized under weak non-resonant excitation, tuning the laser energy around 1.6 eV. We measure the photoluminescence emission from a single chain, resolved either in momentum or real space. Only one linear polarization is considered, e.g. horizontal polarization. We have verified that the energy spectrum is identical in the other orthogonal polarization (except for a global shift of the energies, induced by a small polarization splitting).

Fig. 3.16(a) presents the momentum-space resolved emission spectrum of a chain with $\beta = 0$ and $\lambda = 0.2$ meV. Two sets of bands are clearly visible, identified as $n = 1$ and $n = 2$ subbands. We can also confirm from the bigger gap in the $n = 2$ bands that the modulation amplitude is enhanced with respect to the $n = 1$ modes. Accordingly, $n = 1$ and $n = 2$ modes are also identified in the real-space emission spectrum shown in Fig. 3.16(b), measured on a chain with $\beta = 0$ and $\lambda = 0.6$ meV. It is also possible to obtain the 2D real-space image of individual eigenmodes from the $n = 1$ and $n = 2$ subbands, by spectrally filtering the emission at the energy of these bands. The 2D map of the emission pattern is reconstructed from spectra such as the one shown in Fig. 3.16(b), measured at different lateral positions across the wire. The result is presented in Fig. 3.16(b), top panel, and evidences the nature of the $n = 1$ and $n = 2$ modes: in particular, the second transverse modes $n = 2$ have the characteristic transverse profile with two bright lobes, and a zero at the center of the chain.

3.4.2 Localization transition in the AAH model

First, to confirm the validity of our implementation of the AAHF model, we evidence the localization transition in the limit of the AAH model, i.e. for $\beta = 0$.

According to the theoretical calculations, with letter length $a = 2$ µm the localization transition is expected around $\lambda = 1$ meV. With the $n = 1$ modes, the maximal λ that we could implement is 1.4 meV. This should be enough to observe the localization transition, expected from the numerical simulations at $\lambda \approx 1$, but is not far above this theoretical localization threshold. Thus, we focus on the $n = 2$ modes, which allow to explore up to $\lambda = 5.6$ meV.

The non-resonant characterization of three different wires, with $\beta = 0$ and respectively $\lambda_2 = 0.8$ meV, $\lambda_2 = 1.6$ meV and $\lambda_2 = 2.4$ meV is presented in Fig. 3.17, both in momentum space and real space. For the lowest value $\lambda_2 = 0.8$ meV, in Fig. 3.17(a), the lowest $n = 2$ band is very thin in k space, indicating extended modes. This is confirmed by the real-space spectrum, in which we can see that the modes are delocalized over several letters. Moving to a wire with higher contrast $\lambda_2 = 1.6$ meV, Fig. 3.17(b), the real-space spectrum shows that the lowest energy $n = 2$ modes now consist in isolated bright lobes, each at different energy: these are localized states. Accordingly, in k space the lowest energy modes are very broad and no longer form a band. The same behavior is observed for the highest value $\lambda_2 = 2.4$ meV presented in Fig. 3.17(c). Note, though, that the higher energy $n = 2$ modes are still relatively delocalized for $\lambda_2 = 1.6$ meV, but completely localized for $\lambda_2 = 2.4$ meV (this is best seen in the k space spectrum). As expected, due to their higher kinetic energy, these modes localize for stronger λ.

Note also that the chain with $\lambda_2 = 2.4$ meV corresponds to $\lambda_1 = 0.6$ meV, below the localization threshold. We indeed observe extended $n = 1$ modes in this chain.

In Fig. 3.17, we have also reproduced the theoretical localization phase diagram obtained with the nearly-free AAHF model. The position on the diagram corre-
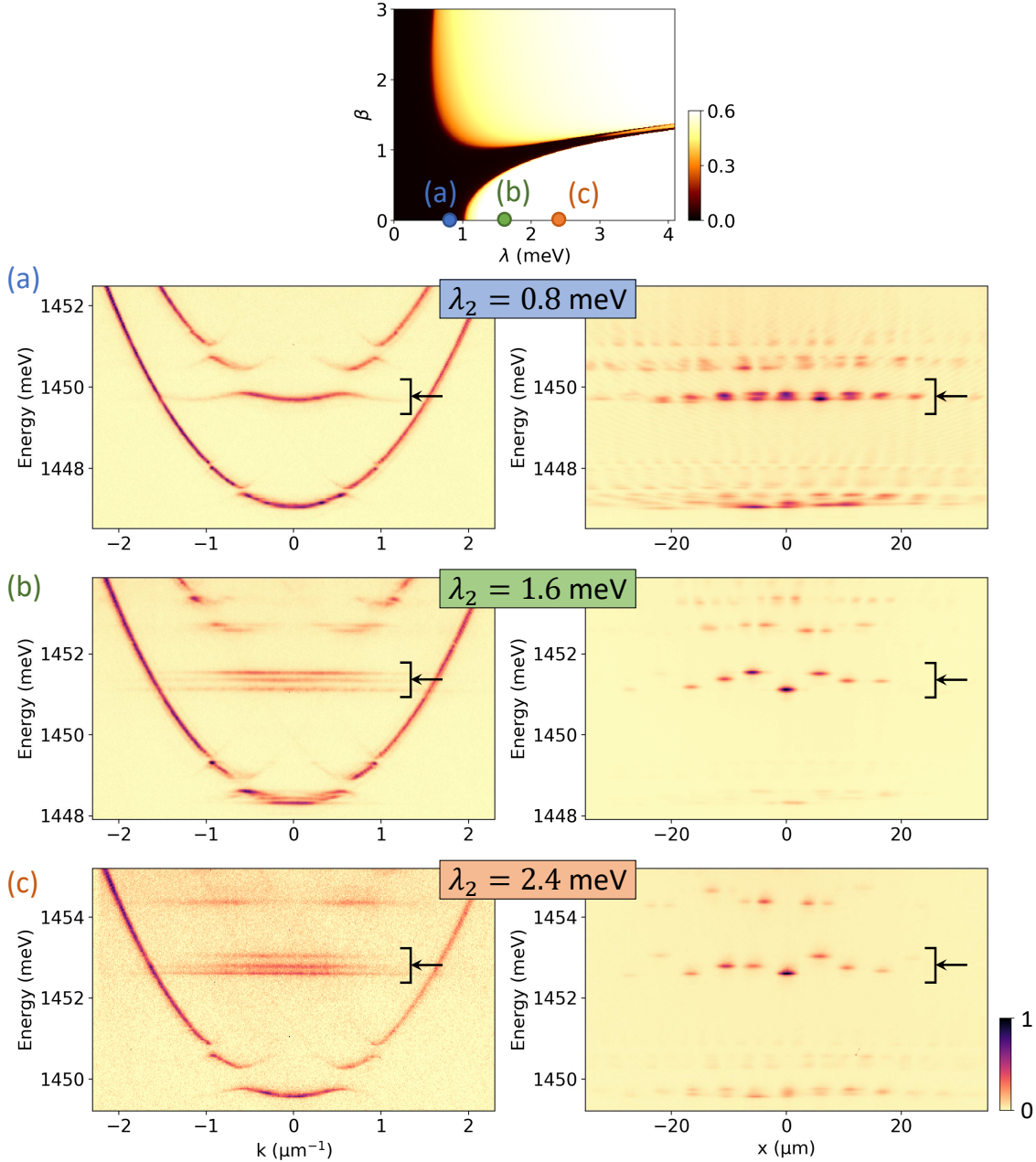
Figure 3.17: Observation of the localization transition for $\beta = 0$. (Left column) Momentum- and (right) real-space resolved PL emission of three modulated wires, with $\beta = 0$ and (a) $\lambda_2 = 0.8$ meV, (b) $\lambda_2 = 1.6$ meV and (c) $\lambda_2 = 2.4$ meV. The corresponding positions on the theoretical localization phase diagram are reported in the upper panel (colored dots). In each panel, the arrow indicates the lowest band of $n = 2$ modes.
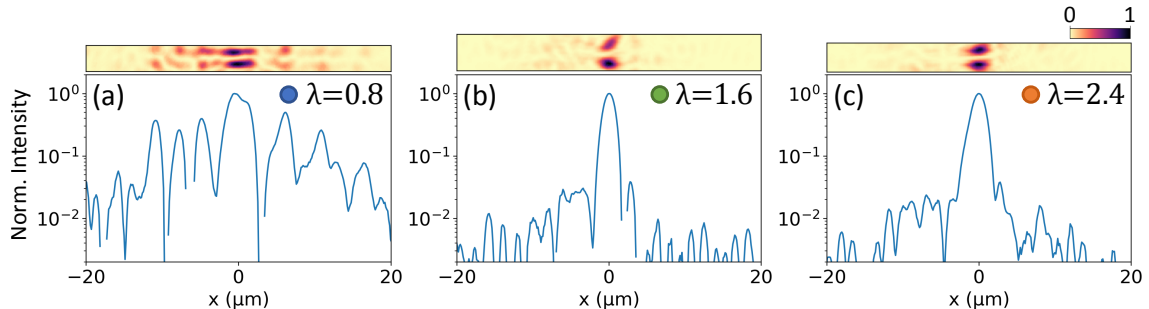
Figure 3.18:   (Top) Real-space image of the emission and (bottom) semi-logarithmic plot of the normalized intensity profile, integrated in the transverse wire direction, measured under resonant excitation of the site at $x = 0$, on the same three wires as in Fig. 3.17 (and same position on the wire), i.e. with $\beta = 0$ and (a) $\lambda_2 = 0.8$ meV, (b) $\lambda_2 = 1.6$ meV and (c) $\lambda_2 = 2.4$ meV.

sponding to the three structures characterized experimentally was reported on this phase diagram. The experimental localization properties of the different structures fall exactly in the localization phase expected in theory, indicating faithful implementation of the AAHF model. More experimental values of λ can be found in Appendix A, and confirm this good agreement.

We can also use resonant excitation, with the pumping laser focused on a single letter, to attest the extended or localized nature of the states. If the states are extended, polaritons can ballistically propagate away from the excitation spot, whereas propagation is impossible in localized states. For each of the three structures presented above, we tune the laser energy in resonance with a $n = 2$ mode and measure the real-space emission pattern. We use very weak pumping power (typically a few μW), to probe the linear eigenmodes and avoid nonlinear effects due to polariton-polariton interactions. Note also that in order to excite resonantly the $n = 2$ mode, we have to move the laser spot slightly to the side of the letter, to couple to one of the two lateral lobes of the $n = 2$ mode only (this is because the two lobes have opposite phase, whereas the resonant laser imposes a constant phase).

The measured real-space emission pattern for each structure is presented in Fig. 3.18, together with the normalized intensity profile obtained by integrating the real-space pattern over the transverse direction of the wire, plotted in logarithmic scale. In each case, the laser spot was exciting the site at $x = 0$, at the same position on the chain as in Fig. 3.17. For $\lambda_2 = 0.8$ meV, polaritons propagate on each side of the excited letter, with an exponential decay of the intensity profile due to the finite polariton lifetime. On the other hand, for $\lambda_2 = 1.6$ meV and $\lambda_2 = 2.4$ meV the polariton emission is clearly limited to the excited letter, confirming that we are above the localization threshold.

3.4.3 Delocalization-localization transition

We now want to evidence the existence of the new delocalization-localization transition discovered in the theoretical (λ, β) phase diagram. To this end, we consider chains with increasing β at a fixed λ. We probe the localization properties of wires with $\lambda_2 = 2.4$ meV, well in the localized phase in the AAH limit, and different values of β.

Figure 3.19 presents the non-resonant characterization of three wires, with $\beta = 0$, $\beta = 1$ and $\beta = 2$. According to the theoretical diagram these should be respectively: in the localized phase, in the delocalization tongue, and above this tongue in the second localized phase, as depicted in the upper panel. For $\beta = 0$, Fig. 3.19(a), it is clear both from the momentum- and real-space spectra that the lowest $n = 2$ modes are localized (this is actually the same chain as in the previous paragraph). The chain with $\beta = 2$ presents similar spectra (see Fig. 3.19(c)), with $n = 2$ modes clearly localized.

Interestingly, for the chain with $\beta = 1$, we see in the real-space spectrum of the $n = 2$ modes with lowest energy that the lobes, corresponding to the different letters, are all at the same energy (or at least in a narrow energy window). Accordingly, in the corresponding momentum-space spectrum, a single, almost flat energy band is visible for the lowest energy $n = 2$ modes. In fact, a zoom on this energy region, shown in Fig. 3.20, reveals the presence of a band with finite effective mass, i.e. a weak curvature, corresponding to a band width of ~ 30 μeV (comparable to the spectral resolution of the spectrometer). Here, the fact that we can observe a proper band with finite width is a clear evidence for the existence of coherence between distant letters (i.e. between the different lobes observed in the real-space spectrum). In other words, it proves that eigenstates are extended, and that we are not in the presence of uncoupled localized states with same energy.

We tried to confirm the extended nature of the eigenstates at $\beta = 1$ with resonant excitation measurements, similar to those discussed earlier. However, in a dissipative system, the propagation distance is determined not only by the finite particle lifetime, but also by the group velocity of the excited eigenstate, defined at a given k as $v_g(k) = 1/\hbar(\partial E/\partial k)$. In the case of the chain with $\beta = 1$, the band is almost flat, thus the group velocity is small: considering a band width of 30 μeV, the maximum group velocity is $v_g \lesssim 0.3$ μm.ps^{-1}. As a consequence, even neglecting the presence of any disorder, the propagation can not exceed a few microns, typically 6 μm for a polariton linewidth of 20 μeV. This means that observing propagation to a single neighboring letter would already be a convincing proof for the existence of delocalized eigenstates at $\beta = 1$.

In Fig. 3.21 we compare the real-space emission pattern, and corresponding intensity profile, obtained upon resonant excitation of a single letter, on the three chains considered in Fig. 3.19 ($\lambda_2 = 2.4$ meV and $\beta = 0; 1; 2$). In each case, the laser spot is focused on the letter at position $x = 0$, and the laser energy is tuned in resonance with the lowest energy $n = 2$ eigenstate. For $\beta = 0$ and $\beta = 2$, Fig. 3.21(a,c),
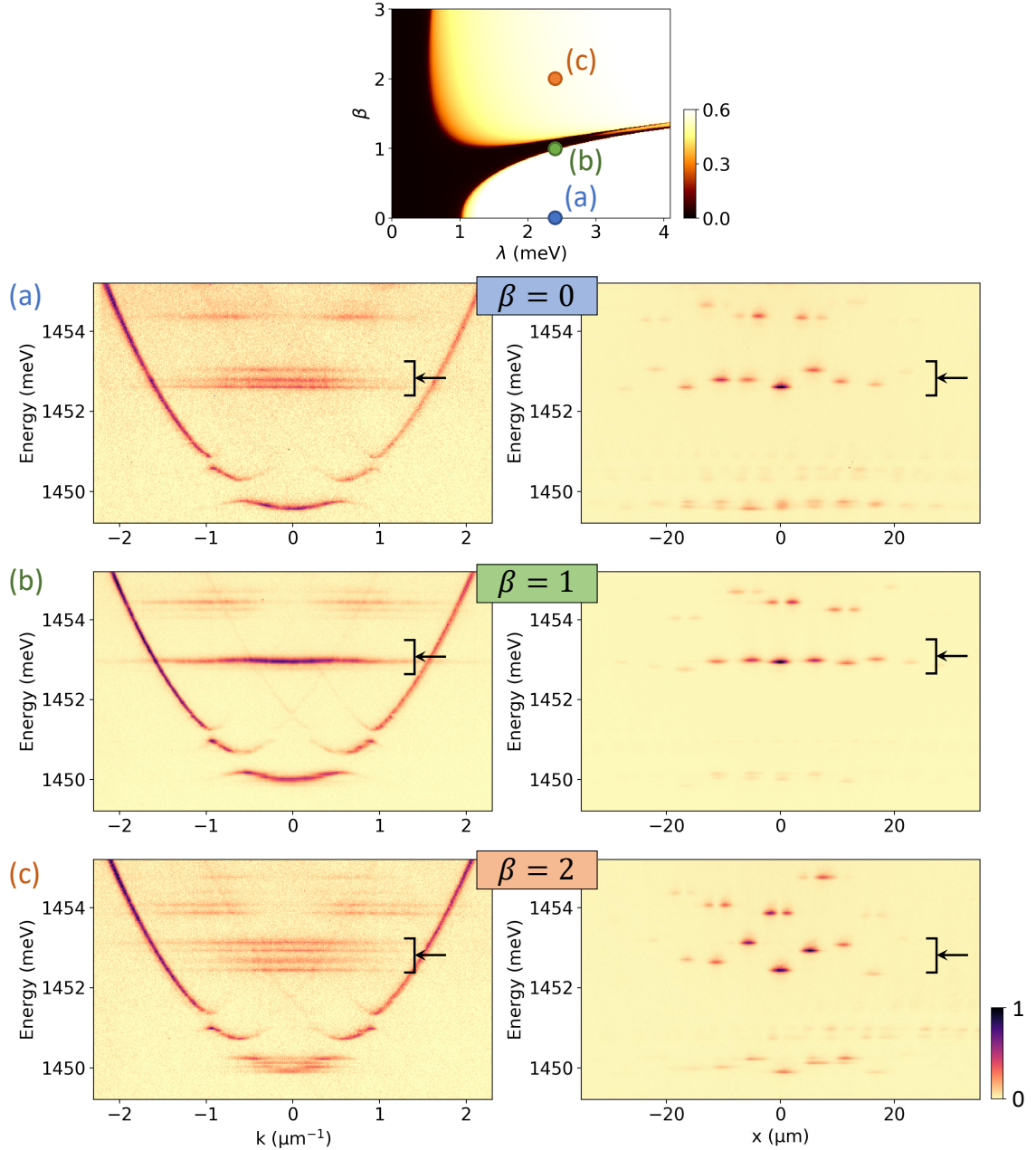
Figure 3.19: Observation of the delocalization-localization transition, at fixed λ. (Left column) momentum- and (right) real-space resolved PL emission of three modulated wires, with $\lambda_2 = 2.4$ meV and (a) $\beta = 0$, (b) $\beta = 1$ and (c) $\beta = 2$. The corresponding positions on the theoretical localization phase diagram are reported in the upper panel (colored dots). In each panel, the arrow indicates the lowest band of $n = 2$ modes.
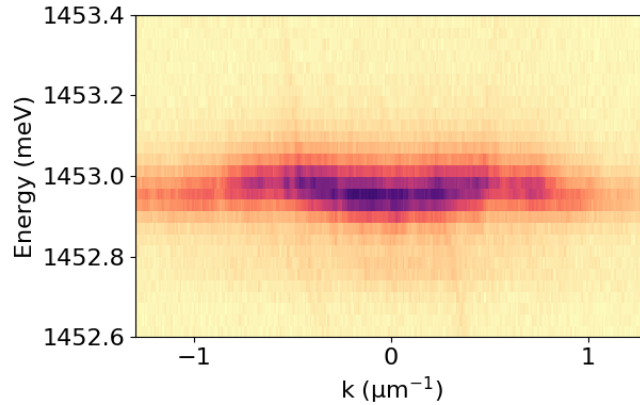
Figure 3.20: Zoom on the momentum-space spectrum of the modulated wire with $\lambda_2 = 2.4$ meV, $\beta = 1$. A band with weak curvature can be identified, indicating long-range coherence, i.e. extended states.
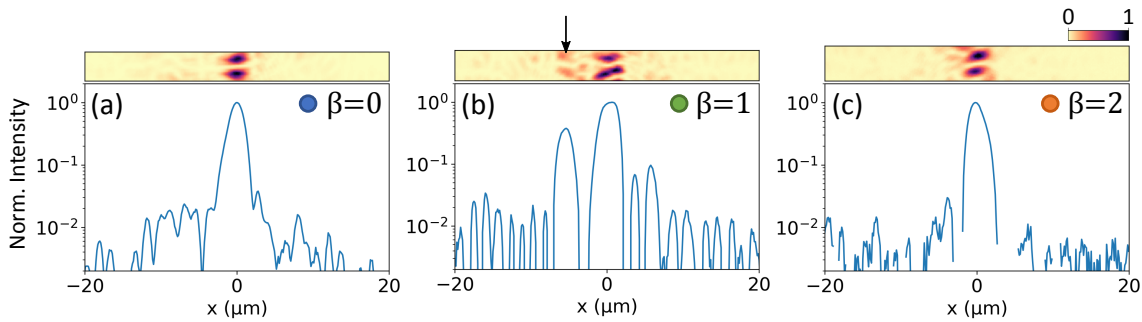
Figure 3.21: (Top) Real-space image of the emission and (bottom) semilogarithmic plot of the normalized intensity profile, integrated in the transverse wire direction, measured under resonant excitation of the site at $x = 0$, on the same three wires as in Fig. 3.19 (and same position on the wire), i.e. with $\lambda_2 = 2.4$ meV and (a) $\beta = 0$, (b) $\beta = 1$ and (c) $\beta = 2$.

only the excited letter is bright, confirming that eigenstates are localized in these structures. On the other hand, for $\beta = 1$, Fig. 3.21(b), we notice polariton emission on a letter at $x = -6$ μm, to the left of the excitation spot (i.e. 3 letters away from the spot), as indicated by the black arrow. As argued above, this propagation in the wire, even small, is sufficient to confirm that the eigenstates are extended.

Finally, we have also characterized 1D chains corresponding to many different values of β and λ, for a more thorough exploration of the localization phase diagram. These measurements are summarized in Fig. 3.22, where we have represented each measured chain as a point in the phase diagram (considering both $n = 1$ and $n = 2$ modes). Applying the same criterion as previously, based on the non-resonant momentum- and real-space spectra, to distinguish between extended and localized states, we assign each point with a color: blue for extended states, light orange for

Figure 3.22: Experimental localization phase diagram, obtained by characterizing chains with different (λ, β). Blue (orange) dots code for extended (localized) lowest energy states. Empty triangle (full circles) indicate $n = 1$ ($n = 2$) modes. The momentum- and real-space spectra used to classify states as extended or localized can be found in Appendix A.

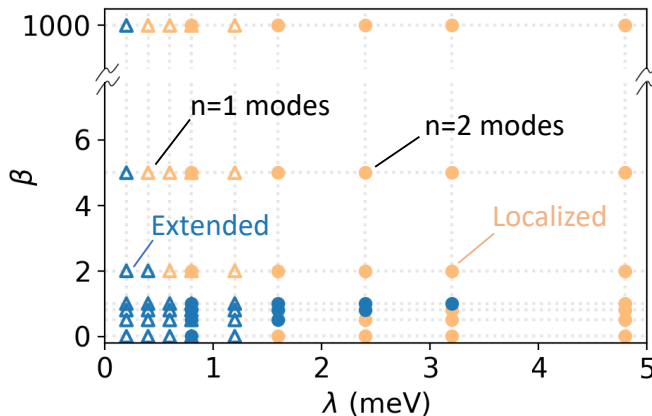localized states. We only consider the band with lowest energy. The momentum- and real-space spectra for all chains can be found in Appendix A. Of course, this remains a qualitative classification, and we are still missing a quantitative figure of merit to establish a rigorous experimental localization phase diagram. Nevertheless, it allows first insight on the extent of the delocalization tongue, and is in very good agreement with the theoretical phase diagram (Fig. 3.13). To conclude, our experiments thus demonstrate experimentally the existence of the novel extended phase predicted by the numerical simulations, which is responsible for a delocalization phase transition, followed by a localization transition, when increasing β at fixed λ .

3.5   Conclusions and perspectives

In this chapter, we have investigated the localization properties of the family of AAHF quasicrystals, i.e. in the continuous deformation between the Aubry-André-Harper and Fibonacci models. Adopting tight-binding formalism to describe the QC, we have established a theoretical localization phase diagram, which in particular features an unexpected and peculiar delocalization tongue, for the lowest energy band. We then extended our theoretical analysis to the case of a free particle in a 1D quasiperiodic potential, and found a localization phase diagram with quantitative features identical to the tight-binding one. Finally, we designed 1D modulated wire for polaritons to implement these QC models, and we probed experimentally the localization properties by non-resonant and resonant excitations measurements. These experiments allowed us to evidence the existence of the predicted delocalization-localization transition when increasing β at a fixed λ. Our re-

sults provide a unification of the localization properties of the AAH and Fibonacci QC, showing a rich phase diagram especially with bulk states that can be tuned from extended to localized, by controlling a single parameter β.

In this study, we have focused mostly on the lower right corner of the localization diagram, i.e low β and high λ values. A natural extension of this work would be to explore the upper half of the diagram, towards the Fibonacci limit ($\beta \to \infty$), to see how criticality sets in. A first challenge, on the theory side, is that the measures that we introduced (inverse localization length, and IPR) do not enable to make clear the distinction between critical states and extended or localized ones. Indeed, the inverse localization length assumes exponentially decaying tails, while the IPR does not provide any information on the nature of the decay, and eventual presence of non-monotonous variations of the wave function amplitude. On the experimental side, since the specificity of critical states arises on long distances, we would need longer propagation in our sample for their experimental evidence. A way to provide this is to use shorter letter length a. We have fabricated such structures, and they are currently being investigated.

From a more general standpoint, in this chapter we only investigated linear eigenstates of polariton microstructure, and completely ignored nonlinearity brought by polariton-polariton interactions. It would be very interesting to inject a nonlinear polariton fluid in the different quasicrystals, and see how the different linear localization regimes affect the nonlinear fluid dynamics. Novel many-body localization and delocalization effects are expected. Finally, we have mentioned in the introduction that the AAHF model has non-trivial topological properties. Consequently, our 1D quasiperiodically modulated wires for polaritons are an ideal platform for the study of topology in the presence of interactions and dissipation.

Chapter 4

Generation and control of dark soliton trains in a polariton fluid

In this chapter, we demonstrate that when the interaction energy provided by polariton-polariton interactions is comparable with the kinetic energy of a nonlinear polariton fluid, the interplay of the two results in a spectacular self-organization of the fluid. We consider a simple one-dimensional wire, in which we inject counterflowing polariton fluids by means of resonant excitation. In the regime of high polariton densities, we report and investigate the formation of dark soliton trains in the fluids.

In section 4.1 we briefly review basic concepts of quantum hydrodynamics, in particular the notion of dark solitons, and discuss microcavity polaritons as a platform for the study of quantum fluids. Section 4.2 presents the experimental configuration for the injection of counterpropagating polariton fluids in a 1D channel. We then show that for high excitation power, polariton-polariton interactions are responsible for the self organization of the fluid into a dark soliton train. When scanning the excitation power, the abrupt disappearance of solitons reflects the discrete nature of these nonlinear excitations. In section 4.3, we apply a phase twist across the wire, enabling the control of both the position of the soliton train, and also more importantly the parity of their number. We evidence a novel type of bistable behavior, appearing when scanning the phase twist up and down, at constant power. Finally, in section 4.4 we conclude and discuss perspectives for this work, in particular we propose schemes for the investigation of soliton-soliton interactions and excitation of the soliton pattern oscillations, based on numerical simulations.

4.1   Dark solitons in polariton superfluids

In this section, we introduce the notion of dark solitons in quantum fluids. We also present a few concepts of quantum fluid hydrodynamics, and review the principal
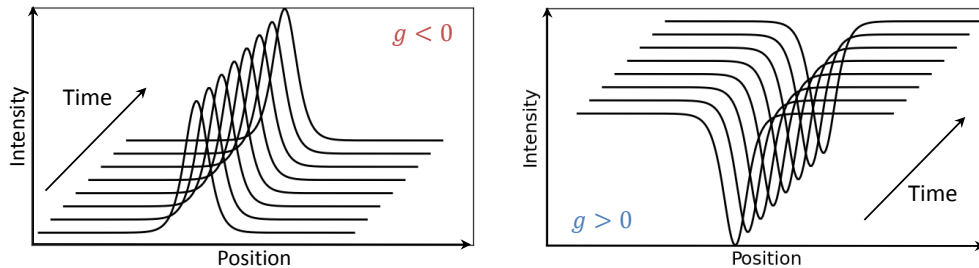
Figure 4.1: Schematic representation of: (left) a bright soliton and (right) a dark soliton.

experimental studies of quantum hydrodynamic effects in exciton polariton systems.

Dark solitons are among the fundamental nonlinear collective excitations of one-dimensional (1D) quantum degenerate fluids with positive mass and repulsive interactions. We call nonlinear quantum fluid a system whose evolution is described by the nonlinear Schrödinger equation (NLSE) [147]:

$$i\hbar\frac{\partial\psi}{\partial t} = -\frac{\hbar^2}{2m}\nabla^2\psi + \hbar g|\psi|^2\psi \tag{4.1}$$

where ψ is the order parameter of the system, e.g. its wave function, m is the particle mass (or effective mass) and g the particle-particle interaction constant. Here, we focus on 1D systems. In the case of attractive particle-particle interactions, $g < 0$, the NLSE is known to support nonlinear localized solutions called bright solitons, whose shape does not evolve during propagation [148]. On the other hand, for repulsive interactions, $g > 0$, the NLSE supports dark solitons. They are characterized by a dip in a uniform background density and a jump of π in the macroscopic phase across it (in this sense they can be seen as a 1D equivalent of a vortex). The shape and size of the dip is given by the interplay of mass and nonlinearity. Because the NLSE is a universal model that describes nonlinear media, dark solitons have been observed in a wide variety of systems ranging from Bose-Einstein condensates of cold atoms [149–151], optical fibers [152], to thin magnetic films [153].

Note that the 1D geometry is particularly suitable to the study of dark solitons, because solitons are unstable with respect to transverse perturbations, leading to their decay into other more stable structures (e.g. vortices). This is the so-called snaking instability, well documented in conservative systems such as atomic BEC [154].

Interestingly, dark solitons have also been observed in nonlinear open-dissipative systems [155], and in particular in semiconductor microcavities [15, 16, 61, 156, 157]. Cavity polariton as a platform for studying quantum hydrodynamics have attracted considerable interest since the demonstration of superfluid polariton flow [11]. As already discussed in chapter 1, the resonant excitation scheme allows precise control of the kinetic energy, interaction energy and phase of the fluid. The evolution of the lower polariton wave function $\Psi(\mathbf{r}, t)$ is given by the driven-dissipative Gross-
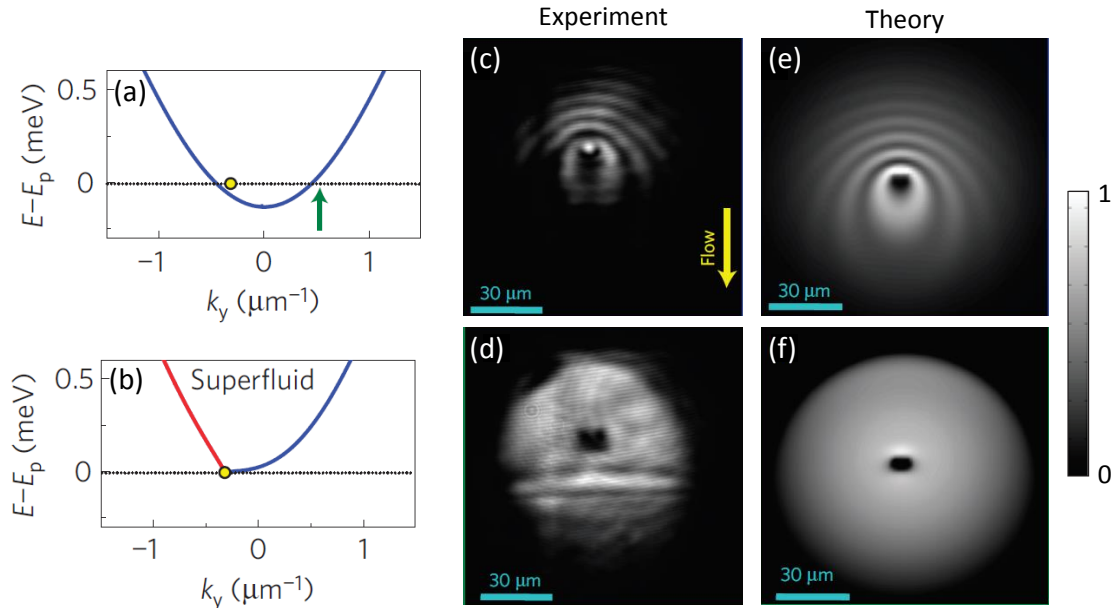
Figure 4.2: (a) Lower polariton dispersion calculated under low-power resonant pumping, at the point indicated by the yellow dot. Injected polaritons can elastically scatter to the same energy states as those indicated by the green arrow. (b) Dispersion renormalized by interactions calculated under strong resonant pumping, corresponding to the Bogolyubov excitation spectrum of a superfluid (red branch). Backscattering is suppressed, owing to the absence of available final states at the energy of the pump (c, d) Experimental images of the real-space polariton density, showing the transition from a (c) normal fluid, at low pumping power to (d) a superfluid at high pumping power. Polariton superfluidity is apparent as a suppression of the real-space density modulation around the point defect. (e, f) Corresponding theoretical results obtained by numerically solving the Gross-Pitaevskii equation. Images taken from [11].

Pitaevskii equation [5]:

$$i\hbar\frac{\partial\Psi(\mathbf{r},t)}{\partial t} = \left(E_0 - \frac{\hbar^2}{2m}\nabla^2 + \hbar g|\Psi(\mathbf{r},t)|^2 - i\frac{\hbar\gamma}{2} \right)\Psi(\mathbf{r},t) + iF(\mathbf{r},t) \qquad (4.2)$$

where m is the lower polariton effective mass, E_0 the energy of the bottom of the lower polariton branch, g the polariton-polariton interaction constant and γ the polariton decay rate. The term $F(\mathbf{r},t)$ accounts for the coherent drive: it is proportional to the incident field.

The interaction term $\hbar g|\Psi|^2$ is responsible for a renormalization of the single-particle parabolic dispersion, as illustrated in Fig. 4.2(a,b). The excitation spectrum of the fluid in the presence of interactions is calculated by linearization of the Gross-Pitaevskii equation. The resulting dispersion is called Bogolyubov dispersion of excitations [1]. It is linear for small excitation energies, allowing to define a sound
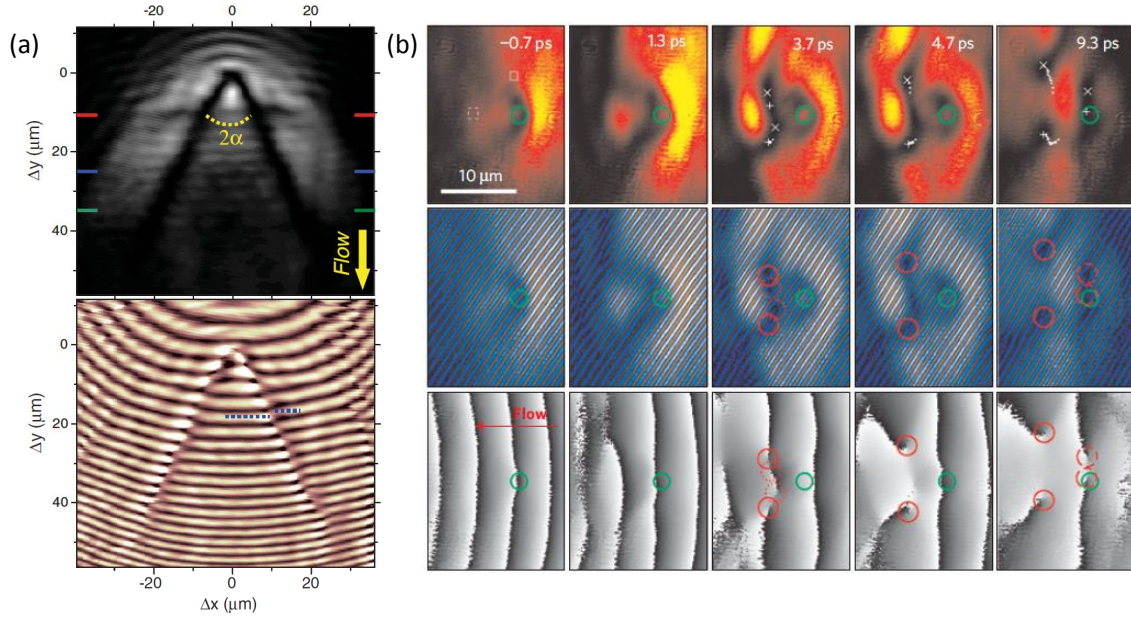
Figure 4.3: (a) Experimental observation of hydrodynamically generated oblique dark solitons in a flowing polariton superfluid hitting a defect (top). The phase interferogram (bottom) clearly reveals a phase jump across the soliton lines (dashed lines). Taken from [15]. (b) Nucleation of vortex pairs in a polariton fluid moving leftwards towards a defect. The three rows show (top) the polariton density, (middle) the fringes of the measured interferogram, and (bottom) the polariton phase, at different times after the excitation pulse. The defect position is indicated by the green circles. Vortices start being visible at $t = 3.7$ ps, and are indicated by white markers on the density plot and red circles on the fringes and phase plots. Taken from [12].

speed in the fluid, given by $c_s = \sqrt{\hbar g |\Psi|^2/m}$. An important advantage of the resonant excitation scheme is that it allows controlling the velocity of the injected polariton fluid, by tuning the drive wave vector k_p. Amo *et al.* [11] demonstrated that when the fluid velocity $v = \hbar k_p/m$ becomes smaller than the sound speed in the fluid c_s, backscattering on a defect placed in the fluid flow is suppressed (see Fig. 4.2). The condition $v < c_s$ corresponds to the Landau criterion for superfluidity, as introduced for conservative systems based on the Bogolyubov dispersion of excitations of a superfluid [1]. Recently, room-temperature superfluity of polariton has also been reported by the group of Sanvitto [158].

Based on a similar experimental configuration, later works demonstrated the hydrodynamic nucleation of vortex pairs [12, 13] and dark solitons [15, 16] in the flow of the superfluid past an obstacle. As illustrations, the results from Refs. [12] and [15] are reproduced in Fig. 4.3. Another key feature from the resonant excitation is that under the pump spot, the coherent drive imposes the phase of the polariton

wave function. In Ref. [11], where the spot completely overlaps with the defect, this prevents the formation of topological defects such as dark solitons and vortices, since the latter are characterized by very specific phase patterns (for a vortex, a winding of 2π for the phase around the vortex core, and for a soliton, a phase jump of π across the soliton core). To circumvent this issue, two different strategies were adopted. Amo *et al.* placed the pump spot slightly upstream of the defect. Subsequently, the phase of the fluid is free to evolve as it encounters the defect. They reported the formation of dark oblique solitons in the wake of the defect, visible as two density dips associated with the characteristic π phase jump across each dip (Fig. 4.3(a)). Nardin *et. al* [12] used pulsed excitation (as is the case in Refs. [13, 16]), instead of continuous wave coherent pumping used in the works discussed above. The pulse injects during a short period of time the fluid, which then evolves freely before decaying due to the finite polariton lifetime. A streak camera was used, in synchroscan mode, to measure time-resolved images of the polariton fluid. As shown in Fig. 4.3(b), the formation of pairs of vortices with opposite winding is clear at $t = 4.7$ ps, as the fluid flows past the defect. Note that in this experiment, the streak camera only allowed to measure images averaged over many realizations. The vortices were visible in these average images only because they were pinned by disorder, i.e. they have the same trajectory in each realization.

Aside from these examples, a number of other quantum fluid effects have been studied in semiconductor microcavities, including diffusive Goldstone modes [159] or Bogolyubov excitation spectrum for the superfluid [160, 161]. Generation of bright solitons was also reported, using a resonant pump at an energy above the inflexion point of the lower polariton dispersion, corresponding to a negative effective mass [17, 162].

Even though we first presented the fact that the resonant drive imposes locally the phase of the fluid as a drawback, this is actually a remarkable feature: it offers the possibility to externally manipulate the boundary conditions and impose a controlled phase pattern across a polariton fluid. This was first explored in a two-dimensional polariton condensate in which a spatial vortex phase profile was imposed on the polariton field, resulting in persistent currents with high orbital momentum [164]. Note that this feature is purely characteristic of the driven-dissipative nature of the system, and opens up a new playground for the exploration of the elementary excitations of polariton quantum fluids. In particular, it has been proposed that by imposing a phase twist across the fluid via the external pumping, the superfluid fraction could be measured [165] and different Josephson dynamical regimes could be addressed [166, 167].

A theoretical proposal for the controlled nucleation of dark solitons was also presented in Ref. [163]. The authors showed, based on numerical simulations, that for resonantly excited counterpropagating polariton superfluids in a 1D channel, imposing a phase twist across the channel would result in a density dip at the center of the channel, with a phase jump of π across the dip for the polariton wave function (Fig. 4.4). More precisely, for certain values of the phase twist, two solutions are
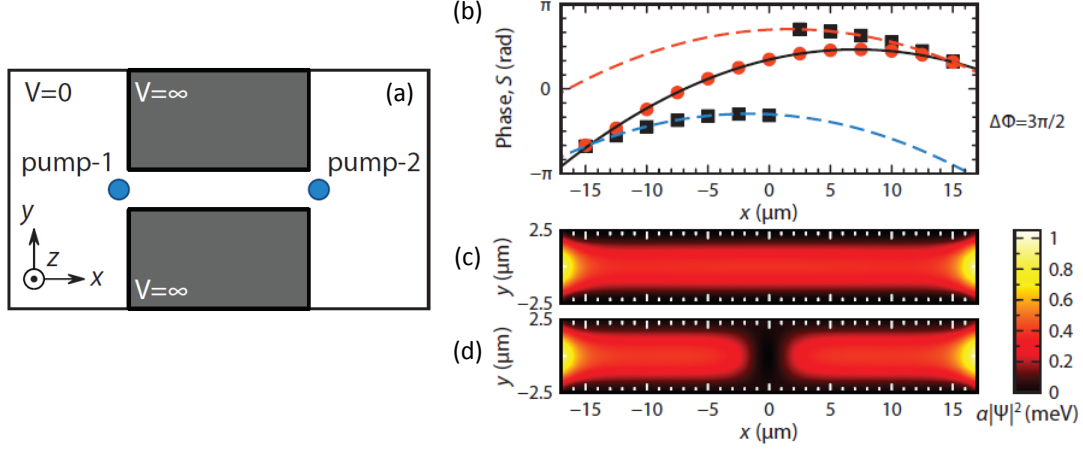
Figure 4.4: (a) Sketch of the configuration considered in [163] for the resonant injection of counterflowing polariton fluids in a 1D channel. (b) Profile of the phase of the polariton wave function across the channel, for the two stable states at a phase twist $\Phi = 3\pi/2$. (c,d) Corresponding density profiles in the channel. Taken from [163].
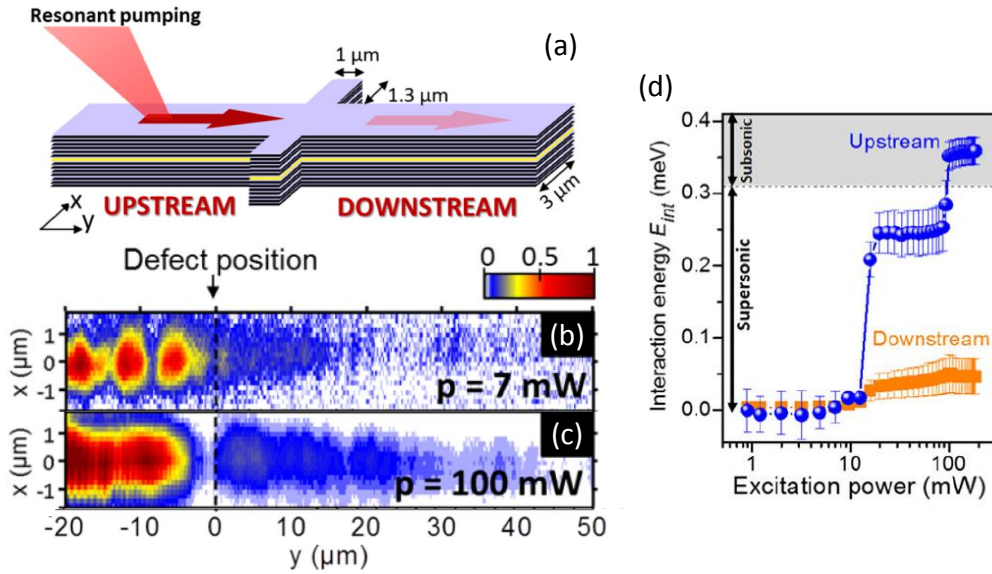
Figure 4.5: Acoustic black hole in a 1D polariton fluid. (a) Sketch of the experimental configuration. (b,c) Spatially resolved emission for excitation powers $p = 7$ mW and $p = 100$ mW, respectively. Backscattering from the defect is suppressed in (c), indicating superfluid flow upstream of the defect. (d) Interaction energy in the upstream (blue circles) and downstream (orange squares) regions as a function of excitation power.

stable: a profile with homogeneous density, and a profile with a density dip. Though the authors did not interpret it explicitly as such, we will show in this chapter that this density dip is indeed a dark soliton.

First experimental investigations of superfluid hydrodynamic effects in a 1D polariton fluid was achieved in our group [93]. The main results are reported in Fig. 4.5. In this work, the authors engineered a defect that was placed in the flow of the resonantly injected polariton fluid. At moderate excitation power, strong backscattering from the defect is present, giving rise to interference upstream of the defect. At high excitation power however, the interaction energy of the fluid overcomes its kinetic energy , and the Landau criterion $v < c_s$ is fulfilled. Accordingly, the backscattering is suppressed, as shown by the absence of intensity modulations upstream of the defect, indicating superfluid flow. More precisely, the author showed that the defect separates a high density subsonic flow from a low-density supersonic flow, setting up an acoustic horizon, as theoretically proposed in Refs. [168, 169] and offering promising perspectives to observe Hawking radiation.

Finally, it should be noted that theoretical studies on the generation, control and stability properties of dark solitons in 1D channels have also been carried out taking into account an incoherent exciton reservoir, i.e. modeling non-resonantly excited polariton condensate [170–172]. However, the non-resonant excitation schemes proposed in the above works do not offer the same level of control over the polariton fluid as resonant excitation. Thus, in this chapter, we consider resonantly injected polariton fluids. We use a counter-propagation geometry similar to the proposal of Ref. [163], which allows fixing the boundary conditions for the fluid in the channel. We show that tuning these boundary conditions, we can trigger the nucleation of dark solitons in a controlled manner.

4.2 Injection of counterpropagating nonlinear polariton fluids in a 1D channel

4.2.1 Experimental configuration

We want to investigate the dynamics of polariton fluids in a one dimensional channel. To this end, we used electron beam lithography and dry etching to fabricate wires of width 3 μm and length 200 μm out of a planar cavity, as schematically represented in Fig. 4.6. The polariton dispersion in a chosen wire has been characterized by measuring the photoluminescence (PL) under nonresonant pumping. Figure 4.6 shows the momentum-space emission, for the polarization parallel to the wire (TE), evidencing the lower and upper polariton 1D subbands (a similar dispersion is measured in the orthogonal polarization (TM). Throughout this chapter we ignore TM polarization and focus only on TE). From these, we deduce a Rabi splitting $\Omega_R = 3.5$ meV, and an exciton-photon detuning $\delta = E_C(k = 0) - E_X(k = 0) = -3.3$ meV, where $E_C(k)$ is the bare photon energy and $E_X(k)$ the bare exciton energy. This corresponds to
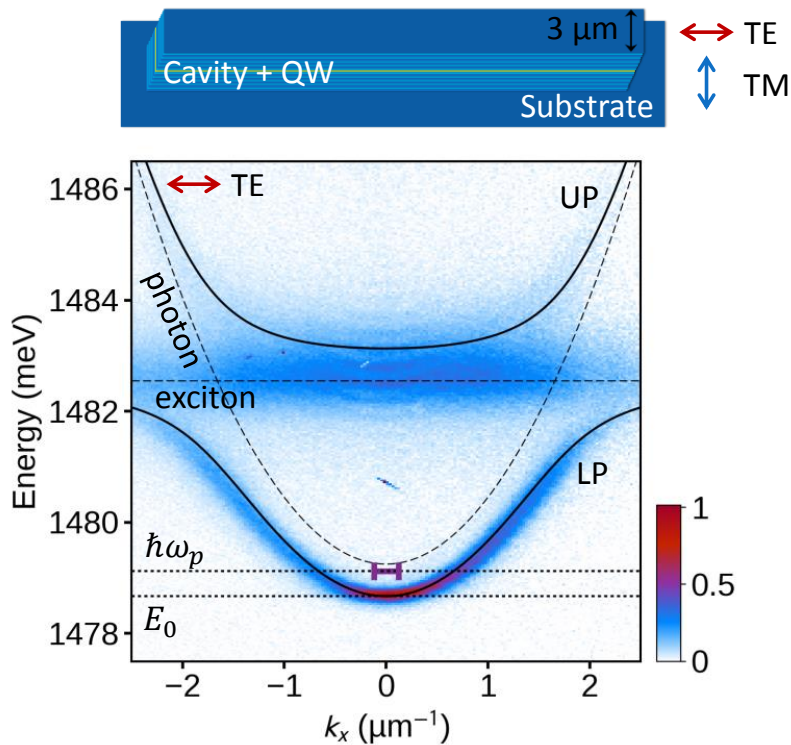
Figure 4.6: Top: schematic representation of 3 μm-wide wire etched out of a planar cavity. Bottom: momentum space-resolved photoluminescence measured under nonresonant pumping, in TE polarization. Solid lines are theoretical fits of the lower (LP) and upper (UP) polariton branches and dashed lines indicate the bare exciton and photon energy. The horizontal segment shows the energy and width for the resonant excitation conditions.

an excitonic fraction $|x|^2 = 0.16$ at $k = 0$. We recall that close to $k = 0$, the lower polariton branch can be approximated by a parabola, $E(k) = E_0 + \hbar^2 k^2 / 2m$. Here the polariton effective mass deduced from the fits is $m = 4 \times 10^{-5} \, m_e$, with m_e the free electron mass. Note that only the first 1D subband is visible in Fig. 4.6. The second subband is not observed, because this measurement is for $k_y = 0$ (in the direction orthogonal to the chain), where the second subband does not radiate due to the antisymmetric nature of its eigenstates ($n = 2$ states as discussed in chapter 3). The other subbands are higher in energy, i.e. outside of the energy window plotted in Fig. 4.6.

The experimental scheme for the resonant injection of counterflowing polariton fluids in this wire is summarized in Fig. 4.7. We use a cw resonant laser split into two separate beams, linearly polarized along the wire (TE) and focused at normal incidence onto two spots separated by a distance d. The laser energy $E_p = \hbar \omega_p$ is blueshifted by $\Delta E = \hbar \omega_p - E_0$ with respect to the lower polariton energy E_0 at $k = 0$ (see Fig. 4.6). The phase difference $\Delta \varphi$ between the two beams can be varied
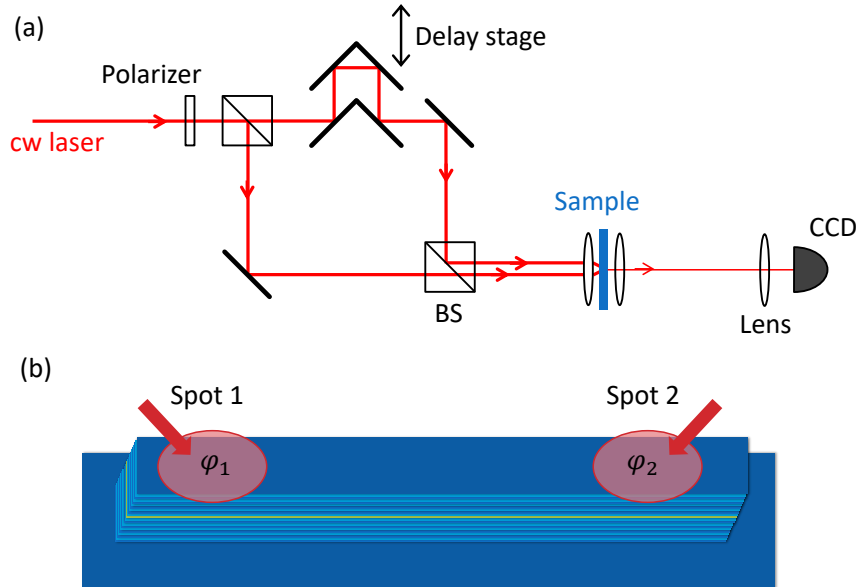
Figure 4.7: (a) Sketch of the experimental setup for the resonant injection of coutnterpropagating fluids in the wire. A delay stage allows to control the phase difference $\Delta\varphi = \varphi_2 - \varphi_1$ between the two pumping spots, as illustrated in (b).

using a delay stage controlled by a piezoelectric actuator added to the path of one of the excitation beams. This is very important, since the phase of the resonant drive sets the phase of the polariton wave function under the pumping spot.

4.2.2 Theoretical model for numerical simulations

To model the experimental configuration described above, we introduce a 1D Gross-Pitaevskii equation comparable to the one already discussed: it includes pump and loss terms, and only the lower polariton branch is considered. The evolution of the polariton wave function $\Psi(x,t)$ is given by:

$$i\hbar\frac{\partial\Psi(x,t)}{\partial t} = \left(E_0 - \frac{\hbar^2}{2m}\frac{\partial^2}{\partial x^2} + \hbar g|\Psi(x,t)|^2 - i\frac{\hbar\gamma}{2}\right)\Psi(x,t) + iF(x)e^{-i\omega_p t} \quad (4.3)$$

where γ is the polariton decay rate and g the polariton-polariton interaction constant. The drive term $F(x)e^{-i\omega_p t}$, at frequency ω_p, is adapted to our experimental scheme: it describes two pumping spots injecting counterflowing polaritons. We use

$$F(x) = F_0(f_1(x) + f_2(x)), \quad (4.4)$$

with $|F_0|^2$ being proportional to the total power of the coherent drive, and $f_{1,2}(x)$ is a complex function describing the spatial profile and the relative phase of the pump beams:

$$f_{1,2}(x) = e^{-(x-x_{1,2})^2/2\sigma^2}e^{\pm ik_p x + i\varphi_{1,2}}, \quad (4.5)$$

for Gaussian spots with width $w = 2\sqrt{2\ln 2}\sigma$, centered on position $x_{1,2} = \pm d/2$. For pumping spots at normal incidence, the central pump wave vector is $k_p = 0$.

The steady-state solutions of Eq. (4.3) in the frame rotating at frequency ω_p are obtained numerically, using parameters values directly extracted from the experiments. The experimentally measured linewidth is $\hbar\gamma = 47$ µeV, and $E_0 = 1478.57$ meV. In the experiment, we use a laser detuning $\Delta E = 0.27$ meV, and Gaussian spots of width $w = 8$ µm separated by $d = 50$ µm. Finally, we take an interaction constant $\hbar g = 0.3$ µeV.µm. This value is obtained by considering an exciton-exciton interaction strength $\hbar g_{exc} = 30$ µeV.µm^2 [46]. The polariton-polariton interaction depends on the excitonic fraction $|x|^2$, and we also need to take into account the 1D nature of the system with a proper rescaling of the 2D interaction strength. In the end, $\hbar g = |x|^4 \hbar g_{exc}/a$, which for $|x|^2 = 0.16$ and wire width $a = 3$ µm gives the above value.

4.2.3 Nonlinear regime: nucleation of dark solitons

Superfluidity and nucleation of dark solitons are features showing up in quantum fluids when the interparticle interaction energy is comparable to the kinetic energy. In our system, the interaction energy is $\hbar g n$, where g is the polariton-polariton interaction constant and n the polariton density, controlled by the excitation power. We thus investigate the dynamics of the injected polariton fluid when the power of the resonant drive is increased. In this section, we fix $\Delta\varphi = 0$. Note that this corresponds to symmetric boundary conditions for the fluid.

It is instructive to discuss first what happens in the linear regime, i.e. at low pumping power, where polariton-polariton interactions are negligible. Figure 4.8(c) shows the polariton emission, spatially resolved along the wire, measured for such low pumping power $P = 8$ mW, well in the linear regime. The two excitation spots positions are indicated by white circles, and the bright regions outside of the wire, above and below the spots, correspond to laser light scattered by the wire edges, and are thus not relevant. Even though the excitation spots are at normal incidence, their finite angular aperture allows injecting polaritons with wavevectors $k_f = \pm\sqrt{2m\Delta E}/\hbar = \pm 0.53$ µm^{-1}, as schematically depicted in Fig. 4.8(a). Between the two excitation spots, we observe a regular fringe pattern with a spacing of $s = 6.0$ µm $= \pi/k_f$, arising from interference of the two counter-propagating polariton waves (the fringe pattern is well fitted by a sinusoid, as shown in Fig. 4.9(a)). The position of the fringe pattern is determined by the boundary conditions imposed by the excitation spots, namely the distance between them and their phase difference $\Delta\varphi$. Here, $\Delta\varphi = 0$, leading to an intensity maximum at $x = 0$, at the center between the two spots.

As shown in Fig. 4.8(b), when the excitation power is increased, a first abrupt jump in the total emission intensity is observed at $P_{th} = 12$ mW. It corresponds to the threshold for the nonlinear regime, precisely when the blueshift due to polariton-polariton interactions under the pump spots equals ΔE. When the power is further
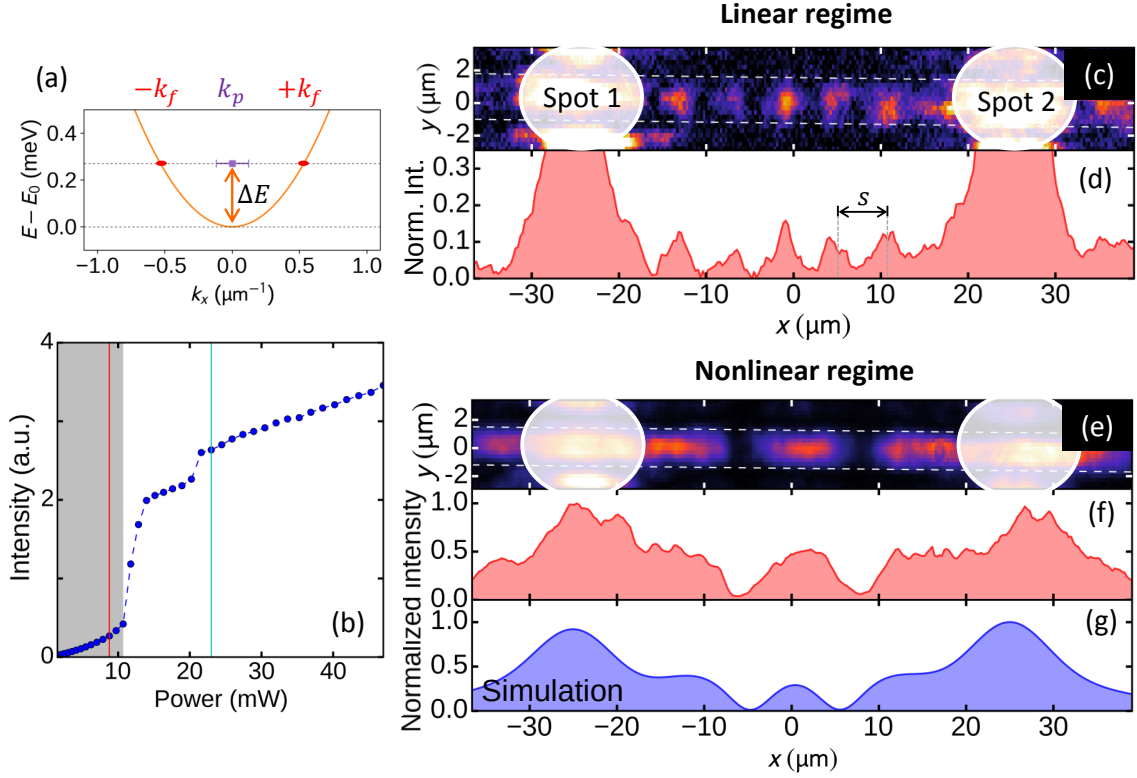
Figure 4.8: (a) Single-particle parabolic lower polariton dispersion. In the linear regime, due to the finite numerical aperture of the excitation spots (with central wave vector k_p), particles are injected with wave vector $\pm k_f$. (b) Total measured emission intensity (integrated along both the transverse and longitudinal directions of the wire) as a function of pump power. The shaded gray region corresponds to the linear regime. **Linear regime**. (c) Spatially resolved emission measured along the wire in the linear regime, for $P = 8$ mW, $\Delta E = 0.27$ meV, $d = 50$ μm and $\Delta\varphi = 0$. Dotted lines indicate the wire edges. (d) Measured intensity profile integrated in the transverse direction. **Nonlinear regime** (e) Spatially resolved emission measured along the wire for $P = 23$ mW, and (f) intensity profile integrated over the transverse direction. (g) Corresponding calculated emission profile.
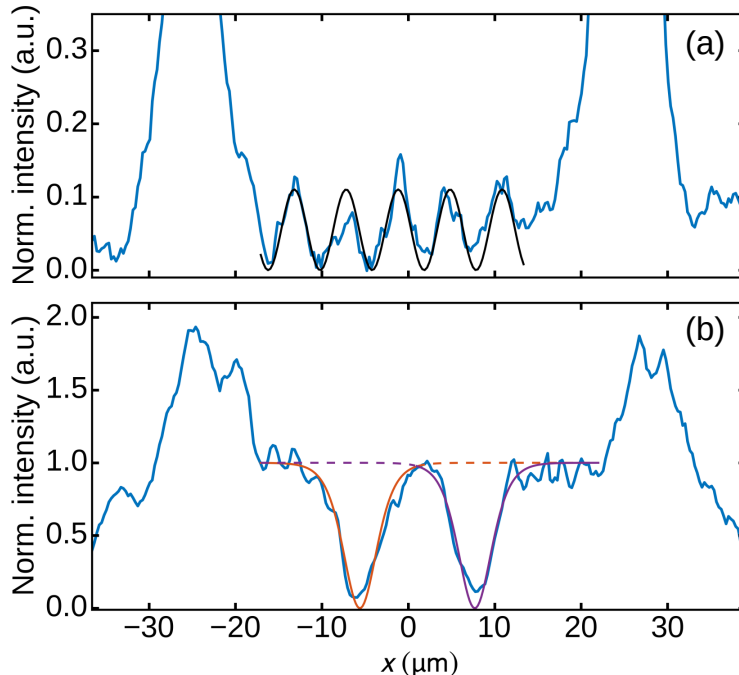
Figure 4.9: (a) Density profile in the linear regime, corresponding to Fig. 4.8(d), fitted by a cosine function (black line). (b) Density profile in the nonlinear regime, corresponding to Fig. 4.8(f). The orange (resp. purple) line is a fit of the left (right) soliton. Dashed lines indicate regions where the fits are not valid due to the presence of the second soliton.

ramped up, a second threshold is observed. This second threshold is associated with a change of the spatial pattern. This behavior is very similar to the observations in Ref. [93] for a 1D polariton fluid in a configuration in which polaritons are excited by a single beam and reflected by an external potential.

A typical emission pattern above the second threshold is shown in Fig. 4.8(e). It strongly differs from the linear case: two density dips, dropping almost to zero, are visible in an otherwise almost constant high density profile. Those dips are identified as dark solitons – nonlinear collective excitations of the fluid. This profile is well reproduced by numerical simulations based on Eq. (4.3) (see Fig. 4.8(f)). We provide a first confirmation that we are indeed in the presence of solitons thanks to a fit to the density profile with a hyperbolic tangent function. Indeed, the analytical solution of the Gross-Pitaevskii equation determining the profile of a soliton train is an elliptic function [1]. In the case of a profile with a single dark soliton, the density evolves as $n(x) = \tanh^2\left((x - x_0)/\sqrt{2}\xi\right)$, with x_0 the soliton position and ξ the healing length of the fluid [148]. In Fig. 4.9(b), we use this single soliton solution to fit the density profile in the nonlinear regime from Fig. 4.8(f). The two soliton dips are fitted independently, using the same soliton width of 5.2 μm, corresponding to a healing length $\xi = 1.8$ μm. The experimental data is well reproduced by

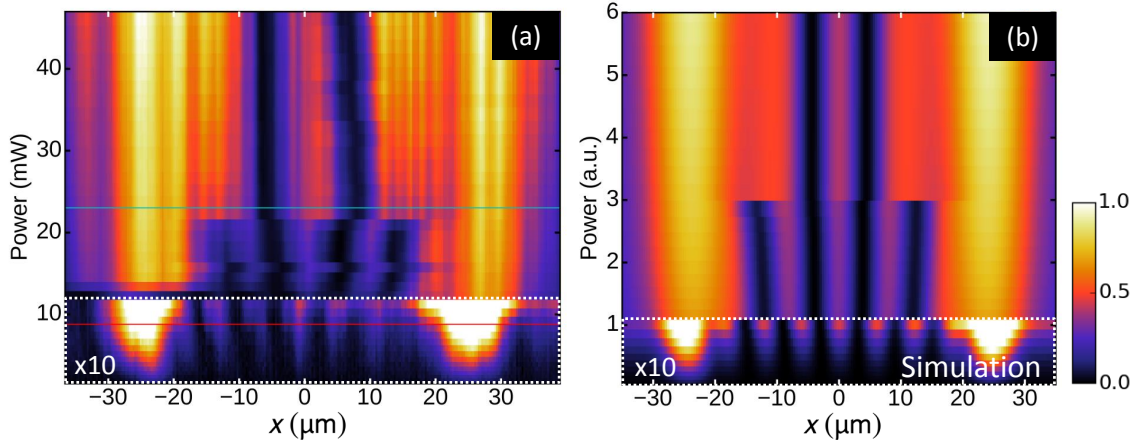**Figure 4.10:** (a) Measured and (b) calculated emission profile when scanning the power up (the low power data have been amplified by a factor 10 for clarity). The horizontal red, blue lines corresponds to the profiles shown in Fig. 4.8(d,f).

the theoretical profile of two independent solitons in the region between the two excitation beams. The fits reproduce the presence of the soliton dips on top of a flat background. The dips are separated by 13.5 μm, significantly more than twice their width. This situation is very different to what is observed in the linear regime, Fig. 4.9(a), in which a standard cosine-like interference pattern is observed with minima separated by exactly twice the FWHM. Note that the theoretical value of the healing length for a laser detuning $\Delta E = 0.27$ meV is $\xi = \hbar/\sqrt{2m\Delta E} = 1.9$ μm, in excellent agreement with the fitting value (recall that in the nonlinear regime, the interaction energy of the fluid is equal to ΔE).

Figure 4.10(a) presents the evolution of the intensity profile when ramping the pumping power up. It reveals that the number of solitons depends on the excitation power. Directly above the first threshold at $P_{th} = 12$ mW, four solitons are present in the region between the spots. Further increasing the excitation power, we observe at $P = 21$ mW the abrupt expulsion of two solitons so that only two of them remain. The abrupt nature of this expulsion is a further proof of the nonlinear character of the density dips: the solitons are elementary excitations of the polariton fluid. Interestingly, the polariton density between the spots, outside of the dark solitons is almost independent of the pumping power. Notice that the observed expulsion of two solitons, replaced by regions of high polariton density, is responsible for the small jump in total emitted intensity that is visible at the second threshold (see Fig. 4.8(d)). Throughout the whole power scan in Fig. 4.10(a), the number of solitons remains even because of the symmetry of the excitation conditions. Indeed, since we impose $\Delta\varphi = 0$, the polariton wave function must remain symmetric, implying an even number of solitons (because of the π phase jump across each soliton).

The numerical simulations, presented in Fig. 4.10(b), perfectly reproduce the

low power interferences and the abrupt transition to the nonlinear regime resulting in the nucleation of four dark solitons and, at higher power, two dark solitons. In particular, this agreement confirms that we can base our interpretation on the Gross-Pitaevskii equation to discuss the mechanism for the soliton formation. This is the topic of the following paragraph.

4.2.4 Interaction and kinetic energy of the fluid

The nucleation of solitons in the nonlinear regime, and the abrupt change in their number when increasing the excitation power can be intuitively understood from the hydrodynamics of the polariton flow. We work in the frame rotating at frequency ω_p. In the steady state, in the central region far from the excitation spots ($F = 0$), the real part of The Gross-Pitaevskii equation (Eq. (4.3)) multiplied by $\Psi^*(x)$ can be written as a "local" energy conservation law as follows:

$$\hbar\omega_p = E_0 - \frac{\hbar^2}{2m}\frac{\mathrm{Re}(\Psi^*\nabla^2\Psi)(x)}{n(x)} + \hbar g n(x) \tag{4.6}$$

with $n(x) = |\Psi(x)|^2$ the local polariton density. Equation (4.6) expresses that the energy per polariton, fixed by ω_p, is locally equal to the sum of three terms: the single-polariton energy E_0 at $k = 0$; a kinetic term $E_{kin}(x) = -(\hbar^2/2m)\mathrm{Re}(\Psi^*\nabla^2\Psi)/n(x)$; and a polariton-polariton interaction term $E_{int}(x) = \hbar g n(x)$.

Let us not forget the imaginary part of the steady-state equation. It writes:

$$0 = -\frac{\hbar^2}{2m}\mathrm{Im}(\Psi^*\nabla^2\Psi)(x) - i\hbar\frac{\hbar\gamma}{2}n(x) \tag{4.7}$$

At this point it is convenient to express the wave function in terms of its modulus and phase $\phi(x)$:

$$\Psi(x) = \sqrt{n(x)}e^{i\phi(x)} \tag{4.8}$$

Inserting this into Eq. (4.7) enables simplification of the term $\mathrm{Im}(\Psi^*\nabla^2\Psi)(x)$. Eq. (4.7) becomes:

$$\nabla(nv) = -i\hbar\gamma n \tag{4.9}$$

where we introduced the fluid velocity, defined as $v(x) = \hbar\nabla\phi(x)/m$ [1]. This is a continuity equation that accounts for the losses due to the finite polariton lifetime. Note that using the same notation, the kinetic term can be written as:

$$E_{kin} = \frac{1}{2}mv^2 - \frac{\hbar^2\nabla^2\sqrt{n}}{2m\sqrt{n}} \tag{4.10}$$

The second term on the right-hand side is the quantum pressure. It cannot be neglected in the case of dark solitons because of the finite density gradient.

The specific dark soliton profile at a given pump power is a result of the local interplay between the kinetic and interaction terms. In the core of a soliton, where
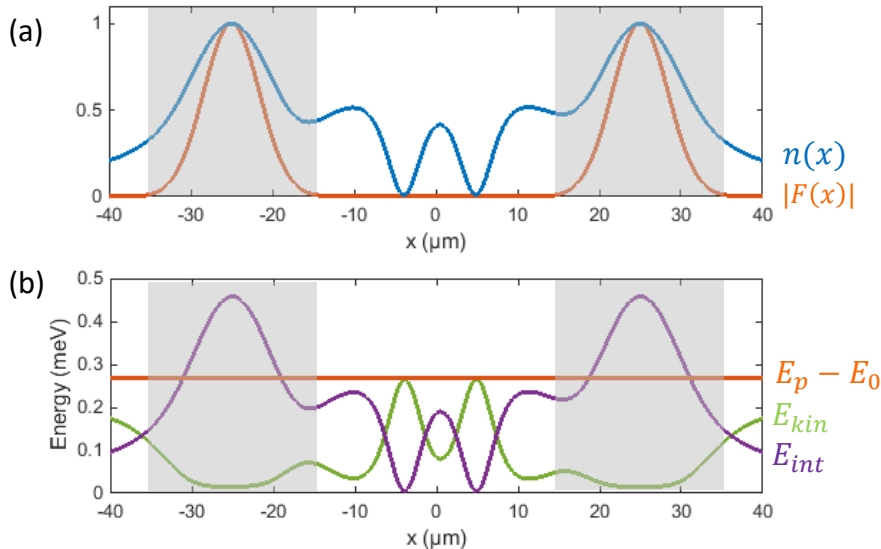
Figure 4.11: (a) Calculated density profile $n(x)$ from Fig. 4.8(g), and corresponding drive amplitude $|F(x)|$ for the two pumping spots. (b) Kinetic and interaction energy terms $E_{kin}(x), E_{int}(x)$ as defined from the main text, calculated from (a), compared with the drive detuning ΔE. Note that equation (4.6) holds true only when the drive amplitude is negligible. This condition is not fulfilled in the shaded gray regions.

the density is low and its second order derivative is high, the kinetic term dominates over interactions, while it is the opposite in the high density regions far from the core. This is illustrated in Fig. 4.11, where we have calculated $E_{kin}(x)$ and $E_{int}(x)$ for a profile with two solitons. In this sense, dark solitons can be viewed as the elementary excitation of a superfluid, which allow for the accommodation of kinetic energy in the fluid. At pump densities just above the first nonlinear threshold, the polariton flow from the pump spots towards the central region contains a high kinetic energy that needs to be accommodated in the form of a large number of solitons, four in the case depicted in Fig. 4.10(a) in the $12-21$ mW range. When the excitation power is further increased, the higher density in the wire results in an increase of interactions. In the balance established by Eq. (4.6), a higher weight of the interaction term must be accompanied by a decrease of the kinetic term, resulting in the expulsion of solitons. The results of the numerical simulations (Fig. 4.10(b)) reproduce nicely the features observed in the experiment: at low pump intensities, there is a linear interference whereas when interactions become significant, the sinusoid transforms into a soliton train, more precisely an elliptic function shape, as first discussed in [173] and [174].

4.2.5 Phase jump of the polariton wave function across the soliton

Let us comment briefly on the characteristic π phase jump of the wave function expected across each soliton. Polaritons offer easy access to the phase of the wave function by interferometric measurements, allowing to verify the presence of this π phase jump. We use the pump laser beam, which has a constant phase, as a reference and we overlap this constant-phase reference beam with the real space emission from the wire (see Fig. 4.12(a)). The phase of the polariton fluid can then be extracted from the resulting interferogram. In particular, a phase jump of π can be detected in the interference pattern as a discontinuity in the fringes. Fig. 4.12(c) presents
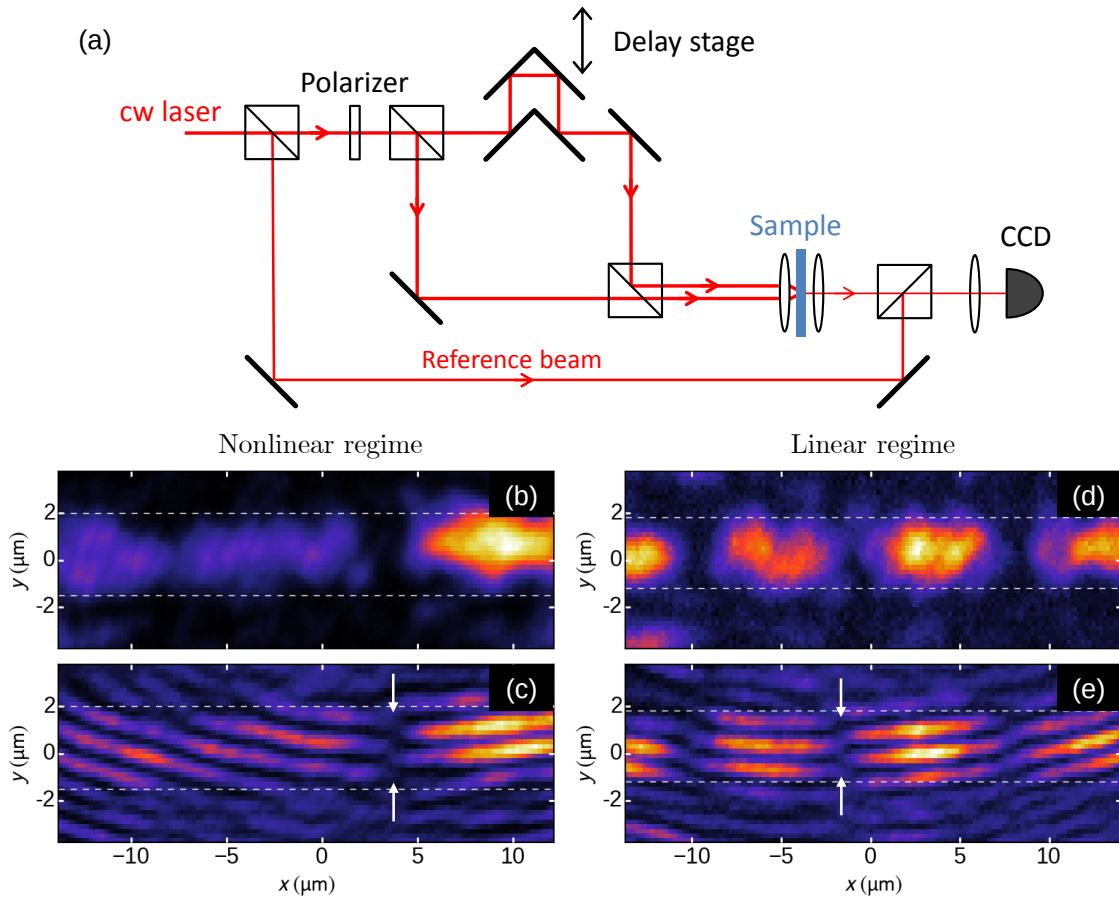
Figure 4.12: (a) Sketch of the experimental setup used to measure the phase of the polariton fluid. (b) Real space emission profile and (c) corresponding interferogram of the wire, in the nonlinear regime. A phase jump of π is clearly visible at the position of the soliton, indicated by the white arrows. (d) Real space emission profile and (e) corresponding interferogram in the linear regime. A phase jump of π is also observed around each node of the standing wave pattern, see, e.g., the position indicated by the white arrows.

an interference pattern measured in the nonlinear regime, but for slightly different parameters as in Fig. 4.8. With the choice of experimental parameters here, a single soliton is present in the wire, as shown in Fig. 4.12(b). A π phase jump across the soliton is clearly evidenced in the interferogram, at the position indicated by the white arrows.

We emphasize, however, that measuring this phase jump of π is not sufficient to ascertain that the density dip in the nonlinear regime is indeed a dark soliton. As mentioned above, in the linear regime, a standing wave is formed between the pumping spots. Hence, also in the linear regime, there is a π phase jump across each density dip, i.e., between each two nodes of the standing wave, as shown in Fig. 4.12(d),(e), for example at the position indicated by the white arrows. The nonlinear nature of the dark solitons present at high pumping power is confirmed by their abrupt generation and expulsion in the power scans, as well as by analysis of their profile. The presence of the π phase jump is a mere sanity check.

4.2.6 Bistability of the soliton pattern

In this section, we present experiments revealing that such a hysteresis is present when scanning the pumping power upward or downward. The hysteresis affects not only the transmitted intensity, but also the field profile in the cavity: we report a bistability of the soliton pattern, controlled by the pumping power.

Fig. 4.13(a) presents the evolution of the real space emission profile along the wire, integrated over the transverse direction, in an upward scan of the pumping
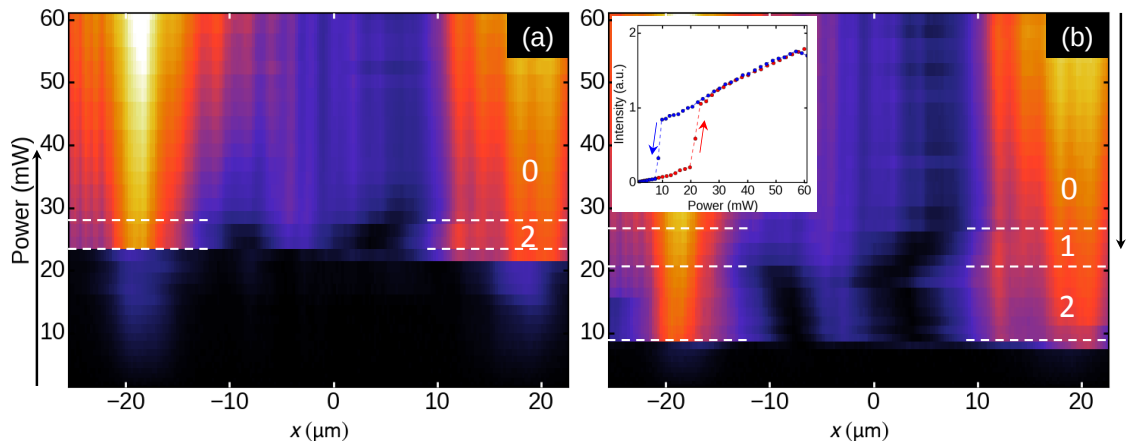
Figure 4.13: (a) Integrated density profile measured as a function of pump power, for an increasing pump power. The number of solitons in the wire for a power range over which it remains constant is indicated in white. $\Delta E = 0.27$ meV, $d = 40$ μm and $\Delta\varphi \approx 0$ (but non zero). (b) Power scan with the same parameters, but for a decreasing pump power. Inset: Total intensity in the wire for the upward (red dots) and downward (blue dots) pump power scans.

power. Fig. 4.13(b) is the corresponding downward scan, with the same experimental parameters and starting from the maximum pumping power reached in the upward scan. $\Delta\varphi$ is fixed to a value close to zero (but non zero). The threshold power corresponding to the transition between the linear and the nonlinear regime is measured at $P = 23$ mW in the upward scan. In the downward scan, this threshold value is lowered, at $P = 9$ mW. As one can see in the inset of Fig. 4.13(b), this behavior corresponds to a hysteresis loop. There exist a power range over which two different profiles can be observed, with either zero or two solitons, depending on the history of the power scan.

Focusing now on the evolution of the profile in the nonlinear regime, we notice, in the upward scan, a second transition at $P = 28$ mW from a profile containing two solitons directly above threshold, to a profile with zero solitons for higher pumping powers. The mechanism responsible for such a transition has already been discussed earlier. In the downward scan however, a profile that contains a single soliton is clearly visible from $P = 27$ mW down to $P = 21$ mW, before the transition to a pattern with two solitons when the power is further decreased. Thus, a bistable behavior of the soliton pattern in the nonlinear regime is identified. Note that the existence of a regime with a single soliton is due to the fact that $\Delta\varphi$ is not exactly 0, which relaxes the parity condition for the polariton fluid. Profiles with an even number of solitons are nevertheless still more favorable, which is why the profile with a single soliton is not observed in the upward scan (the precise influence of $\Delta\varphi$ on the soliton pattern is the topic of the next section).

To summarize, in counterpropagating nonlinear polariton fluids, we have observed the nucleation of dark solitons. Let us summarize briefly what we have demonstrated until now: in counterpropagating nonlinear polariton fluids, we observed the nucleation of dark solitons. The abrupt expulsion of solitons in a scan of the excitation power illustrates that solitons are the discrete elementary excitation of a superfluid, i.e. the way for a superfluid to accommodate kinetic energy. We have also evidenced bistable behavior of the soliton pattern when scanning the excitation power up and down. So far, we only considered $\Delta\varphi = 0$. In the next section, we address the influence of the additional degree of freedom provided by the phase twist $\Delta\varphi$.

4.3 Phase-controlled bistability of the soliton train

4.3.1 Tuning the phase twist across the wire

We now tune the phase twist $\Delta\varphi$ across the polariton fluid imposed by the excitation lasers, at constant excitation power. We investigate how the soliton train evolves when changing $\Delta\varphi$.

Figure 4.14(a)-(d) presents the polariton density profiles for a fixed excitation
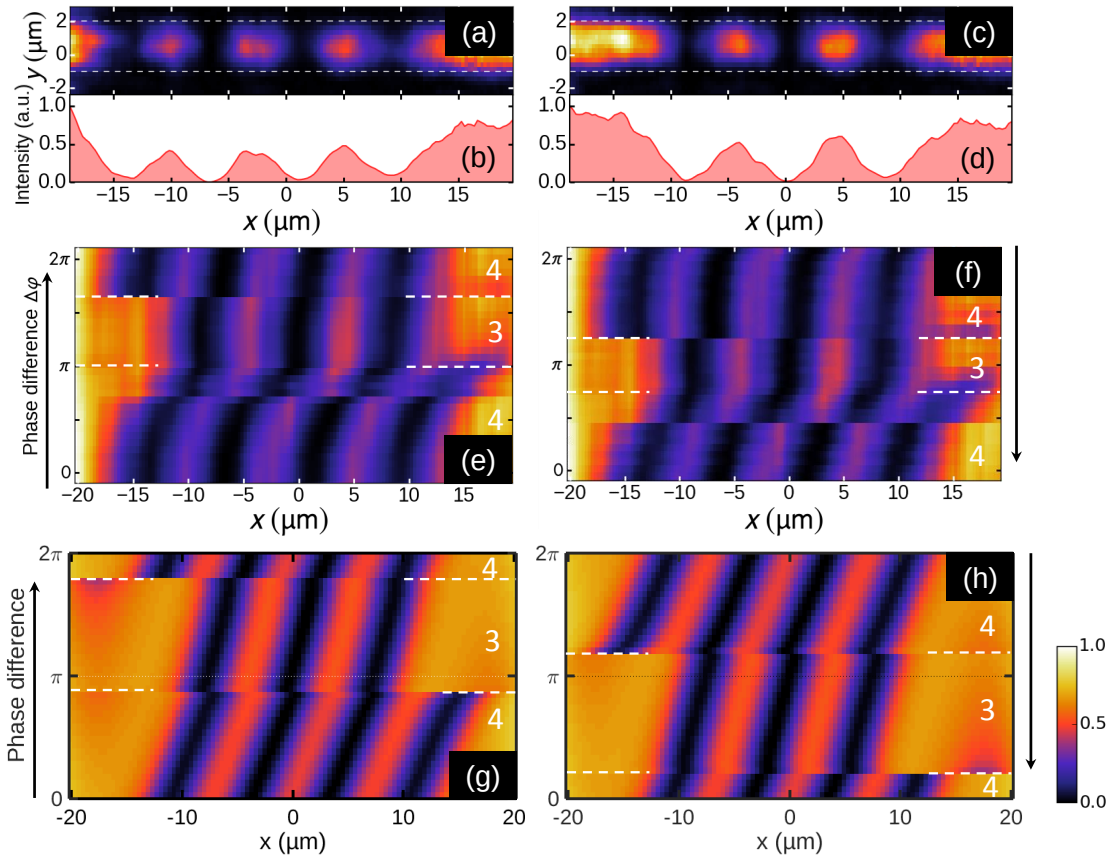
Figure 4.14: (a), (c) Spatially resolved emission for $P = 57$ mW, $\Delta E = 0.37$ meV, $d = 50$ μm and: (a) $\Delta\varphi = 0$; (c) $\Delta\varphi = \pi$. (b), (d) Corresponding intensity profiles integrated over the transverse direction. (e), (f) Measured –(g), (h) calculated– intensity profiles for increasing (e),(g) and decreasing (f),(h) phase difference $\Delta\varphi$ between the spots. White dotted lines indicate the value of $\Delta\varphi$ for which a soliton is expelled or generated. The measured number of solitons is indicated in white.

power $P = 57$ mW ($\Delta E = 0.37$ meV) and different values of $\Delta\varphi$. For $\Delta\varphi = 0$ (Fig. 4.14(a)) a symmetric profile is observed with four solitons (more solitons are present, due to the higher laser energy). On the contrary, when $\Delta\varphi = \pi$ (Fig. 4.14(c)), an antisymmetric profile is measured, with only three solitons, consistent with the antisymmetric boundary conditions.

When scanning $\Delta\varphi$, the transition between the two situations takes place abruptly, as shown in Fig. 4.14(e) (white dashed lines). This is in strong contrast with the linear regime behavior reported in Fig. 4.15: in the linear regime, when $\Delta\varphi$ is scanned, we observe a continuous spatial displacement of the interference pattern. Indeed, when polariton-polariton interactions are negligible, a linear standing wave forms, which position is fixed by $\Delta\varphi$, with linear dependence. In comparison, the abrupt expulsion and generation events attest the nonlinear character of the fluid.
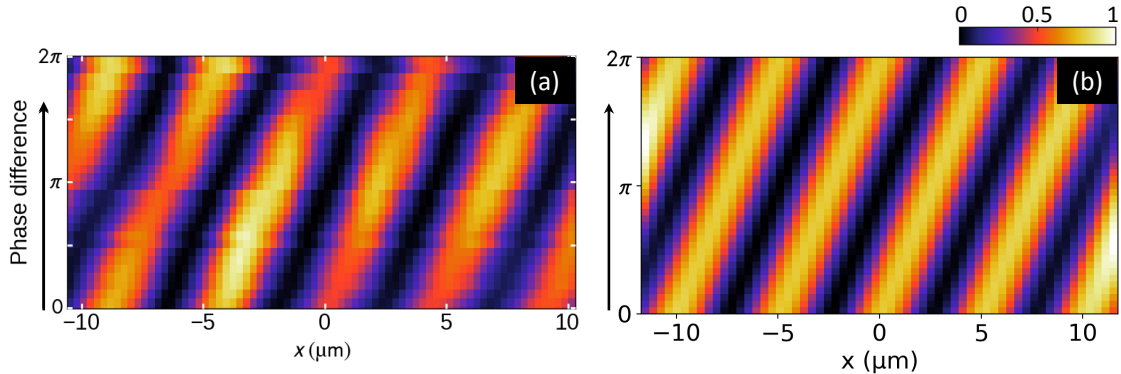
Figure 4.15: Influence of $\Delta\varphi$ in the linear regime. (a) Measured and (b) calculated emission profile when scanning the phase difference up. Note that no hysteresis is observed when scanning $\Delta\varphi$ down (not shown here).
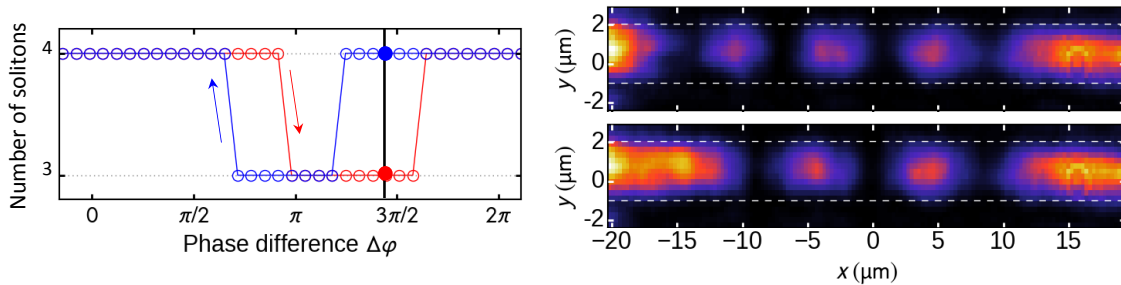
Figure 4.16: Evidence for phase-controlled bistability of the soliton pattern. Left: number of solitons in the upward (red dots) and downwards (blue) scan of $\Delta\varphi$, extracted from Fig. 4.14. Right: Real-space emission profiles for the value of $\Delta\varphi$ indicated on the left panel.

The abrupt transition in the latter case can be understood in a similar way to the case of Fig. 4.10, where a scan in power induces a change in interaction energy. In the present situation, the phase twist results in a change in kinetic energy across the fluid, which is accommodated via the expulsion or addition of a soliton to the fluid pattern. When approaching $\Delta\varphi = \pi$, the choice between the expulsion and the inclusion of a soliton is settled by the most stable solution at the considered excitation power.

Remarkably, when scanning $\Delta\varphi$ in the upward and downward directions for a fixed excitation power, we observe a bistable behavior, as already foreseen in Ref. [163]. In Fig. 4.14(f), $\Delta\varphi$ is now decreased, starting from the situation $\Delta\varphi = 2\pi$ from Fig. 4.14(e). The expulsion or generation of single solitons takes place at different values of $\Delta\varphi$ than in the upward scan. In other words, there exist values of the phase difference between the beams, for which two different profiles –with either four or three solitons– are stable, depending on the history of the phase scan, as shown explicitly in Fig. 4.16. Thus, we evidence a bistability entirely controlled

Figure 4.17: Phase shift of the linear standing wave pattern versus imposed phase difference $\Delta\varphi$, extracted from Fig. 4.15(a). The dashed line indicates the theoretical linear shift. We obtain a standard deviation of 0.03π with respect to the linear shift.

by the relative phase of the pumping beams.

The numerical simulation presented in Fig. 4.14(g,h) is in good qualitative agreement with the measured phase scan, including the bistable behavior. There are however some differences: first, the range of bistability is slightly smaller in the experiments as compared to 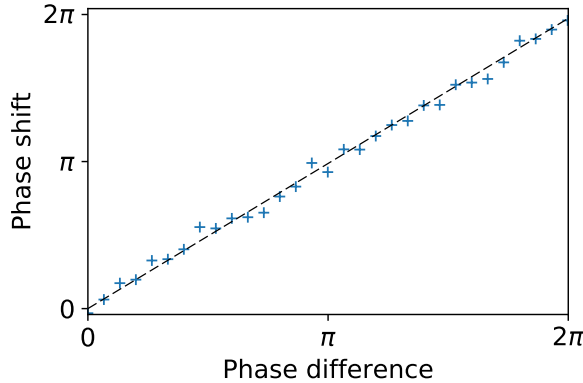simulations. A possible explanation is the presence of phase noise in the pump beams, due to mechanical vibrations of the different optical elements. We can estimate the phase noise from the measured phase scans in the linear regime (Fig. 4.15(a)). We have measured the shift of the interference pattern when we vary linearly the relative phase between the two laser beams, as shown in Fig. 4.17. The standard deviation between the measured interference shift and that expected in the absence of noise (dashed line) provides an estimate of the phase noise/fluctuations induced by the experimental setup. We get a standard deviation of 0.03π, corresponding to vibrations of amplitude of 16 nm, which is less than the phase increase between two successive steps in the phase scan. The small value of these fluctuations is thus not enough to explain the significantly smaller bistability range in the measurement compared to that expected from simulations.

A second difference between experiments and simulations is that the theoretical patterns shown in the two panels from Fig. 4.14(g,h) transform into each other under the $\Delta\varphi \to 2\pi - \Delta\varphi$ transformation, while in the experiment, this symmetry is only approximately satisfied. Indeed the simulation shows a more regular displacement of the soliton pattern than the measurement. For instance, when three solitons are stable, the measured pattern appears almost fixed in space for a wide range of $\Delta\varphi$, whereas it shifts continuously in the simulations. The presence of spatial disorder in the wire also needs to be considered. We show in the next section that this can be explained by the presence of disorder in the wire, as confirmed by simulations when introducing a small potential dip to model a defect. We will see that the introduction of disorder also allows to account for the smaller bistability range mentioned above.

4.3.2 Influence of a defect

Here, we discuss the influence of disorder on the motion of the soliton train when tuning the phase twist. We perform numerical simulations including an additional potential energy term that accounts for the presence of defects in the wire. A defect is modeled by a gaussian potential:

$$V(x) = V_{def} e^{-\frac{(x-x_{def})^2}{w^2}}, \qquad (4.11)$$

where the defect depth V_{def} can be either positive or negative, x_{def} is the defect position and w its width.

From the general theory of solitons in atomic Bose gases [175], it is known that for repulsive $V_{def} > 0$ defect potentials, the energy of a dark soliton is minimum when the soliton is located at the defect position where the background atomic density is lower (and vice-versa for an attractive defect). This is easily understood in a perturbative picture as the interaction energy with the defect is proportional to the local particle density. On the other hand, the effective mass of a dark soliton seen as a quasiparticle is negative, as intuitively understood from the fact that the dark soliton corresponds to missing particles. As a result, while energy minimization suggests that a dark soliton tends to bind to a repulsive defect, its actual kinematics is characterized by a repulsive acceleration [176].

Even if we are not aware of any complete theoretical study for polariton fluids, we can reasonably expect that these features remain valid also in this case. As the dissipative nature of these systems reduces the importance of energetic arguments, the physics is however likely to be dominated by the kinetic aspects and our simulations appear to confirm this naive expectation.

Figure 4.18(a-c) present the results of numerical simulations carried out with various defects (b,c), compared to a simulation without defects (a). The latter corresponds to the simulation of Fig. 4.8(g) discussed in the previous section. In both Fig. 4.18(b) and (c), the defect width is $w = 1$ μm. It is clearly visible that the presence of defects modifies the position of the solitons in the wire. More precisely, a negative defect has an attractive effect for a soliton, while a positive defect repels solitons.

Fig. 4.18(d-f) shows numerical simulations of the evolution of the soliton pattern in a scan of $\Delta\varphi$, highlighting the effect of disorder on the soliton train position. As discussed earlier, the displacement of the soliton pattern, shifted rightwards as $\Delta\varphi$ is increased, is regular in the scan with no defects (d).

In the case of a negative defect (e), the displacement is distorted: due to the attractive effect of the negative defect, a soliton coming close to the defect position is pinned and stays at the defect position in a finite range of $\Delta\varphi$. Beyond a threshold value of $\Delta\varphi$, the soliton is abruptly depinned as indicated by a white arrow in Fig. 4.18(e). Such behavior is very close to the one experimentally observed and shown in Fig. 4.14(e,f).
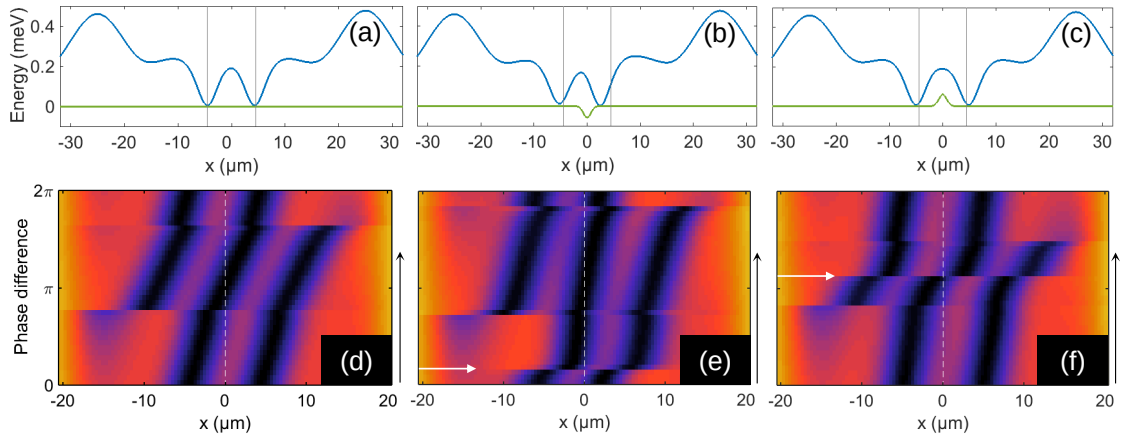
Figure 4.18: Top row – Numerical simulations of the density profile in a wire with $\Delta\varphi = 0$ and: (a) no defect. (b) $V_{def} = -60$ μeV, $x_{def} = 0$ μm. (c) $V_{def} = 60$ μeV, $x_{def} = 0$ μm. On each panel, the blue line is the local interaction energy, proportional to the local polariton density $(E_{int}(x) = \hbar g n(x))$. The green line is the potential energy arising from defects. Gray lines are guides for the eye, indicating the position of the solitons in the profile without defects. Bottom row – Corresponding phase scans in the upward direction. The white dotted line is a guide for the eye, indicating the position of the defect in (e) and (f).

For a positive defect on the other hand (f), there is no value of $\Delta\varphi$ for which a soliton is at the defect position, confirming the repulsive effect of the potential step. Moreover, because of this repulsion, an abrupt jump of the soliton pattern is observed, with a soliton jumping from the left of the defect to its right (indicated by the white arrow), when $\Delta\varphi$ is increased to the point that the solution with two solitons on the right of the defect becomes more stable than two solitons on the left.

This interpretation in terms of disorder is further supported by the observation that different sections of the sample showed slightly different soliton profiles while keeping the same excitation conditions.

Finally, note that the values of $\Delta\varphi$ corresponding to the generation and expulsion of a soliton are affected by the presence of a defect. In particular, the hysteresis range measured during a phase scan depends significantly on the disorder in the wire. This is very clear in Fig. 4.18(d-f), if we remind that the down scan of $\Delta\varphi$ is easily deduced from the up scan, by applying the transformation $\Delta\varphi \rightarrow 2\pi - \Delta\varphi$.

4.3.3 Control of the number of solitons

Eventually, we demonstrate that the number of solitons in the wire can be controlled by the different parameters of the experiment: laser detuning ΔE, distance between the spots d and excitation power P. Figure 4.19 presents the phase scans, at constant pumping power, in the upward and downward direction, for different configurations
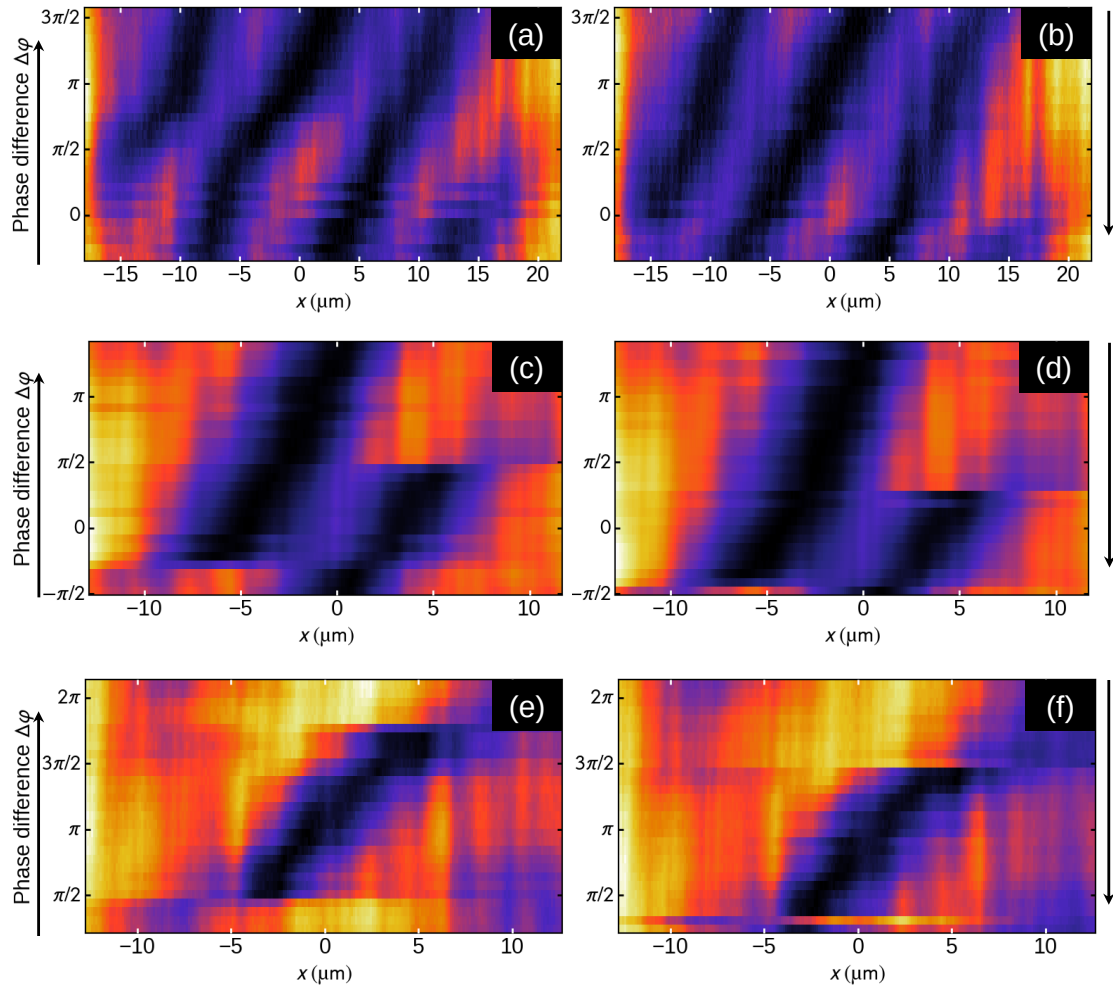
Figure 4.19: Left column – Phase scans in the upward direction ($\Delta\varphi$ increasing). Right column – Corresponding phase scans in the downward direction. The parameters for each scans are: (a),(b) $\Delta E = 0.21$ meV, $P = 42$ mW, $d = 60$ µm. (c),(d) $\Delta E = 0.35$ meV, $P = 90$ mW, $d = 40$ µm. (e),(f) $\Delta E = 0.20$ meV, $P = 103$ mW, $d = 40$ µm. Panels (a), (b) (resp. (c),(d) and (e),(f)) correspond to Fig. 4.20(b) (resp. (c) and (d)).
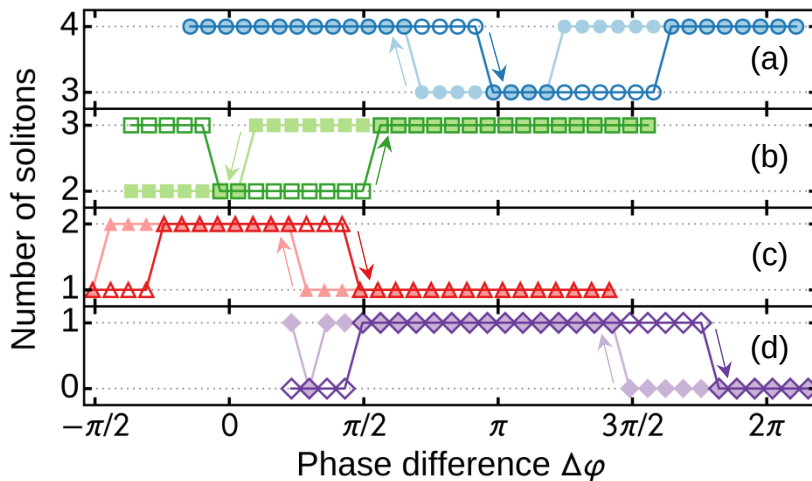
Figure 4.20: (a)-(d) Number of solitons measured when scanning $\Delta\varphi$ up (empty symbols) and down (full symbols). (a) Same parameters as in Fig. 4.10(e),(f); (b) $\Delta E = 0.21$ meV, $P = 42$ mW, $d = 60$ μm; (c) $\Delta E = 0.35$ meV, $P = 90$ mW, $d = 40$ μm; (d) $\Delta E = 0.20$ meV, $P = 103$ mW, $d = 40$ μm.

of excitation powers and distances d (see figure caption for the parameters values). The number of solitons versus $\Delta\varphi$ in the different scans are summarized in Fig. 4.20. Abrupt switching between trains with N and $N+1$ solitons is observed for N ranging from 0 to 3. In each of these situations, we observe a well defined phase-controlled bistability.

The phase-controlled bistability is the counterpart of the power-controlled bistability presented first, in the sense that the number of solitons in the wire can be controlled by two independent parameters: the pumping power P, and the phase twist imposed across the wire, $\Delta\varphi$. Tuning either of these parameters, the expulsion or generation of a soliton is an abrupt event inherent to the discrete nature of the solitons, and additionally such a transition is associated with a hysteresis when scanning a single parameter.

4.4 Conclusion and perspectives

4.4.1 Probing soliton-soliton interactions

We have shown that our experimental configuration allows for the nucleation of dark solitons in a well-controlled manner. We now discuss possible perspectives for this work. As a first example, we propose a configuration where soliton-soliton interactions could be explored.

We discussed previously the influence of defects on the solitons position. In particular, we found that a positive defect has a repulsive effect on dark solitons
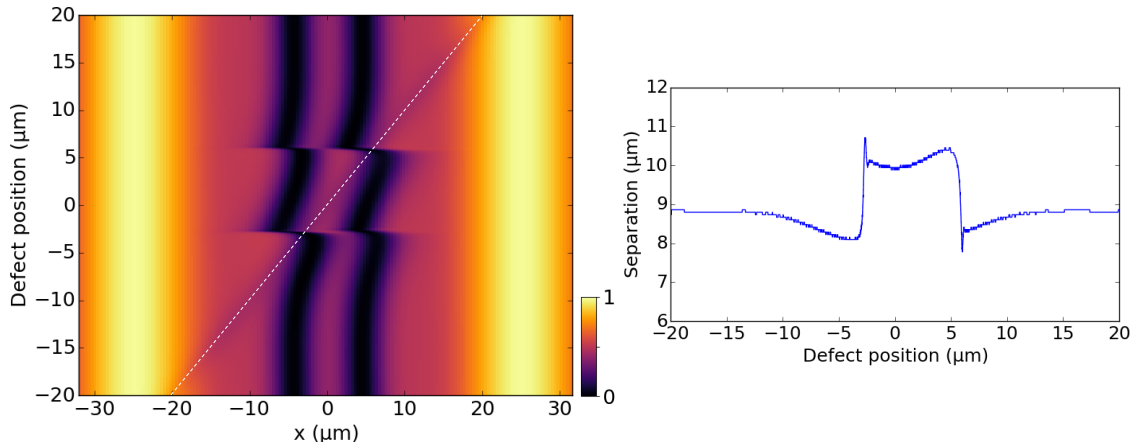
Figure 4.21: (Left) Calculated evolution of the density profile with two solitons, in an adiabatic sweep of a repulsive defect across the wire. The white dashed line indicates the defect position. (Right) Distance between the two solitons in the scan of the defect position.

(Fig. 4.18). The potential hill corresponding to such defect could for example be induced optically, by means of a non-resonant laser [62]. This way, it is possible to manipulate the solitons, by moving the defect along the wire to drag the solitons, in a fully all-optical way. This is illustrated in Fig. 4.21, where we have calculated the steady-state polariton profile in an adiabatic sweep of a repulsive defect across the wire. The drive conditions are identical to those in Fig. 4.18, leading to a density profile with two solitons: $d = 50$ μm, $\Delta\varphi = 0$, $\Delta E = 0.27$ meV. The defect is also the same as in Fig. 4.18(c): it is gaussian-shaped with width $w = 1$ μm and amplitude $V_{def} = +60$ μeV. The defect position x_{def} is swept from left to right, at a speed much slower than all relevant timescales of the system. As x_{def} is increased, the defect repels the leftmost soliton, which is displaced rightwards. Interestingly, the right soliton is also affected shift to the right. The shift increases until at $x_{def} = -3$ μm, the left soliton jumps abruptly to the left of the defect. The right soliton undergoes a similar jump leftwards. Finally, when x_{def} is increased further, the right soliton in turn jumps to the left of the defect, at $x_{def} = 6$ μm.

This behavior clearly indicates a repulsive interaction between the dark solitons. Such behavior is well documented in conservative systems such as in nonlinear optics and in cold atoms, both theoretically [177–179] and experimentally [180, 181]. In particular, the interaction between dark solitons is known to fall off exponentially with distance [177, 182]. Nevertheless, such interactions have not been explored in the driven-dissipative context of cavity polaritons. The present setup offer great and simple control on the dark soliton pattern, and seems particularly suited to such study.

Note that the soliton position is constrained not only by their relative interaction and repulsion from the defects, but also by the presence of the two driving spots

at each end of the wire. Since the phase is locked under the spots, solitons cannot penetrate the driven regions. In this sense the two spots exert a strong repulsive force on the dark solitons, creating an effective trap. In particular, this explains why the solitons jumps to the left on the defect when the latter is swept to the right: the repulsion from the region under the right spot becomes stronger than the one from the defect.

We have underlined that the two spots of the coherent drive create an effective trap for the solitons, which in addition to the repulsive soliton-soliton interactions constrains the soliton position at a fixed $\Delta\varphi$. Another interesting perspective would be to investigate the dynamics of the soliton train. We discuss this topic in the following section.

4.4.2 Collective soliton oscillations

Here, we show that using a resonant probe, it is possible to trigger collective oscillations of the solitons. We are going to excite locally the soliton train and look at its dynamical response.

First, we consider a perturbation of the soliton pattern with a probe pulse, resonant with the drive. We fix the pulse length to 3 ps (Fig. 4.22(a)), the maximal amplitude is half the drive amplitude F. The spatial shape of the pulse is Gaussian, with the same width as each excitation spot ($w = 8$ μm), centered on $x = 0$. In Fig. 4.22(b), we present the calculated time-resolved evolution of the polariton wave function subsequent to the perturbation by the pulse, at $t = 50$ ps. The initial steady-state, a pattern with two dark solitons, corresponds to the same drive parameters as in the previous paragraph. The soliton pattern is strongly affected by the perturbation: the two soliton collapse immediately after the pulse. Then, each soliton trajectory shows damped oscillations, with both the oscillation period and damping on timescales comparable to the polariton lifetime (we recall that in these simulation the polariton decay rate is $\hbar\gamma = 47$ μeV, corresponding to a polariton lifetime of 28 ps). We point out that due to the symmetric nature of the drive conditions and perturbation, the triggered oscillations are out of phase. In Fig. 4.22(c), the same pulse is applied to a profile with four solitons initially present (the spots separation is increased to $d = 70$ μm), triggering similar oscillations.

Note that since the probe pulse is resonant with the drive, its phase is also important. We find that different phase lead to different initial perturbation of the soliton pattern, but qualitatively the behavior is the same (same amplitude and frequency of the soliton oscillations). Additionally, the amplitude of the initial perturbation is proportional to the probe amplitude.

The above scheme allows the excitation of soliton oscillations, but one of the issue is the short damping time, which would hinder the observation of more than one period of oscillations. To circumvent this issue, we now consider a continuous perturbation. A weak probe, with amplitude $0.1F$, is abruptly switched on, with a rise time of a few picoseconds (Fig. 4.22(d)). We consider perturbation of a two-
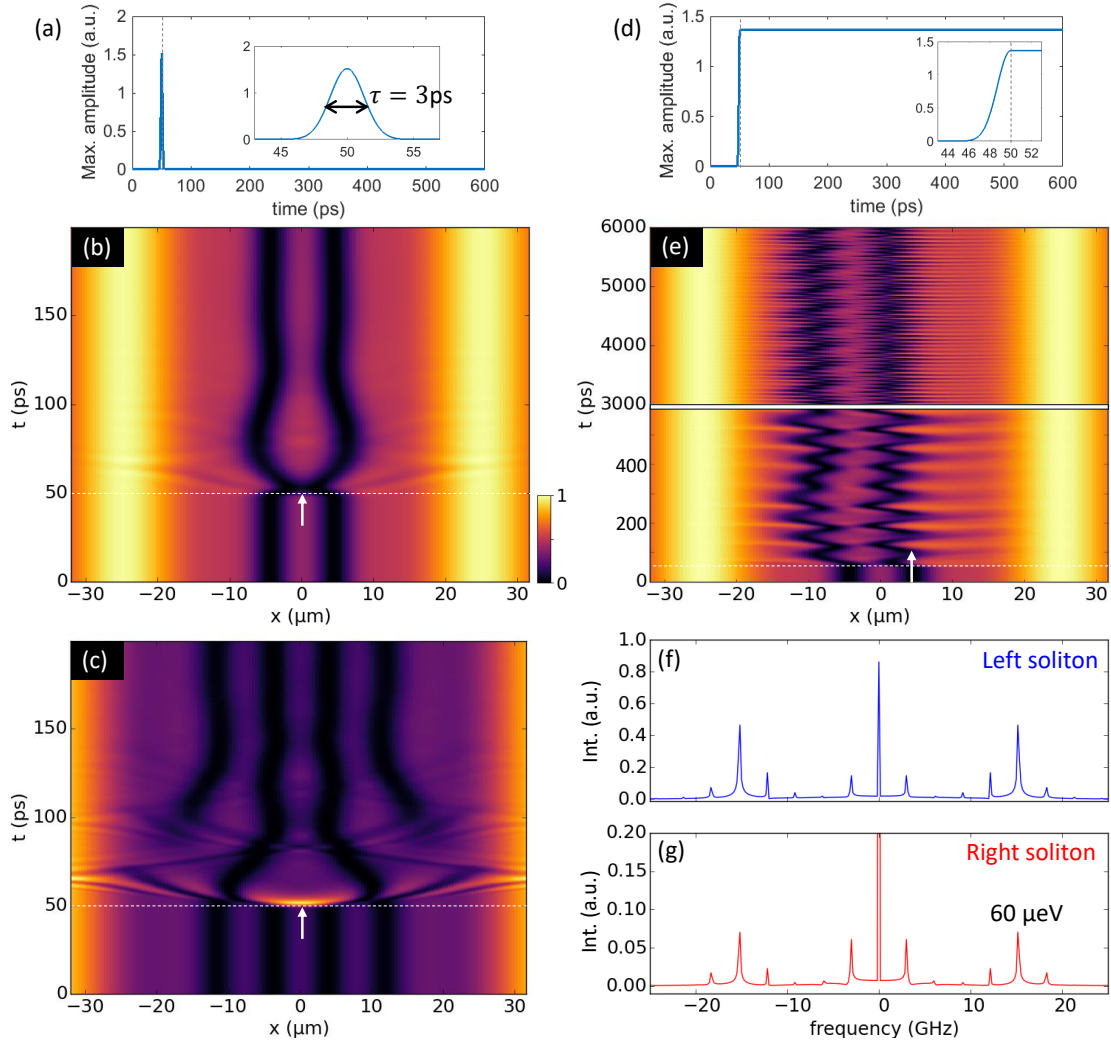
Figure 4.22: (Left) Perturbation with a probe pulse. (a) Temporal profile of the pulse, of length $\tau = 3$ ps, as shown in the inset. (b, c) Time-resolved evolution of the density profile under perturbation by the probe pulse, for a pattern with (b) two solitons and (c) four solitons. The dashed line indicates the time of arrival of the pulse, and the white arrow indicated its central position. (Right) Continuous wave perturbation. (d) Temporal profile of the step-like profile of the probe, with a rise time shown in inset. (e) Time-resolved evolution of the soliton pattern, at (lower half) inital times and (upper half) longer times of the evolution. (f, g) Fourier spectrum of the left, right soliton trajectory.

soliton pattern. The spatial profile of the probe is identical to the previous one, but it is displaced to the right side of the wire, in order to break the mirror symmetry and trigger in-phase soliton oscillations (thus exciting the whole spectrum of soliton oscillations). The calculated time evolution of the density profile under such perturbation is shown in Fig. 4.22(e). After the perturbation is applied, oscillations of the soliton pattern occur, but they are not damped and survive at long times ($t > 6$ ns). Moreover, two oscillation timescales can be identified: a fast oscillation corresponds to out of phase oscillations, while in-phase oscillations are present with a longer period. The Fourier transform of each soliton trajectory reveals the energy scale associated with these oscillations. The two modes can be interpreted as the bonding and antibonding excitation modes of the soliton pair. Note that the antibonding mode has an energy of 60 µeV, above the polariton linewidth, which would enable its experimental observation without time-resolved measurements.

Extending these results to patterns with more solitons, we can consider the soliton train as a Wigner crystal of dark solitons: mutual repulsion between the solitons fixes their position in the wire, resulting in a 1D periodic soliton lattice. The collective oscillations of the soliton train can then be seen as the excitations of the soliton lattice. A similar configuration was discussed in Ref. [183].

It should be noted that similar oscillations of dark solitons have been experimentally reported in Bose-Einstein condensates of cold atoms [184], and subsequently investigated theoretically [182]. However, no experimental work has been carried out in a driven-dissipative context so far.

4.4.3 Conclusion

In conclusion, we have demonstrated in this chapter the ability to generate and control soliton trains in a 1D polariton quantum fluid. The nucleation of dark solitons arises from an interplay between the interaction and kinetic energy of the fluid. Moreover, the ability to impose a controllable phase twist across the fluid using a coherent drive allowed us to reveal a novel bistable behavior. As we have shown with numerical simulations, this experimental configuration offers a new perspective to explore the physics of dark solitons and their interactions, and in particular the excitation spectrum of a soliton lattice, in pump and probe experiments, or other theoretical proposals requiring a high level of control over the soliton train. For example, the realization of a Newton's cradle based on a soliton lattice has been proposed [185].

Moreover, we could exploit the polarization degree of freedom of polaritons, that we have completely ignored in this whole chapter. Using pumping spots with orthogonal linear polarization, the formation of circularly polarized spin domains has been predicted [163]. The formation of half soliton trains, which has been discussed theoretically with different excitation configurations [183, 186, 187] is also at hand. Note that in the two cases, one would need no energy splitting between the TE and TM polarized modes of the wire at $k = 0$, which is in general not the case in our

samples, due to the polarization-dependence of the boundary conditions in the wire (as discussed in detail in the next chapter), and additional effects such as strain in the microstructure induced by etching, so further optimization would be required.

Nonlinear dynamics of a polariton fluid in a flat band

In chapter 4 we have seen how the interplay between kinetic and interaction energy gives rise to a rich variety of phenomena for a nonlinear polariton fluid. In the present chapter, we investigate the response of the nonlinear fluid when additional constraints are imposed to its kinetic energy. In particular, we address the question of the fate of the fluid in a system with infinite effective mass, where the kinetic energy is completely quenched. Such a case occurs when one of the energy band is dispersionless, or completely flat: the energy is independent of wave vector k.

In section 5.1, we review briefly the basics of flat band physics and present the recent progress of its emulation with microcavity polaritons. In section 5.2 we introduce the one dimensional Lieb lattice, investigate the origin of the flat energy band in this lattice, and discuss its implementation for polaritons. Section 5.3 presents the experimental results of the resonant injection of a nonlinear polariton fluid in a flat band. We demonstrate the formation of localized nonlinear domains, in strong contrast with the behavior reported in dispersive bands. Numerical simulations based on the Gross-Pitaevskii equation are carried out, and we discuss the interpretation for the experimental results. In section 5.4, we investigate the influence of disorder on the nonlinear domains, both experimentally and via numerical simulations, introducing in the latter a simplified disorder model. Finally, conclusions and perspectives are discussed in section 5.5. In particular, we present preliminary results on multistability of nonlinear domains, focusing more specifically on the different steady-states that can be obtained from identical initial conditions.

5.1 Introduction to flat band physics

5.1.1 Lattices with a flat band

A flat band is a dispersionless energy band: its energy is independent of the wave vector k. The corresponding effective mass is infinite, so the kinetic energy in such a band is zero and single-particle transport is suppressed. Consequently, flat bands are associated with localized eigenstates. Additionally, due to its dispersionless nature, a flat band is macroscopically degenerate, and the density of state diverges at the flat band energy.

Flat bands can be found in a wide variety of systems, among which Landau levels of a two-dimensional electron gas in a magnetic field [188], Aharonov-Bohm cages in networks of superconducting wires and normal metal lattices [189–191], or frustrated magnets [192, 193]. For the latter case, frustration arise from the geometry of the system. An archetypal example of geometric frustration is found with three spins, located at each vertices of a triangle and linked by antiferromagnetic couplings. The antiferromagnetic alignment cannot be fulfilled for the three spins at once, and in this case the ground state is degenerate. Extending this simple case to a triangular lattice of antiferromagnetic spins results in a macroscopic degeneracy for the ground state of the system (corresponding to a flat band).

Certain types of lattices are also known to host a flat band. The study of such lattices was initiated in 1986 by Sutherland [194]. He described how 'strictly localized states' (now called compact localized states) exist in the dice lattice, giving rise to a flat band. Such states have a vanishing wave function amplitude, except on a finite number of sites, as illustrated in Fig. 5.1(a) (on a side note, Sutherland actually first identified those states in quasiperiodic Penrose tilings, and then found out a design for a periodic lattice where they also exist). The compact localized
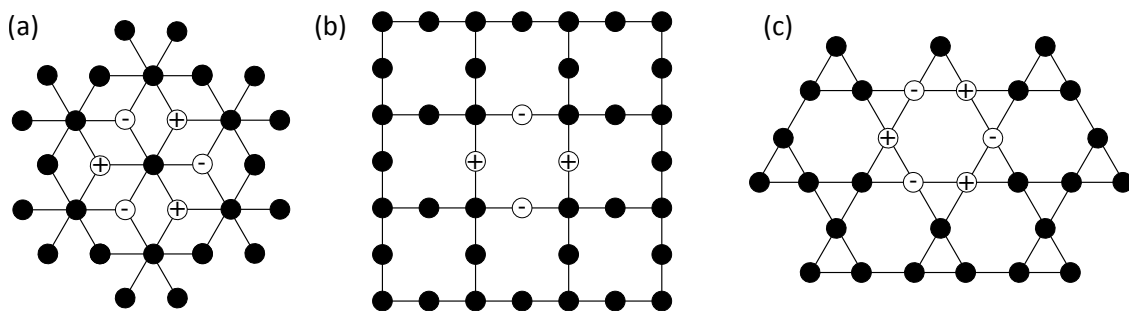

Figure 5.1: Examples of two-dimensional lattices with a flat band in their energy spectrum: (a) the dice lattice; (b) the Lieb lattice and (c) the Kagome lattice. White circles indicate the sites excited by single compact localized states along with the signs of the eigenstate amplitudes required to eliminate hopping to neighboring unexcited sites.

modes arise from a form of geometric frustration similar to the one discussed above, but here it constrains the phase of the wave function (this mechanism, termed phase frustration, will be described in detail in the next section). Later works, in particular by Lieb [195], Mielke [196] and Tasaki [197] extended this idea to different lattice geometries. Nowadays, many examples of lattices with a flat band are known, in one, two or three spatial dimensions (see [198] for a review). Famous two-dimensional lattices with a flat band include the Kagome lattice, and the Lieb lattice (see Fig. 5.1).

General to any flat band conservative system, due to the absence of kinetic energy, any perturbation can have dramatic effect, since no matter how weak the perturbation, it sets a new dominant energy scale for the flat band states. For example, interactions give rise to correlated many-body states, such as fractional quantum Hall states [199], spin liquids and spin ices [200], or itinerant ferromagnetism [195–197]. Note that in a dissipative system, the finite particle lifetime sets a natural energy scale. In this case, the amplitude of the perturbation must overcome the linewidth to affect significantly the behavior of the system.

In the specific case of flat band lattices with repulsive particle-particle interactions, theoretical predictions differ depending on the interaction strength. In the limit of very high interaction, Wigner crystallization is expected at precise values of the filling factor, depending on the considered lattice [201, 202]. For smaller interaction strength, the system can be described with the mean-field nonlinear Schrödinger equation, and discrete solitons (or discrete breathers) typical from periodic systems with nonlinearities are predicted [203–206]. This formalism and the associated predictions will be discussed in more details later in this chapter.

Additional topic of particular interest is superfluidity in a flat band. The cuprates exhibiting high T_c superconductivity have a Lieb lattice structure [207], and the presence of the flat band is thought to be responsible for the high value of the critical temperature [208, 209]. Moreover, it has been proposed that the recent observation of superconductivity in twisted bilayer graphene at magic angle is also due to the presence of almost flat bands [210, 211].

Finally, another important type of perturbations to the system is disorder. In a flat band, it has been predicted that disorder may be responsible for a modified Anderson localization, with unconventional critical exponents and multifractal behavior in certain types of lattices [212], on the other hand induce an inverse Anderson localization in other cases [213], or induce mobility edges if the disorder has specific correlations [214].

In the quest for emulation of this rich physics, intense efforts were made over the past few years to build artificial flat band lattices. A recent review of these pioneering works can be found in Ref. [198]. Among the different platforms in which a flat band in a frustrated lattice was reported, let us mention cold atoms [218–220], as well as several photonic systems: lattices of spoof terahertz resonators [215], arrays of coupled lasers [216] and coupled waveguides [217, 221, 222], and microcavity polaritons [29, 73, 86, 223]. The review of experimental work on flat band in micro-
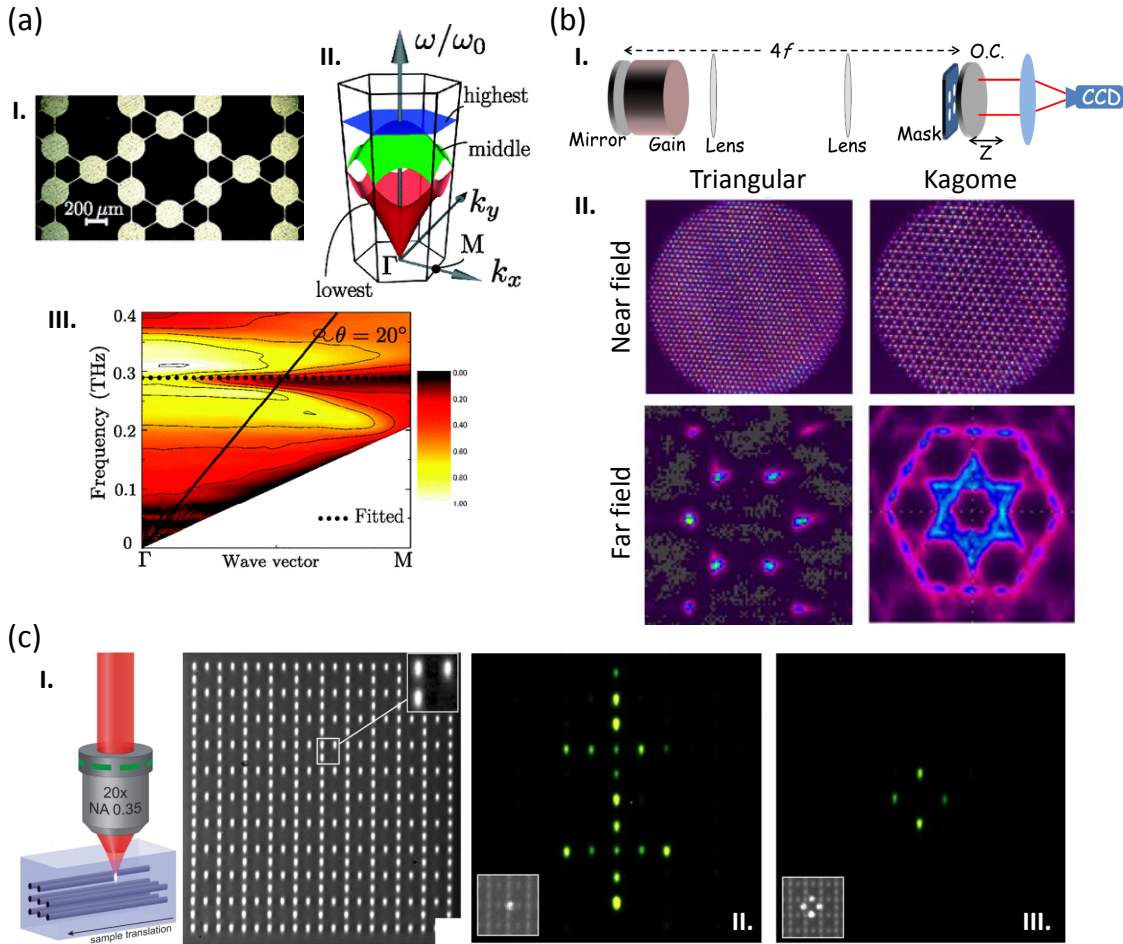
Figure 5.2: Examples of photonic flat bands: (a) I. Kagome lattice for terahertz spoof plasmons. II. Calculated band structure of the lattice. III. Transmission diagram of the lattice. A minimum in the transmission is observed at the flat band frequency (dashed line). Images from [215] (b) I. Experimental arrangement for coupling more than a thousand independent lasers. A mask of apertures placed in the optical cavity forms the many laser channels. II. Near and far field images of the emission, for negatively coupled lasers arranged either in a triangular or Kagome lattice. For the triangular lattice, the sharp Bragg peaks in the far field pattern indicate long range phase ordering. In the Kagome lattice on the other hand, the absence of sharp peaks evidences the absence of long range phase ordering, due to geometric frustration. Images from [216] (c) I. Femtosecond laser-written Lieb lattice waveguide arrays. II, III. Output profiles from the waveguides, for different input conditions: II. single-site excitation, leading to diffraction in the lattice, and III. excitation of a flat band compact state, for which diffraction is suppressed. The inset indicates the input intensity. Images from [217].

cavity polaritons is the topic of the next paragraph. For now, let us focus briefly on the experimental results reported in other photonic platforms, summarized in Fig. 5.2. In Ref. [215], Nakata *et al.* fabricated a Kagome lattice of metallic disk (Fig. 5.2(a)). They characterized the transmission diagram of the lattice in the terahertz range, and observed a resonance at energy independent of wave vector, corresponding to a flat band for a spoof plasmonic mode. In Ref. [216], Nixon *et al.* fabricated arrays of more than a thousand lasers (Fig. 5.2(b)). A mask of apertures was placed inside a cavity with gain medium, forming independent laser channels arranged in a two-dimensional lattice, of arbitrary geometry. Coupling between adjacent lasers is provided by the overlap between neighboring channels. The author measured the far field emission pattern of a Kagome lattice, and compared it to a triangular lattice: they observed for the triangular lattice sharp Bragg peaks attesting coherence between all lasers, i.e. long range phase ordering. On the other hand, for the Kagome lattice no such sharp peak is present in the far field emission pattern. This lack of long range ordering is an evidence of geometric frustration. Note that contrary to Ref. [215], here the couplings were antiferromagnetic, and consequently the flat band is the lowest energy band and the ground state of the system. Finally, Vicencio *et al.* [217] and Mukherjee *et al.* [222] reported two very similar studies, carried out simultaneously and independently, with 2D Lieb lattices of waveguide arrays (Fig. 5.2(c). The lattices are written in a fused silica glass wafer, by means of femtosecond laser pulses. The author of both works reported that when the lattice of coupled waveguides is excited at its input with proper initial conditions, corresponding to the amplitude and phase of a flat band compact state, then light propagates without any spatial spreading in the waveguides. On the other hand, other input states such as a single site excitation leads to diffraction to neighboring sites during propagation in the waveguides. Recently, Aharonov-Bohm cages for photons were also reported [224], offering a new approach to the realization of photonic flat bands.

So far, all these works have been limited to a regime where particle-particle interactions are absent, and the influence of such interactions remains experimentally unexplored.

5.1.2   Bosonic condensation in the flat band

Flat band lattices have been investigated with microcavity polaritons. The idea to implement flat bands for polaritons was pioneered by the group of Yamamoto [73]. In this work, a thin metallic film was deposited on top of a planar cavity, and was patterned into a Kagome lattice (as discussed in chapter 2, a weak confinement potential for polaritons is created under the thin metallic film). The presence of an almost flat energy band was observed in the single-particle polariton dispersion (the confinement potential was too shallow to observe perfectly flat bands). Shortly after, a flat band was also evidenced in our group, in the *p*-bands of a honeycomb lattice of coupled micropillars [29].

More recently, efforts have been oriented towards the observation of bosonic con-
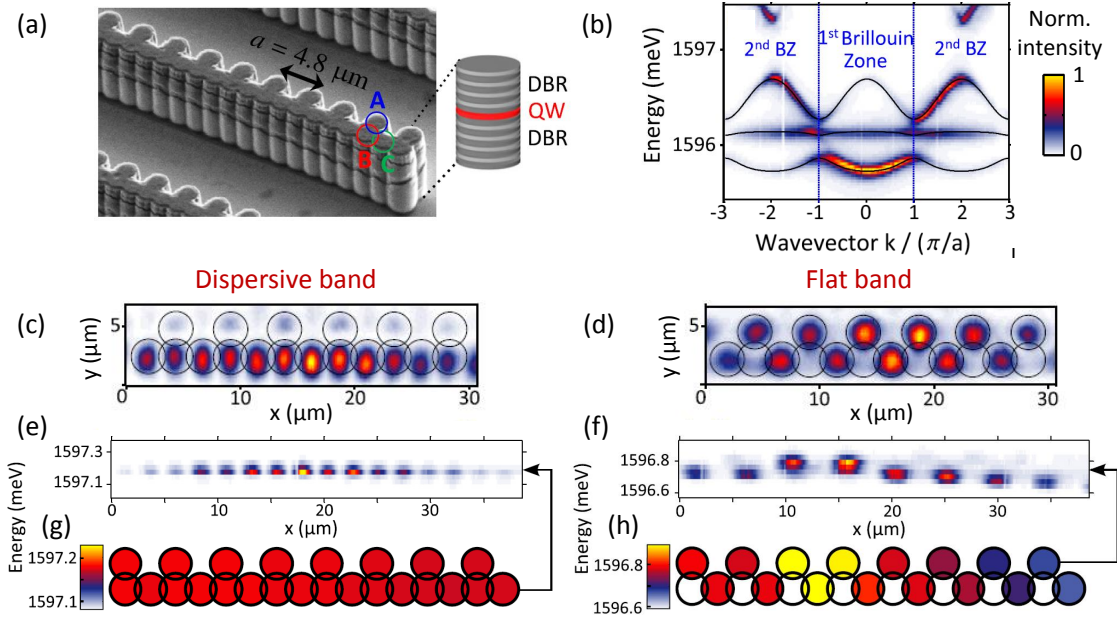
Figure 5.3: (a) SEM image of a one-dimensional Lieb lattice of coupled micropillars. (b) Momentum-space resolved photoluminescence of the lattice. (c,d) Real space image of the condensate in the upper dispersive band and in the flat band. (e) Energy-resolved emission of the dispersive band condensate in real space, measured along the line of pillars B, C. (f) Energy-resolved emission of the flat band condensate, measured along the line of pillars A. (g,h) Spatial map of the emission energy corresponding to (e,f), where the color code indicates the emission energy. Adapted from [223].

densation in a flat band. In particular, a previous work from our group reported bosonic condensation in the flat band of a 1D Lieb lattice of coupled micropillars [223]. The 1D Lieb lattice consists in a stripe of a single unit cell from the 2D Lieb lattice, and similar to its two-dimensional counterpart, it holds a flat band (Fig. 5.3(a,b)). The 1D Lieb lattice and the origin of its flat band will be discussed in details in the next section. Baboux *et al.* reported that depending on the spatial configuration of the non-resonant pump, the bosonic condensation can be triggered either in the upper dispersive band, or in the flat band. The real space image of the flat band condensates shows dark B sites characteristic of the phase frustration, in clear contrast with the dispersive band condensate (Fig. 5.3(c,d)). Moreover, measurements on the spatial coherence of the condensate in the flat band reveals very short coherence length with respect to the dispersive band condensate. The author attributed this difference to the existence of multiple highly localized condensates in the flat band, induced by the presence of disorder in the lattice. They confirmed this with spectral imaging, as shown in Fig. 5.3(e,f). In the dispersive band (Fig. 5.3(e)), a single monomode extended condensate exists. In strong contrast, in the flat band (Fig. 5.3(f)), significant spectral variations are visible across the lattice. The re-
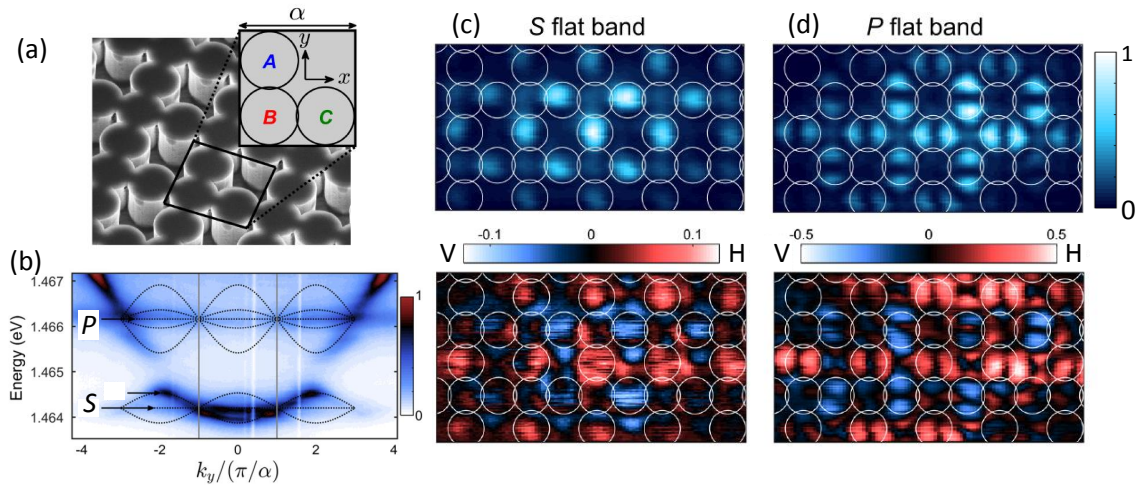
Figure 5.4: (a) SEM image of a two-dimensional Lieb lattice of coupled micropillars. Inset: schematic representation of a single unit cell. (b) Momentum-space resolved photoluminescence of the lattice, with *s*- and *p*-bands visible. (c, d) Top row: real space image of a condensate in the *s* and *p* flat band, respectively. Bottom row: corresponding degree of linear polarization. The color scale is linear with red (blue) representing H (V) polarization. Adapted from [86].

construction of the main energy of emission per site, shown in Fig. 5.3(h), allows to identify localized condensates corresponding to CLS. Because of the absence of kinetic energy in the flat band, any finite amount of disorder localizes the eigenstates and breaks the degeneracy, leading to the observed fragmentation. Here, the disorder arises from several factors: imperfection of the cavity and quantum well during growth, fluctuations in the size of the pillars during the etching, or any other possible defaults during and after fabrication.

Beyond demonstrating bosonic condensation in a flat band, the work in Ref. [223] thus underlines the important role of disorder in a system with quenched kinetic energy. Similar results for polaritons condensates were later reported in 2D Lieb lattices [83, 86]. In particular, in Ref. [86], Whittaker *et al.* investigated condensation in the flat bands formed from the *s* but also the $p_{x,y}$ photonic orbitals (Fig. 5.4). They observed that the flat band condensates exhibit pseudospin textures, which they attributed to a form of spin-orbit coupling for polaritons, arising from the symmetry of the orbital wave functions combined with polarization-dependent hopping energy. Such effect is inherent to the 2D configuration. They also reported fragmentation of the condensate due to disorder.

In these works, polariton-polariton interactions were negligible. A blueshift of the polariton dispersion is observed when increasing the pumping power, but is induced by interaction with the excitonic reservoir, created by non-resonant pumping. Such a blueshift only acts as a global potential, i.e. it is purely a linear contribution to the equation describing the polariton wave function. In this chapter, we

present investigations of the role of polariton-polariton interactions. In particular, this requires injecting a polariton fluid in which the interaction energy overcomes the polariton linewidth (and the amplitude of disorder). To this end, we will use resonant pumping to inject polariton directly in the flat band.

5.2   One dimensional Lieb lattice for polaritons

5.2.1   Phase frustration in the 1D Lieb lattice

The one-dimensional Lieb lattice (also named stub lattice) is one of the simplest example of a lattice known to host a flat band in its energy spectrum. In this section, its properties are studied within the tight binding approximation. As depicted in Fig. 5.5(a), the unit cell consists in three sites, labeled A, B and C, linked by nearest-neighbor couplings, of amplitude t for the link B–C and t' for A–B. Additionally, each site can have a different on-site energy, labeled $E_{A,B,C}$ (only one orbital per site is considered). In the tight-binding approximation, the corresponding single-particle Hamiltonian is:

$$\hat{H} = \sum_{l,n} E_l |l_n\rangle\langle l_n| - \sum_n \left(t\big(|B_n\rangle\langle C_n| + |B_n\rangle\langle C_{n+1}|\big) + t'|A_n\rangle\langle B_n| + \text{h.c.} \right) \quad (5.1)$$

where $|l_n\rangle$, with $l \in \{A, B, C\}$, is the wave function of site l in the nth unit cell. It is convenient to work in momentum space, using the basis of the Fourier transformed states

$$|A(k)\rangle = \frac{1}{\sqrt{N}} \sum_n e^{ikan} |A_n\rangle \quad (5.2)$$

and similar $|B(k)\rangle, |C(k)\rangle$, where N is the total number of unit cells of the lattice and a the lattice parameter (physical size of the unit cell).

In this basis, $\hat{H}$ is recast as a block-diagonal matrix, with 3 x 3 blocks noted $\hat{\mathcal{H}}(k)$, corresponding each to a value of k:

$$\hat{\mathcal{H}}(k) = \begin{pmatrix} E_A & -t' & 0 \\ -t' & E_B & -t(1 + e^{-ika}) \\ 0 & -t(1 + e^{ika}) & E_C \end{pmatrix} \quad (5.3)$$

The diagonalization of $\hat{\mathcal{H}}(k)$ for all k gives the energy spectrum associated with the lattice, separated in three distinct bands. As shown in Fig. 5.5(b), there exist sets of parameters for which one of these bands can be turned completely flat (or dispersionless): the energy is independent of k. In Fig. 5.5(b) this is the case when $E_A = E_B = E_C = 0$ and $t = t'$, while the middle band is dispersive for $E_A = -0.5t$.

Qualitatively, the origin of the flat band can be understood in the following way. In the lower and upper bands, both dispersive, the eigenfunctions are Bloch
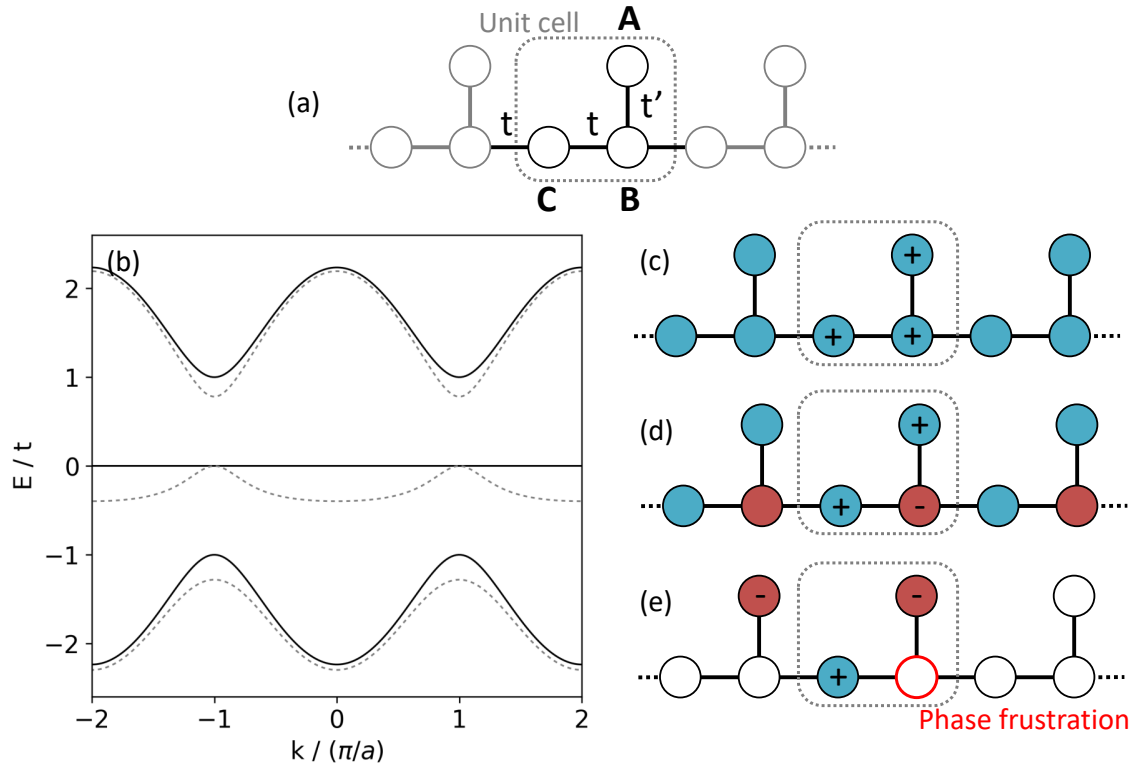
Figure 5.5: (a) Tight-binding representation of the 1D Lieb lattice. The hopping energies between sites $B - C$ and $A - B$ are noted t and t', respectively. (b) Dispersion relation calculated with $t = t'$, and on-site energies $E_B = E_C = 0$ and $E_A = 0$ (solid line), $E_A = -0.5t$ (dashed gray line). (c-e) Schematic representation of an eigenmode in the lower (c), upper (d) and middle (e) bands at k=0 (for $E_A = E_B = E_C = 0$). Filled circles indicate the relative phase ($\pm$) of the wave function on each site, while empty circles correspond to sites where the amplitude vanishes. Panel (e) is an example of a CLS in a flat band.

states, linear combinations of $|A(k)\rangle, |B(k)\rangle, |C(k)\rangle$, delocalized over the whole lattice. We note them $|\psi(k)\rangle = a_k|A(k)\rangle + b_k|B(k)\rangle + c_k|C(k)\rangle$. Due to the positive couplings, the eigenstates with minimum energy are those with the same phase on each site within the unit cell, i.e. with a_k, b_k, c_k of the same sign. The lower band eigenstates thus have all sites in phase, as depicted in Fig. 5.5(c). On the contrary, the eigenstates with maximum energy, the upper band eigenstates, have all sites out of phase with their nearest neighbor. This corresponds to alternating signs for a_k, b_k, c_k, see Fig. 5.5(d). Following this line of thought, the eigenstates for the middle band should be constructed with a site out of phase with its next nearest neighbor within the unit cell. This implies opposite phase on A and C. But in this case, there is no natural choice for the phase of site B: this is precisely a situation of phase frustration on this site (Fig. 5.5(e)). The result is a destructive interference on site B. Depending on the parameters of the lattice, the destructive interference

can be complete, and the wave function amplitude on B is exactly zero. Due to the geometry of the lattice, with the sublattice formed by sites A, C connected only via the B sublattice, zero amplitude on B implies that tunneling to the next unit cell can be completely suppressed. In other words, it is possible to build eigenstates which have non-zero amplitude only on a finite number of sites, in strong contrast with usual Bloch waves. Such states are called compacted localized states (CLS), or plaquettes. The CLS of minimal size $|f_n\rangle$, centered on site n, is represented in Fig. 5.5(e). It extends over 2 unit cells. The flat band eigenspace is the subspace generated by $\{|f_n\rangle\}_n$, the family of CLS centered on each unit cell, which all have the same energy. Note that this implies that the extended Bloch eigenstates of $\hat{\mathcal{H}}(k)$ can be expressed as a linear combinations of CLS. The degeneracy of the flat band is equal to the number of unit cells in the lattice N.

To understand in quantitative ways the condition for the existence of the flat band, let us first consider the simple case of equal couplings $t = t'$, and on-site energies $E_A = E_B = E_C = 0$. In this case, the analytical diagonalization of $\hat{\mathcal{H}}(k)$ gives the eigenenergies $E(k) = 0$; $\pm t\sqrt{3 + 2\cos(ka)}$, corresponding to the three bands plotted in Fig. 5.5(b), solid lines. We seek localized eigenstates of $\hat{H}$ with energy 0. This corresponds to solving the linear system of equations for the wave function amplitudes a_n, b_n, c_n on sites A, B, C:

$$0 = -tb_n \tag{5.4a}$$

$$0 = -ta_n - tc_n - tc_{n+1} \tag{5.4b}$$

$$0 = -tb_n \tag{5.4c}$$

In particular, this confirms, in accordance with our qualitative discussion, that the flat band eigenstates have zero amplitude on B, due to the phase frustration. Note that since $\hat{\mathcal{H}}(k)$ has 0 as eigenenergy, its determinant is 0. The rank of $\hat{\mathcal{H}}(k)$ is thus lower than 3, explaining the two identical equations in (5.4). More importantly, the CLS of minimal size is then:

$$|f_n\rangle = \frac{1}{\sqrt{3}} \left(-|A_{n-1}\rangle + |C_n\rangle - |A_n\rangle \right) \tag{5.5}$$

depicted in Fig. 5.5(e), as discussed earlier. Note the finite overlap between CLS centered on neighboring cells, $|f_n\rangle$ and $|f_{n+1}\rangle$: the CLS form a non-orthogonal basis of the flat band subspace.

Generalization to $t \neq t'$ preserves the existence of the flat band at $E = 0$. Indeed, the determinant of $\hat{\mathcal{H}}(k)$ is still 0: its first and third column are directly proportional, for any k (this can also be interpreted in terms of preserved chiral symmetry, so the band structure is still symmetric [225]). The CLS have modified relative weight on A, C sites: $|f_n\rangle = |C_n\rangle - t/t'(|A_{n-1}\rangle + |A_n\rangle)$ (with a global normalization factor omitted).

Taking now into account different on-site energies, the analytical diagonalization of $\hat{\mathcal{H}}(k)$ becomes delicate. We set $E_C = 0$ without loss of generality. We notice
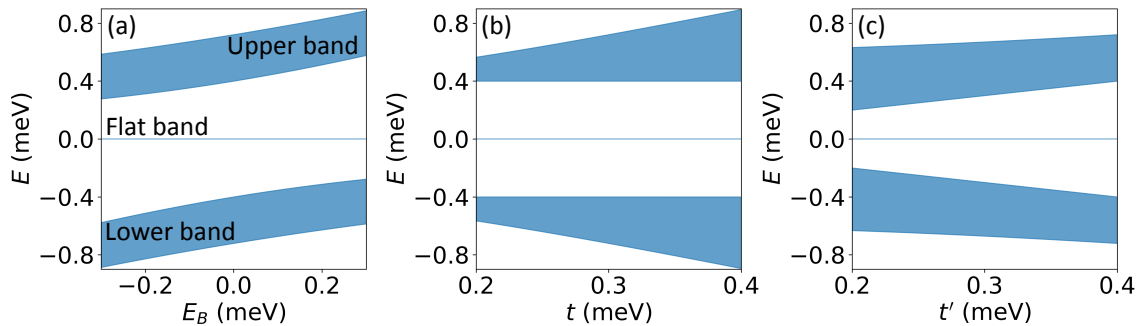
Figure 5.6: Spectral range of the bands as a function of (a) E_B, (b) t and (c) t'. The other parameters are fixed: (a) $t = 0.30$ meV, $t' = 0.30$ meV; (b) $E_B = 0$, $t' = 0.30$ meV; (c) $E_B = 0$, $t = 0.30$ meV. For all plots $E_A = E_C = 0$.

that if $E_A = 0$, we retrieve the proportionality between column 1 and 3 of $\hat{\mathcal{H}}(k)$, independently of k: the rank of the matrix is 2 and consequently, $\hat{\mathcal{H}}(k)$ has 0 as eigenvalue for all k. We have thus found the sufficient condition that $E_A = E_C$ for the existence of a flat band at energy E_C. It is simple to prove that this condition is also necessary.

In the case $E_A \neq E_C$, the middle band becomes dispersive, as shown in Fig. 5.5(b) for $E_A = -0.5t$ (dashed gray lines). The destructive interference on site B is not perfect, and the wave function amplitude on these sites is small but non-zero. We retrieve the Bloch states as the only eigenstates of the system.

To conclude our presentation of the tight-binding model, let us comment on the influence of the other parameters (namely E_B, t, t') on the band structure, when the middle band is flat. For $E_A = E_C = 0$, the lower and upper bands are given by $E(k) = E_B/2 \pm \sqrt{(E_B/2)^2 + t'^2 + t^2(2 + 2\cos(ka))}$. The evolution of the band structure when tuning one parameter only is then easily understood, as summarized in Fig. 5.6): the main effect of tuning E_B is to shift the position of the flat band relative to the other two bands. t controls the width of the lower and upper bands, but has no effect on the gap above and below the flat band. Finally, increasing t' increases the magnitude of gaps around the flat band, and has only little effect on the amplitude of the dispersive bands.

5.2.2 Engineering of the lattice parameters

As discussed in chapter 1, the implementation of a tight-binding model for polaritons is achieved by etching arrays of coupled pillars out of a planar cavity. Each pillar acts as a site of the tight-binding lattice, and the coupling arises from the overlap between neighboring pillars. For a tight-binding model with a single orbital per site, such as the one described in the previous section, we are then interested in the s-bands of the structure, i.e. the bands originating from the hybridization of the lowest energy mode confined in each micropillar. The different parameters from the theoretical
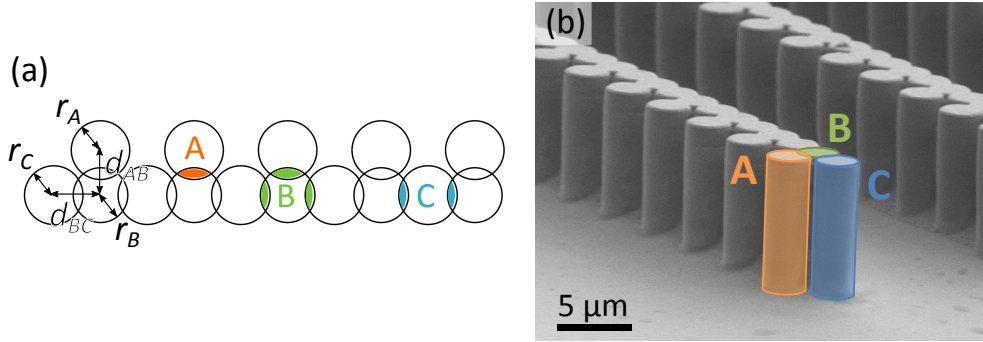
Figure 5.7: (a) Geometric configuration of the micropillars in a 1D Lieb lattice for polaritons. Colored regions indicate the overlap of A, B and C pillars with their respective neighbor, leading to reduced confinement of the mode within a pillar. (b) SEM image of the corresponding lattice, etched out of a planar cavity.

model can be tuned with careful design of the geometry of the structure: in a first approximation, the on-site energy is controlled by the pillar radius, and the coupling strength depends on the distance between neighboring pillars. However, we will see in the present section that these two knobs are not completely independent, and that the precise engineering procedure of the lattice geometry, in order to implement a target set of parameters, is more subtle.

One-dimensional Lieb lattices for polaritons were fabricated, using e-beam lithography to draw a mask of coupled pillars and then etching them out of the planar cavity, resulting in structures such as the one shown in Fig. 5.7(b). Note that similar structures were already fabricated for the work of Baboux *et al.* [223], but on a sample with 12 GaAs quantum wells, i.e. suited to the study of polariton condensation under non-resonant pumping (which requires strong Rabi splitting–with 12 QW, $\Omega_R = 15$ meV). Here, we use a sample dedicated to the study of resonantly injected polaritons fluids, leading to two major differences in sample structure. First, we use a sample embedding a single QW, in order to maximize polariton-polariton interactions. Second, we work with an InGaAs QW, to collect photoluminescence in transmission geometry. Due to the difference in samples, we had to fabricate new structures. The goal of the present section is to detail how these structures were designed.

It is important to realize that the condition $E_A = E_C$ necessary for the middle band to be flat is relatively fragile, due to our implementation of the tight-binding model with overlapping pillars. In particular, we can expect that taking equal diameters for A and C pillars does not result in effective on-site energies $E_A = E_C$. Contrary to the tight-binding approximation, in which the on-site energy is unaffected by couplings to neighboring sites, the confinement energy in a pillar (i.e. effective on-site energy) depends on its number of neighbors. Consider, e.g., pillars A and C: a pillar A has only one neighbor, while pillars C have two. For a fixed pillar diameter, the confinement is thus reduced in C with respect to A, as depicted

in Fig. 5.7(a). Consequently, for $r_A = r_C$ we expect $E_C < E_A$. Anticipating this, we fabricated several lattices, varying the diameter of pillar C for a fixed diameter for pillar A, in order to achieve $E_A = E_C$ and obtain a flat band (it turns out that in the work of Baboux *et al.*, a flat band was indeed observed for a lattice with $r_A = r_C$. We will comment on this specific point later in the discussion).

Aside from getting a flat band, we engineered the lattice parameters with a second objective in mind: we want to inject a nonlinear polariton fluid into the flat band. As we have seen in previous chapters, this requires pumping with a laser slightly blueshifted from the flat band, with a detuning typically equal to few times the polariton linewidth. We thus want to maximize the gap above the flat band to increase the range of laser detunings that can be used experimentally (if the laser energy is above the gap, states from the upper dispersive band might be excited rather than the desired flat band states).

To achieve $E_A = E_C$ and fulfill our primary goal, we varied $2r_C$ in the range [2.8 μm; 3.1 μm], and fixed $2r_A = 3.0$ μm. For the second objective, we choose B pillars with a slightly smaller diameter, $2r_B = 2.8$ μm, to increase effective E_B and shift the dispersive bands upwards with respect to the flat band (see Fig. 5.6(a)). Moreover, the distance between pillars A and B is set to $d_{A-B} = 2.3$ μm, while d_{B-C} is fixed to 2.4 μm. Each lattice consists in 40 unit cells.

We characterize optically the band structure of these lattices in the linear regime. A single lattice is excited non-resonantly tuning the laser energy around 1.6 eV. The momentum-space resolved emission for both linear polarizations, parallel (H) and orthogonal (V) to the chain, of three different structures is shown in Fig. 5.8. In each case, three bands are evidenced, arising from the hybridization of the s modes in each pillar.

These bands (dashed lines) are fitted with a tight-binding model, to which we added a next nearest neighbor coupling term t_{NNN} to $\hat{H}$, with unphysical negative values. Indeed, an important deviation from tight binding present in the experiment is the nonorthogonality of orbitals on neighboring sites, i.e. here between s states in neighboring pillars. It is in particular responsible for the asymmetry between the lower and upper bands, visible e.g. in Fig. 5.8(c). As originally explained in Ref. [226], to the first oder, the effect of nonorthogonality on the relation dispersion can be taken into account by the introduction of a next nearest neighbor coupling term to the Hamiltonian. However, this does absolutely not correspond to a physical hopping of polaritons from a pillar to its next nearest neighbor.

The value of the fitting parameters is summarized in Fig. 5.8. Note that for the upper band, the band folding expected from the tight-binding fit is not observed in the experiment. This is due to another deviation from our model: the mixing between the s-and p-bands (p modes are the second lowest energy confined modes in the pillars). This mixing cannot be captured by our tight-binding model, that considers only a single s orbital per site. Inclusion of p orbitals in the model is possible, but beyond the scope of the present study.

Let us first focus on the dispersions measured in H polarization. When r_C

Pol. H ↔

Pol. V ↕
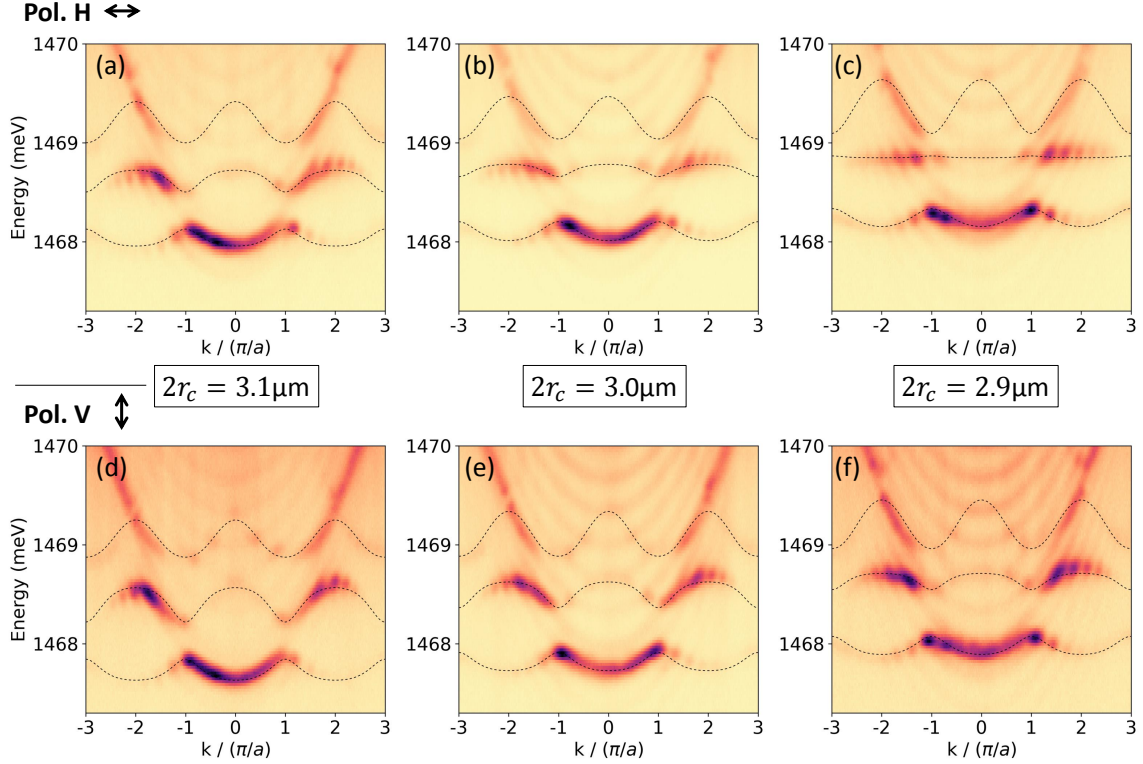
Figure 5.8: Momentum-space resolved photoluminescence of three distinct 1D Lieb lattices, for H and V polarizations. The three chains differ by the diameter of pillar C: (a,d) $2r_C = 3.1$ μm, (b,e) $2r_C = 3.0$ μm and (c,f) $2r_C = 2.9$ μm. Dotted lines are fits obtained with the tight-binding model. The faint intensity modulation arises from multiple reflections between the bottom mirror and the polished back side of the substrate.

	Pol. H			Pol. V		
$2r_C$ (μm)	3,1	3,0	2,9	3,1	3,0	2,9
E_A	1468,85	1468,87	1468,88	1468,74	1468,76	1468,81
E_B	1468,39	1468,46	1468,63	1468,10	1468,17	1468,34
E_C	1468,62	1468,75	1468,92	1468,35	1468,50	1468,66
t	0,31	0,30	0,32	0,34	0,34	0,33
t'	0,33	0,34	0,34	0,34	0,32	0,33
t_{NNN}	-0,06	-0,05	-0,04	-0,06	-0,07	-0,06

Figure 5.9: Parameters of the tight-bing Hamiltonian used to fit the dispersion from Fig. 5.8. A next nearest neighbor term t_{NNN} is added to take into account deviations from the tight-binding approximation.

is reduced, starting from 3.1 μm down to 2.9 μm, the width of the middle band decreases, and finally the band is flat for $2r_C = 2.9$ μm (Fig. 5.8(a-c)). As seen in Fig. 5.9, in terms of parameters for the tight binding model extracted from the fits, the decrease of r_C is the cause for an increase of the on-site energy E_C. The band is flat when $E_A = E_C$. In accordance with our expectations, the latter does not happen for the lattice with $r_A = r_C$, but for $2r_c = 2.9$ μm, i.e. $r_C < r_A$.

Let us now compare the energy spectrum measured in H and V polarizations. Similar to Baboux *et al.*, we observe a strong difference between H and V polarized dispersions: in all the lattices shown in Fig. 5.8, the width of the middle band is significantly larger in polarization V than in H. For a given lattice, e.g. the one with $2r_C = 3.1$ μm, we can see from Fig. 5.9 that this difference in the measured dispersions is associated with a redshift of the on-site energy of each pillar (in V polarization, with respect to H), while the couplings remain roughly the same. The origin of this shift lies in the polarization dependence of the boundary conditions for the photonic modes in the pillars. Indeed, for an isotropic pillar, H and V polarized modes are degenerate. In the present situation, however, the overlap with neighboring pillars creates a local anisotropy. Because of the polarization-dependent boundary conditions, the anisotropy lifts the degeneracy and creates an energy splitting between H and V polarized modes. Moreover, pillars A, B and C have each a different geometry, i.e. different boundary conditions. Thus, the H-V splitting is different for the three types of pillars. This is indeed the case in the experiment: we extract from tight-binding fits a splitting of ~ 0.1 meV for A pillars, ~ 0.3 meV for B and ~ 0.25 meV for C pillars (Fig. 5.9). Note that these values are independent of r_C.

Finally, we point out that this polarization splitting may differ from sample to sample, in particular when changing the sample structure (number and composition of Bragg pairs and QWs). It can also depend on the cavity-exciton detuning. In the work of Baboux *et al.* for example, the polarization splitting was of opposite sign as here. This explains why a flat band was observed in a lattice with $r_A = r_C$ (in one polarization, the shift compensated the reduced confinement in pillars C). In particular, this implies that fabricating several lattices, i.e. tuning r_C, is necessary to achieve a flat band, since the polarization-dependent shift cannot be known before etching.

An important consequence of the splitting is that in the same chain, we get a perfectly flat band in H polarization, while in V the middle band is dispersive (for $2r_C = 2.9$ μm, Fig. 5.8(c,f)). We will later take advantage of this feature to compare the behavior of a nonlinear polariton fluid in a flat and a dispersive band, with identical disorder.

5.3 Injection of a nonlinear polariton fluid in the flat band

5.3.1 Resonant excitation of the flat band

To investigate the nonlinear dynamics of a polariton fluid in the flat band, we select a Lieb lattice of pillars which has dispersionless middle band : we work with the chain that has $2r_C = 2.9$ μm, in H polarization. The dispersion in both H and V polarizations is reproduced in Fig. 5.10. Note that in this sample, the exciton energy is 1473.8 meV. Taking into account the Rabi splitting $\Omega_R = 3.2$ meV, in the chosen lattice the photon-exciton detuning is -4.3 meV in the flat band, and the excitonic fraction $|x|^2 = 0.10$.

Polaritons are injected into the flat band using a resonant cw laser. As described in chapter 4, the detuning Δ between the excitation and the flat band controls the interaction energy of the injected polariton fluid. The laser is focused into a Gaussian-shaped elongated spot, of 40μm x 3μm FWHM, centered on the line of B, C pillars (Fig. 5.11(a)).

Additionally, the angle of incidence of the beam is of importance to address the flat band modes. This can be understood by studying the momentum-space resolved photoluminescence (PL) of the flat band modes. This pattern can be obtained by spectrally filtering the emission at the flat band energy. The (k_x, k_y) map of the emission is then reconstructed from spectra such as the one shown in Fig. 5.10 measured at different values of k_y. The result is presented in Fig. 5.11(b): the intensity is zero at the center of the BZ ($(k_x, k_y) = 0$), and is maximal at the BZ edges
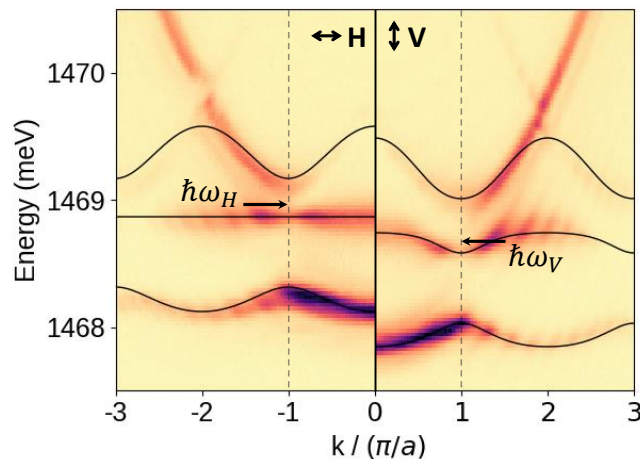
Figure 5.10: Energy-resolved far field photoluminescence, in H and V polarizations, of the Lieb chain of micropillars used for experiments involving resonant injection of polaritons into a flat band. Solid lines are the tight-binding fits. Arrows indicate the energy and wave vector of the resonant pump.
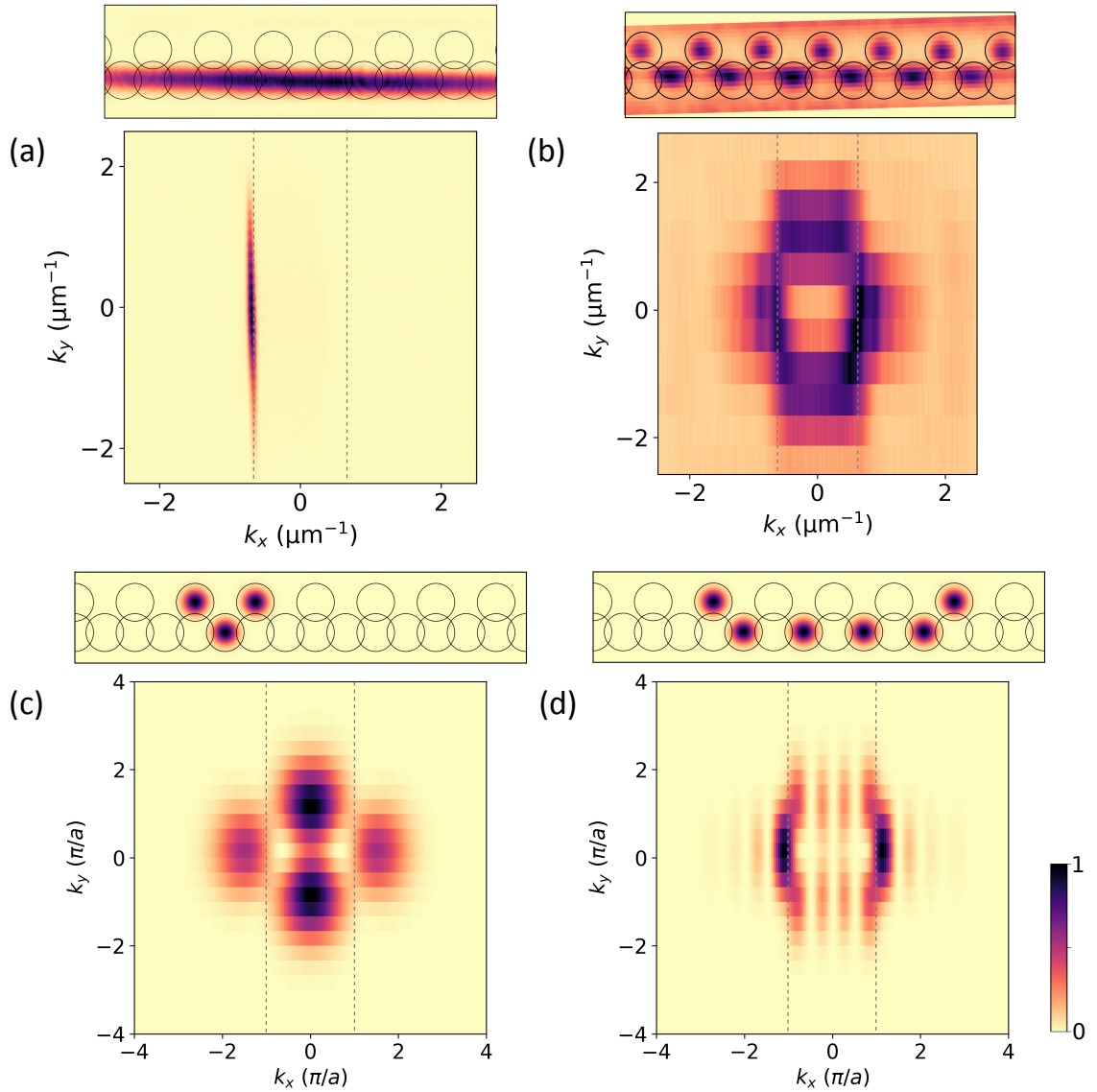
Figure 5.11: (a) Real- (top) and momentum-space (bottom) images of the laser spot used for resonant excitation. (b) Measured real- and momentum-space photoluminescence at the flat band energy. (c,d) Calculated real- and momentum-space emission pattern of two examples of flat band eigenstates: (c) a single CLS $|f_n\rangle$; and (d) a linear combination of four CLS with alternating sign on neighboring cells $\sum_{j=0}^{3}(-1)^j|f_{n+j}\rangle$. In all panels, dotted lines indicate the edges of the first Brillouin zone.

($k_x = \pi/a$). This reflects the antisymmetric nature of the flat band eigenmodes (opposite phase on A, C pillars). Thus, exciting the flat band at the BZ edge ensures efficient coupling to the polariton states in the flat band. In consequence, the pumping beam is tilted from normal incidence by an angle of $5.0°$ in the x direction (along the chain). In momentum space, this corresponds indeed to the edge of the first Brillouin zone (BZ) of the lattice, as shown in Fig. 5.11(a).

Note that the real-space photoluminescence at the energy of the flat band can also be obtained with a similar method (with spectral filtering of the real-space energy resolved PL). As expected due to geometric frustration, we measure vanishing intensity on sites B (Fig. 5.11(b), top).

Let us comment briefly on the consequence of exciting the flat band at the BZ edge. For a Bloch state with wave vector k at the BZ edge, i.e. $k = \pi/a$, there is a phase difference of exactly π between one unit cell and the next. In the case of the Lieb lattice, the middle band Bloch eigenstate at the BZ edge, obtained from the diagonalization of $\hat{\mathcal{H}}(k)$, is $|\psi(\pi/a)\rangle = |C(\pi/a)\rangle = 1/\sqrt{N} \sum_n (-1)^n |C_n\rangle$. In other words, only pillars C have a non-zero occupation. This state can easily be written in the basis of CLS: $|\psi(\pi/a)\rangle = 1/\sqrt{N} \sum_n (-1)^n |f_n\rangle$. It is nothing but the sum of CLS on neighboring unit cells, with a phase difference of π between them. The opposite sign on C sites in neighboring unit cells leads to a destructive interference also on A sites. Even though in the flat band the relevant eigenstates are not the Bloch states but the CLS, the coupling of the resonant laser at the BZ edge will be greater with modes that have a structure similar to the Bloch state $|C(\pi/a)\rangle$. For example, in Fig. 5.11(c,d) we have calculated the real- and momentum-space emission pattern of two different localized eigenstates: a single CLS $|f_n\rangle$ (as given by Eq. (5.5)), and a linear superposition of four CLSs, of same magnitude but alternating sign on neighboring sites, which can be written $\sum_{j=0}^{3} (-1)^j |f_{n+j}\rangle$. To compute these radiation patterns we have used a simplistic model to describe the eigenfunctions of the chain of pillars: we considered a Gaussian-shaped orbital per pillar (corresponding to the s mode). The orbital at each site was attributed the amplitude given by the eigenstates from the 0D model, resulting in a real-space wave function for the whole lattice. The momentum-space radiation pattern was simply obtained by Fourier transformation of this wave function. The state in Fig. 5.11(d), with a phase difference of π between neighboring CLS, corresponds exactly to the Bloch state $|C(\pi/a)\rangle$, but truncated to only 4 unit cells. As a consequence, the intensity of the radiation pattern in k space is maximal at the edge of the Brillouin zone, in contrast with the radiation pattern associated with the single CLS. With our excitation scheme, it is thus easier to excite states of the type of Fig. 5.11(d) rater than of Fig. 5.11(c), due to the bigger overlap with the pumping spot in momentum space.

Note that the experimentally measured k-space emission pattern from Fig. 5.11(b) is the sum of the emission pattern of all flat band eigenmodes. In particular, this is why it does not correspond perfectly to either Fig. 5.11(c) or (d). Nevertheless, the experimental ring-shaped pattern from Fig. 5.11(b) is closer to the

pattern in Fig. 5.11(d) than (c). This tends to indicate that the flat band eigenmodes are not single CLS, but are rather localized over a few unit cells. Since the localization length in the flat band is strongly influenced by disorder, this gives a first information on disorder in the lattice (thorough investigation of disorder and its role is the topic of a later section).

5.3.2   Nonlinear regime

We now investigate the dynamics of the polariton fluid in the flat band in the nonlinear regime. The energy of the resonant laser is set to $\hbar\omega_H = 1468.99$ meV, i.e detuned from the flat band by $\Delta = 60$ μeV, which corresponds to one fifth of the gap width separating the flat band from the upper dispersive band. Figure 5.12(a) presents the measured total emitted intensity when scanning the excitation power P up and down. A complex evolution is observed with several consecutive abrupt jumps. Moreover, the jumps in the upward and downward scans occur for different excitation powers such that a clear hysteretic behavior is observed. To understand the origin of the observed features, we investigate the spatial pattern of the emission. Fig. 5.12(c-g) show the spatially resolved emission for different excitation powers, indicated by the arrows in Fig. 5.12(a). We first point out that in all cases, pillars B are completely dark: the destructive interference due to geometric frustration in the linear regime survives in the nonlinear regime. In the following, we disregard pillars B.

For $P = 7$ mW, above the lowest power intensity jump, Fig. 5.12(c) evidences the formation of a 4 unit cell (u.c.) nonlinear domain. It is located around the center of the excitation spot and its shape does not evolve when P is further increased, up to a power of 10 mW, where the next jump is reached. We then observe the formation of a larger nonlinear domain with 10 u.c. Actually, in both scans up and down, all jumps correspond to an evolution of the domain size by a discrete number of unit cells. This is shown in Fig. 5.13(e), where we have plotted the integrated intensity profile versus pumping power in the up scan. The profile at a given power was obtained by integrating the intensity on pillars A and C (see for example Fig. 5.13(a-d)). We also plot the size of the nonlinear domains in Fig. 5.13(f). Note that the size of the domains is well defined because their edges are extremely sharp: the emission intensity drops by more than an order of magnitude over one unit cell on each side.

Due to the hysteretic behavior mentioned above, several patterns can be observed at a given pump power, for example at P = 11 mW where both patterns in Fig. 5.12(d) and (g) are stable: this is an evidence of bistability of the patterns. In fact, each abrupt jump event is associated with an hysteresis cycle. To evidence this we repeat the power scans but with different sweep histories. For example, starting from the lowest power, we ramp the power up, and immediately after the jump at $P = 10$ mW we ramp the power down. Repeating similar procedure at various abrupt jumps allows to explore the different stable branches. Fig. 5.14(a) shows the measured total intensity resulting from these various scans. It evidences
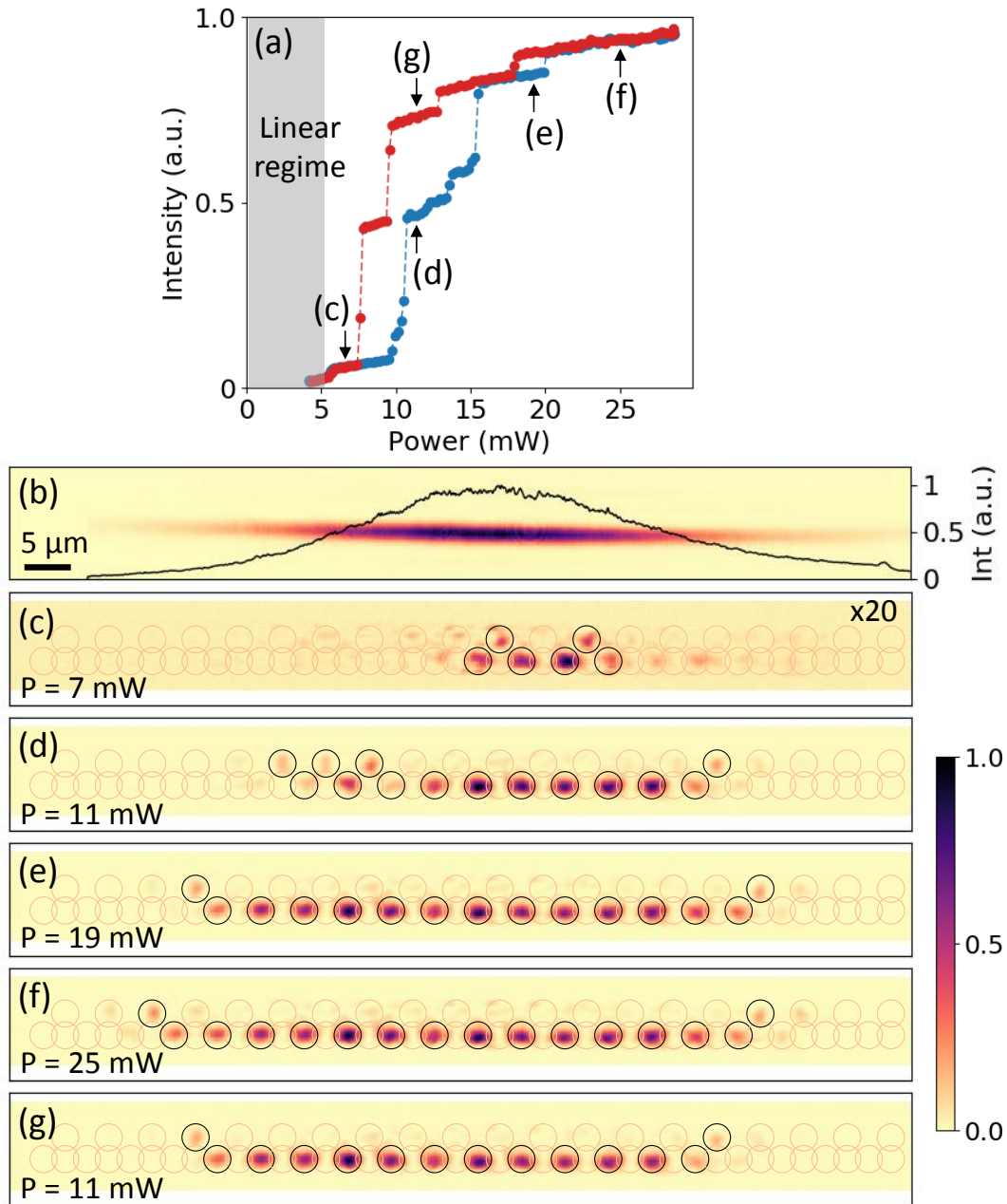
Figure 5.12: Nonlinear regime in the flat band, measured with a H polarized pumping laser at energy $\hbar\omega_H$, as indicated in Fig. 5.10. (a) Total emission intensity from the lattice, measured as a function of resonant pumping power. Blue (resp. red) dots are measured under increasing (decreasing) pumping power. (b) Real-space resolved image of the excitation spot. Black line is the spot profile, integrated over the transverse direction. (c-g) Real-space resolved emission from the chain, measured at the pumping powers indicated in (a). The position of micropillars is indicated by circles. Black circles are a guide for the eye, denoting pillars for which intensity is higher than an arbitrary threshold.
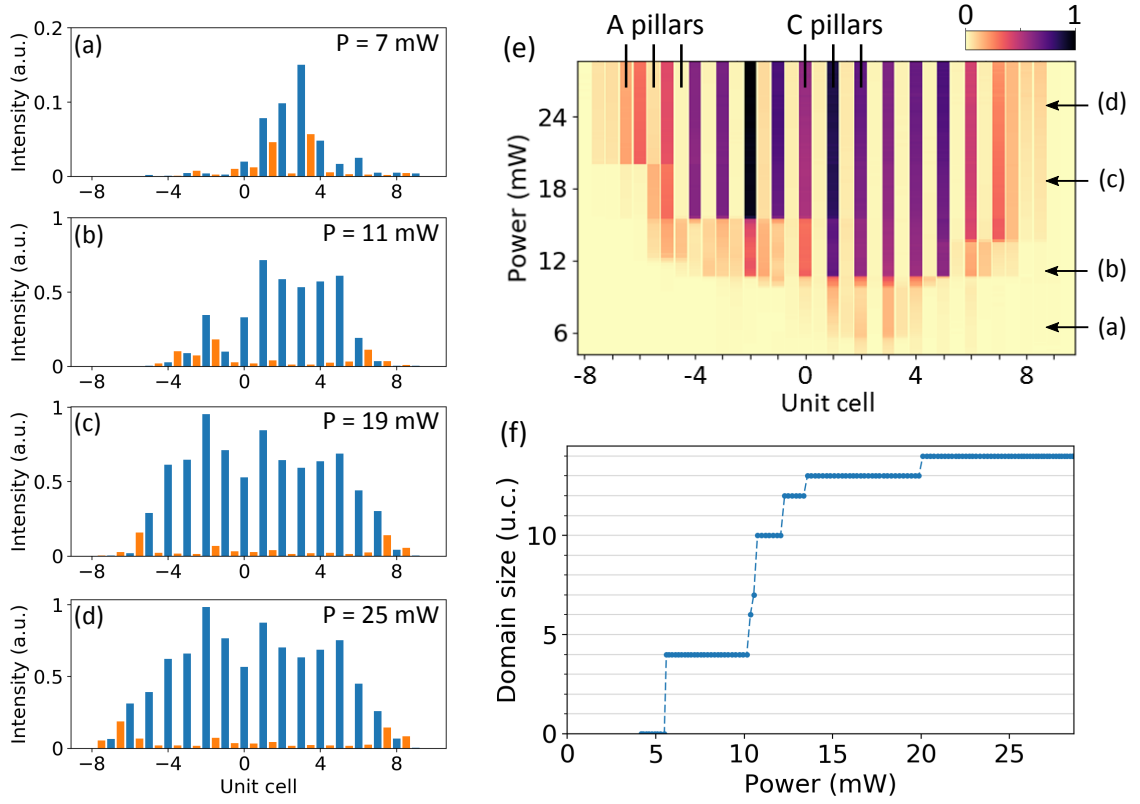
Figure 5.13: (a-d) Intensity profiles, integrated on pillars A (orange bars) and C (blue), corresponding to the images in Fig. 5.12(d-f). (e) Intensity profile versus pump power in the upward power scan of Fig. 5.12. The arrows indicate the profiles corresponding to panels (a-d). (f) Size of the nonlinear domain versus power, deduced from (e).
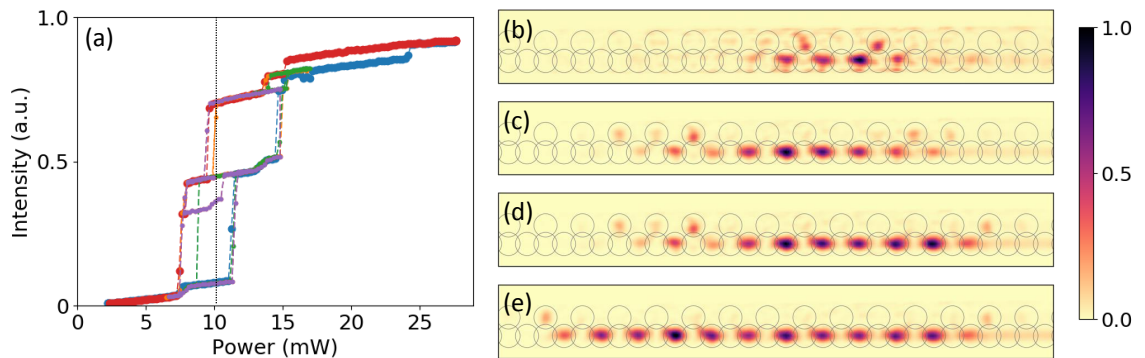
Figure 5.14: (a) Total emission intensity from the lattice, measured as a function of resonant pumping power. Each plot color corresponds to a different power scan history. (b-d) Real-space image of the four stable states at $P = 10$ mW

Figure 5.15: Measurement of the phase of the wave function in the nonlinear regime. (Top) Real-space image of the emission from the lattice. (bottom) Corresponding normalized interference pattern, obtained by superposition with a constant-phase reference beam.

the coexistence of multiple stable branches, e.g. four branches at $P = 10$ mW, which correspond to the four emission patterns shown in Fig. 5.14(b-e). We thus demonstrate multistability of the nonlinear domains when resonantly driving the flat band.

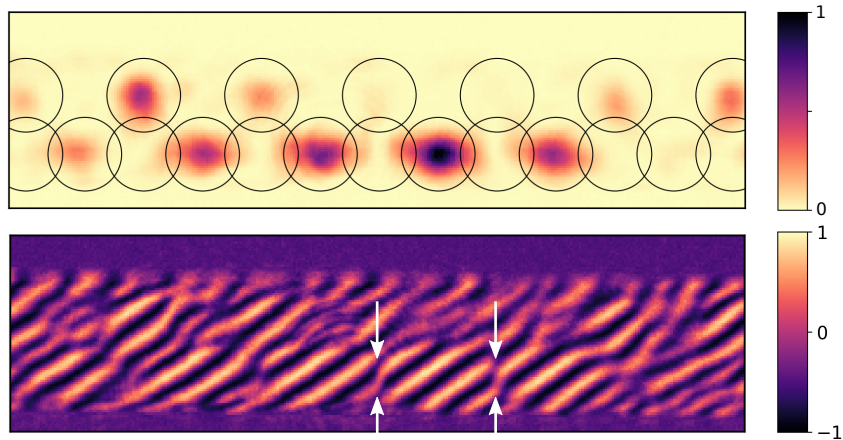Finally, we underline the fact that in each of the nonlinear domains, a broad spatial region is present where pillars A are completely dark. As discussed in the previous section, this is inherited from the linear regime, where the pumping at the BZ edge imposes a phase difference of π between neighboring unit cells, leading to a destructive interference on sites A. We verify that the latter argument still holds in the nonlinear regime: we measure the phase of the polariton fluid in the lattice, by means of interferometric techniques. Fig. 5.15(b) shows the normalized interference pattern obtained by overlapping the pumping laser beam, which serves as a constant-phase reference beam, to the real space emission from the chain of pillars (same method as discussed in chapter 4, see Fig. 4.12). In cells with a dark A site, a discontinuity in the fringes is clearly visible between neighboring C pillars, as indicated by the white arrows. This corresponds indeed to a phase jump of π between the two C sites.

5.3.3 Comparison with a dispersive band

To emphasize the specificity of the physics of a nonlinear polariton fluid injected in a flat band, we compare the previously described features with the behavior of a fluid injected in a dispersive band. We take advantage of the polarization dependence of the band structure of our chain of micropillars: pumping the chain with a V polarized beam enables the excitation of the now dispersive middle band, while keeping all
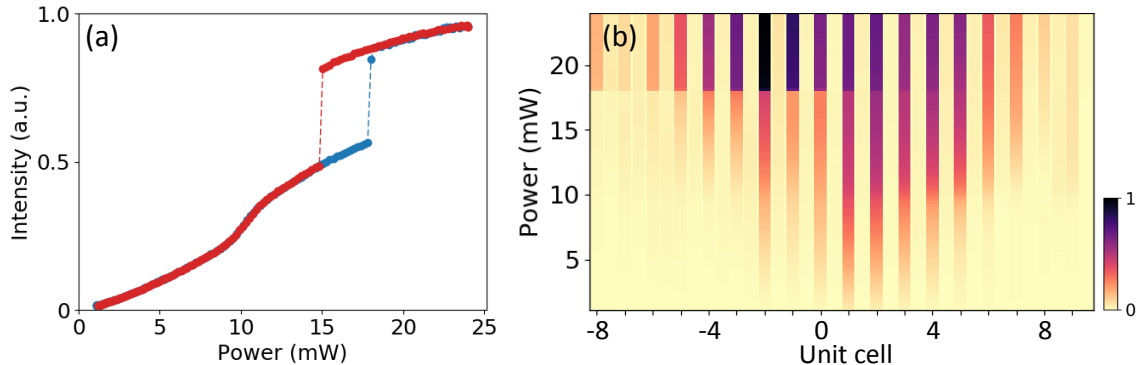
Figure 5.16: Nonlinear regime in the dispersive middle band, measured with a V polarized pumping laser at energy $\hbar\omega_V$ (a) Total emission intensity from the lattice, measured as a function of resonant pumping power. Blue (resp. red) dots are measured under increasing (decreasing) pumping power. (b) Intensity profile, extracted on pillars A and C, versus pump power in the upward power scan.

other excitation conditions identical (see Fig. 5.10). Additionally, this guarantees the same disorder configuration in the two cases. Note that in V polarization, the curvature of the middle band at the BZ edge corresponds to a positive effective mass, avoiding complications which could arise in a band with negative effective mass.

In Fig. 5.16 we present the results for the nonlinear regime. We use the same detuning $\Delta = 60$ µeV with respect to the bottom of the band as in Fig. 5.12, working on the same portion of the lattice. A much simpler behavior as in the flat band is observed: first a nonlinear increase in the total emitted intensity is observed at $P = 10$ mW, followed by a jump at $P = 17$ mW in the upward scan, with an associated bistability range. Additionally, the integrated intensity profile shows that the intensity evolves smoothly along the lattice, so no clear domain edge can be defined.

In Fig. 5.17, we compare the spatial profile in the dispersive and flat band, for the same P. Fig. 5.17(b,d) presents the integrated intensity profile corresponding to the spatial profiles in panels (a,c), considering only C pillars. For the dispersive band, we can fit an exponential decay corresponding to a propagation distance of 13.6 µm (2.8 u.c.) for the fluid. In contrast, in the flat band, the abrupt end of the nonlinear domain is very clear, with more than two orders of magnitude decrease in pillar intensity over two unit cells, yielding a propagation distance of only 2.1 µm (0.4 u.c.).

5.3.4 Gross-Pitaevskii equation for the Lieb lattice

We now perform numerical simulations to reproduce and explain the experimental observations described above. We use the tight-binding formalism to model a lattice with N unit cells ($3N$ sites in total). We introduce a discrete version of the driven-
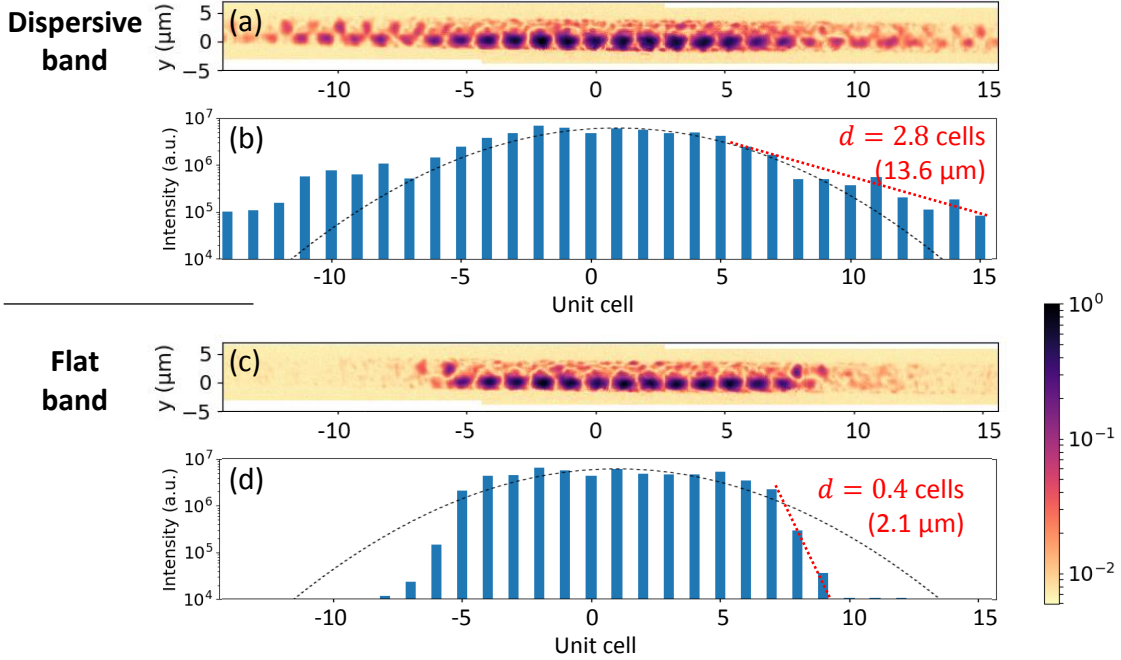
Figure 5.17: (a,c) Spatially resolved emission for $P = 19$ mW, $\Delta = 60$ μeV, in logarithmic color scale, for (a) the dispersive middle band (pol. V) and (c) the flat band (pol. H). The corresponding intensity profiles integrated on pillars C are shown in (b,d). The dotted line indicates the shape of the pumping spot.

dissipative Gross-Pitaevskii equation (GPE), to describe the time evolution of the wave function $|\psi(\tau)\rangle$. Basically, this correspond to replacing the kinetic energy term $\hbar^2\nabla^2/2m$ in the continuous GPE used in previous chapters, with the couplings given by the Lieb Hamiltonian $\hat{H}$ from Eq. (5.1) (this is easily understood since this kinetic term describes the unitary evolution of the wave function, as does the Hamiltonian in a tight-binding model). In the frame rotating at the drive frequency ω, the time evolution of the wave function $|\psi(\tau)\rangle$ is described by a set of $3N$ coupled nonlinear equations for the wave function amplitudes $a_n(\tau), b_n(\tau), c_n(\tau)$:

$$i\hbar\frac{da_n}{d\tau} = \left(E_A - \hbar\omega + \hbar g|a_n|^2 - i\frac{\hbar\gamma}{2}\right)a_n - t'b_n + iF_n^A \tag{5.6a}$$

$$i\hbar\frac{db_n}{d\tau} = \left(E_B - \hbar\omega + \hbar g|b_n|^2 - i\frac{\hbar\gamma}{2}\right)b_n - t'a_n - t(c_n + c_{n+1}) + iF_n^B \tag{5.6b}$$

$$i\hbar\frac{dc_n}{d\tau} = \left(E_C - \hbar\omega + \hbar g|c_n|^2 - i\frac{\hbar\gamma}{2}\right)c_n - t(b_n + b_{n-1}) + iF_n^C \tag{5.6c}$$

where we have considered implicit time dependence for a_n, b_n, c_n. In the above equations, $\hbar g$ is the polariton-polariton interaction energy and γ the polariton decay rate. The drive is described by vector $\boldsymbol{F} = (..., F_n^A, F_n^B, F_n^C, ...)$. We use a Gaussian
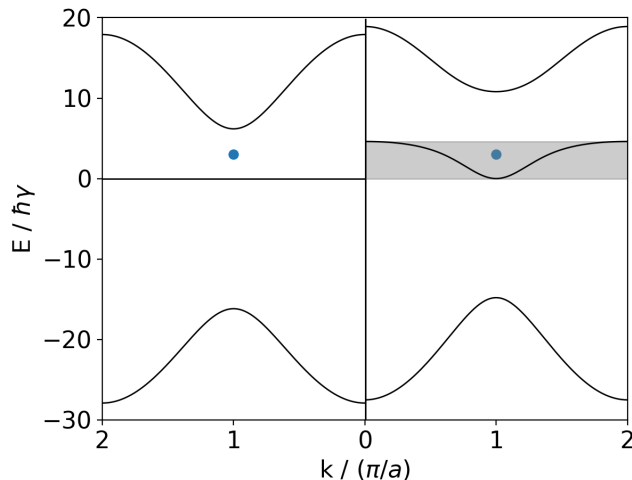
Figure 5.18: Dispersion relations calculated from the parameters used in the numerical simulations, for $E_A = 0$ (left) and $E_A = 6\hbar\gamma$ (right). The dot indicates the drive energy Δ and wave vector used in Fig. 5.20. The shaded gray region is a guide for the eye, indicating the total spectral width of the middle dispersive band.

spot of width σ and wave vector k_p, such that:

$$F_n^l = F e^{-(x_n^l)^2/4\sigma^2} e^{-ik_p x_n^l} \tag{5.7}$$

where F is real and describes the drive amplitude, and x_n^l is the spatial coordinate of site l in the nth unit cell, along the lattice direction: $x_n^{A,B} = na + a/2$ and $x_n^C = na$ (note that with the above definition, σ is the Gaussian width of the drive intensity $|F_n^l|^2$). Note also that $|\psi\rangle$ is not a normalized wave function; in fact $|a_n|^2$ gives the number of polaritons on site A_n (and similar for B, C of course). In the following, we use either the term population or occupation per site to describe this quantity.

It is convenient to introduce the drive detuning $\Delta = \hbar\omega - E_C$. We notice from Eq. (5.3) that the eigenenergy of the middle band at the BZ edge is always E_C, whatever the value of the other parameters (and in particular, whether the band is flat or not). Thus, this definition of Δ indeed corresponds to the detuning of the drive energy from the middle band at $k = \pi/a$. In the following we take site C as the reference energy, i.e. $E_C = 0$, so we can simply identify $\hbar\omega$ with Δ in Eqs. (5.6).

In the following, we solve for the steady-state of Eqs. (5.6) using parameter values extracted from the experiment: we take $\hbar\gamma = 30$ µeV, obtained from the measured linewidth in Fig. 5.26. Considering an exciton-exciton interaction strength $\hbar g_{exc} = 30$ µeV.µm^2 [46] and excitonic fraction $|x|^2 = 0.10$, we get a polariton-polariton interaction $\hbar g = |x|^4 \hbar g_{exc}/\mathcal{A} = 0.04$ µeV for a pillar with area $\mathcal{A} = 7.0$ µm^2 (corresponding to radius 1.5 µm). The spot width is $\sigma = 3.0$ unit cells, and the wave vector $k_p = \pi/a$. We consider a chain with 40 unit cells. Finally, the on-site energies and couplings are extracted from the fits to the dispersion in Fig.5.10

141

(see also Fig. 5.9): we use $t = t' = 0.3$ meV, $E_B = -0.3$ meV. To model the experiments in H polarization (flat band), we take $E_A = 0$, and $E_A = 0.18$ meV for the experiments in polarization V (dispersive middle band). The corresponding band structures are represented in Fig. 5.18.

5.3.5   Numerical simulations

First, we address the power scan in the flat band. Choosing $E_A = 0$ and $\Delta = 3\hbar\omega$, we compute the steady-state of Eqs. (5.6) for different drive intensities F^2. The up and down power scans are obtained by increasing (decreasing) F^2 by small steps and letting the system evolve to its new steady-state. Figure 5.19(a) presents the calculated total population in the lattice $\langle\psi|\psi\rangle = \sum_{l,n} |l_n|^2$, in the up and down scans of the drive intensity. We observe qualitatively similar behavior as the one reported experimentally: a series of abrupt jumps, happening at different powers for the up and down scans, resulting in a clear hysteresis. Moreover, the spatial profiles at a given F, shown for example in Fig. 5.19(b,c), are characterized by a region with high occupation on sites A, C (while sites B remain dark), delimited by sharp edges where the occupation drops abruptly. Between each jump event, the size s of these nonlinear domain remains constant. A jump in the total population corresponds to a change of the domain size by exactly one unit cell, except for the biggest jump (at $F^2 = 120$ in the up scan) which marks the onset of the nonlinear regime. This is shown in Fig. 5.20(a), where we have plotted the steady-state occupation profile on sites C, for various values of F^2 in the up scan. Note that in all cases, the
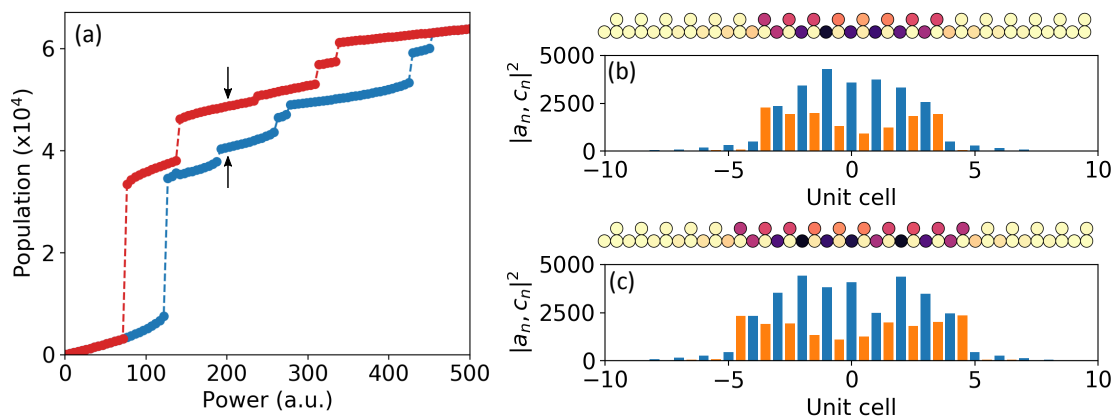
Figure 5.19: Numerical calculations of the polariton population in the nonlinear regime in a flat band, for $\Delta = 3\hbar\gamma$. (a) Total population in the lattice versus drive power, when increasing (blue dots) and decreasing (red) the drive power. (b,c) Bistable steady-state profiles in (b) the up scan and (c) the down scan, at the same power indicated by the arrows in (a). The population $|a_n|^2$ on sites A (resp. $|c_n|^2$ on sites C) is indicated by orange bars (blue).
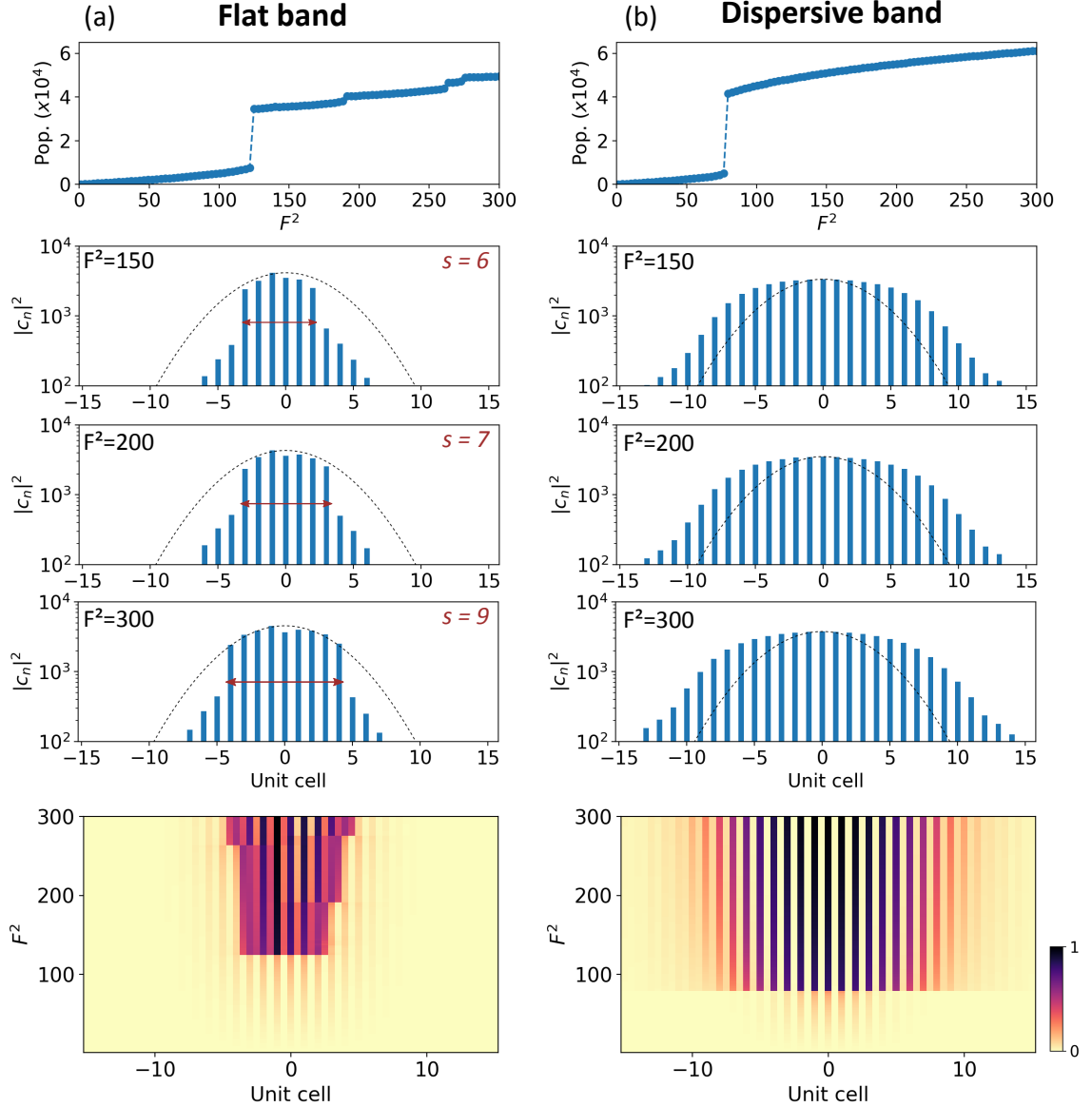
Figure 5.20: Comparison between the nonlinear regime in a flat (a) and a dispersive band (b), for $\Delta = 3\hbar\gamma$. Top: total population in the chain versus drive intensity F^2, scanning F^2 upwards. Middle: steady-state occupation $|c_n|^2$ on sites C at various drive intensities. The dashed line indicates the shape of the pumping spot. Bottom: occupation profile $|a_n|^2, |c_n|^2$ on sites A, C versus drive intensity.

occupation drops by approximately one order of magnitude at the domain edges, which are thus clearly defined. Additionally, we confirm that each jump in the scan of F^2 is associated with an hysteresis, giving rise to multistability (only bistability is explicitly demonstrated in Fig. 5.19 since we did not implement various scan histories to explore all the stable branches).

Note that the fact that each jump corresponds to domain size increase of exactly one unit cell is not in agreement with the experiment, where jumps of several unit cells at once are observed (see Fig. 5.13(f)). We explain this later in this chapter, by taking into account disorder in the numerical simulations.

Also, since we use a symmetric pumping spot, centered on a C site, we could expect symmetric profiles (i.e with an odd number of sites, and jump event happening at equal F^2 on each side of the spot), which is not what we obtain in the calculations (this is especially visible in Fig. 5.20(a), bottom row). We attribute the asymmetry to fluctuations introduced by numerical errors in the calculation.

Next, we repeat the numerical simulation of the power scan, but for $E_A = 6\hbar\gamma$, i.e. when the middle band is dispersive. The total population versus drive intensity, shown in Fig. 5.20(b) for the up scan, displays a single jump. It corresponds to the onset of the nonlinear regime, when the blueshift due to polariton-polariton interactions under the pump spot equals Δ. The spatial profile is shown for various values of F^2: the occupation diminishes smoothly towards the outside of the driving spot, contrary to the sharp edges observed in the flat band. In accordance with the experimental observations, the dispersive band behavior corresponds to the propagation of a nonlinear fluid in the lattice, on each side of the pumping spot. Such a propagation was discussed in details in Ref. [227], where the authors reported the propagation of nonlinear switching fronts away from a localized excitation spot in a planar cavity. In a flat band however, our results demonstrate that the propagation of the switching fronts is frozen: the kinetic energy of the polariton fluid is quenched. As a result, discrete nonlinear domains are formed.

As for the flat band, we also note a quantitative difference between the power scan in the dispersive band in the experiment (Fig. 5.18) and in the numerical simulation (Fig. 5.20(b)). In the experiment we observe a nonlinear increase before the abrupt jump, whereas only a single jump is present in the simulation. We show in the next section that this discrepancy is also solved by taking into account disorder.

We now investigate the influence of the interaction energy, which is directly set by Δ, by computing the power scan for different values of Δ. In particular, we want to know how the nonlinear domains build up when increasing the interaction energy. These scans are presented in Fig. 5.21. For the smallest value of the detuning considered, $\Delta = \hbar\Gamma$, a nonlinear increase of the total population is observed but no abrupt jump. Above the nonlinear increase, the occupation profile has no clear domain edges, even though the occupation drops rapidly. This regime is weakly nonlinear, interactions are too small to play a significant role (here the relevant energy scale is the polariton lifetime. In particular, note that $\Delta = \hbar\gamma$ is just above the minimal detuning for which bistability occurs, $\Delta > \sqrt{3/4}\hbar\gamma$). As Δ is increased
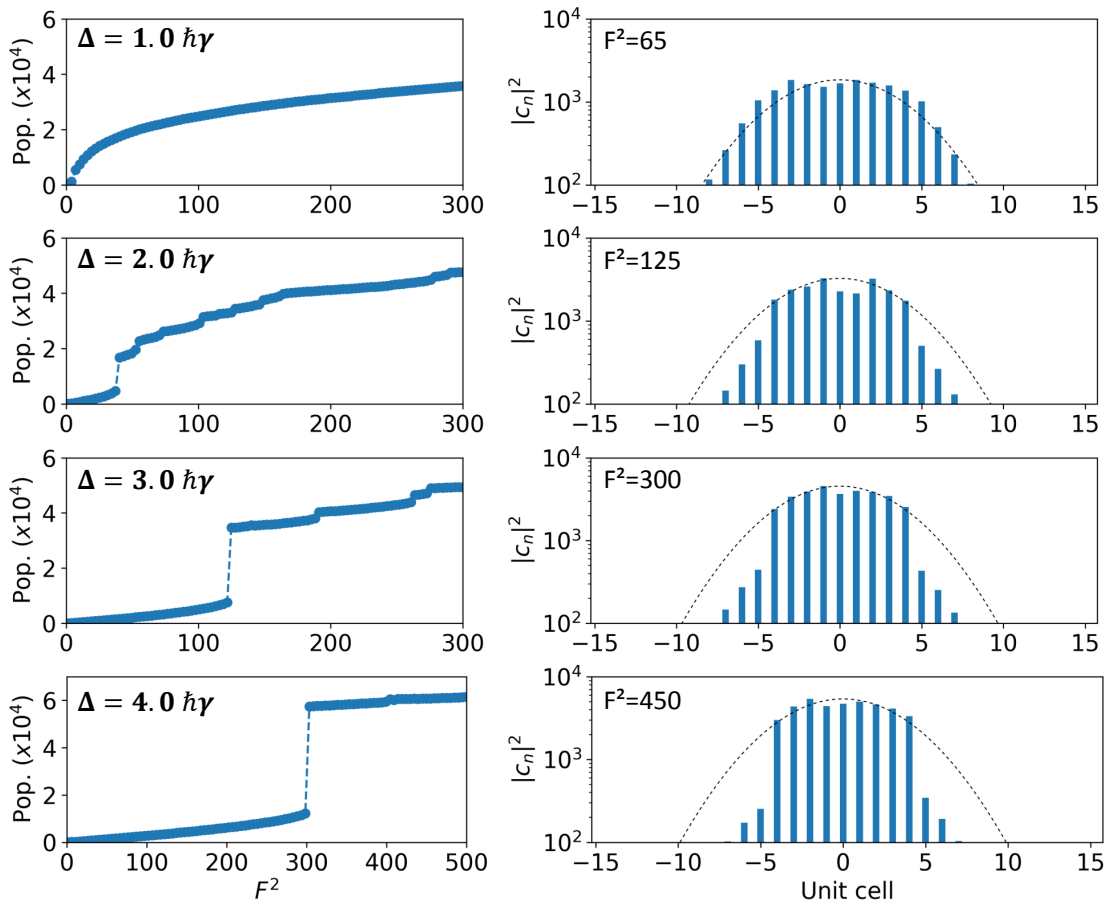
Figure 5.21: Influence of drive detuning Δ on the nonlinear regime in the flat band ($E_A = 0$). Left column: total population in the chain in an increasing drive intensity scan. Right column: corresponding steady-state occupation $|c_n|^2$ on sites C for a given value of F^2.
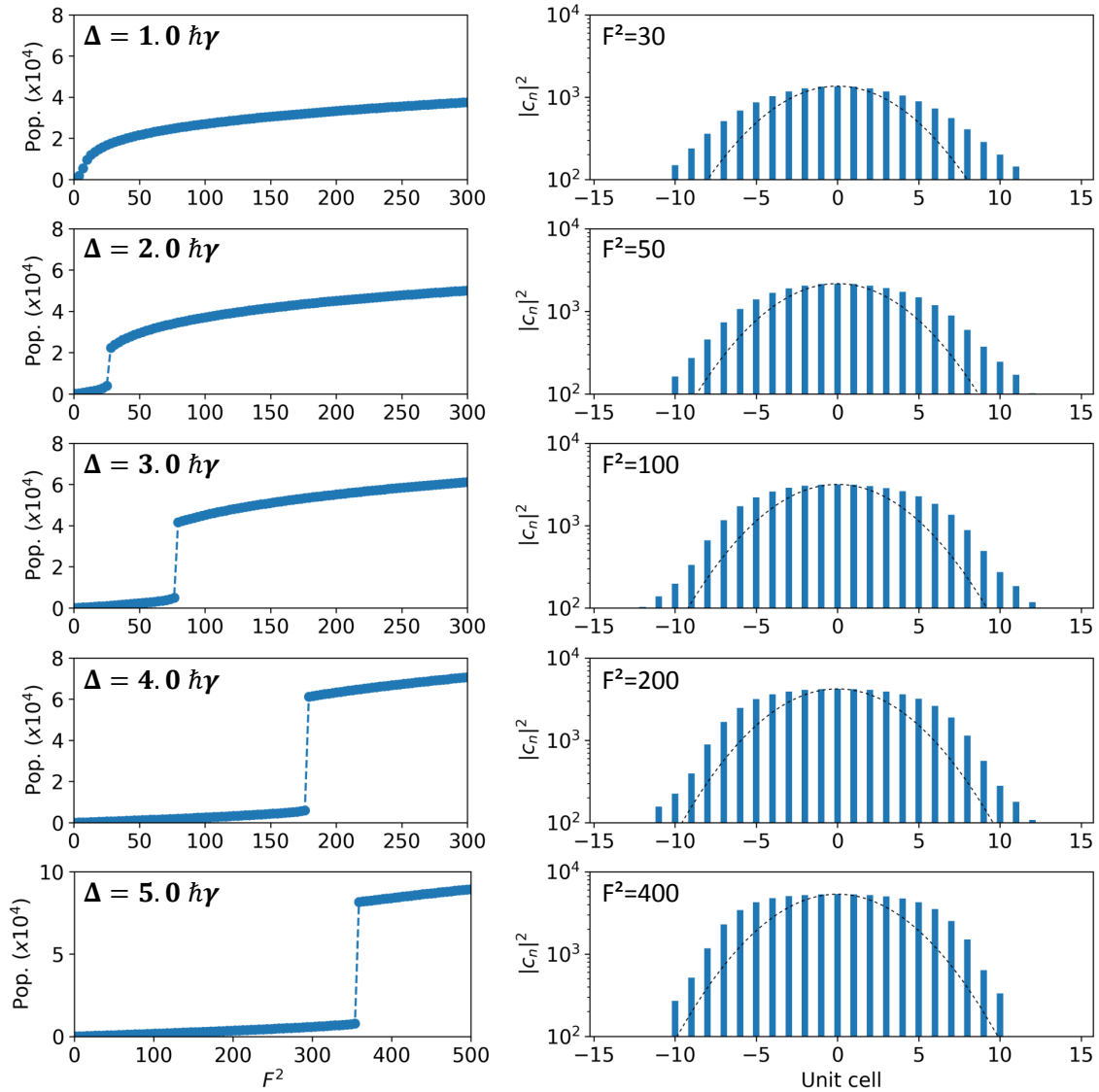
Figure 5.22: Influence of drive detuning Δ on the nonlinear regime in the dispersive band ($E_A = 6\hbar\gamma$). Left column: total population in the chain in an increasing drive intensity scan. Right column: corresponding steady-state occupation $|c_n|^2$ on sites C for a given value of F^2.

further into the gap above the flat band, abrupt jump events appear and become sharper with higher Δ. Correspondingly, the edges of the nonlinear domain are visible already at $\Delta = 2\hbar\gamma$ as a drop by a factor ≈ 5 in the occupation of sites C (at u.c. ± 5 for $F^2 = 125$ in Fig. 5.21). For $\Delta = 4\hbar\gamma$ the drop is increased to more than an order of magnitude.

In comparison, we study the influence of increasing Δ in the dispersive band. The different scans are presented in Fig. 5.22. As for the flat band case, for $\Delta = \hbar\gamma$ only a nonlinear increase is observed. For higher values of Δ, a sharp jump appears, which gets bigger with increasing Δ. As discussed previously, only a single jump is present in the up scan, and for $\Delta \leq 4\hbar\gamma$ the spatial profile demonstrates propagation of the nonlinear fluid. We comment on the profile with $\Delta = 5\hbar\gamma$ (for which the drive energy is in the gap above the middle band) a bit later.

5.3.6 Influence on the spot shape

We have underlined that the formation of nonlinear domains in the flat band is inherent to the absence of kinetic energy in such a system. An important consequence is that the Gaussian shape of the pumping spot has a strong influence on the precise size of the domain that forms in the nonlinear regime, as we demonstrate now.

Qualitatively, the dependence on the drive intensity of the domain size can be understood in terms of the CLS $|f_n\rangle$ discussed previously (Eq. (5.5)). There have been recent theoretical predictions that the linear CLS, and any linear superposition of them, are still eigenstates in the presence of interactions [203, 204]. However, these nonlinear CLS require precise shaping of the pump intensity and phase in order to be addressed with a resonant pump [228]. In the present situation, the Gaussian shape of the pumping spot does not allow for the observation of these states. Still, for a qualitative discussion on the domain formation we can consider them as a relevant basis to describe the nonlinear steady-states. As discussed in chapter 4 and for the dispersive band, the onset of the nonlinear regime for a single CLS happens when the polariton population is such that the interaction-induced blueshift equals Δ. This corresponds to a threshold value for the drive intensity F_{th}. But because of the absence of propagation, we can also consider a CLS on a given unit as independent from CLS on neighboring cells. Consequently, at a given F, the size of the domain is determined only by the number of unit cells for which the local drive intensity (determined by the Gaussian shape of the spot) is higher than F_{th}. As the power is ramped up, an abrupt increase in the domain size is observed whenever the drive intensity on the unit cell right outside the domain edge reaches this threshold value, and the domain size increases by one unit cell as one CLS is brought to the nonlinear regime.

This is of course a simplistic picture, in particular because neighboring CLS have a finite overlap and thus cannot be considered as independent. However, it gives a good intuition of how the domain size is affected by the spot shape. To confirm this, we repeat the numerical simulations for the power scan in the flat band, but
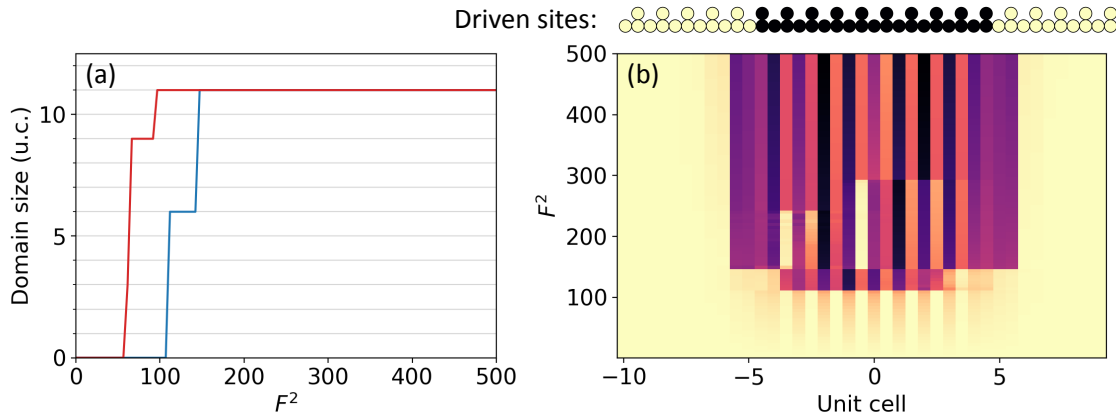
Figure 5.23: Numerical simulations of the nonlinear regime in a flat band pumped with a top hat spot. (a) Size of the nonlinear domain in the up (blue) and down (red) power scan. (b) Occupation profile on sites A, C versus drive intensity F^2, in the up scan. The image on top depicts the shape of the pumping spot (sites where $F_n^l \neq 0$ are in black).

this time using a top-hat spot. The drive amplitude F_n^l on a given site l_n is given by:

$$F_n^l = \begin{cases} Fe^{-ik_p x_n^l} & \text{if } |x_n^l| \leq w/2 \\ 0 & \text{otherwise} \end{cases} \tag{5.8}$$

where w is the width of the spot. We set $w = 9$ u.c. and take the same detuning $\Delta = 3\hbar\gamma$ as previously (and keep $k_p = \pi/a$).

The results are presented in Fig. 5.23, and confirm the picture discussed above: as seen in panel (a), in both the up and down scan, the size of the nonlinear domain shows two jumps close to the threshold for the nonlinear regime, but remains constant for the highest values of F^2. The evolution of the occupation on sites A, C shown in Fig. 5.23(b) confirms the sharp edges of the domain. With the top-hat spot profile, each site is either driven or undriven, so the size of the nonlinear domain is directly fixed by the spot width (even though all sites should jump together, at the same drive intensity). Here, the initial consecutive jumps in the up scan are attributed to the sensitivity to fluctuations around the threshold for the nonlinear regime (and similar for the down scan). Note also that the size of the domain is bigger than the spot size by one unit cell on each side. This is due to the overlap between the outer CLS and the pumping spot on the last site A of the driven region.

5.3.7 Interpretation of the domains as Truncated Bloch Waves

The nonlinear domains that form in the flat band can actually be classified as a specific form of gap solitons, namely Truncated Bloch Waves. To evidence this, we
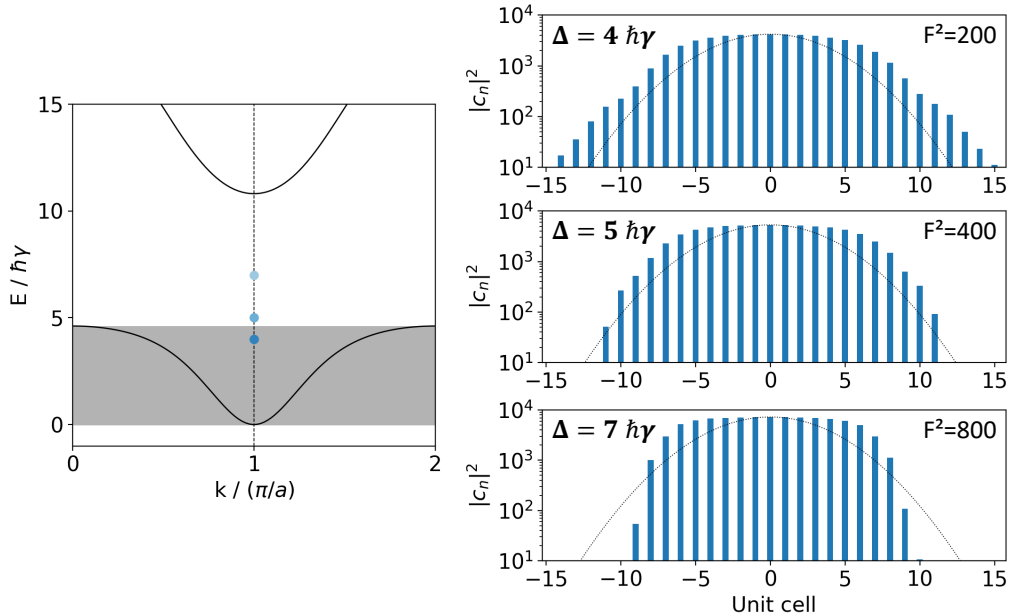
Figure 5.24: Left: zoom on the middle band and the gap above it, calculated for $E_A = 6\hbar\gamma$. The shaded gray region is a guide for the eye, indicating the total spectral width of the middle band. Blue dots indicate the drive energy and wave vector used in each of the right panels. Right: steady-state occupation $|c_n|^2$ on sites C for different values of Δ, in the nonlinear regime (for a value of F^2 indicated in each panel).

first investigate with numerical simulations the behavior of a nonlinear fluid injected in the gap above a dispersive band. Indeed, a significant difference between the flat and dispersive band is that for a flat band, for any finite detuning Δ, the drive energy is in the gap. We have seen that in comparison, in a dispersive band, for values of Δ smaller than the bandwidth there is propagation in the lattice. But what happens when Δ is larger than the bandwidth, i.e. when the drive energy is in the gap ?

Figure 5.24 presents the steady-state profiles calculated for $E_A = 6\hbar\gamma$, and different values of the drive energy: $\Delta = 4, 5$ and $7\hbar\gamma$, in the nonlinear regime. Note that for $E_A = 6\hbar\gamma$, the width of the middle band is $\sim 4.6\hbar\gamma$. For $\Delta = 4\hbar\gamma$, i.e. for a drive below the band edge, the propagation outside the spot is visible as an exponentially decaying polariton occupation. The slope of this decay depends on γ and on the group velocity $1/\hbar(\partial E/\partial k)$ at energy Δ. Increasing the drive energy to $\Delta = 5\hbar\gamma$, in the gap above the middle band, a sharp decrease in the occupation is now observed at u.c ±11. This is reminiscent of the flat band nonlinear domains. Here the propagation of particles is prevented because the drive injects polaritons with an energy within a gap: there is no single-particle state at this energy. The tunneling from a highly occupied site (where the energy is renormalized by interactions) to a neighboring site with low occupation is impossible. For $\Delta = 7\hbar\gamma$,

(a) **Theory**

(b) **TBW in atomic BEC**

(c) **TBW in nonlinear fibers**

(d) **TBW in temporal lattices**
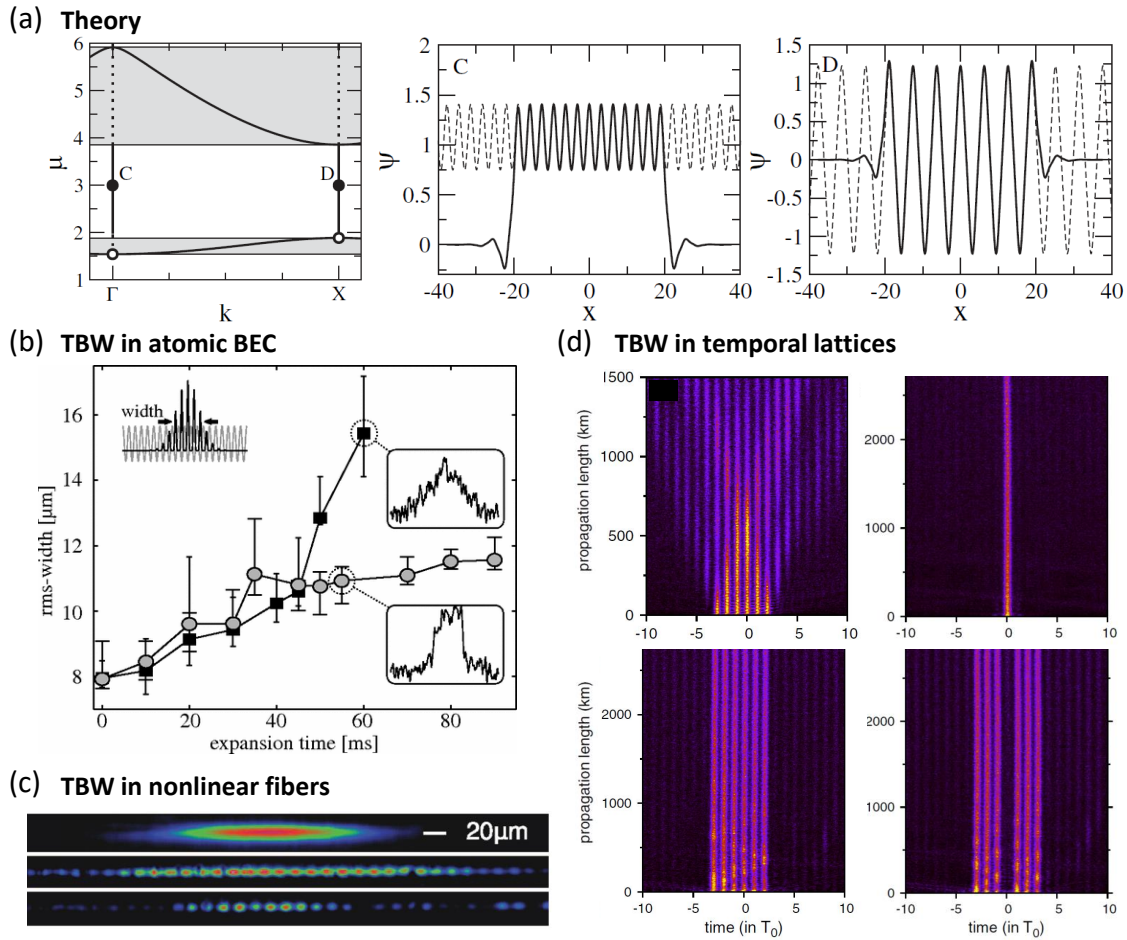
Figure 5.25: (a) Left: theoretical band-gap diagram of a 1D lattice showing bifurcation of nonlinear Bloch waves from the band edges. Solid circles correspond to the TBW shown in panels C,D. Dashed lines in C,D are the associated nonlinear extended Bloch waves. Images from [229]. (b) Observation of self-trapping in a BEC of cold atoms loaded in a deep periodic lattice. In contrast to the diffusive regime observed for a low initial number of atoms (black squares), repulsive atom-atom interactions lead to a stopping of the global expansion of the wave packet for a high initial atom number (gray circles). In this self-trapping regime, the wave packet develops steep edges (shown in the lower inset), i.e. a TBW is formed. Images from [230]. (c) Experimental observation of TBW in periodic arrays of optical waveguides with defocusing nonlinearity. (Top) Input beam profile, (middle) diffraction pattern in the linear regime at the output and (bottom) localization for high nonlinearities. Images from [231]. (d) Observation of TBW in a temporal lattice, using a recirculating fiber-loop setup. Top left: Linear evolution of a six-pulse sequence, in the absence of nonlinearity, resulting in a discrete diffraction pattern. Other panels: formation and stable propagation, in presence of nonlinearities, of (top right) a single gap soliton, (bottom left) a TBW with six peaks and (bottom right) a different TBW, with a defect at its center. Images from [232].

further into the gap, the renormalization caused by interactions is increased, and accordingly, the domain edge is even sharper.

This self-trapping localization mechanism arising from the interplay between interactions and the existence of an energy gap is precisely the one at play for so-called gap solitons [233, 234]. In particular, the existence of soliton clusters extending over few lattice sites was discussed from a theoretical standpoint a few years ago by the group of Kivshar [229, 235, 236]. These states were called Truncated Bloch Waves (TBW), as they correspond to nonlinear Bloch waves truncated to a few unit cells, as represented in Fig. 5.25(a). They bifurcate from the band edges. Their experimental observation was also reported in conservative systems such as cold atoms [230], arrays of coupled waveguides [231] or optical fiber loops [232]. These experimental results are summarized in Fig. 5.25(b-d).

From the above considerations, it follows that the nonlinear domains created in the flat band can also be classified as TBW: because the band width is zero, for any finite value of Δ the drive energy is in the gap. This facilitates their experimental observation, since it reduces the interaction energy required to the self-trapping mechanism. Our results thus demonstrate the generation of TBW in a driven-dissipative context. In particular, the drive and dissipation allow to generate such structures and control their size via the pumping power, and observe multistability of the different patterns.

5.4 Influence of disorder

5.4.1 Experimental disorder characterization

We already mentioned that disorder is an important element to take into account in a flat band. We also pointed out a discrepancy between the experiment and numerical simulation: the fact that in the simulation, the nonlinear domain size always increases by one unit cell only, whereas jumps of several cells are observed in the experiment. We suggested that disorder was responsible for such effects. In this section, we investigate the precise effect of disorder on the size and shape of the nonlinear domains.

First, we characterize the disorder present in our lattice. We can access partial information on this disorder with resonant spectroscopy of the flat band eigenstates, in the linear regime. To this end, we tune the laser in resonance with the flat band, and scan the energy across the band, using a very weak pumping power, well in the linear regime (typically $P \sim 10$ μeV). The results for the same portion of the chain as in Fig. 5.16 are presented in Fig 5.26. In particular, Fig. 5.26(a) shows the emission intensity on pillars A and C versus the resonant laser energy. When the laser is in resonance with an eigenstate, an intensity maximum is observed: this reveals that the energy of the flat band eigenstates changes slightly over few unit cells wide regions. Eigenstates are detected over a range of approx. 100 μeV. For example, Fig. 5.26(b) and (c) show the real-space emission for two different energies,
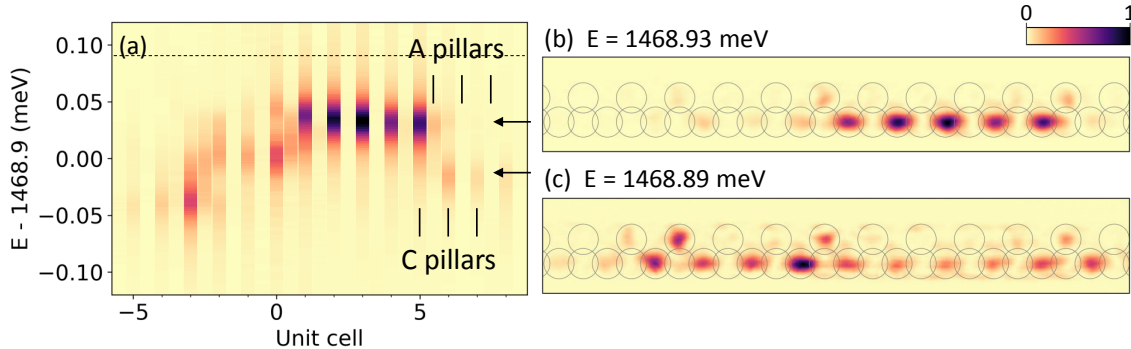
Figure 5.26: Measured intensity profile on pillars A, C as a function of resonant drive energy, in the linear regime ($P = 10$ mW). The dotted line indicates the drive energy $\hbar\omega_H$ used for the power scans in Fig. 5.12. (b,c) Real-space emission patterns measured for a drive energy indicated by the arrows in panel (a).

corresponding to two different eigenstates. In accordance with the results reported in Ref. [223], we find that disorder fragments the flat band into smaller domains.

We remind that since the k of the pump is at the BZ edge, it couples better to specific eigenmodes, which have high intensity at $k = \pi/a$ in their momentum-space radiation pattern. For this reason, note that the disorder characterization from Fig. 5.26 is only partial: it does not reveal all of the eigenstates (in particular, we miss the modes close to the single CLS, see Fig. 5.11 and the associated discussion).

To evidence the effect of disorder in the nonlinear regime, we now repeat the power scan on a different portion of the chain. The disorder landscape of this new portion is presented in Fig. 5.27(a). The power scan is carried out using similar Δ (precisely, with $\hbar\omega_H = 1468.94$ meV, as indicated by the dotted line on Fig. 5.27(a)). The results are presented in Fig. 5.27(b-d): the global features described previously are still present, namely the observation of a nonlinear domain of finite size, which increases by abrupt jumps as the power is ramped up. A hysteresis is also present when the power is ramped down. However, the precise shape and size of the pattern is significantly different from the scan in the first portion of the chain, reproduced in Fig. 5.27(e,f). Since the only difference between these two situations is the disorder landscape, these results suggest that disorder has a pinning effect for the edges of the nonlinear domain, influencing the exact domain size for a given power.

5.4.2 Modeling disorder

The above experimental observations have underlined the crucial role of disorder on the shape and size of the nonlinear domains. To confirm the pinning effect of disorder on the switching fronts (i.e. the domain edges), we perform numerical simulations that take disorder into account. We consider disorder on the on-site energies only, since disorder on the couplings does not fragment the flat band into eigenstates with different energies.
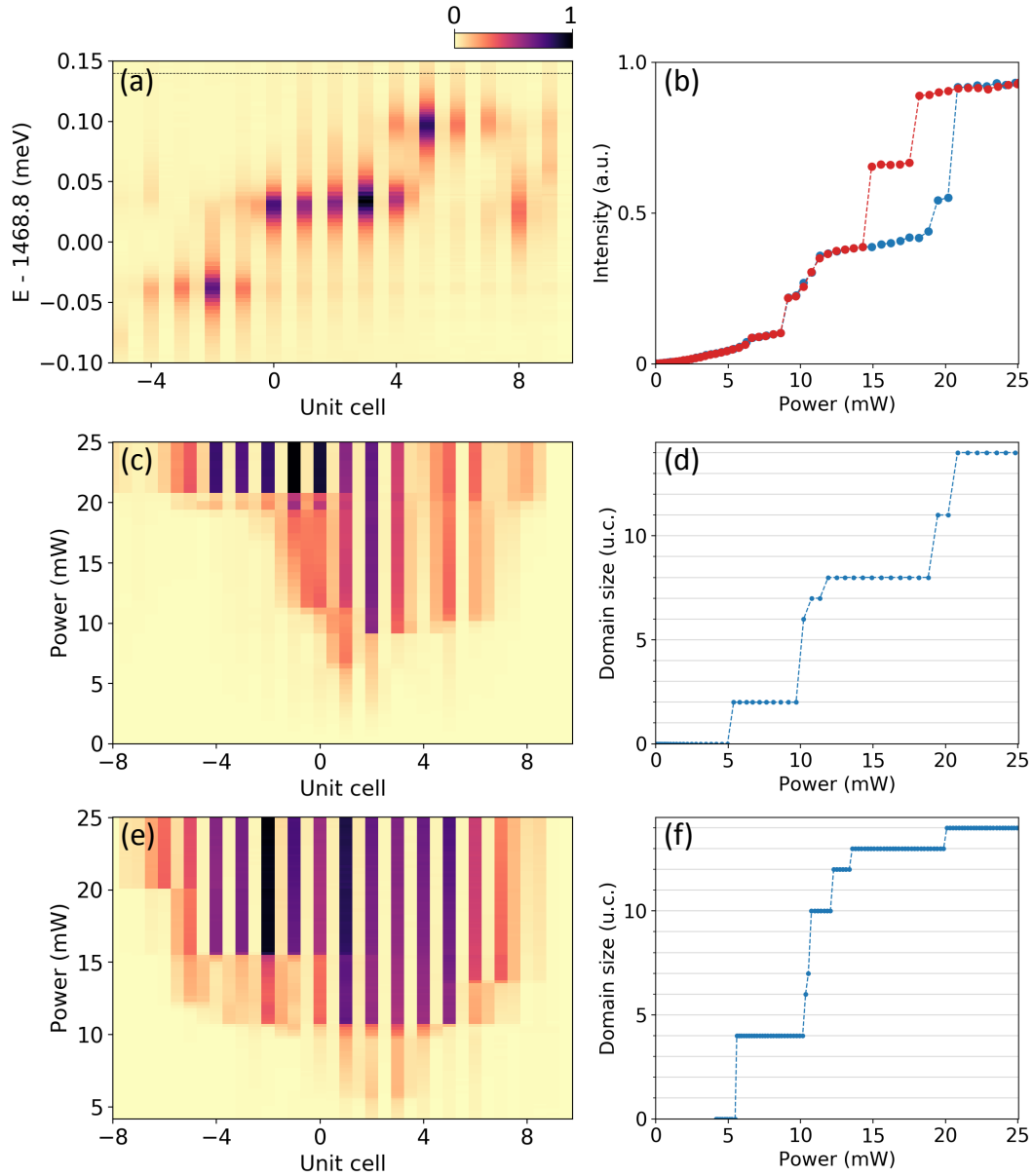
Figure 5.27: (a) Measured intensity profile on pillars A, C as a function of resonant drive energy, in the linear regime, on a different portion of the lattice than that studied in section 5.4 and Fig. 5.26. (b-d) Nonlinear regime in this portion. (b) Total emission intensity from the lattice, measured as a function of resonant pumping power, scanning the power up (blue dots) and down (red). (c) Integrated intensity profile versus pump power in the upward power scan and (d) corresponding size of the nonlinear domain. (e, f) Same as (c,d) but on the previous portion of the lattice (reproduced from Fig. 5.13).
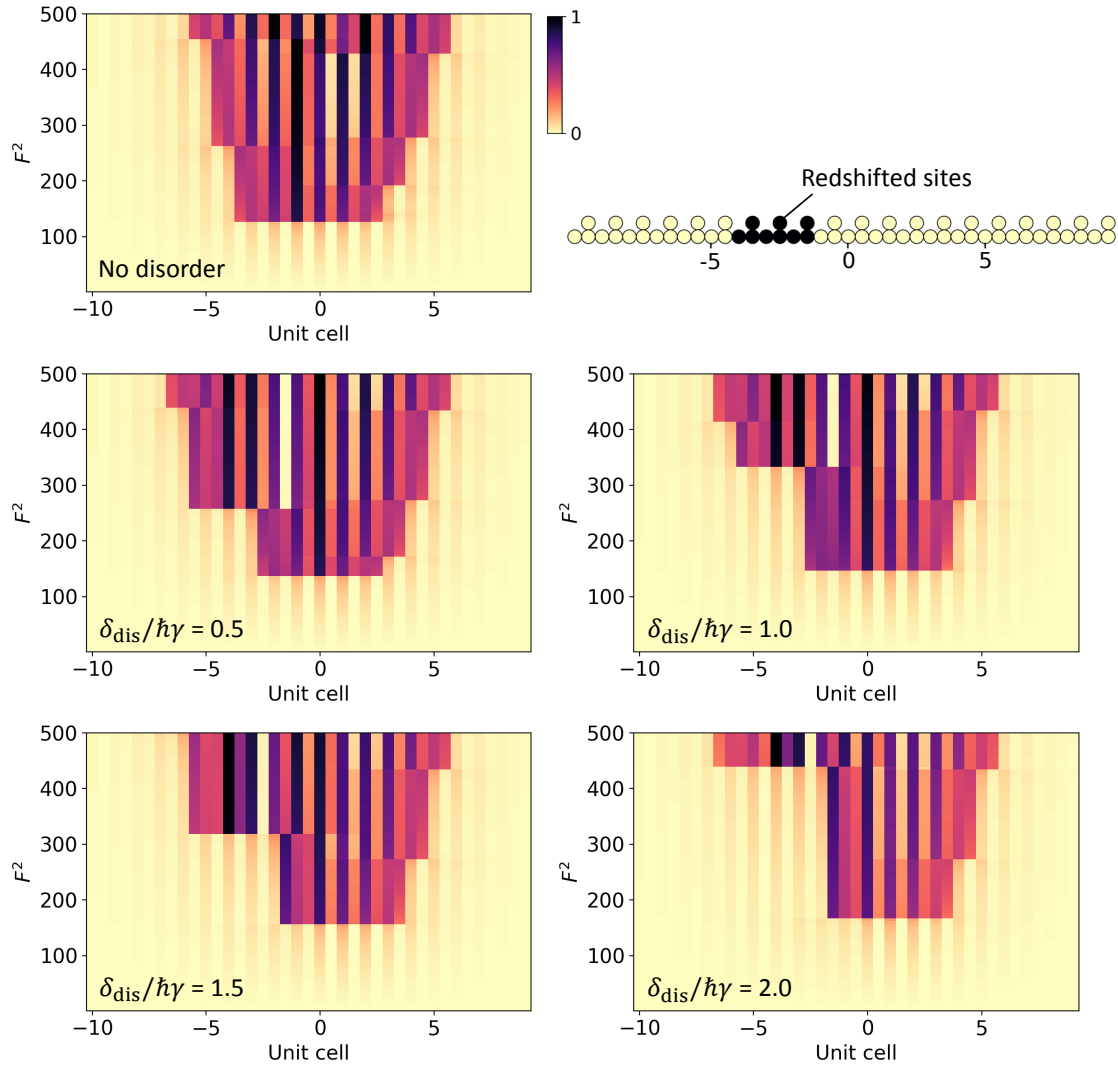
Figure 5.28: Influence of disorder in the nonlinear regime for the flat band. Occupation profile $|a_n^2, |c_n|^2$ on sites A, C versus drive intensity in the up scan, for different redshift amplitudes δ_{dis}, and $\Delta = 3\hbar\gamma$. The redshift is applied to sites indicated in black in the schematic representation of the lattice in the top right.
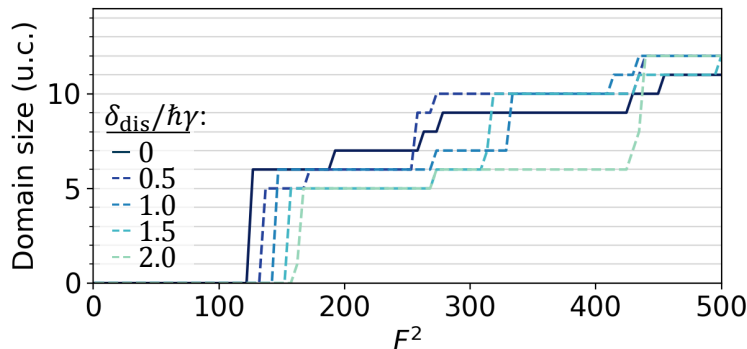
Figure 5.29: Size of the nonlinear domain versus drive intensity for the power scans presented in Fig. 5.28.

Even though we were able to perform a characterization of the disorder landscape in the lattice (Fig. 5.26), we have already pointed out that such a characterization was only partial due to the specific pump wave vector at the BZ edge. Moreover, even with a measurement giving complete access to the linear eigenstates, the deconvolution to reconstruct the precise on-site energy on each pillar would be a challenging task. We thus consider a simplified model for disorder in our numerical simulations: we add a redshift δ_{dis} on the sites of 3 unit cells. These cells are located to the left of the pumping spot, as depicted in Fig. 5.28. This creates locally similar redshifted eigenstates as the ones observed experimentally in Fig. 5.26 at position -3u.c.

Figure 5.28 presents the occupation on sites A, C in an increasing F^2 scan, computed for different values of δ_{dis} and $\Delta = 3\hbar\gamma$. The domain size versus drive intensity is extracted from all of these scans and plotted in Fig. 5.29. Recall that in the absence of disorder ($\delta_{\text{dis}} = 0$, solid line), the domain edge progresses by one unit cell at each jump. When disorder is included, e.g for $\delta_{\text{dis}} = 0.5\hbar\gamma$, a bigger jump from 6 to 9 u.c at $F^2 = 250$ is observed. For the spatial pattern, it corresponds to a progression of the domain edge through all disordered sites at once. For bigger disorder amplitude, even bigger jumps in the domain size are observed, at higher drive intensity. In other words, for increasing δ_{dis}, there is an increasing range of drive intensities F^2 for which the left domain edge is pinned at the position of the rightmost redshifted state (at u.c. -2). Note, on the other hand, that as we could expect, the evolution of the domain size on the right side of the spot, where no disorder was added, is only very little affected by the increase of δ_{dis}. From this we can conclude that the redshifted sites create a barrier for the polariton fluid, which has a strong pinning effect for the domain edges. We can understand this from our previous discussion on the formation of the nonlinear domains: on the redshifted sites, the effective detuning between the drive and flat band modes is bigger (by δ_{dis}). Thus, the threshold power corresponding to the onset of the nonlinear regime is increased on these sites. A higher drive intensity is required for the domain to extend on the redshifted sites, with respect to the other sites, resulting in the pinning effect described above.

155
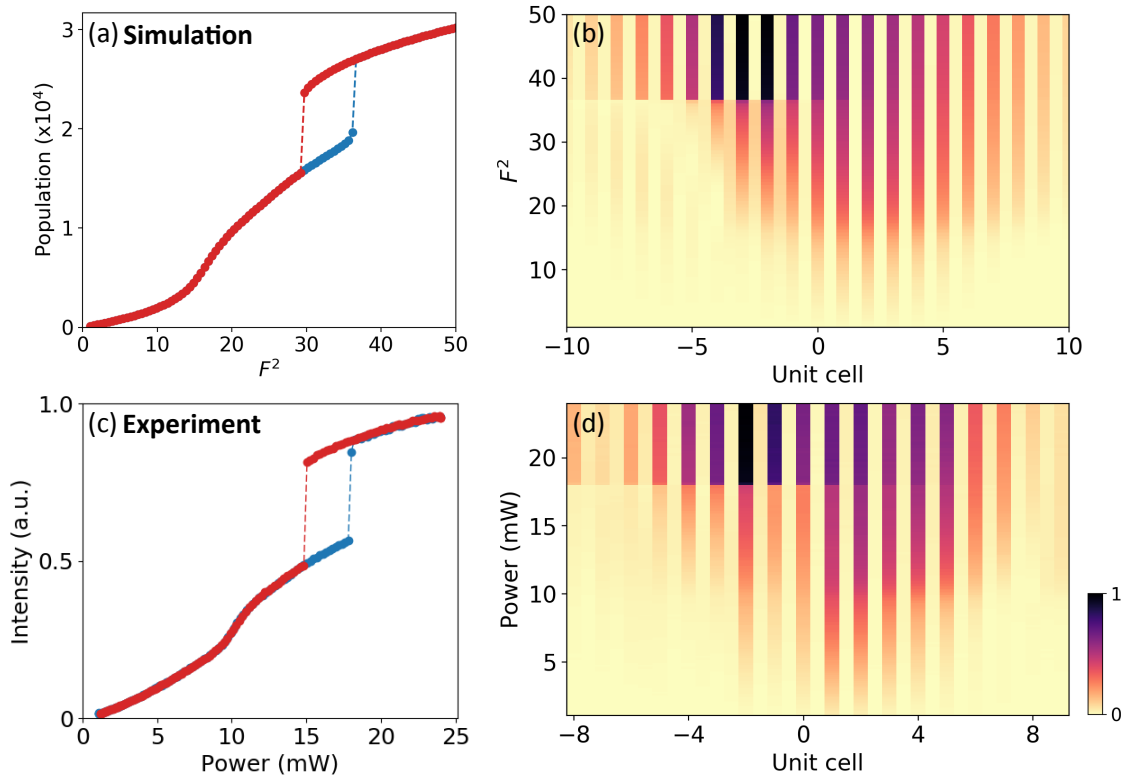
Figure 5.30: Influence of disorder in the nonlinear regime for the dispersive band. (a) Calculated total population in the lattice versus F^2, in the up (blue) and down (red) scan. (b) Occupation profile on sites A, C versus F^2 in the up scan. The redshift amplitude was $\delta_{\mathrm{dis}} = 2\hbar\gamma$ on the same sites as for the flat band, and $\Delta = 1.5\hbar\gamma$. (c,d) Comparison with the total emission intensity and intensity profile measured in the dispersive band (reproduced from Fig. 5.16.)

These simple simulations confirm the determinant influence of disorder on the precise size of the domain at a given F^2. In the experiment, the disorder landscape is certainly more complex, and complete deconvolution of the role of disorder is harder. However, if we were able to implement the experimental disorder configuration in the numerical simulations, we could expect to reproduce with high fidelity the evolution of the domain size versus power.

Finally, note that disorder also has an influence on the nonlinear regime in the dispersive band. This is due to the fact that the disorder amplitude in the experiment, on the order of 50 μeV, is comparable to the interaction and kinetic energy of the fluid with our choice of laser detuning $\Delta = 60$ μeV. In Fig. 5.30, we present the results of a numerical simulation taking disorder into account in the dispersive band: we have set $\delta_{\mathrm{dis}} = -2\gamma$, $\Delta = 1.5\hbar\gamma$ and $E_A = 6\hbar\gamma$. The total population versus drive intensity in the up and down scans, as well as the spatial occupation profile on sites A, C in the up scan are in excellent agreement with the experimental

results, reproduced in Fig. 5.30(c,d). In particular, the presence of disorder explains the first nonlinear increase in the total population before the abrupt jump (only one jump was observed in disorder free simulations, see e.g. Fig. 5.28). We point out that the effect of disorder is easier to capture in the dispersive band because the finite kinetic energy attenuates the impact of disorder on the fluid dynamics, allowing for a faithful reproduction of the experimental features in the numerical simulations.

5.5 Conclusion and perspectives

5.5.1 Excitation on a single site

All of the experiments discussed so far used an elongated excitation spot. We now present preliminary studies on excitation with a small spot, addressing a single pillar of the chain.

First, we point out that excitation with a long spot presents important limitations. To understand this, and see why single site excitation might be of interest, let us come back briefly to our discussion on disorder. We have underlined that in the nonlinear regime, the domain size at a given power is the result of a competition between disorder and interactions. In particular, we confirmed this with the introduction of a simple model for disorder in the numerical simulations. However, as we already mentioned, the experimental disorder landscape is more complicated, and even its characterization by resonant spectroscopy (as presented in Fig. 5.26) was only partial. But actually, it is possible to gain more information on disorder in the lattice, by changing the excitation conditions. As a first example, changing the pump central wave vector enables coupling to eigenmodes which have a different radiation pattern, such as the single CLS (see Fig. 5.11). Thus, we repeat the resonant spectroscopy of the flat band, with an elongated spot, but changing the angle of incidence of the pumping beam to normal incidence, such that the pump central wave vector is $k_p = 0$ (i.e. exciting at the BZ center). The result is presented in Fig. 5.31(b), whereas the previous characterization with $k_p = \pi/a$ on the same portion is reproduced in Fig. 5.31(a). The measurement with $k_p = 0$ reveals that the region between u.c -1 and +4 is fragmented by disorder, even though no disordered modes were visible in the scan with $k_p = \pi/a$. In other words, this illustrates the fact that using an elongated spot reduces the effective number of eigenmodes that we can couple to (due to the verify specific phase profile that the pump imposes). Opting for single-site excitation allows to relax this constraint, retrieving the full degeneracy of the flat band.

Note that single-site excitation provides yet another way to probe disorder. Figure 5.31(c,d) presents the resonant spectroscopy of the flat band using a small spot, i.e. with single-site excitation (still on the same portion of the chain). There, the spot was exciting a single pillar C, on two neighboring unit cells for the two scans. These measurements reveal all of the eigenstates that have a finite overlap with the
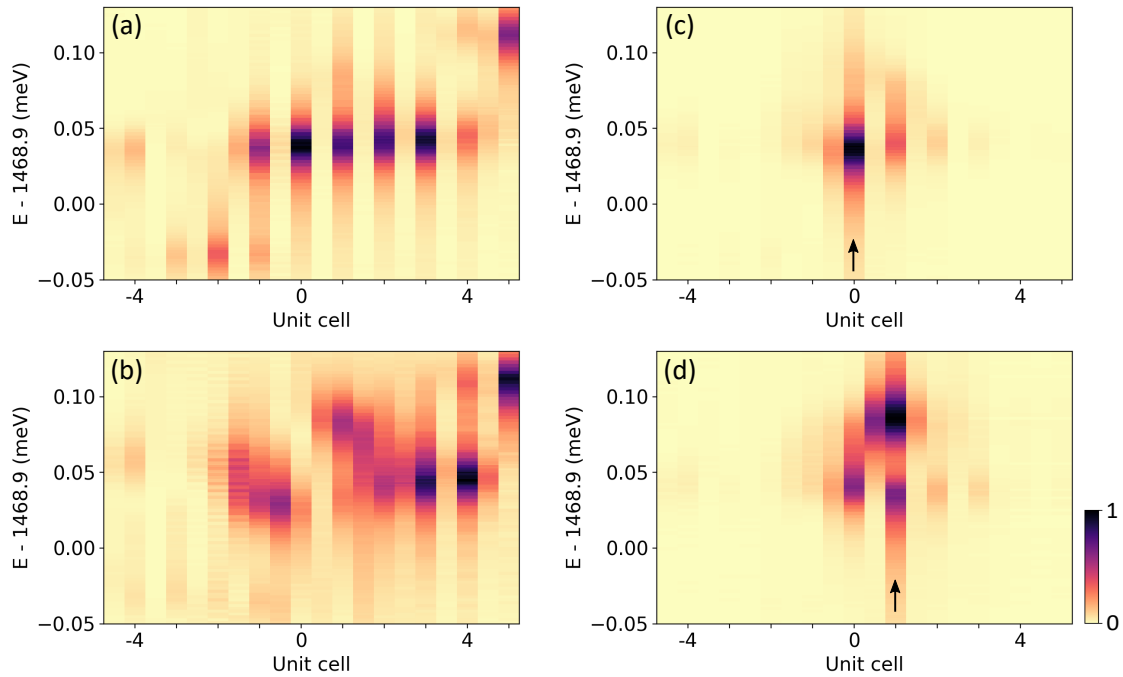
Figure 5.31: Disorder characterization of a single portion of the chain with different drive conditions. (a,b) Pumping with an elongated Gaussian spot, with central wave vector (c) at the BZ edge, $k_p = \pi/a$ and (d) at the BZ center, $k_p = 0$. (c,d) Pumping a single C site, indicated by the arrow.

excited site. In this sense they are complementary with the long spot measurements from Fig. 5.31(a,b) (they contain redundant information–a full disorder characterization could be obtained either by repeating the long spot resonant scan for all k or equivalently the small spot scan on all sites).

We repeat the power scan experiments with a laser slightly blueshifted from the flat band, but this time using single-site excitation. Figure 5.32 presents the results of multiple power scans, with different scanning histories, for a pumping beam focused on the pillar A indicated by the arrow in panel (b) (and with $\Delta = 120\mu$eV). The total intensity versus power in Fig. 5.32(a) shows multiple abrupt jumps and multistability. The real-space pattern corresponding to the three nonlinear branches in (a) are shown in Fig. 5.32(b-d). Similar to the long spot experiments, we observe the formation of localized nonlinear domains. The domain size changes by abrupt jumps, with an associated hysteresis for each jump. However, the multistability presented here has a very peculiar feature: starting from the steady-state in Fig. 5.32(c) with $P = 20$mW and decreasing the power, we observe at $P = 15$mW a jump which corresponds to an *increase* of the total intensity in the chain. This goes against the usual paradigm of increasing polariton population with increasing pumping power. We attribute this effect to the competition between disorder and interactions. Even though further investigation would be required, our interpretation is that the ef-
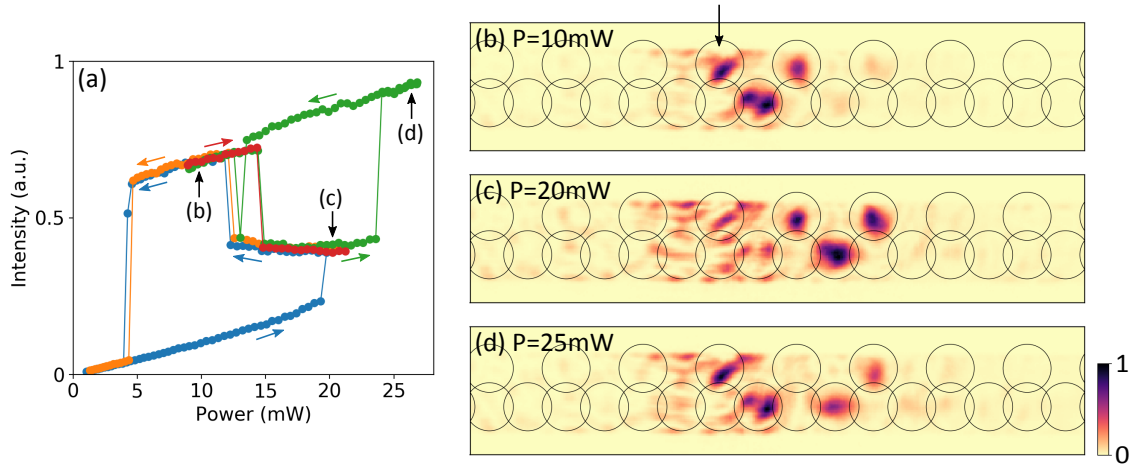
Figure 5.32: Evidence of multistability for single-site drive. (a) Total emission intensity versus power, for various sweep directions. Each color corresponds to a different scanning history, as indicated by the colored arrows. (b-d) Spatially-resolved emission corresponding to the powers and branches indicated by black arrows in (a). The arrow in (b) indicates the driven site.

fective detuning and overlap with the drive is different for each of the disordered linear eigenstates. This affects the power range of stability for the different nonlinear branches associated with each of these eigenstates, resulting in the complex multistability observed in the experiment.

A confirmation for this interpretation is that this effect is very fragile: it depends heavily on disorder as well as on the laser energy. This can be easily understood: it is demonstrated in Ref. [46] that for a much simpler setting, i.e two coupled pillars, with only two linear eigenstates, up to 5 stable modes can be found in the nonlinear regime. In the present situation, with a complex disorder landscape such as the one in Fig. 5.31(d), where several eigenmodes with different energies coexist on the driven pillar as well as on neighboring pillars, predicting the number of stable modes and their stability range becomes a very challenging task. Even slightly different disorder configurations might lead to very different nonlinear behavior.

In fact, for specific disorder and laser detuning, we could even observe more intriguing behavior. In the multistability from Fig. 5.32, the steady-state pattern that we observe is always fully determined by the history of the power scan. In particular, identical initial conditions lead to an identical steady-state pattern. To the contrary, we have found experimental conditions where it is possible to obtain different steady-state patterns from the same initial conditions. The experimental parameters were the following: we excited the same pillar C as in Fig. 5.31(c), and set the laser energy $\hbar\omega_H = 1469.11$meV and power $P = 23$mW. Several initializations of the system (simply realized by switching the laser off and on again, on timescales of a few milliseconds, i.e. much slower than any relevant timescales for exciton-polaritons) resulted in the observation of the three distinct patterns shown
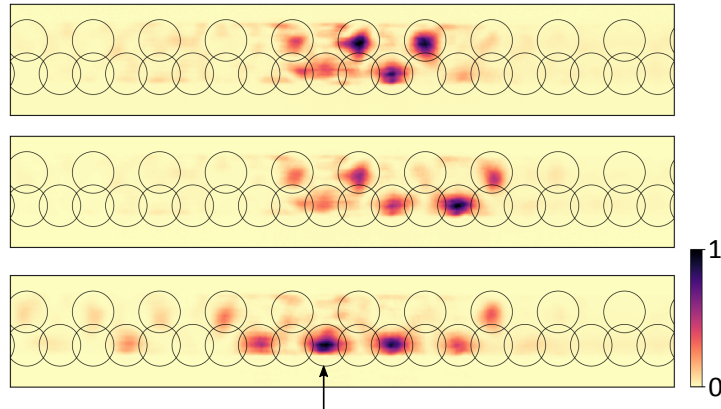
Figure 5.33: Spatially-resolved emission patterns measured with identical pumping conditions, but after several initializations of the system. The arrow indicates the driven site.

in Fig. 5.33. This effect is very fragile when changing either laser detuning or disorder configuration. Even though we were able to reproduce these observations on the same position on the chain but on different dates (several months apart), further investigations would be required to ascertain the origin of this seemingly chaotic behavior.

5.5.2 Conclusion

In conclusion, we have investigated the dynamics of a nonlinear polariton fluid resonantly injected in a flat band. We have demonstrated that due to the absence of kinetic energy, propagation of the nonlinear switching fronts is suppressed, resulting in the formation of domains of discrete size, that can be interpreted as Truncated Bloch Waves. We have shown that the size of these domains is controlled by the power of the drive laser, and have evidenced multistability of the domains of different size.

These results mark a first step in the exploration of the physics of flat bands in the presence of particle interactions. A natural extension of this work would be to different lattice geometries with a flat band, and in particular in higher dimensions. For example, in the 2D Lieb lattice, the flat band is not gapped from the other two bands, and it is not clear whether the switching fronts propagation would still be frozen. Additionally, determination of the excitation spectrum of the nonlinear fluid might be of interest, regarding interpretations in terms of superfluidity. We have also shown that the interplay between disorder and interactions leads to very rich multistability diagrams and seemingly chaotic behavior, which calls for further investigations.

Another possible future prospect is studying quantum fluctuations, as was done in recent polariton works [237, 238], but in a frustrated lattice. It has been predicted

that in a 1D Lieb lattice with partial driving (on sites A), the photon emitted from the dark sites show strong bunching, for a strength of nonlinearity comparable to ours [239, 240]. This is an interesting proposal towards the realization of strongly correlated phases of light, beyond the mean field approximation. However, the main challenge is that the proposed experiment relies on measuring the correlations of photons emitted by dark B sites, meaning that the rate of photon emission would be extremely small. A very efficient single photon detector is thus required for this experiment.

Finally, a topic attracting great interest recently is the interplay between topology and a flat band. For example, a recent theoretical proposal from Ozawa [241] presents a scheme to measure the quantum geometric tensor of the flat band in a photonic 2D Lieb lattice. Additionally, there is an intense effort to realize topological flat bands, i.e. flat bands with nontrivial Chern numbers [242, 243]. A precious ingredient for the realization of such a flat band is spin-orbit coupling, which has been engineered in a 2D Lieb lattice of coupled pillars [86]. This should allow to further explore the delicate interplay of frustration, interactions, and topology, which has been predicted, in the regime of strong interactions, to lead to the emergence of fractional quantum Hall states, without Landau levels [244–246]. Let us mention that so far, polariton-polariton interactions are too weak to observe such effects. However, reaching the regime of strong polariton-polariton interactions, where nonlinear effects could be observed at the single-particle level, is currently one of the main goals of the research field of microcavity polaritons. Promising strategies are being explored [247, 248], and the requirements in terms of interaction strength for the above proposals could be reached in a near future.

Conclusion

In this thesis, we have investigated the dynamics of polaritons fluids in various one-dimensional structures. The possibility to etch microstructures with controlled geometry allowed to engineer the band structure and localization properties of the linear polariton eigenstates. We have used this feature to explore the interplay between kinetic and interaction energy in nonlinear polariton fluids.

In the first part, we have studied the linear localization properties of the Aubry-André-Harper-Fibonacci family of quasi-crystals. Our collaborators from the group of O. Zilberberg have established a theoretical localization phase diagram in the case a tight-binding model of quasicrystal, and identified an unexpected delocalization-localization transition when continuously deforming a Aubry-André-Harper quasicrystal towards a Fibonacci quasicrystal. We have extended the theoretical localization diagram to the case of a nearly-free particle model, more suited to implementation with 1D polariton microstructures. Our analysis confirmed the presence of the delocalization tongue in this nearly-free model. We have then designed and etched 1D wires with modulated lateral dimension, in order to implement the quasiperiodic AAHF potential. The localization properties were probed using photoluminescence measurements both under non-resonant excitation and in resonant spectroscopy experiments. We have been able to establish an experimental localization phase diagram, and evidenced the delocalization-localization transition predicted by our theoretical analysis.

In the second part of this thesis, we have considered the counter-propagation of two nonlinear polariton fluids in a 1D channel. The fluids were injected using resonant excitation. When ramping the pumping power up, the linear interference pattern transformed into a train of dark solitons. We explained the formation of dark solitons as the result of the interplay between the kinetic and interaction energy of the fluid. More precisely, dark solitons are the elementary excitation of a superfluid. The discrete nature of these excitations was evidenced by the observation of abrupt soliton expulsion events in the power scan. We then considered an additional degree of freedom, offered by the application of a phase twist across the wire. We demonstrated that this phase twist controls not only the position of solitons in the wire, but also the parity of their number. We even evidenced phase-controlled bistability of the soliton pattern. Control of the bistability by the phase of the external drive constitute a novel paradigm for optical bistability.

Finally, in the last part, we have investigated the fate of a nonlinear polariton fluid injected into a flat band, where the fluid kinetic energy is quenched. First, we have shown that upon careful engineering of the lattice parameters of a 1D Lieb lattice of coupled micropillars, geometric frustration leads to a perfectly flat middle band in the linear polariton dispersion. We have used resonant excitation to inject nonlinear polariton fluids directly into the flat band. In the nonlinear regime, we have observed the formation of domains of quantized size, due to the frozen propagation of the switching fronts. The size of the domains can be controlled by the resonant pumping power, and we reported multistability of these domains. A comparison with the nonlinear dynamics of a fluid in a dispersive band with same disorder clearly highlights the difference in non linear dynamics in presence or absence of kinetic energy. The nonlinear domains observed for the flat band can be related to a family of gap solitons, named Truncated Bloch Waves which had never been observed in a driven dissipative context.

The present work demonstrates the potential of the microcavity polariton platform for the study of nonlinear quantum fluids of light in engineered potential landscapes. The different configurations considered in this thesis open a broad range of perspectives. In the case of quasicrystal, the exploration of the localization phase diagram in the presence of interactions might lead to exotic many-body localization and delocalization phase transitions. In the case of counterpropagating nonlinear fluids, we have shown how the collective excitation spectrum of the soliton train could be explored. Finally, our work in the Lieb lattice constitute the first experimental investigation on the influence of nonlinearities in a flat band, and paves the way to further investigations, for stronger on-site interactions.

Another promising perspective lies in the rapidly-growing field of topological photonics [249, 250]. The main goal of this field of research is to transpose the mathematical concepts of topology, used to classify the transport properties of electrons in solids, into the realm of photonics. For example, one objective is the realization of topologically protected transport of light, robust to disorder and perturbations. The observation of non-trivial topological phases requires in general complex Hamiltonians, with time-reversal symmetry breaking mechanism, which can for example be achieved by engineering artificial gauge fields, spin polarized excitation or by applying an external magnetic field. First studies on topological effects were already achieved in polariton systems, for example in our group with the demonstration of a lasing regime in a topologically protected edge state of a one-dimensional Su-Schrieffer-Heeger lattice of coupled pillars [97], which was also a part of my PhD work. More recently, a milestone has been reached with the realization of a 2D polariton topological insulator [84]. So far, these works have addressed regimes where polariton-polariton interactions are negligible. Taking advantage of their nonlinearity, microcavity polaritons now appear as a particularly promising platform for the exploration of topological phases of interacting bosons.

On the longer term, a particularly interesting goal of the research on microcavity polaritons is achieve stronger polariton-polariton interactions, in order to achieve

non-linearity at the single-particle level. An intense effort is currently under progress towards this direction. A seemingly promising strategy is to make use of indirect excitons, which have their electron and hole spatially separated, for example in two different quantum wells. This results in a strong exciton dipole moment, which in turn enhances the exciton-exciton interactions [247, 251]. Another possibility is to couple polaritons to a Fermi sea of electrons [248]. Higher polariton interactions would enable going beyond the mean-field approximation used throughout this thesis, and for example allow for the observation of correlated many-body states out of thermal equilibrium in artificial lattices [201, 244–246, 252]. First reports of quantum correlations between polaritons have recently been reported [47, 48], opening the way to the realization of strongly interacting photonic systems in a near future.

Finally, the recent observation at room-temperature of quantum hydrodynamic effects, such as superfluidity [158], offers promising perspectives towards the realization of polaritonic devices, with practical applications for integrated photonics [253].

Publications and conferences

List of publications

1. <u>V. Goblot</u>, B. Rauer, F. Vicentini, A. Le Boité, E. Galopin, A. Lemaître, L. Le Gratiet, A. Harouri, I. Sagnes, J. Bloch, "Quantized nonlinear domains of a polariton fluid in a flat band", to be submitted.

2. S. R. K. Rodriguez, <u>V. Goblot</u>, N. Carlon Zambon, A. Amo and J. Bloch, "Non-reciprocity and zero reflection in nonlinear cavities with tailored loss", Physical Review A **99**, 013851 (2019).

3. F. Baboux, D. De Bernardis, <u>V. Goblot</u>, V.N. Gladilin, C. Gomez, E. Galopin, L. Le Gratiet, A. Lemaître, I. Sagnes, I. Carusotto, M. Wouters, A. Amo, J. Bloch, "Unstable and stable regimes of polariton condensation", Optica **5**, 1163-1170 (2018)

4. P. St-Jean, <u>V. Goblot</u>, E. Galopin, A. Lemaître, T. Ozawa, L. Le Gratiet, I. Sagnes, J. Bloch and A. Amo, "Lasing in topological edge states of a one-dimensional lattice", Nature Photonics **11**, 651–656 (2017).

5. <u>V. Goblot</u>, H. S. Nguyen, I. Carusotto, E. Galopin, A. Lemaître, I. Sagnes, A. Amo and J. Bloch, "Phase-controlled bistability of a dark soliton train in a polariton fluid", Physical Review Letters **117**, 217401 (2016).

Conferences

1. "One-Dimensional Lieb Lattice for polaritons: Linear and nonlinear regime", International Conference on Physics of Light-Matter Coupling in Nanostructures, PLMCN19, Chengdu, China, May 15-19, 2018

2. "Phase-controlled bistability in counterpropagating polariton superfluids", International Conference on Spontaneous Coherence in Excitonic Systems, IC-SCE8, April 25-29, 2016, Edinburgh, United Kingdom, 2016

3. "Phase-controlled bistability in counterpropagating polariton superfluids", International Conference on Physics of Light-Matter Coupling in Nanostructures, PLMCN17, Nara, Japan, March 28-April 1, 2016

Non-resonant characterization of AAHF chains

Here, we present additional experimental data, that correspond to the experimental localization phase diagram of the AAHF model presented in Fig. 3.22, chapter 3. We present both the momentum- and real-space spectrum, measured under non-resonant excitations, for chains with $\beta \in [0; 0.5; 0.8; 1; 2; 1000]$ and $\lambda_1 \in [0.2; 0.4; 0.6; 0.8]$ meV.

λ_1 = 0.2 meV ; λ_2 = 0.8 meV

Figure A.1: Momentum-space spectra, measured on 1D chains with $\lambda_1 = 0.2$ meV and $\beta \in [0; 0.5; 0.8; 1; 2; 1000]$

Figure A.2: Real-space spectra, measured on 1D chains with $\lambda_1 = 0.2$ meV and $\beta \in [0; 0.5; 0.8; 1; 2; 1000]$. In each case, $n = 1$ modes and $n = 2$ modes were measured separately, corresponding to the energy window below (above) the dashed line for $n = 1$ ($n = 2$) modes.
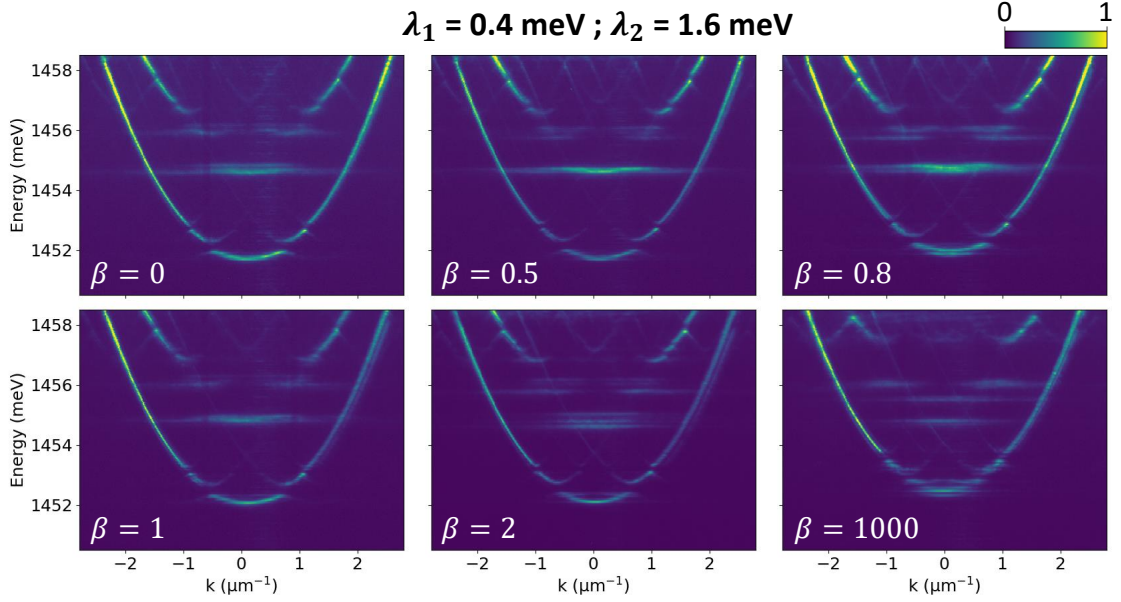
Figure A.3: Momentum-space spectra, measured on 1D chains with $\lambda_1 = 0.4$ meV and $\beta \in [0; 0.5; 0.8; 1; 2; 1000]$
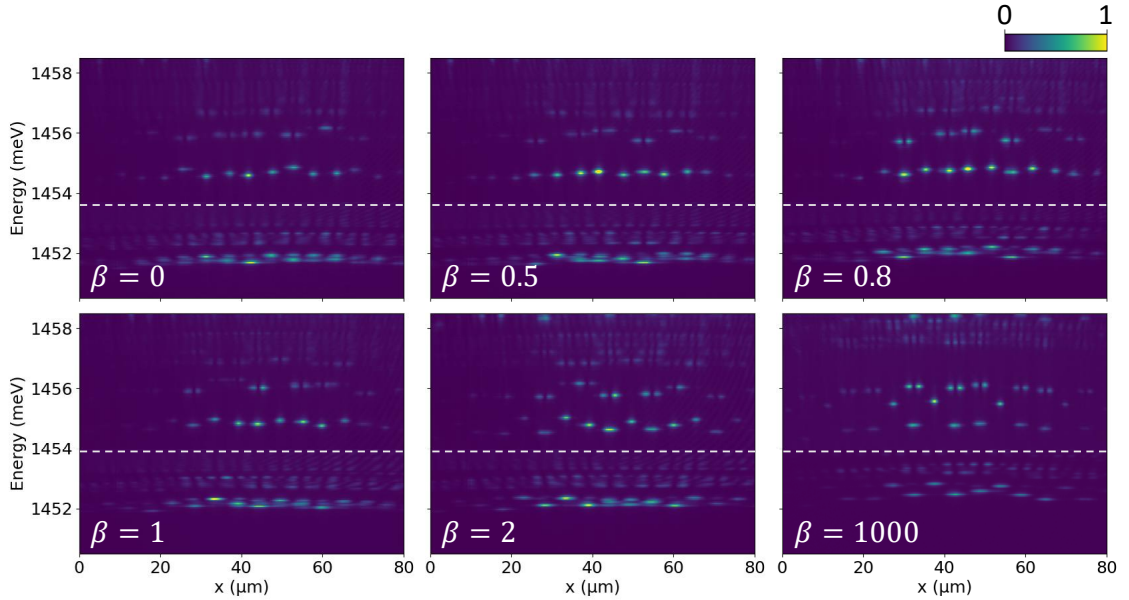
Figure A.4: Real-space spectra, measured on 1D chains with $\lambda_1 = 0.4$ meV and $\beta \in [0; 0.5; 0.8; 1; 2; 1000]$. In each case, $n = 1$ modes and $n = 2$ modes were measured separately, corresponding to the energy window below (above) the dashed line for $n = 1$ ($n = 2$) modes.
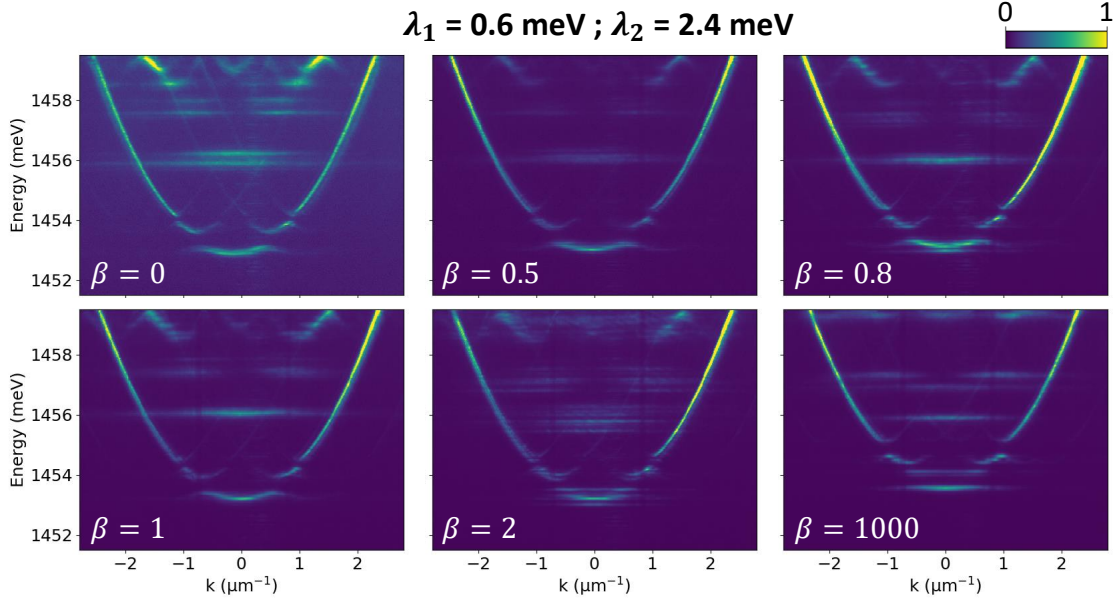
Figure A.5: Momentum-space spectra, measured on 1D chains with $\lambda_1 = 0.6$ meV and $\beta \in [0; 0.5; 0.8; 1; 2; 1000]$
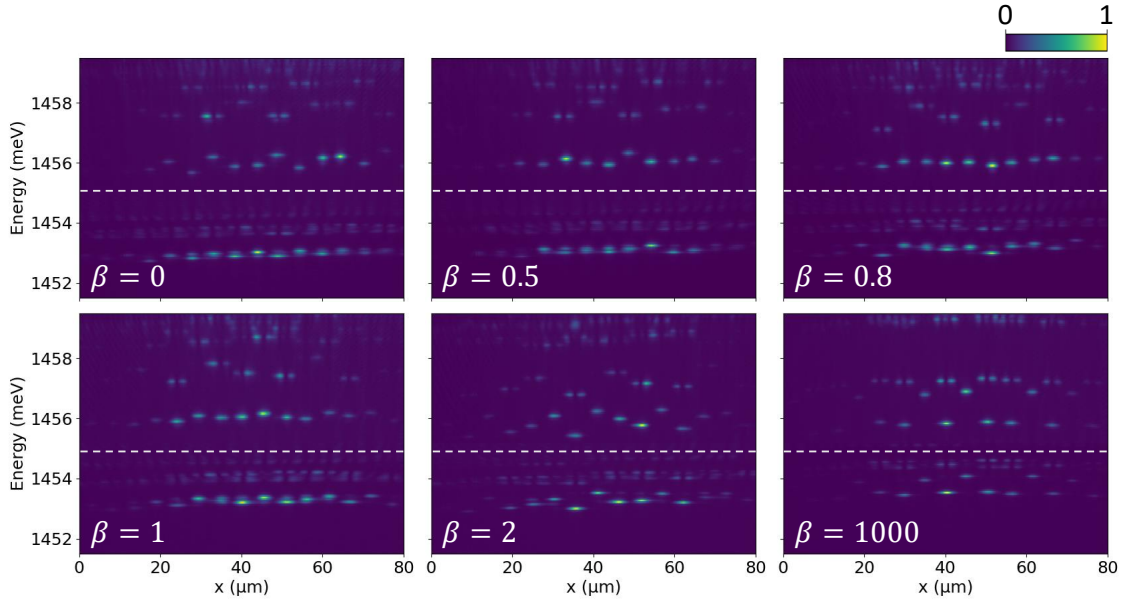
Figure A.6: Real-space spectra, measured on 1D chains with $\lambda_1 = 0.6$ meV and $\beta \in [0; 0.5; 0.8; 1; 2; 1000]$. In each case, $n = 1$ modes and $n = 2$ modes were measured separately, corresponding to the energy window below (above) the dashed line for $n = 1$ ($n = 2$) modes.
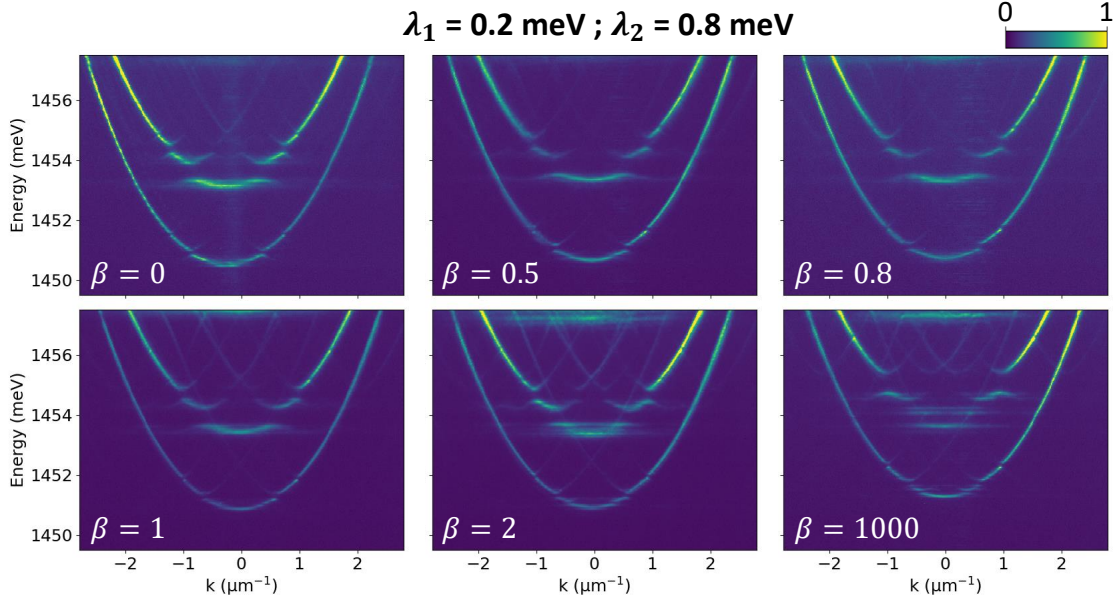
Figure A.7: Momentum-space spectra, measured on 1D chains with $\lambda_1 = 0.8$ meV and $\beta \in [0; 0.5; 0.8; 1; 2; 1000]$
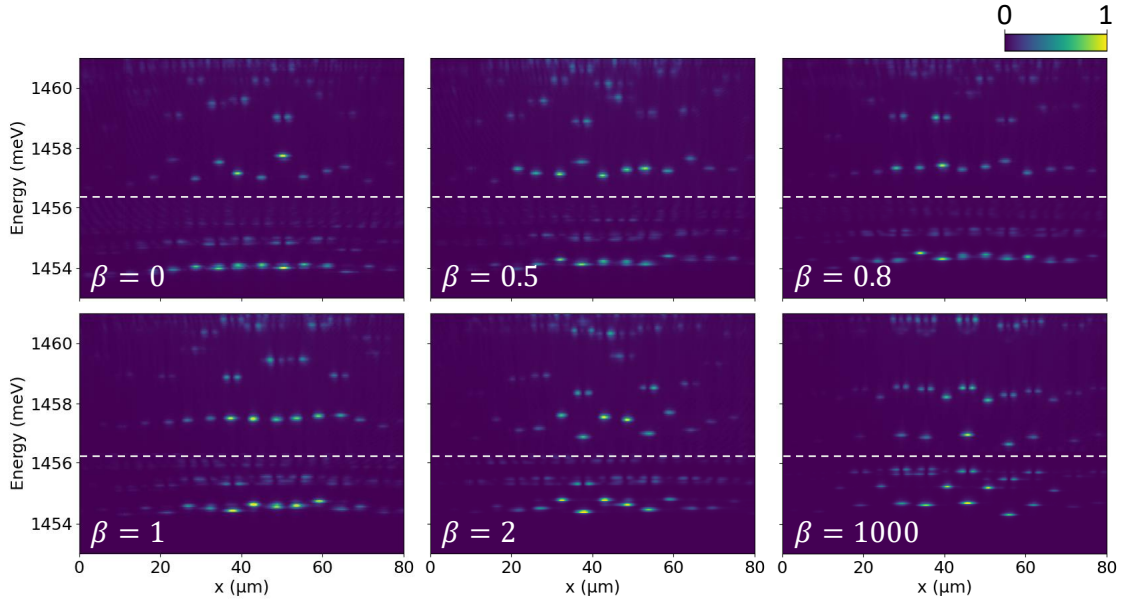
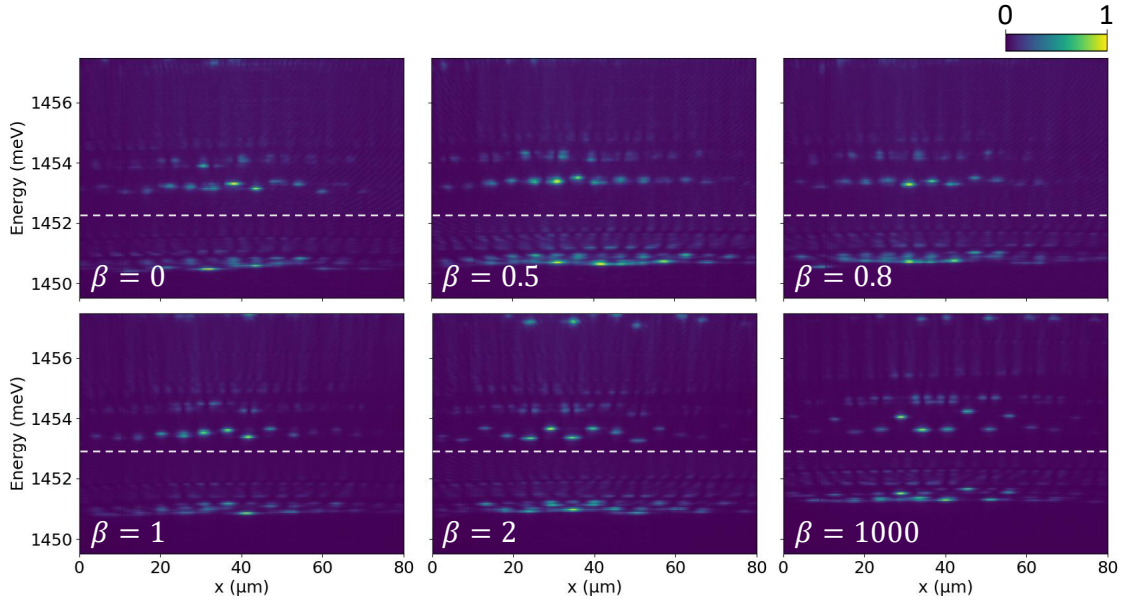**Figure A.8:** Real-space spectra, measured on 1D chains with $\lambda_1 = 0.8$ meV and $\beta \in [0; 0.5; 0.8; 1; 2; 1000]$. In each case, $n = 1$ modes and $n = 2$ modes were measured separately, corresponding to the energy window below (above) the dashed line for $n = 1$ ($n = 2$) modes.
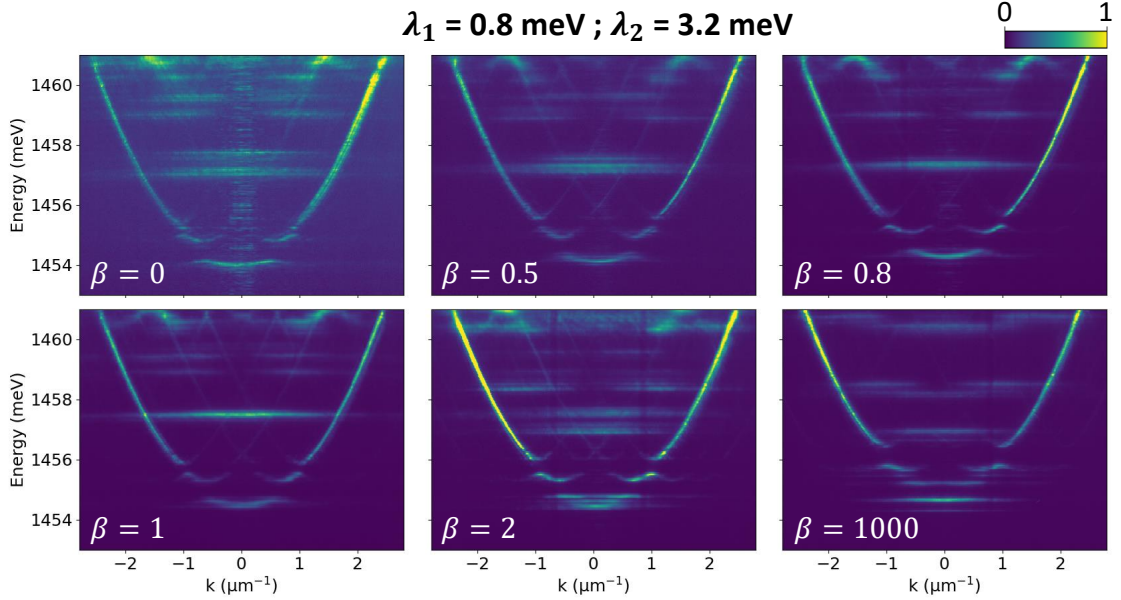
Bibliography

[1] L. Pitaevskii and S. Strindgari, *Bose-Einstein Condensation* (Oxford University Press, Oxford, 2003).

[2] K. B. Davis, M. O. Mewes, M. R. Andrews, N. J. van Druten, D. S. Durfee, D. M. Kurn, and W. Ketterle, "Bose-einstein condensation in a gas of sodium atoms," Phys. Rev. Lett. **75**, 3969–3973 (1995).

[3] A. J. Leggett, "Superfluidity," Rev. Mod. Phys. **71**, S318–S323 (1999).

[4] J. Bardeen, L. N. Cooper, and J. R. Schrieffer, "Theory of superconductivity," Phys. Rev. **108**, 1175–1204 (1957).

[5] I. Carusotto and C. Ciuti, "Quantum fluids of light," Rev. Mod. Phys. **85**, 299–366 (2013).

[6] C. Weisbuch, M. Nishioka, A. Ishikawa, and Y. Arakawa, "Observation of the coupled exciton-photon mode splitting in a semiconductor quantum microcavity," Phys. Rev. Lett. **69**, 3314–3317 (1992).

[7] A. Imamoglu, R. J. Ram, S. Pau, and Y. Yamamoto, "Nonequilibrium condensates and lasers without inversion: Exciton-polariton lasers," Phys. Rev. A **53**, 4250–4253 (1996).

[8] R. M. Stevenson, V. N. Astratov, M. S. Skolnick, D. M. Whittaker, M. Emam-Ismail, A. I. Tartakovskii, P. G. Savvidis, J. J. Baumberg, and J. S. Roberts, "Continuous wave observation of massive polariton redistribution by stimulated scattering in semiconductor microcavities," Phys. Rev. Lett. **85**, 3680–3683 (2000).

[9] H. Deng, G. Weihs, C. Santori, J. Bloch, and Y. Yamamoto, "Condensation of semiconductor microcavity exciton polaritons," Science **298**, 199–202 (2002).

[10] J. Kasprzak, M. Richard, S. Kundermann, A. Baas, P. Jeambrun, J. M. J. Keeling, F. M. Marchetti, M. H. Szymańska, R. André, J. L. Staehli, V. Savona, P. B. Littlewood, B. Deveaud, and L. S. Dang, "Bose-einstein condensation of exciton polaritons," Nature **443**, 409–414 (2006).

[11] A. Amo, J. Lefrère, S. Pigeon, C. Adrados, C. Ciuti, I. Carusotto, R. Houdré, E. Giacobino, and A. Bramati, "Superfluidity of Polaritons in Semiconductor Microcavities," Nat. Phys. **5**, 805–810 (2009).

[12] G. Nardin, G. Grosso, Y. Leger, B. Pietka, F. Morier-Genoud, and B. Deveaud-Pledran, "Hydrodynamic nucleation of quantized vortex pairs in a polariton quantum fluid," Nat. Phys. **7**, 635–641 (2011).

[13] D. Sanvitto, S. Pigeon, A. Amo, D. Ballarini, M. De Giorgi, I. Carusotto, R. Hivet, F. Pisanello, V. G. Sala, P. S. S. Guimaraes, R. Houdré, E. Giacobino, C. Ciuti, A. Bramati, and G. Gigli, "All-optical control of the quantum flow of a polariton condensate," Nat. Photonics **5**, 610–614 (2011).

[14] T. Boulier, E. Cancellieri, N. D. Sangouard, Q. Glorieux, A. V. Kavokin, D. M. Whittaker, E. Giacobino, and A. Bramati, "Injection of orbital angular momentum and storage of quantized vortices in polariton superfluids," Phys. Rev. Lett. **116**, 116402 (2016).

[15] A. Amo, S. Pigeon, D. Sanvitto, V. G. Sala, R. Hivet, I. Carusotto, F. Pisanello, G. Leménager, R. Houdré, E. Giacobino, C. Ciuti, and A. Bramati, "Polariton superfluids reveal quantum hydrodynamic solitons," Science **332**, 1167–1170 (2011).

[16] G. Grosso, G. Nardin, F. Morier-Genoud, Y. Léger, and B. Deveaud-Plédran, "Soliton instabilities and vortex street formation in a polariton quantum fluid," Phys. Rev. Lett. **107**, 245301 (2011).

[17] M. Sich, D. N. Krizhanovskii, M. S. Skolnick, A. V. Gorbach, R. Hartley, D. V. Skryabin, E. A. Cerda-Mendez, K. Biermann, R. Hey, and P. V. Santos, "Observation of bright polariton solitons in a semiconductor microcavity," Nat. Photonics **6**, 50–55 (2012).

[18] C. Schneider, K. Winkler, M. D. Fraser, M. Kamp, Y. Yamamoto, E. A. Ostrovskaya, and S. Höfling, "Exciton-polariton trapping and potential landscape engineering," Reports on Progress in Physics **80**, 016503 (2017).

[19] A. Amo and J. Bloch, "Exciton-polaritons in lattices: A non-linear photonic simulator," Comptes Rendus Physique **17**, 934 – 945 (2016).

[20] R. Balili, V. Hartwell, D. Snoke, L. Pfeiffer, and K. West, "Bose-Einstein condensation of microcavity polaritons in a trap." Science (New York, N.Y.) **316**, 1007–10 (2007).

[21] R. Cerna, D. Sarchi, T. K. Paraïso, G. Nardin, Y. Léger, M. Richard, B. Pietka, O. El Daif, F. Morier-Genoud, V. Savona, M. T. Portella-Oberli, and B. Deveaud-Plédran, "Coherent optical control of the wave function of zero-dimensional exciton polaritons," Phys. Rev. B **80**, 121309 (2009).

[22] M. Galbiati, L. Ferrier, D. D. Solnyshkov, D. Tanese, E. Wertz, A. Amo, M. Abbarchi, P. Senellart, I. Sagnes, A. Lemaître, E. Galopin, G. Malpuech, and J. Bloch, "Polariton condensation in photonic molecules," Phys. Rev. Lett. **108**, 126403 (2012).

[23] V. G. Sala, D. D. Solnyshkov, I. Carusotto, T. Jacqmin, A. Lemaître, H. Terças, A. Nalitov, M. Abbarchi, E. Galopin, I. Sagnes, J. Bloch, G. Malpuech, and A. Amo, "Spin-orbit coupling for photons and polaritons in microstructures," Phys. Rev. X **5**, 011034 (2015).

[24] C. W. Lai, N. Y. Kim, S. Utsunomiya, G. Roumpos, H. Deng, M. D. Fraser, T. Byrnes, P. Recher, N. Kumada, T. Fujisawa, and Y. Yamamoto, "Coherent zero-state and π-state in an exciton–polariton condensate array," Nature **450**, 529–532 (2007).

[25] E. Wertz, L. Ferrier, D. D. Solnyshkov, R. Johne, D. Sanvitto, A. Lemaître, I. Sagnes, R. Grousson, A. V. Kavokin, P. Senellart, G. Malpuech, and J. Bloch, "Spontaneous formation and optical manipulation of extended polariton condensates," Nature Physics **6**, 19 (2010).

[26] D. Tanese, E. Gurevich, F. Baboux, T. Jacqmin, A. Lemaître, E. Galopin, I. Sagnes, A. Amo, J. Bloch, and E. Akkermans, "Fractal energy spectrum of a polariton gas in a fibonacci quasiperiodic potential," Phys. Rev. Lett. **112**, 146404 (2014).

[27] E. A. Cerda-Méndez, D. N. Krizhanovskii, M. Wouters, R. Bradley, K. Biermann, K. Guda, R. Hey, P. V. Santos, D. Sarkar, and M. S. Skolnick, "Polariton condensation in dynamic acoustic lattices," Phys. Rev. Lett. **105**, 116402 (2010).

[28] N. Y. Kim, K. Kusudo, C. Wu, N. Masumoto, A. Löffler, S. Höfling, N. Kumada, L. Worschech, A. Forchel, and Y. Yamamoto, "Dynamical d-wave condensation of exciton–polaritons in a two-dimensional square-lattice potential," Nature Physics **7**, 681–686 (2011).

[29] T. Jacqmin, I. Carusotto, I. Sagnes, M. Abbarchi, D. D. Solnyshkov, G. Malpuech, E. Galopin, A. Lemaître, J. Bloch, and A. Amo, "Direct observation of dirac cones and a flatband in a honeycomb lattice for polaritons," Phys. Rev. Lett. **112**, 116402 (2014).

[30] M. Born and E. Wolf, *Principles of optics* (Cambridge University Press, Cambridge, 1999).

[31] H. Deng, H. Haug, and Y. Yamamoto, "Exciton-polariton bose-einstein condensation," Rev. Mod. Phys. **82**, 1489–1537 (2010).

[32] G. Bastard, *Wave Mechanics Applied to Semiconductor Heterostructures* (Les éditions de physique, Les Ulis, 1988).

[33] M. E. Levinshtein and S. L. Rumyantsev, "Gallium arsenide (¡inline-formula¿¡roman¿gaas¡/roman¿¡/inline-formula¿)," in *Handbook Series on Semiconductor Parameters* (World Scientific, London, 1996) pp. 77–103.

[34] S. Schmitt-Rink, D. S. Chemla, and D. A. B. Miller, "Theory of transient excitonic optical nonlinearities in semiconductor quantum-well structures," Phys. Rev. B **32**, 6601–6609 (1985).

[35] G. Rochat, C. Ciuti, V. Savona, C. Piermarocchi, A. Quattropani, and P. Schwendimann, "Excitonic bloch equations for a two-dimensional system of interacting excitons," Phys. Rev. B **61**, 13856–13862 (2000).

[36] M. Combescot and C. Tanguy, "New criteria for bosonic behavior of excitons," Europhysics Letters **55**, 390 (2001).

[37] L. Kappei, J. Szczytko, F. Morier-Genoud, and B. Deveaud, "Direct observation of the mott transition in an optically excited semiconductor quantum well," Phys. Rev. Lett. **94**, 147403 (2005).

[38] L. C. Andreani, "Optical transitions, excitons, and polaritons in bulk and low-dimensional semiconductor structures," in *Confined Electrons and Photons: New Physics and Applications*, edited by E. Burstein and C. Weisbuch (Springer, Boston, MA, 1995) pp. 57–112.

[39] V. Savona, C. Piermarocchi, A. Quattropani, P. Schwendimann, and F. Tassone, "Optical properties of microcavity polaritons," Phase Transitions **68**, 169–279 (1999).

[40] J. J. Hopfield, "Theory of the contribution of excitons to the complex dielectric constant of crystals," Phys. Rev. **112**, 1555–1567 (1958).

[41] E. T. Jaynes and F. W. Cummings, "Comparison of quantum and semiclassical radiation theories with application to the beam maser," Proceedings of the IEEE **51**, 89–109 (1963).

[42] C. Leyder, M. Romanelli, J. P. Karr, E. Giacobino, T. C. H. Liew, M. M. Glazov, A. V. Kavokin, G. Malpuech, and A. Bramati, "Observation of the optical spin hall effect," Nature Physics **3**, 628–631 (2007).

[43] C. Ciuti, V. Savona, C. Piermarocchi, A. Quattropani, and P. Schwendimann, "Role of the exchange of carriers in elastic exciton-exciton scattering in quantum wells," Phys. Rev. B **58**, 7926–7933 (1998).

[44] F. Tassone and Y. Yamamoto, "Exciton-exciton scattering dynamics in a semiconductor microcavity and stimulated scattering into polaritons," Phys. Rev. B **59**, 10830–10842 (1999).

[45] L. Ferrier, E. Wertz, R. Johne, D. D. Solnyshkov, P. Senellart, I. Sagnes, A. Lemaître, G. Malpuech, and J. Bloch, "Interactions in confined polariton condensates," Phys. Rev. Lett. **106**, 126401 (2011).

[46] S. R. K. Rodriguez, A. Amo, I. Sagnes, L. L. Gratiet, E. Galopin, A. Lemaitre, and J. Bloch, "Interaction-induced hopping phase in driven-dissipative coupled photonic microcavities," Nat. Commun. **7**, 11887 (2016).

[47] A. Delteil, T. Fink, A. Schade, S. Höfling, C. Schneider, and A. Imamoglu, "Quantum correlations of confined exciton-polaritons," (2018), arXiv:1805.04020 .

[48] G. Muñoz-Matutano, A. Wood, M. Johnson, X. V. Asensio, B. Baragiola, A. Reinhard, A. Lemaitre, J. Bloch, A. Amo, B. Besga, M. Richard, and T. Volz, "Quantum-correlated photons from semiconductor cavity polaritons," (2017), arXiv:1712.05551 .

[49] M. Vladimirova, S. Cronenberger, D. Scalbert, K. V. Kavokin, A. Miard, A. Lemaître, J. Bloch, D. Solnyshkov, G. Malpuech, and A. V. Kavokin, "Polariton-polariton interaction constants in microcavities," Phys. Rev. B **82**, 075301 (2010).

[50] A. Verger, C. Ciuti, and I. Carusotto, "Polariton quantum blockade in a photonic dot," Phys. Rev. B **73**, 193306 (2006).

[51] S. Kéna-Cohen and S. R. Forrest, "Room-temperature polariton lasing in an organic single-crystal microcavity," Nature Photonics **4**, 371–375 (2010).

[52] M. Wouters and I. Carusotto, "Excitations in a nonequilibrium bose-einstein condensate of exciton polaritons," Phys. Rev. Lett. **99**, 140402 (2007).

[53] P. G. Savvidis, J. J. Baumberg, R. M. Stevenson, M. S. Skolnick, D. M. Whittaker, and J. S. Roberts, "Angle-resonant stimulated polariton amplifier," Phys. Rev. Lett. **84**, 1547–1550 (2000).

[54] J. J. Baumberg, P. G. Savvidis, R. M. Stevenson, A. I. Tartakovskii, M. S. Skolnick, D. M. Whittaker, and J. S. Roberts, "Parametric oscillation in a vertical microcavity: A polariton condensate or micro-optical parametric oscillation," Phys. Rev. B **62**, R16247–R16250 (2000).

[55] C. Diederichs, J. Tignon, G. Dasbach, C. Ciuti, A. Lemaître, J. Bloch, P. Roussignol, and C. Delalande, "Parametric oscillation in vertical triple microcavities," Nature **440**, 904–907 (2006).

[56] A. Baas, J. P. Karr, H. Eleuch, and E. Giacobino, "Optical bistability in semiconductor microcavities," Phys. Rev. A **69**, 023809 (2004).

[57] T. K. Paraïso, M. Wouters, Y. Leger, F. Mourier-Genoud, and B. Deveaud-Pledran, "Multistability of a coherent spin ensemble in a semiconductor microcavity," Nat. Mater. **10**, 80 (2011).

[58] C. Ouellet-Plamondon, G. Sallen, F. Morier-Genoud, D. Y. Oberli, M. T. Portella-Oberli, and B. Deveaud, "Spatial multistability induced by cross interactions of confined polariton modes," Phys. Rev. B **93**, 085313 (2016).

[59] J. P. Karr, A. Baas, R. Houdré, and E. Giacobino, "Squeezing in semiconductor microcavities in the strong-coupling regime," Phys. Rev. A **69**, 031802 (2004).

[60] K. G. Lagoudakis, T. Ostatnický, A. V. Kavokin, Y. G. Rubo, R. André, and B. Deveaud-Plédran, "Observation of half-quantum vortices in an exciton-polariton condensate," Science **326**, 974–976 (2009).

[61] R. Hivet, H. Flayac, D. D. Solnyshkov, D. Tanese, T. Boulier, D. Andreoli, E. Giacobino, J. Bloch, A. Bramati, G. Malpuech, and A. Amo, "Half-solitons in a polariton quantum fluid behave like magnetic monopoles," Nat. Phys. **8**, 724–728 (2012).

[62] G. Tosi, G. Christmann, N. G. Berloff, P. Tsotsis, T. Gao, Z. Hatzopoulos, P. G. Savvidis, and J. J. Baumberg, "Sculpting oscillators with light within a nonlinear quantum fluid," Nature Physics **8**, 190–194 (2012).

[63] E. A. Cerda-Méndez, D. Sarkar, D. N. Krizhanovskii, S. S. Gavrilov, K. Biermann, M. S. Skolnick, and P. V. Santos, "Exciton-polariton gap solitons in two-dimensional lattices," Phys. Rev. Lett. **111**, 146401 (2013).

[64] A. Amo, S. Pigeon, C. Adrados, R. Houdré, E. Giacobino, C. Ciuti, and A. Bramati, "Light engineering of the polariton landscape in semiconductor microcavities," Phys. Rev. B **82**, 081301 (2010).

[65] G. Tosi, G. Christmann, N. G. Berloff, P. Tsotsis, T. Gao, Z. Hatzopoulos, P. G. Savvidis, and J. J. Baumberg, "Geometrically locked vortex lattices in semiconductor quantum fluids," Nature communications **3**, 1243 (2012).

[66] A. Askitopoulos, H. Ohadi, A. V. Kavokin, Z. Hatzopoulos, P. G. Savvidis, and P. G. Lagoudakis, "Polariton condensation in an optically induced two-dimensional potential," Phys. Rev. B **88**, 041308 (2013).

[67] R. Dall, M. D. Fraser, A. S. Desyatnikov, G. Li, S. Brodbeck, M. Kamp, C. Schneider, S. Höfling, and E. A. Ostrovskaya, "Creation of orbital angular momentum states with chiral polaritonic lenses," Phys. Rev. Lett. **113**, 200404 (2014).

[68] H. Ohadi, Y. del Valle-Inclan Redondo, A. J. Ramsay, Z. Hatzopoulos, T. C. H. Liew, P. R. Eastham, P. G. Savvidis, and J. J. Baumberg, "Synchronization crossover of polariton condensates in weakly disordered lattices," Phys. Rev. B **97**, 195109 (2018).

[69] N. G. Berloff, M. Silva, K. Kalinin, A. Askitopoulos, J. D. Töpfer, P. Cilibrizzi, W. Langbein, and P. G. Lagoudakis, "Realizing the classical xy hamiltonian in polariton simulators," Nature Materials **16**, 1120–1126 (2017).

[70] T. Gutbrod, M. Bayer, A. Forchel, J. P. Reithmaier, T. L. Reinecke, S. Rudin, and P. A. Knipp, "Weak and strong coupling of photons and excitons in photonic dots," Phys. Rev. B **57**, 9950–9956 (1998).

[71] B. Zhang, Z. Wang, S. Brodbeck, C. Schneider, M. Kamp, S. Höfling, and H. Deng, "Zero-dimensional polariton laser in a subwavelength grating-based vertical microcavity," Light: Science & Applications **3**, e135–e135 (2014).

[72] B. Besga, C. Vaneph, J. Reichel, J. Estève, A. Reinhard, J. Miguel-Sánchez, A. Imamoğlu, and T. Volz, "Polariton boxes in a tunable fiber cavity," Phys. Rev. Applied **3**, 014008 (2015).

[73] N. Masumoto, N. Y. Kim, T. Byrnes, K. Kusudo, A. Löffler, S. Höfling, A. Forchel, and Y. Yamamoto, "Exciton–polariton condensates with flat bands in a two-dimensional kagome lattice," New J. Phys. **14**, 065002 (2012).

[74] N. Y. Kim, K. Kusudo, A. Löffler, S. Höfling, A. Forchel, and Y. Yamamoto, "Exciton–polariton condensates near the dirac point in a triangular lattice," New Journal of Physics **15**, 035032 (2013).

[75] R. I. Kaitouni, O. El Daïf, A. Baas, M. Richard, T. Paraiso, P. Lugan, T. Guillet, F. Morier-Genoud, J. D. Ganière, J. L. Staehli, V. Savona, and B. Deveaud, "Engineering the spatial confinement of exciton polaritons in semiconductors," Phys. Rev. B **74**, 155311 (2006).

[76] O. El Daïf, A. Baas, T. Guillet, J.-P. Brantut, R. I. Kaitouni, J. L. Staehli, F. Morier-Genoud, and B. Deveaud, "Polariton quantum boxes in semiconductor microcavities," Applied Physics Letters **88**, 061105 (2006).

[77] K. Winkler, J. Fischer, A. Schade, M. Amthor, R. Dall, J. Geßler, M. Emmerling, E. A. Ostrovskaya, M. Kamp, C. Schneider, and S. Hööfling, "A polariton condensate in a photonic crystal potential landscape," New Journal of Physics **17**, 023001 (2015).

[78] J. Bloch, R. Planel, V. Thierry-Mieg, J. Gérard, D. Barrier, J. Marzin, and E. Costard, "Strong-coupling regime in pillar semiconductor microcavities," Superlattices and Microstructures **22**, 371–374 (1997).

[79] A. Kuther, M. Bayer, T. Gutbrod, A. Forchel, P. A. Knipp, T. L. Reinecke, and R. Werner, "Confined optical modes in photonic wires," Phys. Rev. B **58**, 15744–15748 (1998).

[80] M. Bayer, T. Gutbrod, A. Forchel, T. L. Reinecke, P. A. Knipp, R. Werner, and J. P. Reithmaier, "Optical demonstration of a crystal band structure formation," Phys. Rev. Lett. **83**, 5374–5377 (1999).

[81] G. Dasbach, M. Bayer, M. Schwab, and A. Forchel, "Spatial photon trapping: tailoring the optical properties of semiconductor microcavities," Semiconductor Science and Technology **18**, S339 (2003).

[82] J. Fischer, I. G. Savenko, M. D. Fraser, S. Holzinger, S. Brodbeck, M. Kamp, I. A. Shelykh, C. Schneider, and S. Höfling, "Spatial coherence properties of one dimensional exciton-polariton condensates," Phys. Rev. Lett. **113**, 203902 (2014).

[83] S. Klembt, T. H. Harder, O. A. Egorov, K. Winkler, H. Suchomel, J. Beierlein, M. Emmerling, C. Schneider, and S. Höfling, "Polariton condensation in s- and p-flatbands in a two-dimensional lieb lattice," Applied Physics Letters **111**, 231102 (2017).

[84] S. Klembt, T. H. Harder, O. A. Egorov, K. Winkler, R. Ge, M. A. Bandres, M. Emmerling, L. Worschech, T. C. H. Liew, M. Segev, C. Schneider, and S. Höfling, "Exciton-polariton topological insulator," Nature **562**, 552–556 (2018).

[85] D. V. Skryabin, Y. V. Kartashov, O. A. Egorov, M. Sich, J. K. Chana, L. E. Tapia Rodriguez, P. M. Walker, E. Clarke, B. Royall, M. S. Skolnick, and D. N. Krizhanovskii, "Backward cherenkov radiation emitted by polariton solitons in a microcavity wire," Nature Communications **8**, 1554 (2017).

[86] C. E. Whittaker, E. Cancellieri, P. M. Walker, D. R. Gulevich, H. Schomerus, D. Vaitiekus, B. Royall, D. M. Whittaker, E. Clarke, I. V. Iorsh, I. A. Shelykh, M. S. Skolnick, and D. N. Krizhanovskii, "Exciton polaritons in a two-dimensional lieb lattice with spin-orbit coupling," Phys. Rev. Lett. **120**, 097401 (2018).

[87] S. Kim, B. Zhang, Z. Wang, J. Fischer, S. Brodbeck, M. Kamp, C. Schneider, S. Höfling, and H. Deng, "Coherent polariton laser," Phys. Rev. X **6**, 011026 (2016).

[88] S. Dufferwiel, F. Li, A. A. P. Trichet, L. Giriunas, P. M. Walker, I. Farrer, D. A. Ritchie, J. M. Smith, M. S. Skolnick, and D. N. Krizhanovskii, "Tunable polaritonic molecules in an open microcavity system," Applied Physics Letters **107**, 201106 (2015).

[89] D. Tanese, H. Flayac, D. Solnyshkov, A. Amo, A. Lemaître, E. Galopin, R. Braive, P. Senellart, I. Sagnes, G. Malpuech, and J. Bloch, "Polariton condensation in solitonic gap states in a one-dimensional periodic potential," Nature Commun. **4**, 1749 (2013).

[90] H. S. Nguyen, D. Vishnevsky, C. Sturm, D. Tanese, D. Solnyshkov, E. Galopin, A. Lemaître, I. Sagnes, A. Amo, G. Malpuech, and J. Bloch, "Realization of a double-barrier resonant tunneling diode for cavity polaritons," Phys. Rev. Lett. **110**, 236601 (2013).

[91] C. Sturm, D. Tanese, H. S. Nguyen, H. Flayac, E. Galopin, A. Lemaître, I. Sagnes, D. D. Solnyshkov, A. Amo, G. Malpuech, and J. Bloch, "All-optical phase modulation in a cavity-polariton mach-zehnder interferometer," Nature Commun. **5**, 3278 (2014).

[92] F. Marsault, H. S. Nguyen, D. Tanese, A. Lemaître, E. Galopin, I. Sagnes, A. Amo, and J. Bloch, "Realization of an all optical exciton-polariton router," Applied Physics Letters **107** (2015), 10.1063/1.4936158.

[93] H. S. Nguyen, D. Gerace, I. Carusotto, D. Sanvitto, E. Galopin, A. Lemaître, I. Sagnes, J. Bloch, and A. Amo, "Acoustic black hole in a stationary hydrodynamic flow of microcavity polaritons," Phys. Rev. Lett. **114**, 036402 (2015).

[94] F. Baboux, E. Levy, A. Lemaître, C. Gómez, E. Galopin, L. Le Gratiet, I. Sagnes, A. Amo, J. Bloch, and E. Akkermans, "Measuring topological invariants from generalized edge states in polaritonic quasicrystals," Phys. Rev. B **95**, 161114 (2017).

[95] M. Abbarchi, A. Amo, V. G. Sala, D. D. Solnyshkov, H. Flayac, L. Ferrier, I. Sagnes, E. Galopin, A. Lemaitre, G. Malpuech, and J. Bloch, "Macroscopic quantum self-trapping and josephson oscillations of exciton polaritons," Nat. Phys. **9**, 275–279 (2013).

[96] N. Carlon Zambon, P. St-Jean, M. Milićević, A. Lemaître, A. Harouri, L. LeGratiet, O. Bleu, D. Solnyshkov, G. Malpuech, I. Sagnes, S. Ravets, A. Amo, and J. Bloch, "Optically controlling the emission chirality of microlasers," (2018), arXiv:1806.04590 .

[97] P. St-Jean, V. Goblot, E. Galopin, A. Lemaître, T. Ozawa, L. Le Gratiet, I. Sagnes, J. Bloch, and A. Amo, "Lasing in topological edge states of a one-dimensional lattice," Nature Photonics **11**, 651–656 (2017).

[98] M. Milićević, T. Ozawa, P. Andreakou, I. Carusotto, T. Jacqmin, E. Galopin, A. Lemaître, L. L. Gratiet, I. Sagnes, J. Bloch, and A. Amo, "Edge states in polariton honeycomb lattices," 2D Materials **2**, 034012 (2015).

[99] M. Milićević, T. Ozawa, G. Montambaux, I. Carusotto, E. Galopin, A. Lemaître, L. Le Gratiet, I. Sagnes, J. Bloch, and A. Amo, "Orbital edge states in a photonic honeycomb lattice," Phys. Rev. Lett. **118**, 107403 (2017).

[100] M. Milićević, G. Montambaux, T. Ozawa, I. Sagnes, A. Lemaître, L. L. Gratiet, A. Harouri, J. Bloch, and A. Amo, "Tilted and type-iii dirac cones emerging from flat bands in photonic orbital graphene," (2018), arXiv:1807.08650 .

[101] F. Baboux, D. D. Bernardis, V. Goblot, V. N. Gladilin, C. Gomez, E. Galopin, L. L. Gratiet, A. Lemaître, I. Sagnes, I. Carusotto, M. Wouters, A. Amo, and J. Bloch, "Unstable and stable regimes of polariton condensation," Optica **5**, 1163–1170 (2018).

[102] Y. E. Kraus and O. Zilberberg, "Topological equivalence between the fibonacci quasicrystal and the harper model," Phys. Rev. Lett. **109**, 116404 (2012).

[103] D. Shechtman, I. Blech, D. Gratias, and J. W. Cahn, "Metallic phase with long-range orientational order and no translational symmetry," Phys. Rev. Lett. **53**, 1951–1953 (1984).

[104] D. Levine and P. J. Steinhardt, "Quasicrystals: A new class of ordered structures," Phys. Rev. Lett. **53**, 2477–2480 (1984).

[105] W. Gellermann, M. Kohmoto, B. Sutherland, and P. C. Taylor, "Localization of light waves in fibonacci dielectric multilayers," Phys. Rev. Lett. **72**, 633–636 (1994).

[106] T. Hattori, N. Tsurumachi, S. Kawato, and H. Nakatsuka, "Photonic dispersion relation in a one-dimensional quasicrystal," Phys. Rev. B **50**, 4220–4223 (1994).

[107] Y. Lahini, R. Pugatch, F. Pozzi, M. Sorel, R. Morandotti, N. Davidson, and Y. Silberberg, "Observation of a localization transition in quasiperiodic photonic lattices," Phys. Rev. Lett. **103**, 013901 (2009).

[108] Y. E. Kraus, Y. Lahini, Z. Ringel, M. Verbin, and O. Zilberberg, "Topological states and adiabatic pumping in quasicrystals," Phys. Rev. Lett. **109**, 106402 (2012).

[109] P. Vignolo, M. Bellec, J. Böhm, A. Camara, J.-M. Gambaudo, U. Kuhl, and F. Mortessagne, "Energy landscape in a penrose tiling," Phys. Rev. B **93**, 075141 (2016).

[110] Z. V. Vardeny, A. Nahata, and A. Agrawal, "Optics of photonic quasicrystals," Nature Photonics **7**, 177–187 (2013).

[111] L. Levi, M. Rechtsman, B. Freedman, T. Schwartz, O. Manela, and M. Segev, "Disorder-enhanced transport in photonic quasicrystals," Science **332**, 1541–1544 (2011).

[112] L. Fallani, J. E. Lye, V. Guarrera, C. Fort, and M. Inguscio, "Ultracold atoms in a disordered crystal of light: Towards a bose glass," Phys. Rev. Lett. **98**, 130404 (2007).

[113] G. Roati, C. D'Errico, L. Fallani, M. Fattori, C. Fort, M. Zaccanti, G. Modugno, M. Modugno, and M. Inguscio, "Anderson localization of a non-interacting bose–einstein condensate," Nature **453**, 895–898 (2008).

[114] M. Schreiber, S. S. Hodgman, P. Bordia, H. P. Lüschen, M. H. Fischer, R. Vosk, E. Altman, U. Schneider, and I. Bloch, "Observation of many-body localization of interacting fermions in a quasirandom optical lattice." Science (New York, N.Y.) **349**, 842–5 (2015).

[115] W. Steurer and D. Sutter-Widmer, "Photonic and phononic quasicrystals," Journal of Physics D: Applied Physics **40**, R229 (2007).

[116] L.-J. Lang, X. Cai, and S. Chen, "Edge states and topological phases in one-dimensional optical superlattices," Phys. Rev. Lett. **108**, 220401 (2012).

[117] S. Ganeshan, K. Sun, and S. Das Sarma, "Topological zero-energy modes in gapless commensurate aubry-andré-harper models," Phys. Rev. Lett. **110**, 180403 (2013).

[118] M. Verbin, O. Zilberberg, Y. E. Kraus, Y. Lahini, and Y. Silberberg, "Observation of topological phase transitions in photonic quasicrystals," Phys. Rev. Lett. **110**, 076403 (2013).

[119] A. Dareau, E. Levy, M. B. Aguilera, R. Bouganne, E. Akkermans, F. Gerbier, and J. Beugnon, "Revealing the topology of quasicrystals with a diffraction experiment," Phys. Rev. Lett. **119**, 215304 (2017).

[120] Y. E. Kraus, Z. Ringel, and O. Zilberberg, "Four-dimensional quantum hall effect in a two-dimensional quasicrystal," Phys. Rev. Lett. **111**, 226401 (2013).

[121] M. Lohse, C. Schweizer, H. M. Price, O. Zilberberg, and I. Bloch, "Exploring 4D quantum Hall physics with a 2D topological charge pump," Nature **553**, 55–58 (2018).

[122] O. Zilberberg, S. Huang, J. Guglielmon, M. Wang, K. P. Chen, and M. C. Kraus, Yaacov E. Rechtsman, "Photonic topological boundary pumping as a probe of 4d quantum hall physics," Nature **553**, 59–62 (2018).

[123] F. Mei, S.-L. Zhu, Z.-M. Zhang, C. H. Oh, and N. Goldman, "Simulating Z_2 topological insulators with cold atoms in a one-dimensional optical lattice," Phys. Rev. A **85**, 013638 (2012).

[124] D.-T. Tran, A. Dauphin, N. Goldman, and P. Gaspard, "Topological hofstadter insulators in a two-dimensional quasicrystal," Phys. Rev. B **91**, 085125 (2015).

[125] M. A. Bandres, M. C. Rechtsman, and M. Segev, "Topological photonic quasicrystals: Fractal topological spectrum and protected transport," Phys. Rev. X **6**, 011016 (2016).

[126] E. Maciá, "Exploiting aperiodic designs in nanophotonic devices," Reports on Progress in Physics **75**, 036502 (2012).

[127] P. G. Harper, "Single band motion of conduction electrons in a uniform magnetic field," Proc. Phys. Society. A **68**, 874 (1955).

[128] S. Aubry and G. André, "Analyticity breaking and anderson localization in incommensurate lattices," Ann. Isr. Phys. Soc. **3** (1980).

[129] J. Sokoloff, "Unusual band structure, wave functions and electrical conductance in crystals with incommensurate periodic potentials," Physics Reports **126**, 189–244 (1985).

[130] B. Kramer and A. MacKinnon, "Localization: theory and experiment," Reports on Progress in Physics **56**, 1469 (1993).

[131] X. Li, X. Li, and S. Das Sarma, "Mobility edges in one-dimensional bichromatic incommensurate potentials," Phys. Rev. B **96**, 085119 (2017).

[132] H. P. Lüschen, S. Scherg, T. Kohlert, M. Schreiber, P. Bordia, X. Li, S. Das Sarma, and I. Bloch, "Single-particle mobility edge in a one-dimensional quasiperiodic optical lattice," Phys. Rev. Lett. **120**, 160404 (2018).

[133] D. R. Hofstadter, "Energy levels and wave functions of bloch electrons in rational and irrational magnetic fields," Phys. Rev. B **14**, 2239–2249 (1976).

[134] D. J. Thouless, M. Kohmoto, M. P. Nightingale, and M. den Nijs, "Quantized hall conductance in a two-dimensional periodic potential," Phys. Rev. Lett. **49**, 405–408 (1982).

[135] M. Kohmoto, L. P. Kadanoff, and C. Tang, "Localization problem in one dimension: Mapping and escape," Phys. Rev. Lett. **50**, 1870–1872 (1983).

[136] S. Ostlund, R. Pandit, D. Rand, H. J. Schellnhuber, and E. D. Siggia, "One-dimensional schrödinger equation with an almost periodic potential," Phys. Rev. Lett. **50**, 1873–1876 (1983).

[137] M. Kohmoto and J. R. Banavar, "Quasiperiodic lattice: Electronic properties, phonon properties, and diffusion," Phys. Rev. B **34**, 563–566 (1986).

[138] M. Kohmoto, B. Sutherland, and C. Tang, "Critical wave functions and a cantor-set spectrum of a one-dimensional quasicrystal model," Phys. Rev. B **35**, 1020–1033 (1987).

[139] R. B. Capaz, B. Koiller, and S. L. A. de Queiroz, "Gap states and localization properties of one-dimensional fibonacci quasicrystals," Phys. Rev. B **42**, 6402–6407 (1990).

[140] J. M. Luck, "Cantor spectra and scaling of gap widths in deterministic aperiodic systems," Phys. Rev. B **39**, 5834–5849 (1989).

[141] J. Bellissard, A. Bovier, and J.-M. Ghez, "Gap labelling theorems for one dimensional discrete schrödinger operators," Reviews in Mathematical Physics **4**, 1–37 (1992).

[142] R. Merlin, K. Bajema, R. Clarke, F. Y. Juang, and P. K. Bhattacharya, "Quasiperiodic gaas-alas heterostructures," Phys. Rev. Lett. **55**, 1768–1770 (1985).

[143] M. Kohmoto, B. Sutherland, and K. Iguchi, "Localization of optics: Quasiperiodic media," Phys. Rev. Lett. **58**, 2436–2438 (1987).

[144] L. Dal Negro, C. J. Oton, Z. Gaburro, L. Pavesi, P. Johnson, A. Lagendijk, R. Righini, M. Colocci, and D. S. Wiersma, "Light transport through the band-edge states of fibonacci quasicrystals," Phys. Rev. Lett. **90**, 055501 (2003).

[145] M. Ghulinyan, C. J. Oton, L. Dal Negro, L. Pavesi, R. Sapienza, M. Colocci, and D. S. Wiersma, "Light-pulse propagation in fibonacci quasicrystals," Phys. Rev. B **71**, 094204 (2005).

[146] M. Verbin, O. Zilberberg, Y. Lahini, Y. E. Kraus, and Y. Silberberg, "Topological pumping over a photonic fibonacci quasicrystal," Phys. Rev. B **91**, 064201 (2015).

[147] A. Bramati and M. Modugno, eds., *Physics of Quantum Fluids* (Springer, Berlin, Heidelberg, 2013).

[148] Y. S. Kivshar and G. P. Agrawal, *Optical Solitons* (Academic Press, New York, 2003).

[149] S. Burger, K. Bongs, S. Dettmer, W. Ertmer, K. Sengstock, A. Sanpera, G. V. Shlyapnikov, and M. Lewenstein, "Dark solitons in bose-einstein condensates," Phys. Rev. Lett. **83**, 5198–5201 (1999).

[150] J. Denschlag, J. E. Simsarian, D. L. Feder, C. W. Clark, L. A. Collins, J. Cubizolles, L. Deng, E. W. Hagley, K. Helmerson, W. P. Reinhardt, S. L. Rolston, B. I. Schneider, and W. D. Phillips, "Generating solitons by phase engineering of a bose-einstein condensate," Science **287**, 97–101 (2000).

[151] P. Engels and C. Atherton, "Stationary and nonstationary fluid flow of a bose-einstein condensate through a penetrable barrier," Phys. Rev. Lett. **99**, 160405 (2007).

[152] A. M. Weiner, J. P. Heritage, R. J. Hawkins, R. N. Thurston, E. M. Kirschner, D. E. Leaird, and W. J. Tomlinson, "Experimental observation of the fundamental dark soliton in optical fibers," Phys. Rev. Lett. **61**, 2445–2448 (1988).

[153] M. Chen, M. A. Tsankov, J. M. Nash, and C. E. Patton, "Microwave magnetic-envelope dark solitons in yttrium iron garnet thin films," Phys. Rev. Lett. **70**, 1707–1710 (1993).

[154] B. P. Anderson, P. C. Haljan, C. A. Regal, D. L. Feder, L. A. Collins, C. W. Clark, and E. A. Cornell, "Watching dark solitons decay into vortex rings in a bose-einstein condensate," Phys. Rev. Lett. **86**, 2926–2929 (2001).

[155] T. Ackemann, W. Firth, and G.-L. Oppo, "Chapter 6 fundamentals and applications of spatial dissipative solitons in photonic devices," Adv. At. Mol. Opt. Phys. **57**, 323 – 421 (2009).

[156] Y. Larionova, W. Stolz, and C. O. Weiss, "Optical bistability and spatial resonator solitons based on exciton-polariton nonlinearity," Opt. Lett. **33**, 321–323 (2008).

[157] P. M. Walker, L. Tinkler, B. Royall, D. V. Skryabin, I. Farrer, D. A. Ritchie, M. S. Skolnick, and D. N. Krizhanovskii, "Dark solitons in high velocity waveguide polariton fluids," Phys. Rev. Lett. **119**, 097403 (2017).

[158] G. Lerario, A. Fieramosca, F. Barachati, D. Ballarini, K. S. Daskalakis, L. Dominici, M. De Giorgi, S. A. Maier, G. Gigli, S. Kéna-Cohen, and D. Sanvitto, "Room-temperature superfluidity in a polariton condensate," Nature Physics **13**, 837–841 (2017).

[159] D. Ballarini, D. Sanvitto, A. Amo, L. Viña, M. Wouters, I. Carusotto, A. Lemaitre, and J. Bloch, "Observation of long-lived polariton states in semiconductor microcavities across the parametric threshold," Phys. Rev. Lett. **102**, 056402 (2009).

[160] V. Kohnle, Y. Léger, M. Wouters, M. Richard, M. T. Portella-Oberli, and B. Deveaud-Plédran, "From single particle to superfluid excitations in a dissipative polariton gas," Phys. Rev. Lett. **106**, 255302 (2011).

[161] S. Utsunomiya, L. Tian, G. Roumpos, C. W. Lai, N. Kumada, T. Fujisawa, M. Kuwata-Gonokami, A. Löffler, S. Höfling, A. Forchel, and Y. Yamamoto, "Observation of Bogoliubov excitations in exciton-polariton condensates," Nature Physics **4**, 700–705 (2008).

[162] A. Amo, D. Sanvitto, F. P. Laussy, D. Ballarini, E. del Valle, M. D. Martin, A. Lemaitre, J. Bloch, D. N. Krizhanovskii, M. S. Skolnick, C. Tejedor, and L. Vina, "Collective fluid dynamics of a polariton condensate in a semiconductor microcavity," Nature (London) **457**, 291–295 (2009).

[163] M. Y. Petrov and A. V. Kavokin, "Polariton transport in one-dimensional channels," Phys. Rev. B **88**, 035308 (2013).

[164] D. Sanvitto, F. M. Marchetti, M. H. Szymanska, G. Tosi, M. Baudisch, F. P. Laussy, D. N. Krizhanovskii, M. S. Skolnick, L. Marrucci, A. Lemaitre, J. Bloch, C. Tejedor, and L. Vina, "Persistent currents and quantized vortices in a polariton superfluid," Nat. Phys. **6**, 527–533 (2010).

[165] A. Janot, T. Hyart, P. R. Eastham, and B. Rosenow, "Superfluid stiffness of a driven dissipative condensate with disorder," Phys. Rev. Lett. **111**, 230403 (2013).

[166] D. Sarchi, I. Carusotto, M. Wouters, and V. Savona, "Coherent dynamics and parametric instabilities of microcavity polaritons in double-well systems," Phys. Rev. B **77**, 125324 (2008).

[167] I. A. Shelykh, D. D. Solnyshkov, G. Pavlovic, and G. Malpuech, "Josephson effects in condensates of excitons and exciton polaritons," Phys. Rev. B **78**, 041302 (2008).

[168] D. D. Solnyshkov, H. Flayac, and G. Malpuech, "Black holes and wormholes in spinor polariton condensates," Phys. Rev. B **84**, 233405 (2011).

[169] D. Gerace and I. Carusotto, "Analog hawking radiation from an acoustic black hole in a flowing polariton superfluid," Phys. Rev. B **86**, 144505 (2012).

[170] L. A. Smirnov, D. A. Smirnova, E. A. Ostrovskaya, and Y. S. Kivshar, "Dynamics and stability of dark solitons in exciton-polariton condensates," Phys. Rev. B **89**, 235310 (2014).

[171] X. Ma, O. A. Egorov, and S. Schumacher, "Creation and manipulation of stable dark solitons and vortices in microcavity polariton condensates," Phys. Rev. Lett. **118**, 157401 (2017).

[172] A. Opala, M. Pieczarka, N. Bobrovska, and M. Matuszewski, "Dynamics of defect-induced dark solitons in an exciton-polariton condensate," Phys. Rev. B **97**, 155304 (2018).

[173] J. H. Marburger and F. S. Felber, "Theory of a lossless nonlinear fabry-perot interferometer," Phys. Rev. A **17**, 335–342 (1978).

[174] L. D. Carr, C. W. Clark, and W. P. Reinhardt, "Stationary solutions of the one-dimensional nonlinear schrödinger equation. i. case of repulsive nonlinearity," Phys. Rev. A **62**, 063610 (2000).

[175] V. V. Konotop and L. Pitaevskii, "Landau dynamics of a grey soliton in a trapped condensate," Phys. Rev. Lett. **93**, 240403 (2004).

[176] D. J. Frantzeskakis, G. Theocharis, F. K. Diakonos, P. Schmelcher, and Y. S. Kivshar, "Interaction of dark solitons with localized impurities in bose-einstein condensates," Phys. Rev. A **66**, 053608 (2002).

[177] Y. S. Kivshar and W. Królikowski, "Lagrangian approach for dark solitons," Optics Communications **114**, 353 – 362 (1995).

[178] R. N. Thurston and A. M. Weiner, "Collisions of dark solitons in optical fibers," J. Opt. Soc. Am. B **8**, 471–477 (1991).

[179] L. Lerner, D. J. Mitchell, and A. W. Snyder, "Interacting gray solitons," Opt. Lett. **19**, 1302–1304 (1994).

[180] D. Foursa and P. Emplit, "Investigation of black-gray soliton interaction," Phys. Rev. Lett. **77**, 4011–4014 (1996).

[181] S. Stellmer, C. Becker, P. Soltan-Panahi, E.-M. Richter, S. Dörscher, M. Baumert, J. Kronjäger, K. Bongs, and K. Sengstock, "Collisions of dark solitons in elongated bose-einstein condensates," Phys. Rev. Lett. **101**, 120406 (2008).

[182] G. Theocharis, A. Weller, J. P. Ronzheimer, C. Gross, M. K. Oberthaler, P. G. Kevrekidis, and D. J. Frantzeskakis, "Multiple atomic dark solitons in cigar-shaped bose-einstein condensates," Phys. Rev. A **81**, 063604 (2010).

[183] H. Terças, D. D. Solnyshkov, and G. Malpuech, "Topological wigner crystal of half-solitons in a spinor bose-einstein condensate," Phys. Rev. Lett. **110**, 035303 (2013).

[184] A. Weller, J. P. Ronzheimer, C. Gross, J. Esteve, M. K. Oberthaler, D. J. Frantzeskakis, G. Theocharis, and P. G. Kevrekidis, "Experimental observation of oscillating and interacting matter wave dark solitons," Phys. Rev. Lett. **101**, 130401 (2008).

[185] M. Ma, R. Navarro, and R. Carretero-González, "Solitons riding on solitons and the quantum newton's cradle," Phys. Rev. E **93**, 022202 (2016).

[186] F. Pinsker and H. Flayac, "On-demand dark soliton train manipulation in a spinor polariton condensate," Phys. Rev. Lett. **112**, 140405 (2014).

[187] H. Terças, D. D. Solnyshkov, and G. Malpuech, "High-speed dc transport of emergent monopoles in spinor photonic fluids," Phys. Rev. Lett. **113**, 036403 (2014).

[188] K. v. Klitzing, G. Dorda, and M. Pepper, "New method for high-accuracy determination of the fine-structure constant based on quantized hall resistance," Phys. Rev. Lett. **45**, 494–497 (1980).

[189] J. Vidal, R. Mosseri, and B. Douçot, "Aharonov-bohm cages in two-dimensional structures," Phys. Rev. Lett. **81**, 5888–5891 (1998).

[190] C. C. Abilio, P. Butaud, T. Fournier, B. Pannetier, J. Vidal, S. Tedesco, and B. Dalzotto, "Magnetic field induced localization in a two-dimensional superconducting wire network," Phys. Rev. Lett. **83**, 5102–5105 (1999).

[191] C. Naud, G. Faini, and D. Mailly, "Aharonov-bohm cages in 2d normal metal networks," Phys. Rev. Lett. **86**, 5104–5107 (2001).

[192] A. P. Ramirez, "Strongly geometrically frustrated magnets," Annu. Rev. Mater. Sci. **24**, 453–480 (1994).

[193] R. Moessner and A. P. Ramirez, "Geometrical frustration," Physics Today **59**, 24–29 (2006).

[194] B. Sutherland, "Localization of electronic wave functions due to local topology," Phys. Rev. B **34**, 5208–5211 (1986).

[195] E. H. Lieb, "Two theorems on the hubbard model," Phys. Rev. Lett. **62**, 1201–1204 (1989).

[196] A. Mielke, "Ferromagnetism in the hubbard model on line graphs and further considerations," Journal of Physics A: Mathematical and General **24**, 3311 (1991).

[197] H. Tasaki, "Ferromagnetism in the hubbard models with degenerate single-electron ground states," Phys. Rev. Lett. **69**, 1608–1611 (1992).

[198] D. Leykam, A. Andreanov, and S. Flach, "Artificial flat band systems: from lattice models to experiments," Advances in Physics: X **3**, 1473052 (2018).

[199] D. C. Tsui, H. L. Stormer, and A. C. Gossard, "Two-dimensional magnetotransport in the extreme quantum limit," Phys. Rev. Lett. **48**, 1559–1562 (1982).

[200] L. Balents, "Spin liquids in frustrated magnets," Nature **464**, 199 (2010).

[201] C. Wu, D. Bergman, L. Balents, and S. Das Sarma, "Flat bands and wigner crystallization in the honeycomb optical lattice," Phys. Rev. Lett. **99**, 070401 (2007).

[202] S. D. Huber and E. Altman, "Bose condensation in flat bands," Phys. Rev. B **82**, 184502 (2010).

[203] D. López-González and M. I. Molina, "Linear and nonlinear compact modes in quasi-one-dimensional flatband systems," Phys. Rev. A **93**, 043847 (2016).

[204] G. Gligorić, A. Maluckov, L. Hadžievski, S. Flach, and B. A. Malomed, "Nonlinear localized flat-band modes with spin-orbit coupling," Phys. Rev. B **94**, 144302 (2016).

[205] R. A. Vicencio and M. Johansson, "Discrete flat-band solitons in the kagome lattice," Phys. Rev. A **87**, 061803 (2013).

[206] P. P. Beličev, G. Gligorić, A. Maluckov, M. Stepić, and M. Johansson, "Localized gap modes in nonlinear dimerized lieb lattices," Phys. Rev. A **96**, 063838 (2017).

[207] B. Keimer, S. A. Kivelson, M. R. Norman, S. Uchida, and J. Zaanen, "From quantum matter to high-temperature superconductivity in copper oxides," Nature **518**, 179–186 (2015).

[208] S. Peotta and P. P. Törmä, "Superfluidity in topologically nontrivial flat bands," Nature Communications **6**, 8944 (2015).

[209] A. Julku, S. Peotta, T. I. Vanhala, D.-H. Kim, and P. Törmä, "Geometric origin of superfluidity in the lieb-lattice flat band," Phys. Rev. Lett. **117**, 045303 (2016).

[210] Y. Cao, V. Fatemi, S. Fang, K. Watanabe, T. Taniguchi, E. Kaxiras, and P. Jarillo-Herrero, "Unconventional superconductivity in magic-angle graphene superlattices," Nature **556**, 43–50 (2018).

[211] Y. Cao, V. Fatemi, A. Demir, S. Fang, S. L. Tomarken, J. Y. Luo, J. D. Sanchez-Yamagishi, K. Watanabe, T. Taniguchi, E. Kaxiras, R. C. Ashoori, and P. Jarillo-Herrero, "Correlated insulator behaviour at half-filling in magic-angle graphene superlattices," Nature **556**, 80–84 (2018).

[212] J. T. Chalker, T. S. Pickles, and P. Shukla, "Anderson localization in tight-binding models with flat bands," Phys. Rev. B **82**, 104209 (2010).

[213] M. Goda, S. Nishino, and H. Matsuda, "Inverse anderson transition caused by flatbands," Phys. Rev. Lett. **96**, 126401 (2006).

[214] J. D. Bodyfelt, D. Leykam, C. Danieli, X. Yu, and S. Flach, "Flatbands under correlated perturbations," Phys. Rev. Lett. **113**, 236403 (2014).

[215] Y. Nakata, T. Okada, T. Nakanishi, and M. Kitano, "Observation of flat band for terahertz spoof plasmons in a metallic kagomé lattice," Phys. Rev. B **85**, 205128 (2012).

[216] M. Nixon, E. Ronen, A. A. Friesem, and N. Davidson, "Observing geometric frustration with thousands of coupled lasers," Phys. Rev. Lett. **110**, 184102 (2013).

[217] R. A. Vicencio, C. Cantillano, L. Morales-Inostroza, B. Real, C. Mejía-Cortés, S. Weimann, A. Szameit, and M. I. Molina, "Observation of localized states in lieb photonic lattices," Phys. Rev. Lett. **114**, 245503 (2015).

[218] G.-B. Jo, J. Guzman, C. K. Thomas, P. Hosur, A. Vishwanath, and D. M. Stamper-Kurn, "Ultracold atoms in a tunable optical kagome lattice," Phys. Rev. Lett. **108**, 045305 (2012).

[219] M. Aidelsburger, M. Lohse, C. Schweizer, M. Atala, J. T. Barreiro, S. Nascimbène, N. R. Cooper, I. Bloch, and N. Goldman, "Measuring the Chern number of Hofstadter bands with ultracold bosonic atoms," Nature Physics **11**, 162–166 (2015).

[220] S. Taie, H. Ozawa, T. Ichinose, T. Nishio, S. Nakajima, and Y. Takahashi, "Coherent driving and freezing of bosonic matter wave in an optical lieb lattice," Sci. Adv. **1** (2015), 10.1126/sciadv.1500854.

[221] D. Guzmán-Silva, C. Mejía-Cortés, M. A. Bandres, M. C. Rechtsman, S. Weimann, S. Nolte, M. Segev, A. Szameit, and R. A. Vicencio, "Experimental observation of bulk and edge transport in photonic lieb lattices," New J. of Phys. **16**, 063061 (2014).

[222] S. Mukherjee, A. Spracklen, D. Choudhury, N. Goldman, P. Öhberg, E. Andersson, and R. R. Thomson, "Observation of a localized flat-band state in a photonic lieb lattice," Phys. Rev. Lett. **114**, 245504 (2015).

[223] F. Baboux, L. Ge, T. Jacqmin, M. Biondi, E. Galopin, A. Lemaître, L. Le Gratiet, I. Sagnes, S. Schmidt, H. E. Türeci, A. Amo, and J. Bloch, "Bosonic condensation and disorder-induced localization in a flat band," Phys. Rev. Lett. **116**, 066402 (2016).

[224] S. Mukherjee, M. Di Liberto, P. Öhberg, R. R. Thomson, and N. Goldman, "Experimental observation of aharonov-bohm cages in photonic lattices," Phys. Rev. Lett. **121**, 075502 (2018).

[225] A. Ramachandran, A. Andreanov, and S. Flach, "Chiral flat bands: Existence, engineering, and stability," Phys. Rev. B **96**, 161104 (2017).

[226] B. A. McKinnon and T. C. Choy, "Significance of nonorthogonality in tight-binding models," Phys. Rev. B **52**, 14531–14538 (1995).

[227] A. Amo, T. C. H. Liew, C. Adrados, R. Houdré, E. Giacobino, A. V. Kavokin, and A. Bramati, "Exciton–polariton spin switches," Nat. Photon. **4**, 361 (2010).

[228] B. Real, C. Cantillano, D. López-González, A. Szameit, M. Aono, M. Naruse, S.-J. Kim, K. Wang, and R. A. Vicencio, "Flat-band light dynamics in stub photonic lattices," Sci. Rep. **7**, 15085 (2017).

[229] T. J. Alexander, E. A. Ostrovskaya, and Y. S. Kivshar, "Self-trapped nonlinear matter waves in periodic potentials," Phys. Rev. Lett. **96**, 040401 (2006).

[230] T. Anker, M. Albiez, R. Gati, S. Hunsmann, B. Eiermann, A. Trombettoni, and M. K. Oberthaler, "Nonlinear self-trapping of matter waves in periodic potentials," Phys. Rev. Lett. **94**, 020403 (2005).

[231] F. H. Bennet, T. J. Alexander, F. Haslinger, A. Mitchell, D. N. Neshev, and Y. S. Kivshar, "Observation of nonlinear self-trapping of broad beams in defocusing waveguide arrays," Phys. Rev. Lett. **106**, 093901 (2011).

[232] C. Bersch, G. Onishchukov, and U. Peschel, "Optical gap solitons and truncated nonlinear bloch waves in temporal lattices," Phys. Rev. Lett. **109**, 093903 (2012).

[233] J. E. Sipe, "Gap Solitons," in *Guided Wave Nonlinear Optics* (Springer Netherlands, Dordrecht, 1992) pp. 305–318.

[234] D. K. Campbell, S. Flach, and Y. S. Kivshar, "Localizing Energy Through Nonlinearity and Discreteness," Physics Today **57**, 43–49 (2004).

[235] T. Alexander and Y. Kivshar, "Soliton complexes and flat-top nonlinear modes in optical lattices," Applied Physics B **82**, 203–206 (2006).

[236] J. Wang, J. Yang, T. J. Alexander, and Y. S. Kivshar, "Truncated-bloch-wave solitons in optical lattices," Phys. Rev. A **79**, 043610 (2009).

[237] S. R. K. Rodriguez, W. Casteels, F. Storme, N. Carlon Zambon, I. Sagnes, L. Le Gratiet, E. Galopin, A. Lemaître, A. Amo, C. Ciuti, and J. Bloch, "Probing a dissipative phase transition via dynamical optical hysteresis," Phys. Rev. Lett. **118**, 247402 (2017).

[238] T. Fink, A. Schade, S. Höfling, C. Schneider, and A. Imamoglu, "Signatures of a dissipative phase transition in photon correlation measurements," Nature Physics **14**, 365–369 (2018).

[239] W. Casteels, R. Rota, F. Storme, and C. Ciuti, "Probing photon correlations in the dark sites of geometrically frustrated cavity lattices," Phys. Rev. A **93**, 043833 (2016).

[240] R. Rota, W. Casteels, and C. Ciuti, "On the robustness of strongly correlated multi-photon states in frustrated driven-dissipative cavity lattices," Eur. Phys. J. Spec. Top. **226**, 2805–2814 (2017).

[241] T. Ozawa, "Steady-state hall response and quantum geometry of driven-dissipative lattices," Phys. Rev. B **97**, 041108 (2018).

[242] S. A. Parameswaran, R. Roy, and S. L. Sondhi, "Fractional quantum hall physics in topological flat bands," Comptes Rendus Physique **14**, 816–839 (2013).

[243] E. J. Bergholtz and Z. Liu, "Topological flat band models and fractional chern insulators," International Journal of Modern Physics B **27**, 1330017 (2013).

[244] E. Tang, J.-W. Mei, and X.-G. Wen, "High-temperature fractional quantum hall states," Phys. Rev. Lett. **106**, 236802 (2011).

[245] K. Sun, Z. Gu, H. Katsura, and S. Das Sarma, "Nearly flatbands with non-trivial topology," Phys. Rev. Lett. **106**, 236803 (2011).

[246] T. Neupert, L. Santos, C. Chamon, and C. Mudry, "Fractional quantum hall states at zero magnetic field," Phys. Rev. Lett. **106**, 236804 (2011).

[247] P. Cristofolini, G. Christmann, S. I. Tsintzos, G. Deligeorgis, G. Konstantinidis, Z. Hatzopoulos, P. G. Savvidis, and J. J. Baumberg, "Coupling quantum tunneling with cavity photons," Science **336**, 704–7 (2012).

[248] S. Ravets, P. Knüppel, S. Faelt, O. Cotlet, M. Kroner, W. Wegscheider, and A. Imamoglu, "Polaron polaritons in the integer and fractional quantum hall regimes," Phys. Rev. Lett. **120**, 057401 (2018).

[249] L. Lu, J. D. Joannopoulos, and M. Soljačić, "Topological photonics," Nature Photonics **8**, 821–829 (2014).

[250] T. Ozawa, H. M. Price, A. Amo, N. Goldman, M. Hafezi, L. Lu, M. Rechtsman, D. Schuster, J. Simon, O. Zilberberg, and I. Carusotto, "Topological photonics," (2018), arXiv:1802.04173 .

[251] E. Togan, H.-T. Lim, S. Faelt, W. Wegscheider, and A. Imamoglu, "Enhanced interactions between dipolar polaritons," Phys. Rev. Lett. **121**, 227402 (2018).

[252] I. Carusotto, D. Gerace, H. E. Tureci, S. De Liberato, C. Ciuti, and A. Imamoğlu, "Fermionized photons in an array of driven dissipative nonlinear cavities," Phys. Rev. Lett. **103**, 033601 (2009).

[253] D. Sanvitto and S. Kéna-Cohen, "The road towards polaritonic devices," Nature Materials **15**, 1061–1073 (2016).

Titre : Fluides quantiques de polartions dans des réseaux unidimensionnels synthétiques : localisation, propagation et interactions

Mots clés : Polaritons de cavité, Fluides quantiques, Non-linéarité, Microstructures, Spectroscopie optique

Résumé : Les microcavités à semiconducteurs apparaissent aujourd'hui comme une plateforme particulièrement propice à l'étude des fluides quantiques en interactions. Dans ces cavités, la lumière et les excitations électroniques sont confinées dans de petits volumes et leur couplage est rendu si fort que les propriétés optiques sont gouvernées par des quasi-particules hybrides lumière-matière appelées polaritons de cavité. Ces quasi-particules se propagent comme des photons, mais interagissent avec leur environnement via leur partie matière. Elles peuvent occuper massivement un même état quantique et se comporter comme une onde macroscopique cohérente et non-linéaire. On parle alors de fluide quantique de lumière.

Dans cette thèse, nous étudions la dynamique de fluides quantiques de polaritons dans différentes microstructures unidimensionnelles. La technologie de gravure de microcavités planaires, développée au C2N, permet de réaliser une ingénierie complète du potentiel dans lequel nous générons ces fluides de polaritons et d'implémenter des géométries complexes. Dans une première partie, nous avons étudié les propriétés de localisation des états propres de réseaux synthétiques quasi-périodiques. L'exploration théorique du diagramme de phase de localisation des modes propres a dévoilé une nouvelle transition de type délocalisation-localisation lors d'une déformation originale d'un quasi-cristal, transition que nous avons pu observer expérimentalement. Une deuxième partie de la thèse est consacrée à l'étude de la dynamique non-linéaire de deux fluides contra-propageant dans un canal unidimensionnel. La compétition entre énergie cinétique et énergie d'interactions conduit alors à l'apparition de solitons sombres, dont le nombre discret et la position peuvent être contrôlés optiquement. Nous avons mis en évidence une bistabilité contrôlée par la différence de phase imprimée sur les deux fluides. La dernière partie du travail concerne l'étude des non-linéarités pour un fluide de polaritons occupant une bande plate. L'énergie cinétique du fluide y est nulle, si bien que sa propagation est gelée. Nous observons alors la formation de domaines non-linéaires de taille quantifiée.

Ce travail ouvre des perspectives prometteuses, tout particulièrement pour l'exploration de phases topologiques de bosons en interactions. De plus, augmenter les interactions permettrait d'utiliser notre plate-forme comme un simulateur quantique.

Title: Polariton quantum fluids in 1D synthetic lattices: localization, propagation and interactions

Keywords: Cavity polaritons, Quantum fluids, Nonlinearity, Microstructures, Optical spectroscopy

Abstract: Semiconductor microcavities have emerged as a powerful platform for the study of interacting quantum fluids. In these cavities, light and electronic excitations are confined in small volumes, and their coupling is so strongly enhanced that optical properties are governed by hybrid light-matter quasiparticles, known as cavity polaritons. These quasiparticles propagate like photons and interact with their environment via their matter part. They can macroscopically occupy a single quantum state and then behave as an extended coherent nonlinear wave, i.e. as a quantum fluid of light.

In this thesis, we study the nonlinear dynamics of polariton quantum fluids in various one-dimensional microstructures. The possibility to etch microstructures out of planar cavities, a technology developed at C2N, allows full engineering of the potential landscape for the polariton fluid, and implementing complex geometries. In a first part, we have studied the localization properties of the eigenstates in synthetic quasiperiodic lattices. Theoretical exploration of the localization phase diagram revealed a novel delocalization-localization transition in an original deformation of a quasicrystal and we have experimentally evidenced this transition. A second part of the thesis is dedicated to the study of the nonlinear dynamics of two counterpropagating polariton fluids in a one-dimensional channel. The interplay between kinetic and interaction energy is responsible for the formation of dark solitons, whose number and position can be controlled by optical means. We have evidenced a bistable behaviour controlled by the phase twist imprinted on the two fluids. The last part of this work addresses the study of nonlinearities for a fluid injected in a flat band. Therein, the kinetic energy of the fluid is quenched, so that propagation is frozen. We then observe the formation of nonlinear domains with quantized size.

This work opens us exciting perspectives, specifically towards the exploration of topological phases of interacting bosons. Enhancing interactions would also allow using our platform for quantum simulation.